Hard X-Ray Detection and Timing of Accretion-Powered Pulsars with BATSE

Thesis by
Deepto Chakrabarty

In Partial Fulfillment of the Requirements
for the Degree of
Doctor of Philosophy

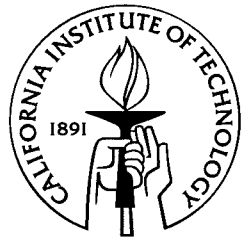

California Institute of Technology
Pasadena, California
1996
(Submitted December 21, 1995)

And this is my Quest,
To follow that star,
No matter how hopeless,
No matter how far...

—Joe Darion, *The Man of La Mancha* (1965)

Acknowledgements

Unwept, unhonor'd, and unsung.
—Sir Walter Scott (1805)

I am indebted to Tom Prince for being an outstanding advisor and mentor. I am full of admiration for the various attributes which constitute his style of doing science: the skill at choosing important problems to study, the rigorous approach to posing and defining the boundaries of these problems, the elegant and ambitious tools aggressively applied to solve them, the polished communication of the results, and the cool, professional detachment with which unexpected difficulties are confronted, appraised, and overcome. The sheer number of projects he is able to pursue successfully is mind-boggling. I very much appreciate Tom's indulgence in allowing me to pursue a wide variety of projects myself, and also his admonitions to maintain sufficient focus to make important contributions rather than merely skim the surface.

I am also grateful to Lars Bildsten, who has played a very large role in my development as an astrophysicist. His unerring ability to a reduce a problem to its basic physics after a few minutes at the blackboard, the clarity of his explanations and insights, and his seemingly endless and encyclopedic knowledge of astronomy and astrophysics have been an education in how to think about problems and what questions to ask. His practical insights and candid advice on the daily trials of doing science and his cheerful willingness to always look at "just one more cool plot" were also greatly appreciated.

In working on the BATSE Pulsar Key Project, I have been fortunate to collaborate with some outstanding researchers, especially John Grunsfeld and my fellow graduate student Danny Koh here at Caltech, and Mark Finger of the BATSE instrument team at NASA/MSFC. I owe special thanks to John, who trained me in the day-to-day business of high-energy astrophysics and oversaw much of my work during my first two years here. His enthusiasm, ambition, and tenacity were a lesson by example. I am glad that I overlapped with the recent arrival of Brian Vaughan, and with the even more recent arrival of Rob Nelson; they were both welcome additions to the Caltech effort. Thanks to Jerry Fishman, Bob Wilson and the entire BATSE group at MSFC for many useful discussions throughout my thesis work, and especially during my visits to Huntsville; and to Jerry Fishman in

particular for acting as agency sponsor for a NASA graduate fellowship. Special thanks are due to the entire BATSE instrument team, which has had the difficult task of supporting BATSE, its operations, and its guest investigators, while also pursuing a wide range of science topics.

One of the privileges of working in astrophysics at Caltech is the large number of faculty, staff, and postdoctoral scientists on hand to learn from. I happily acknowledge many useful discussions with Stuart Anderson, Lee Armus, Roger Blandford, John Carlstrom, Curt Cutler, Melvyn Davies, Fiona Harrison, Vicky Kaspi, Dong Lai, Rob Nelson, Gerry Neugebauer, Neill Reid, Maarten Schmidt, Tom Soifer, Steve Thorsett, Marten van Kerkwijk, and Brian Vaughan. One of Caltech's most precious resources in astrophysics has been its Astrophysics Library and its librarians, Helen Knudsen and Anne Snyder. Our community has suffered a serious loss with Helen's recent retirement. I have been further privileged to work in Caltech's Space Radiation Laboratory. Thanks to Frances Spalding and Louise Sartain at SRL for flawlessly navigating me through administrative hurdles; Laura Carriere, Minerva Calderon, and Bruce Sears for working day and night (literally) to keep our computers crunching numbers and exchanging e-mail; and Debby Kubly for doing her best to find me good mail every day.

I have pursued several optical follow-up projects related to my thesis work. These efforts have been both productive and fun, in large part due to my long-time collaborator in much of this work, Paul Roche. Thank you to Malcolm Coe for his hospitality and support during a visit to Southampton work with Paul. Jim McCarthy, Xiaopei Pan, Marshall Cohen, Angela Putney, Ian Thompson, and Bob Hill answered many questions while I was learning to use the instruments at Palomar Observatory, and Skip Staples and Jean Mueller kept things running smoothly during the observations. I am grateful to my old friend Stephen Levine for helping to put together a productive visit to the Observatorio Astronómico Nacional 2.1-m telescope on an isolated mountain top in San Pedro Mártir, Baja California, and I thank Luis Aguilar and the UNAM Insituto de Astronomía in Ensenada for covering my expenses during this trip. I am also grateful for a generous travel grant and observing time allocation from the Cerro Tololo Inter-American Observatory in Chile for thesis-related work. It is a pleasure to thank Andy Layden, Ramon Galvez, Patricio Ugarte, Arlo Landolt, and Bruce Margon for helpful assistance, discussions, and guidance during my visit to CTIO. Thanks also to Paul Eskridge and Stefanie Wachter for taking some finder images for me on other CTIO telescopes.

I probably would not have been invited to study at Caltech had it not been for the research opportunities given me by Richard Muller at LBL, and I would not have thought to contact Rich about a job after finishing at MIT had it not been suggested by my old friend Don Alvarez. Thanks to both of them for helping to get me here. Since then, my 5.2 years at Caltech have been made much easier by the wonderful friends I've met here. From the very first day on campus, no physics graduate student at Caltech can fail to appreciate the care with which Donna Driscoll looks after us. Getting through the first year courses would have much more unpleasant without the weekly late-night get-togethers in the LIGO conference room with Ruth Brain, Aaron Gillespie, James Larkin, Torrey Lyons, Sima Setayeshgar, Selmer Wong, and our other classmates. For close friendships forged through work, lunch, coffee, dinner, spirited arguments, idle chatting, and evenings of random cosmopolitanism (kudos to Charlene Reichert for coining this apt term), I would especially like to thank Paul Ray, Biff Heindl, Fiona Harrison, Lars Bildsten, Steve Thorsett, Andrea Ghez, Tom LaTourrette, Alycia Weinberger, David Hogg, Vicky Kaspi, Dominic Benford, and Alan Wiseman. Some of these people left Caltech before me, while others will remain after I leave, but they are all a large part of what I will remember when I think back to these years.

I have been lucky to share a spacious and comfortable apartment with my friend Robert Knop. I thank Robert for his patience with me and for endless hours of shared zaniness involving musical revues, physics, theatre, neural nets, chamber music, waltz orchestras, pizza, ice cream, the Oph object, Unix, and various incarnations of *Star Trek*. I also thank him in advance for teaching me to solder. A large fraction of my waking hours have been spent at the lab, and these hours have been made more fun and interesting by my office-mates: David Palmer, Jeff Hammond, Tim Shippert, Alycia Weinberger, Stinson Gibner, Biff Heindl, Daniel Williams, Yu Cao, Song Wang, and Stéphane Corbel. I thank Shirley Marneus, Delores Bing, and Allen Gross for my providing me with opportunities to indulge my interests in the arts. In these activities, I have had the pleasure of working with some fine musicians, especially Tom LaTourrette, Diana Lorden, Jamie Schlessman, Russ Litchfield, Peter Hofstee, Jerome Claverie, Ari Kaplan, Missy Richmond, and Elizabeth Boer.

Life in graduate school is a lengthy and trying effort, especially in the bizarre land that is Los Angeles, and the connections to my family and old friends back in civilized places like New York, Boston, and the Bay Area were necessary to get through it. All

the visits and talks with people like Beth Multer, Larry Arnold, Corinne Wayshak, Patrick Beard, and Tim Sasseen were essential to maintaining my sanity. For the last two years, getting to know my very special and sweet friend Susan Elia has brought me great joy. For more than half a lifetime, I have been able to depend on one of my oldest and best friends, Nina Sonenberg. But I am most grateful for the lifelong and unconditional love, support, and encouragement always offered by my parents and my sister, even when they did not understand what I was doing or why.

It is a pleasure to acknowledge support from a National Aeronautics and Space Administration Graduate Student Research Program fellowship, under grant NGT-51184. I also thank the National Science Foundation for generous travel support which allowed me to attend two NATO Advanced Study Institutes: "The Gamma-Ray Sky with Compton GRO and SIGMA" in Les Houches, France, in January 1994; and "Evolutionary Processes in Binary Stars" in Cambridge, England, in July 1995. The research in this thesis was supported in part by the NASA *Compton Observatory* Guest Observer Program, under grant NAG 5-1458; and by the NASA Long-Term Space Astrophysics Program, under grant NAGW-4517.

Hard X-Ray Detection and Timing of Accretion-Powered Pulsars with BATSE

Deepto Chakrabarty

California Institute of Technology

Abstract

The BATSE all-sky monitor on the *Compton Gamma Ray Observatory* is a superb tool for the study of accretion-powered pulsars. In the first part of this thesis, I describe its capabilities for hard X-ray observations above 20 keV, present techniques for timing analysis of the BATSE data, and discuss general statistical issues for the detection of pulsed periodic signals in both the time and frequency domains. BATSE's 1-day pulsed sensitivity in the 20–60 keV range is ≈ 15 mCrab for pulse periods 2 s$\lesssim P_{\rm pulse} \lesssim$400 s, covering most of the known accreting pulsars. Its sensitivity degrades substantially outside of this range.

In the second part of this thesis, I present the results of several science investigations applying these techniques. Half the 42 known accreting pulsars have been detected with BATSE and are monitored whenever they are active. Except for a few which lie outside of BATSE's sensitivity range, the rest are all transient sources which may eventually be detected in outburst. The detected systems include four new transients discovered by BATSE, one of which is discussed in detail. A new technique used to localize this source, GRO J1948+32, is described.

Observations of the 38-s pulsar OAO 1657–415 discovered that it is in a 10.4-d eccentric orbit and undergoes regular X-ray eclipses by its massive companion, making it only the seventh known eclipsing X-ray pulsar. Constraints placed by the pulsar mass function and the eclipse duration indicate that the undetected binary companion must be an OB supergiant. If the companion can be identified and its orbital velocity measured, the neutron star mass can be determined.

The 7.7-s pulsar 4U 1626–67 was found to be in an extended spin-down state, ending over a decade of rapid, steady spin-up. It is only the second steady-state disk accreter known to have undergone a torque reversal. The other, the 2-min pulsar GX 1+4, underwent two torque reversals during our observations and is detected up to 160 keV. During spin-down, we find that pulsed flux and torque in GX 1+4 are *anticorrelated*, the opposite of what is predicted by the usual theories of magnetic accretion torques.

Thesis supervisor: Thomas A. Prince, Professor of Physics

Contents

List of Figures

List of Tables

Note on Terms, Units, and Names

In this thesis, *soft X-ray* refers to a photon with energy $\lesssim 10$ keV, while *hard X-ray* or *soft gamma-ray* refers to a photon with energy $\gtrsim 10$ keV. These terms are historical artifacts arising from the observational techniques used to detect these photons.

Physical quantities in this thesis are generally quoted in the standard Gaussian CGS system, with a few exceptions. Photon energy is quoted in *kilo-electron-volts* (keV), where 1 keV $= 1.6 \times 10^{-9}$ erg. Orbital distances are quoted in *light-seconds* (lt-s), where 1 lt-s $= 3 \times 10^{10}$ cm. Stellar distances are quoted in *kiloparsecs* (kpc), where 1 kpc $= 3 \times 10^{21}$ cm. Masses and radii of stellar objects are quoted in *solar masses* ($M_\odot$) and *solar radii* ($R_\odot$), where 1 $M_\odot = 2 \times 10^{33}$ g and 1 $R_\odot = 8 \times 10^{10}$ cm. In standard astronomical usage, dates are quoted using the *Julian date* (JD) system, which gives the time in days elapsed since Greenwich mean noon on 4713 B.C. January 1, Julian proleptic calendar. I quote dates using *Modified Julian dates* (MJD), which are defined by MJD = JD − 2,400,000.5. In BATSE operations work, dates are often quoted as *Truncated Julian dates* (TJD), which are defined as TJD = JD − 2,440,000.5 = MJD − 40,000.0. Note that while dates on the JD system begin at Greenwich mean noon, dates on the MJD and TJD systems (as well as, obviously, UT civil dates) begin at Greenwich mean midnight. This is an endless source of confusion in the astrophysical literature.

It is often useful in X-ray and gamma-ray astronomy to refer the photon flux in a given bandpass to a known fiducial, the total emission of the Crab Nebula in the same bandpass. In this usage,

$$1 \text{ Crab} \approx \int_{E_{\rm lo}}^{E_{\rm hi}} 10\, E^{-2.15} dE \text{ photon cm}^{-2} \text{ s}^{-1},$$

where photon energy is measured in keV. The Crab is also sometimes used as a fiducial for flux *density* in a bandpass. These usages are equivalent for Crab-like spectra. Both comparisons are of limited utility for spectral shapes dissimilar to the Crab.

The standard naming conventions for cosmic X-ray and gamma-ray sources fall into three categories. The oldest bright X-ray sources were named in order of discovery in the nearest constellation (e.g., Cygnus X-1). Now that many more sources are known, they are generally named according to their celestial coordinates. Some X-ray sources lying in the Galactic plane were named according to their Galactic longitude and latitude; for example, GX 301–2 lies near $l = 301°$ and $b = -2°$. More commonly, sources are named according to their right ascension and declination, along with a prefix indicating the spacecraft which discovered the source or the catalog listing it. For example, GRO 1948+32 was discovered by BATSE on the *Compton Gamma Ray Observatory* and lies near $\alpha = 19^{\rm h}\,48^{\rm m}$ and $\delta = 32°$.

Chapter 1

Accretion-Powered Pulsars and BATSE

You can observe a lot by watching.
—Yogi Berra

1.1 Overview and Project History

1.1.1 Accretion-Powered Pulsars and the Role of BATSE

Accretion-powered binary X-ray pulsars are rotating, highly magnetized neutron stars which are capturing matter from a stellar companion. As in rotation-powered (radio) pulsars, the dipole axis of the magnetosphere is thought to be tilted with respect to the spin axis of the neutron star. Accreting matter is channeled by the magnetosphere onto the magnetic poles and is gravitationally accelerated to a velocity $\sim 0.1c$ by the time it reaches the neutron star surface. The rapid deceleration of this matter at the polar surface releases gravitational potential energy as X-rays, and the rotation of these X-ray hot spots through our line of sight gives rise to periodic pulsed emission. Since the discovery of pulsations from Centaurus X-3 a quarter century ago, over 40 accretion-powered pulsars have been detected. These objects are a valuable laboratory for a wide variety of topics, including binary evolution, neutron star structure, accretion physics, and the physics of radiation and plasma in a strong magnetic field.

Throughout the 1970s and 1980s, a series of X-ray telescopes accumulated detailed observations of accreting pulsars. Although these sensitive missions built up a rich archive of data on many sources, there were limitations imposed by the sparse time sampling inherent in the use of pointed telescopes. X-ray sources tend to be dramatically time-variable,

sometimes undergoing a bright outburst and then remaining dormant for months or years. Observations of some sources depended upon serendipitously scheduled pointings, hampering measurement of orbital parameters and timing histories. Although scanning wide-field instruments capable of rudimentary all-sky coverage did exist in these years, they typically had limited sensitivity and poor time resolution.

The launch of the Burst and Transient Source Experiment (BATSE) on the *Compton Gamma Ray Observatory* in 1991 April revolutionized timing studies of accreting pulsars. The continuous, all-sky coverage provided by BATSE allows simultaneous study of a large fraction of the known pulsars on a wide variety of time scales (from a few seconds to several years), with no bias against transient systems. The large area of the BATSE detectors makes them substantially more sensitive then previous wide-field monitors. The good (1.024 s) timing resolution allows coverage of most of the pulsation phase space ($P > 2$ s) of the known accreting pulsars. In addition, the rapid (within 1 day) availability of the data for processing allows BATSE to act as a trigger for multiwavelength follow-up of unusual events.

BATSE does suffer from some important limitations. While most of the luminosity of accreting pulsars is emitted at energies below 20 keV, BATSE is only sensitive to emission above 20 keV. Moreover, because its detectors are totally uncollimated and the pulsar observations are background-limited, only the pulsed component of the flux can be easily detected. The steady unpulsed component is indistinguishable from the background unless the source is bright enough to detect using Earth occultations. The strong modulation of the background on *Compton* orbital time scales makes long-period ($P \gtrsim 500$ s) pulsars difficult to detect. At the same time, the normal 1-s sampling rate excludes very short period ($P \lesssim 2$ s) pulsars, perpetuating an observational bias which has existed for some time. Finally, BATSE's poor spatial resolution leaves it unable to localize new pulsars to better than $\sim 1°$, insufficient for identification of an optical companion.

Despite these limitations, BATSE has proven a superb tool for the study of accreting pulsars. Immediately after the launch of *Compton*, a program to explore BATSE's capabilities in this area was begun at Caltech under the overall direction of Prof. Thomas Prince, in close cooperation with the BATSE instrument team at NASA Marshall Space Flight Center (MSFC) in Huntsville, Alabama. As part of that effort, a "first generation" system for reducing and analyzing BATSE timing observations was developed at Caltech by the author, in collaboration with Prof. Prince, Dr. John Grunsfeld, Dr. Lars Bild-

sten, and graduate student Towsian Koh. Investigations with this first generation system concentrated on several known accreting pulsars as a way to develop the necessary tools, characterize the data, and optimize the analysis. Searches for new pulsars were also pursued. Related work was pursued in parallel at MSFC by Dr. Mark Finger and Dr. Robert Wilson.

These first generation efforts have concentrated on three general scientific topics:

- **Population and Activity.** More than half the known accreting pulsars are transient sources which were discovered during bright outbursts. Due to incomplete and non-uniform sky coverage in the past, the population and recurrence history of transient systems are poorly determined. Studies with *Ginga* suggest that there is a very large number of undiscovered, low-luminosity transients in the Galaxy (Koyama et al. 1989). BATSE's long-term uniform coverage is ideal for probing this population, and it retains good sensitivity in the Galactic plane since hard X-ray emission is not subject to any significant interstellar absorption. Of the 42 accreting pulsars currently known, 20 have already been detected with BATSE as of this writing (Table 1.1) and are monitored whenever they are active. Of the remaining systems, 7 have pulse periods outside of BATSE's sensitivity range and 3 have spectra known to cut off below 20 keV, but most of the rest are transients which may eventually be detected in outburst. The detected systems include four *new* transients discovered by BATSE.

- **Orbital Parameters and Neutron Star Masses.** Precise measurement of binary orbital parameters are possible with accreting pulsars. Measurement of orbital evolution in these systems provides a sensitive probe of the role of tidal torques in the evolution of massive binaries. In systems which undergo X-ray eclipses by the pulsar's companion, it is possible to use pulsar orbital measurements to constrain the mass of the neutron star if a radial velocity curve is available for the companion. This has been done in only 6 eclipsing X-ray pulsar systems, and these types of measurements may eventually be able to point out any evolutionary differences between these neutron stars and ones in radio pulsar binaries. BATSE has measured or improved orbital parameters in 9 of the 15 systems in which these parameters are known (Table 1.2). BATSE has also discovered X-ray eclipses in a seventh accreting pulsar system, raising the possibility of a new neutron star mass measurement.

- **Accretion torques.** The torque exerted on an accreting star is an important issue in

binary evolution, star formation, neutron star structure, and the origin of millisecond radio pulsars. Accreting pulsars are the best available laboratory for studying these torques. BATSE discovered the extended spin-down state of the accreting pulsar 4U 1626–67, identifying only the second steady disk-accreter to undergo a torque reversal. BATSE has also discovered an anticorrelation between torque and luminosity in another accreting pulsar, GX 1+4. This behavior is the opposite of what is predicted by most theories of disk accretion.

In light of the outstanding success of the first generation program and the experience gained in developing it, Caltech and MSFC have embarked on a joint effort for a systematic and comprehensive reanalysis of the BATSE data with the goal of producing a uniform data archive for the known accreting pulsars. At Caltech, the second generation analysis is currently being developed and executed by graduate student Towsian Koh and Dr. Brian Vaughan in collaboration with the investigators listed above. This analysis is still in progress, and its results will be presented elsewhere.

1.1.2 Thesis Organization

This thesis describes BATSE's technical capabilities as a tool for the detection and timing of accretion-powered pulsars and presents the results of several science investigations by the author and collaborators with the first generation analysis. The remainder of this chapter gives a brief introduction to accreting pulsars. Chapter 2 describes the BATSE instrument, its capabilities for observations of pulsed X-ray sources, and methods for analyzing BATSE data. Chapter 3 reviews statistical issues involving the detection and strength measurement of pulsed signals in both the time domain and the frequency domain.

Chapter 4 presents BATSE timing observations of the 38 s accreting X-ray pulsar OAO 1657–415, which have revealed a 10.4-d binary orbit with a 2-d X-ray eclipse by the stellar companion. A pulse arrival time analysis of 20–60 keV data was used to determine the binary orbital parameters. From the pulsar mass function [$f_x(M) = 11.7 \pm 0.2\ M_\odot$] and the measured eclipse half-angle ($\theta_e = 29°.7 \pm 1°.3$), it is inferred that the stellar companion is a supergiant of spectral class B0–B6. If the companion can be identified and its orbital velocity measured, the neutron star mass can be constrained. Both intrinsic spin-up and spin-down of the pulsar were observed.

Chapter 5 describes the discovery of an 18.7 s transient X-ray pulsar in the Cygnus

region. GRO J1948+32 has been localized to within 10 deg^2 using a method developed for positioning weak pulsed sources with BATSE. During the 33 d outburst, the phase-averaged 20–75 keV pulsed flux rose from 25 mCrab to 50 mCrab over 10 days and then decayed below our detection threshold over nearly 25 days. A photon spectral index of $\gamma = 2.65 \pm 0.15$ (assuming photon flux density $dN/dE \propto E^{-\gamma}$) was measured during a bright interval. The observed modulation of the neutron star's pulse frequency is suggestive of orbital variation over less than one orbit cycle. Assuming a constant spin frequency derivative over the outburst, we can place limits on the pulsar parameters: orbital period 35 d $< P_{\rm orb} <$ 70 d; orbital radius 75 lt-s $< a_{\rm x} \sin i <$ 300 lt-s, eccentricity $e < 0.25$, spin frequency derivative 5×10^{-13} Hz s^{-1} $< \dot{\nu} < 2.5 \times 10^{-11}$ Hz s^{-1}, X-ray mass function $0.5 M_\odot < f_{\rm x}(M) < 5 M_\odot$. The stellar type of the mass donor is still not known.

Chapter 6 reports on over 4 years of monitoring of the 7.66 s accretion-powered pulsar 4U 1626–67. These observations revealed that the source is now steadily spinning down, in marked contrast to the steady spin-up observed during 1977–1989. Remarkably, the magnitudes of the spin-up and spin-down torques differ by only 15%, with the neutron star spin changing on a time scale $|\nu/\dot{\nu}| \approx 5000$ yr in both states. This is only the second accreting pulsar (the other is GX 1+4) which has shown extended, steady intervals of both spin-up and spin-down. The current spin-down rate of 4U 1626–67 is itself decreasing on a time scale $|\dot{\nu}/\ddot{\nu}| \approx 12$ yr. After subtracting the $\dot{\nu}$ and $\ddot{\nu}$ trends, the pulse phase residuals show aperiodic oscillatory excursions consistent with a random walk in pulse frequency of strength $\sim 10^{-22}$ Hz^2 s^{-1}. The spin frequency second derivative $\ddot{\nu}$ is too large to arise from this random walk process.

Chapter 7 reports on almost five years of continuous observations of the 2 min accretion-powered pulsar GX 1+4. Pulsed emission was detected at energies up to 160 keV. On average, the neutron star is spinning down rapidly on a time scale $|\nu/\dot{\nu}| \approx 70$ yr. This trend was interrupted in 1994 November by a brief interval of spin-up which ended in 1995 March. The mean spin-down rate is itself decreasing on a time scale $|\dot{\nu}/\ddot{\nu}| \approx 10$ yr. After subtracting the $\dot{\nu}$ and $\ddot{\nu}$ trends, the timing data show $1/f$ fluctuations in torque, similar to Cen X-3 but in marked contrast to Her X-1, Vela X-1, and 4U 1626–67. The hard X-ray pulsed flux history consists of a steady, quiescent level with a number of short ($\sim$ 20 d) flares superimposed, as well as a sustained (200 d) bright state during the spin-up episode. During spin down, the pulsed flux and torque are *anticorrelated*, with the short flares in luminosity accompanied by an enhanced spin-down torque. If the hard X-ray pulsed intensity is a good

tracer of accretion rate, then this spin-down behavior is the opposite of what is predicted by the usual theories of magnetic disk accretion.

1.2 Background on Accretion-Powered Pulsars

1.2.1 Early History[1]

The study of compact objects began with the discovery of white dwarfs, stars with mass $\sim 1\,M_\odot$ but with a very small radius $\sim 10^4$ km (Adams 1915, 1925). The contemporaneous revolution in physics soon provided an explanation for these surprising objects, and Fowler (1926) was able to point out that electron degeneracy pressure must prevent the gravitational collapse of these cold stars, immediately following the development of Fermi-Dirac statistics (Dirac 1926). Chandrasekhar (1931) and Landau (1932) computed models for white dwarf structure and showed that there is a maximum stable mass of $\sim 1.3\,M_\odot$ for a degenerate electron gas. It was soon realized that a similar limit applied to a degenerate neutron gas.

That realization was made possible by the discovery of the neutron (Chadwick 1932). Shortly thereafter, Baade & Zwicky (1934) proposed the existence of neutron stars, which they suggested might be formed in supernova explosions. Oppenheimer & Volkoff (1939) made the first calculations for the structure of a star composed of a degenerate neutron gas. There was speculation at this time that the formation of neutron cores might be a power source for massive normal stars (Gamow 1937; Landau 1938; Oppenheimer & Serber 1938), but the overwhelming success of nuclear fusion models for stellar evolution soon put this idea to rest. Neutron stars remained little more than an intellectual curiosity for the next 20 years (see Harrison et al. 1965).

The discovery of Scorpius X-1 with a rocket-borne experiment (Giacconi et al. 1962) heralded the dawn of high energy astrophysics and revived theoretical interest in neutron stars. During the next few years, a series of rocket and balloon experiments discovered more than a dozen cosmic X-ray sources. The identification of an optical counterpart of Sco X-1 (Sandage et al. 1966) led Shklovsky (1967) to propose that the X-ray emission arises from the accretion of gas onto a neutron star from a close binary stellar companion.

[1] I have drawn heavily from the detailed historical sketches given by Shapiro & Teukolsky (1983) and Harrison et al. (1965). A wonderful personal account of the observational history of X-ray binaries is given by Lewin (1994).

Table 1.1
Known Accretion-Powered Pulsars

	System[a]	P_{spin} (s)	P_{orb} (d)	References
	Low-mass binaries			
•	4U 1656+354 (Her X-1)	1.24	1.7	Wilson, Finger, & Scott 1994
•	4U 1626–67	7.66	0.02	Chapter 6 of this thesis
•	4U 1728–247 (GX 1+4)	120	?	Chapter 7 of this thesis
	High-mass supergiant and giant systems			
	4U 0115–737 (SMC X-1)	0.717	3.89	Levine et al. 1993
•	4U 1119–603 (Cen X-3)	4.8	2.09	Finger, Wilson, & Fishman 1994
	RX J0648.1–4419 (HD 49798)	13.18	1.54	Israel et al. 1995
	4U 0532–66 (LMC X-4)	13.5	1.408	Levine et al. 1991
•	OAO 1657–415	37.7	10.4	Chapter 4 of this thesis
•	4U 0900–40 (Vela X-1)	283	8.96	see Nagase 1989
	1E 1145–614	297	5.648	see Nagase 1989
	4U 1907+09	438	8.38	see Nagase 1989
•	4U 1538–52	530	3.73	Rubin et al. 1994
•	4U 1223–624 (GX 301–2)	681	41.5	Koh et al. 1996
	Transient Be-binary systems			
	A 0535–668	0.069	16.66	see Nagase 1989
•	4U 0115+63	3.6	24.31	Cominsky et al. 1994
	V 0331+53	4.37	34.25	see Nagase 1989
	1E 1048–593	6.44	?	see Nagase 1989
	2E 0050.1–7247	8.9	?	Israel et al. 1995
	2S 1553–542	9.26	30.7	see Nagase 1989
•	2S 1417–624	17.6	42.1	Finger et al. 1996
•	EXO 2030+375	41.8	46.03	Stollberg et al. 1994
•	GRO J1008–57	93.5	260	Wilson et al. 1994a
•	A 0535+26	105	110.58	Finger, Wilson, & Harmon 1996
	4U 1258–61 (GX 304–1)	272	133	see Nagase 1989
•	4U 1145–619	292	187.5	see Nagase 1989
•	A 1118–616	405	?	see Nagase 1989
	4U 0352+309 (X Per)	835	?	see Nagase 1989
	RX J0146.9+6121 (LSI +61° 235)	1413	?	Hellier 1994
	Transient systems with an undetermined companion			
•	RX J0059.2–7138	2.7632	?	Hughes 1994
	RX J0502.9–6626	4.0635	?	Schmidtke et al. 1995
•	GRO J1750–27	4.4	?	Koh et al. 1995
	RX J1838.4–0301	5.45	?	Schwentker 1994
	1E 2259+586	6.98	?	see Nagase 1989
	4U 0142+614	8.7	?	Israel et al. 1994
•	GS 0834–430	12.3	110.5	Wilson et al. 1996
•	GRO J1948+32	18.7	?	Chapter 5 of this thesis
	GS 1843+00	29.5	?	see Nagase 1989
	GS 2137+57 (Cep X-4)	66.2	?	see Nagase 1989
	GS 1843–024	94.8	?	see Nagase 1989
	4U 1833–076 (Sct X-1)	111	?	see Nagase 1989
•	GRO J2058+42	198	?	Wilson et al. 1995
	GPS 1722–363	413	?	see Nagase 1989

[a]Sources marked with bullets (•) have been detected with BATSE.

Table 1.2
Orbital Parameters of Accreting Pulsar Systems[a]

	Source Name	Orbital epoch [MJD]	$P_{\rm orb}$ [d]	$a_{\rm x} \sin i$ [lt-sec]	e	ω [°]	$f_{\rm x}(M)$ [$M_\odot$]	Refs.[b]
	Low-mass system							
•	Her X-1	48799.61235(1)[c]	1.700167412(40)[g]	13.1853(2)	$< 1.3 \times 10^{-4}$ (2σ)	···	0.8517(1)	[1], [2]
	High-mass supergiant systems							
	LMC X-4	47741.9904(2)[d]	1.40839(1)[j]	26.31(3)	0.006(2)	···	9.86(3)	[3]
•	Cen X-3	48561.656702(71)[c]	2.08706533(49)	39.627(18)	$< 1.6 \times 10^{-3}$ (3σ)	···	15.343(21)	[4]
•	4U 1538–52	45278.979(20)[c]	3.72840(3)[h]	52.8(18)[f]	···	···	11.4(12)	[5], [6], [7]
	SMC X-1	47740.35906(3)[c]	3.89229118(48)[e]	53.4876(4)	< 0.00004 (3σ)	···	10.8481(2)	[8]
	4U 1907+09	45575.465(35)[i]	8.3745(42)	80.2(72)	$0.16^{+0.14}_{-0.11}$	330^{+18}_{-56}	7.9(21)	[9], [10]
•	Vela X-1	48563.5364(33)[c]	8.964416(49)[f]	113.61(30)	0.0883(23)	153.2(17)	19.60(16)	[11], [12]
•	OAO 1657–415	48515.99(5)[c]	10.44809(30)	106.0(5)	0.104(5)	93(5)	11.7(2)	[13], [22]
	GX 301–2	43906.06(16)[d]	41.508(7)	371.2(33)	0.472(11)	309.9(26)	31.9(8)	[14]
	Be-binary systems							
•	4U 0115+63	48355.206(4)[d]	24.309(10)[f]	140.13(8)[f]	0.3402(2)[f]	47.66(3)	5.00(1)	[15], [16]
	2S 1553–54	42596.67(3)[c]	30.2(1)	162.7(10)	···	···	5.0(1)	[17]
	V 0332+53	45651.5(1)[d]	34.25(10)	48(4)	0.31(3)	313(10)	0.10(2)	[18]
•	EXO 2030+375	48798.2(7)[d]	46.03(1)	268(25)	0.33(3)	228.2(57)	9.8(27)	[19]
•	A 0535+26	49058.7(06)[d]	110.3(3)	267(13)	0.47(2)	130(5)	1.64(23)	[20]
	System with undetermined companion							
•	GS 0834–430	48594.3(6)[c]	110.5(3)	211(7)	0.12(2)	265(7)	0.83(10)	[21]

[a] Orbital elements for sources marked with bullets (•) have been measured with BATSE. $P_{\rm orb}$=orbital period, $a_{\rm x} \sin i$=projected semimajor axis, e=eccentricity, ω=longitude of periastron, and $f_{\rm x}(M)$=X-ray mass function.

[b] REFERENCES: [1] Deeter et al. 1991; [2] Wilson et al. 1994b; [3] Levine et al. 1991; [4] Finger et al. 1993; [5] Makishima et al. 1987; [6] Corbet et al. 1993; [7] Rubin et al. 1994; [8] Levine et al. 1993; [9] Makishima et al. 1984; [10] Cook & Page 1987; [11] Deeter et al. 1987; [12] Finger 1993; [13] Chakrabarty et al. 1993; [14] Sato et al. 1986; [15] Rappaport et al. 1978; [16] Cominsky et al. 1994; [17] Kelley et al. 1983; [18] Stella et al. 1985; [19] Stollberg et al. 1994; [20] Finger et al. 1994; [21] Wilson et al. 1996; [22] Finger 1995.

[c] $T_{\pi/2}$ = epoch of 90° mean orbital longitude.

[d] T_0 = epoch of periastron passage.

[e] Epoch MJD 42836.18277 ± 0.00020. $\dot{P}_{\rm orb}/P_{\rm orb} = (-3.36 \pm 0.02) \times 10^{-6}$ yr^{-1}.

[f] This element held fixed at this value in fitting other elements.

[g] Orbital period for specified orbital epoch, computed using $P_{\rm orb}$ and $\dot{P}_{\rm orb}$ from Deeter et al. 1991. Held fixed in fitting other elements.

[h] Orbital period for specified orbital epoch, computed using $P_{\rm orb}$ and $\dot{P}_{\rm orb}$ from Rubin et al. (1994).

[i] Orbital epoch for longitude 309° ± 15°. Held fixed in fitting other elements.

[j] Epoch MJD 43067.5. $\dot{P}_{\rm orb}/P_{\rm orb} = (1.1 \pm 0.8) \times 10^{-6}$ yr^{-1}.

It is interesting to note that, at this point, there was observational evidence for neither the binary nor the compact nature of these sources.

The existence of neutron stars was finally confirmed with the 1967 discovery of radio pulsars (Hewish et al. 1968). Just prior to this discovery, Pacini (1967) had proposed that a rapidly rotating, magnetized neutron star was powering the Crab nebula; and just after the discovery, Gold (1968) independently showed that such a star could explain the observations and correctly predicted very slow spin-down due to the loss of rotational energy to radiation. The subsequent discovery of rapid ($P_{\rm spin} < 1$ s) pulsars in the Crab and Vela supernova remnants (too fast for white dwarf pulsar models) and the detection of spin-down in the Crab pulsar secured the neutron star model for these systems. Today, over 600 radio pulsars are known with periods ranging from 1.6 ms to ~5 s (Taylor, Manchster, & Lyne 1993). The identification of cosmic X-ray sources with compact objects was finally established a few years later with the discovery of X-ray pulsations from Centaurus X-3 by the *Uhuru* mission (Giacconi et al. 1971). The further discovery that these pulsations undergo periodic Doppler shifts and regular X-ray eclipses clearly indicated the binary nature of these sources (Schreier et al. 1972). The basic picture of the interaction between the accreting matter and the pulsar magnetosphere was worked out from these early observations (Pringle & Rees 1972; Davidson & Ostriker 1973; Lamb, Pethick, & Pines 1973).

It is useful to note that, in recent years, pulsed X-ray and gamma-ray emission has been detected from several young radio pulsars. The emission mechanism in these isolated, rotation-powered pulsars is completely different than in the accretion-powered binary pulsars. Historically, the term *X-ray pulsar* is usually reserved for accretion-powered binary pulsars, and that will be the usage in this thesis. (Likewise, the term *gamma-ray pulsar* generally refers to rotation-powered pulsars, even though gamma-ray emission has been seen from some accretion-powered pulsars.)

1.2.2 Observed Characteristics

A comprehensive review of accretion-powered pulsars was given by Nagase (1989), and X-ray binaries in general are reviewed by White, Nagase, & Parmar (1995). We briefly summarize the essential points here.

Nearly 40 accreting pulsars are known as of this writing, with pulse periods ranging from 0.069 s to 23.5 minutes. Most of these lie in the Galactic plane; a few are observed in

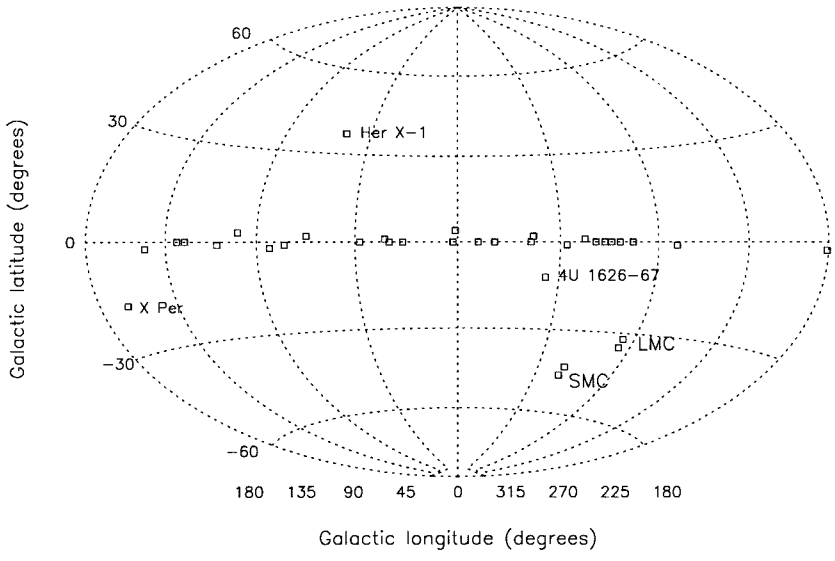

Figure 1.1: Distribution of accretion-powered binary pulsars in Galactic coordinates. Most lie in the Galactic plane. The Large and Small Magellanic Clouds are indicated. Her X-1 and 4U 1626–67 are distant Galactic pulsars which lie out of the plane, but X Per is close by.

the Magellanic clouds, and a few others are high-latitude Galactic sources (see Figure 1.1). The systems can be divided into three categories:

- **High-mass X-ray binaries** with OB supergiant companions. These can be further divided into two subcategories: systems with short pulse periods and high X-ray luminosities (e.g., SMC X-1, Cen X-3), in which the mass transfer occurs via Roche lobe overflow mediated by an accretion disk; and systems with long pulse periods and moderate X-ray luminosities (e.g., Vela X-1), in which the mass transfer is due to accretion of the supergiant's stellar wind. These systems are steady X-ray sources and tend to be very luminous ($> 10^{37}$ erg s^{-1}).

- **(High-mass) Be-star X-ray binaries** with rapidly-rotating main sequence Be companions (e.g., 4U 0115+63, A0535+62). These systems are transient X-ray sources, with outbursts often occurring near the periastron passage of an eccentric orbit. They are sometimes in quiescence for months or years; the X-ray outbursts do not always occur regularly.

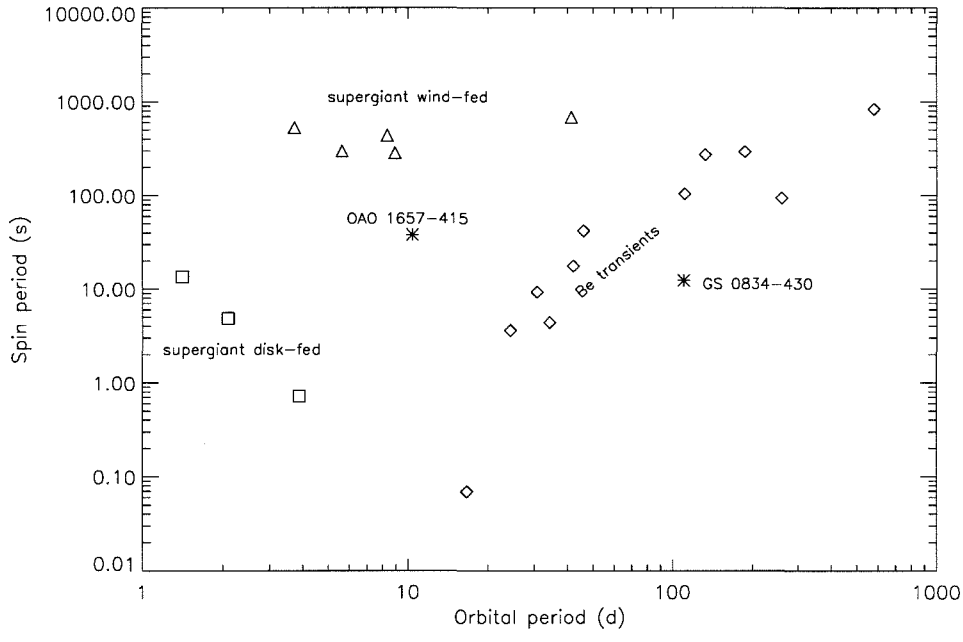

Figure 1.2: Spin period versus orbital period for the accreting pulsars with massive companions.

- **Low-mass X-ray binaries** with late type or degenerate dwarf companions (e.g., Her X-1, GX 1+4, 4U 1626–67). These systems are steady, low-luminosity X-ray sources.

The high-mass systems can be roughly organized by plotting spin period versus orbital period (Figure 1.2). The disk-fed supergiant systems have short spin periods and short orbital periods. The short orbital period tends to ensure Roche-lobe overflow and a large disk-fed accretion rate. The resulting steady accretion torque rapidly spins the pulsar up to an equilibrium period (typically ~ 1 s; see, e.g., Frank, King, & Raine 1992). In the wind-fed supergiants, the orbital separations are large enough that the companions do not fill their Roche lobe. Instead, the pulsar accretes erratically from the strong supersonic wind of the supergiant, without any strong trend in the torque. A rough correlation between orbital period and spin period is observed in the Be-star/X-ray binary pulsars (Corbet 1986; Waters & van Kerkwijk 1989).

The emission from X-ray binaries is powered by the release of gravitational energy,

$$L_{\rm x} = \frac{GM_{\rm x}\dot{M}}{R_{\rm x}} = 10^{37}\,{\rm erg\ s^{-1}} \left(\frac{M_{\rm x}}{1.4\,M_\odot}\right) \left(\frac{\dot{M}}{10^{-10}\,M_\odot\ {\rm yr^{-1}}}\right) \left(\frac{R_{\rm x}}{10\ {\rm km}}\right)^{-1}, \qquad (1.1)$$

where $L_{\rm x}$ is the bolometric X-ray luminosity, $M_{\rm x}$ and $R_{\rm x}$ are the mass and radius of the

neutron star, and $\dot{M}$ is the mass accretion rate. The free-fall velocity of the accreting matter when it reaches the surface of the neutron star is $\sim 0.1c$. The characteristic blackbody temperature of this emission

$$T_{\rm bb} = \left(\frac{L_{\rm x}}{4\pi R_{\rm x}^2 \sigma_{\rm sb}}\right)^{1/4} \sim 10^7 \text{ K} \tag{1.2}$$

corresponds to $kT \sim 1$ keV, clearly indicating the X-ray nature of these sources. However, the energy spectrum of accreting pulsars is highly non-thermal. The typical spectrum can be described by a broken power law, with a photon index ~ 1 below the break energy and ~ 3 above the break energy, with the break occurring at $\sim$20 keV. Individual sources vary widely (see White, Swank, & Holt 1983). Comparing the typical spectrum with BATSE's energy response (see Figure 2.3), we see that BATSE is probing only the high-energy tail of the pulsar emission. Pulsars with low break energies (e.g., LMC X-4) are difficult to detect at all with BATSE.

Radiation pressure on the infalling matter will set an upper limit on steady accretion. We can calculate this limit, called the *Eddington luminosity*, by equating radiation pressure and gravity. Assuming spherical accretion of pure hydrogen, we find

$$L_{\rm Edd} = \frac{4\pi c G M_{\rm x} m_p}{\sigma_{\rm T}} = 1.8 \times 10^{38} \text{ erg s}^{-1} \left(\frac{M_{\rm x}}{1.4\ M_\odot}\right), \tag{1.3}$$

where m_p is the proton mass and $\sigma_{\rm T}$ is the Thomson scattering cross-section. Note that this limit only applies to *steady* accretion. The assumption of spherical symmetry is not really applicable to accreting pulsars, since the accretion is channeled onto the polar caps. Still, the above expression is useful to set the luminosity scale. Most accreting pulsars have luminosities well below $L_{\rm Edd}$.

Accreting pulsars are strongly magnetized, with surface magnetic fields $B \gtrsim 10^{12}$ G. Close to the neutron star, the field disrupts the accretion flow, attaching matter onto the field lines and channeling it onto the magnetic poles. The resulting accretion luminosity thus emanates from two restricted "hot spots" on the neutron star. The pulsed emission is thought to arise from a misalignment of the magnetic axis and the spin axis which causes the hot spots to sweep across our line of sight at the spin period. The pulse profiles of X-ray pulsars tend to be fairly broad and sinusoidal, particularly above 10 keV. This is especially true in comparison to the sharp, narrow profiles typically observed in the radio pulsars. The pulse shapes can be roughly described as either single-peaked or double-peaked (although some have complex substructure, particularly at low energies). This is

believed to reflect whether the emission from one or both magnetic poles is crossing our line of sight. Some accreting pulsars (e.g., Vela X-1, GX 301–2) which are single peaked at soft X-ray energies become double peaked in BATSE's energy range.

References

Adams, W. S. 1915. The spectrum of the companion of Sirius. *Pub. Astron. Soc. Pacific*, **27**, 236.

Adams, W. S. 1925. The relativity displacement of the spectral lines of the companion of Sirius. *Proc. Natl. Acad. Sci. (USA)*, **11**, 382.

Baade, W. & Zwicky, F. 1934. Supernovae and cosmic rays. *Phys. Rev.*, **45**, 138.

Chadwick, J. 1932. The existence of a neutron. *Proc. R. Soc. London A*, **136**, 692.

Chandrasekhar, S. 1931. The maximum mass of ideal white dwarfs. *Astrophys. J.*, **74**, 81.

Cominsky, L., Roberts, M., & Finger, M. H. 1994. An April 1991 outburst from 4U 0115+63 observed by BATSE. In *Second Compton Symposium*, ed. C. E. Fichtel, N. Gehrels, & J. P. Norris (New York: AIP), 294.

Cook87 Cook, M. C. & Page, C. G. 1987. The X-ray properties of 3A 1907+09. *Mon. Not. R. Astron. Soc.*, **225**, 381.

Corbet, R. H. D. 1986. The three types of high-mass X-ray pulsator. *Mon. Not. R. Astron. Soc.*, **220**, 1047.

Corbet, R. H. D., Woo, J. W., & Nagase, F. 1993. The orbit and pulse period of X1538–522 from Ginga observations. *Astron. & Astrophys.*, **276**, 52.

Davidson, K. & Ostriker, J. P. 1973. Neutron star accretion in a stellar wind: model for a pulsed X-ray source. *Astrophys. J.*, **179**, 585.

Deeter, J. E. et al. 1987. Pulse timing study of Vela X-1 based on Hakucho and Tenma data: 1980–1984. *Astron. J.*, **93**, 877.

Deeter, J. E. et al. 1991. Decrease in the orbital period of Hercules X-1. *Astrophys. J.*, **383**, 324.

Dirac, P. A. M. 1926. On the theory of quantum mechanics. *Proc. R. Soc. London A*, **112**, 661.

Finger, M. H. 1993. Personal communication.

Finger, M. H. 1995. Personal communication.

Finger, M. H. et al. 1993. BATSE observations of Cen X-3. In *Compton Gamma Ray Observatory*, ed. M. Friedlander et al. (New York: AIP), 386.

Finger, M. H. et al. 1994. Hard X-ray observations of A0535+262. In *Evolution of X-Ray Binaries*, ed. S. S. Holt & C. S. Day (New York: AIP Press), 459.

Finger, M. H., Wilson, R. B., & Chakrabarty, D. 1996. Reappearance of the X-ray binary pulsar 2S 1417–624. *Astron. & Astrophys.*, in press.

Finger, M. H., Wilson, R. B., & Fishman, G. J. 1994. Observations of accretion torques in Cen X-3. In *Second Compton Symposium*, ed. C. E. Fichtel, N. Gehrels, & J. P. Norris (New York: AIP Press), 304.

Finger, M. H., Wilson, R. B., & Harmon, B. A. 1996. Quasi-periodic oscillations during a giant outburst of A0535+26. *Astrophys. J.*, in press.

Fowler, R. H. 1926. On dense matter. *Mon. Not. R. Astron. Soc.*, **87**, 114.

Frank, J., King, A., & Raine, D. 1992. *Accretion Power in Astrophysics* (Cambridge: Cambridge U. Press).

Gamow, G. 1937. *Structure of Atomic Nuclei and Nuclear Transformations* (Oxford: Clarendon).

Giacconi, R., Gursky, H., Paolini, F. R., & Rossi, B. B. 1962. Evidence for X-rays from sources outside the solar system. *Phys. Rev. Lett.*, **9**, 439.

Giacconi, R., Gursky, H., Kellogg, E., Schreier, E., & Tananbaum, H. 1971. Discovery of periodic X-ray pulsations in Centaurus X-3 from Uhuru. *Asrophys. J.*, **167**, L67.

Gold, T. 1968. Rotating neutron stars as the origin of the pulsating radio sources. *Nature*, **218**, 731.

Harrison, B. K., Thorne, K. S., Wakano, M., & Wheeler, J. A. 1965. *Gravitation Theory and Gravitational Collapse* (Chicago: U. Chicago Press).

Hellier, C. 1994. 4U 0142+614 and RX J0146.9+6121. *IAU Circ.*, No. 5994.

Hewish, A., Bell, S. J., Pilkington, J. D. H., Scott, P. F., & Collins, R. A. 1968. Observation of a rapidly pulsating radio source. *Nature*, **217**, 709.

Hughes, J. P. 1994. A new transient pulsar in the Small Magellanic Cloud with an unusual X-ray spectrum. *Astrophys. J.*, **427**, L25.

Israel, G. L., Mereghetti, S., & Stella, L. 1994. The discovery of 8.7 second pulsations from the ultrasoft X-ray source 4U 0142+61. *Astrophys. J.*, **433**, L25.

Israel, G. L., Stella, L., Angelini, L., White, N. E., & Giommi, P. 1995. HD 49798 and 2E 0050.1–7247. *IAU Circ.*, No. 6277.

Kelley, R. L., Rappaport, S., & Ayasli, S. 1983. Discovery of 9.3-s X-ray pulsations from 2S 1553–542 and a determination of the orbit. *Astrophys. J.*, **274**, 765.

Koh, T. et al. 1995. GRO J1750–27 and GRO J1735–27. *IAU Circ.*, No. 6222.

Koh, T. et al. 1996. BATSE observations of the accreting X-ray pulsar GX 301–2. *Astrophys. J.*, in preparation.

Koyama, K. et al. 1989. Are there many Be star binary X-ray pulsars in the Galactic ridge? *Pub. Astron. Soc. Japan*, **41**, 483.

Lamb, F. K., Pethick, C. J., & Pines, D. 1973. A model for compact X-ray sources: accretion by rotating magnetic stars. *Astrophys. J.*, **184**, 271.

Landau, L. D. 1932. On the theory of stars. *Physikalische Zeitschrift der Sowjetunion*, **1**, 285.

Landau, L. D. 1938. Origin of stellar energy. *Nature*, **141**, 333.

Levine, A. et al. 1991. LMC X-4: Ginga observations and search for orbital period changes. *Astrophys. J.*, **381**, 101.

Levine, A. et al. 1993. Discovery of orbital decay in SMC X-1. *Astrophys. J.*, **410**, 328.

Lewin, W. H. G. 1994. Three decades of X-ray astronomy from the point of view of a biased observer. In *Evolution of X-Ray Binaries*, ed. S. S. Holt & C. S. Day (New York: AIP Press), 3.

Makishima, K. et al. 1984. Discovery of a 437.5-s pulsation from 4U 1907+09. *Pub. Astron. Soc. Japan*, **36**, 679.

Makishima, K. et al. 1987. Spectra and pulse period of the binary X-ray pulsar 4U 1538–52. *Astrophys. J.*, **314**, 619.

Nagase, F. 1989. Accretion-powered X-ray pulsars. *Pub. Astron. Soc. Japan*, **41**, 1.

Oppenheimer, J. R. & Serber, R. 1938. On the stability of stellar neutron cores. *Phys. Rev.*, **54**, 540.

Oppenheimer, J. R. & Volkoff, G. M. 1939. On massive neutron cores. *Phys. Rev.*, **55**, 374.

Pacini, F. 1967. Energy emission from a neutron star. *Nature*, **216**, 567.

Pringle, J. E. & Rees, M. J. 1972. Accretion disc models for compact X-ray sources. *Astron. & Astrophys.*, **21**, 1.

Rappaport, S. et al. 1978. Orbital elements of 4U 0115+63 and the nature of the hard X-ray transients. *Astrophys. J.*, **224**, L1.

Rubin, B. C. et al. 1994. BATSE observations of 4U 1538–52: a 530 second pulsar. In *Evolution of X-Ray Binaries*, ed. S. S. Holt & C. S. Day (New York: AIP Press), 455.

Sandage, A. R. et al. 1966. On the optical identification of Sco X-1. *Astrophys. J.*, **146**, 316.

Sato, N. et al. 1986. Orbital elements of the binary X-ray pulsar GX 301–2. *Astrophys. J.*, **304**, 241.

Schmidtke, P. C., Cowley, A. P., McGrath, T. K., & Anderson, A. L. 1995. Discovery of an X-ray pulsar in the LMC. *Pub. Astron. Soc. Pacific*, **107**, 450.

Schwentker, O. 1994. Evidence for a low-luminosity X-ray pulsar associated with a supernova remnant. *Astron. & Astrophys.*, **286**, L47.

Schreier, E., Levinson, R., Gursky, H., Kellogg, E., Tananbaum, H., & Giacconi, R. 1972. Evidence for the binary nature of Centaurus X-3 from Uhuru X-ray observations. *Astrophys. J.*, **172**, L79.

Shapiro, S. L. & Teukolsky, S. A. 1983. *Black Holes, White Dwarfs, and Neutron Stars* (New York: Wiley).

Shklovsky, I. S. 1967. On the nature of the source of X-ray emission of Sco XR-1. *Astrophys. J.*, **148**, L1.

Stella, L. et al. 1985. The discovery of 4.4 second X-ray pulsations from the rapidly variable X-ray transient V0332+53. *Astrophys. J.*, **288**, L45.

Stollberg, M. H. et al. 1994. Recent observations of EXO 2030+375 with BATSE. In *Evolution of X-Ray Binaries*, ed. S. S. Holt & C. S. Day (New York: AIP Press), 255.

Taylor, J. H., Manchester, R. N., & Lyne, A. G. 1993. Catalog of 558 pulsars. *Astrophys. J. Suppl.*, **88**, 529.

Waters, L. B. F. M. & van Kerkwijk, M. H. 1989. The relation between orbital and spin periods in massive X-ray binaries. *Astron. & Astrophys.*, **223**, 196.

White, N. E., Nagase, F., & Parmar, A. N. 1995. The properties of X-ray binaries. In *X-Ray Binaries*, ed. W. H. G. Lewin, J. van Paradijs, & E. P. J. van den Heuvel (Cambridge: Cambridge U. Press), 1.

White, N. E., Swank, J. H., & Holt, S. S. 1983. Accretion powered X-ray pulsars. *Astrophys. J.*, **270**, 711.

Wilson, C. A. et al. GRO J2058+42. *IAU Circ.*, No. 6238.

Wilson, C. A., Finger, M. H., Harmon, B. A., Scott, D. M., Wilson, R. B., Bildsten, L., Chakrabarty, D., & Prince, T. A. 1996. BATSE observations and orbital determination of the X-ray pulsar GS 0834–430. *Astrophys. J.*, submitted.

Wilson, R. B. et al. 1994a. Discovery of the hard X-ray pulsar GRO J1008–57 by BATSE. In *Evolution of X-Ray Binaries*, ed. S. S. Holt & C. S. Day (New York: AIP Press), 451.

Wilson, R. B. et al. 1994b. Observation of a correlation between main-on intensity and spin behavior in Her X-1. In *Evolution of X-Ray Binaries*, ed. S. S. Holt & C. S. Day (New York: AIP Press), 475.

Chapter 2

Acquisition and Reduction of BATSE Data

There is likely to be a still undetected but entirely measurable flux of γ-rays bearing astronomical information of the highest interest.
—Philip Morrison (1958)

It is important to understand your background at least as well as you understand your signal.
—Thomas A. Prince (1992)

2.1 The *Compton Gamma Ray Observatory*

The *Compton Gamma Ray Observatory* (*GRO*; Figure 2.1) was launched from NASA Kennedy Space Center, Cape Canaveral, Florida, on the space shuttle *Atlantis* (STS-37) on 1991 April 5. The 15900 kg satellite, which is the heaviest unmanned scientific payload ever deployed in space, is in a 400 km orbit inclined 28.5° with respect to Earth's equator. *Compton* is the second of four planned elements of the NASA Great Observatories program[1]. It carries four instruments which span the 20 keV–30 GeV gamma-ray spectrum. The Burst and Transient Source Experiment (BATSE; Fishman et al. 1989) provides a nearly continuous all-sky monitor of the gamma-ray sky in the 20 keV–1.8 MeV range using uncollimated NaI scintillators. The Oriented Scintillation Spectroscopy Experiment (OSSE; Johnson et al. 1993) measures gamma-ray spectra in the 50 keV–10 MeV range using collimated NaI/CsI scintillators. The Compton Telescope (COMPTEL; Schönfelder et

[1]The others are the *Hubble Space Telescope* (*HST*), launched in 1990; the *Advanced X-ray Astrophysics Facility* (*AXAF*; see Weisskopf 1988), scheduled for launch in 1998; and the *Space Infrared Telescope Facility* (*SIRTF*; see Fazio & Eisenhardt 1990), scheduled for launch in 2001.

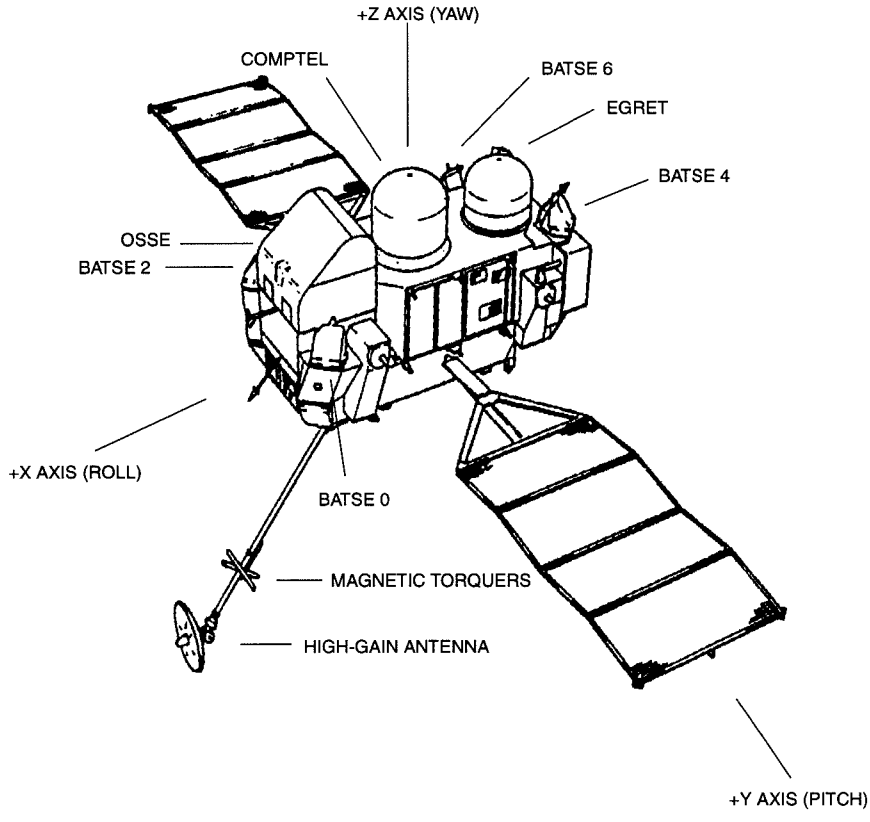

Figure 2.1: The *Compton Gamma Ray Observatory*. The 8 BATSE detector modules are situated on the corners of the spacecraft's main body. Modules 0, 2, 4, and 6 are visible in this diagram.

al. 1993) provides imaging observations in the 1–30 MeV range using a combination liquid scintillator/NaI scintillator detector. The Energetic Gamma Ray Experiment Telescope (EGRET; Thompson et al. 1993) provides imaging in the 20 MeV–30 GeV range using a spark chamber detector. A recent review of *Compton Observatory* science was given by Shrader & Gehrels (1995).

2.2 The Burst and Transient Source Experiment

BATSE, whose instrumentation is described in detail by Fishman et al. (1989) and Horack (1991), consists of eight identical uncollimated detector modules arranged on the corners of the *Compton* spacecraft. Each detector module contains three detectors: a large-area detector (LAD), a smaller spectroscopy detector (SD), and a charged-particle

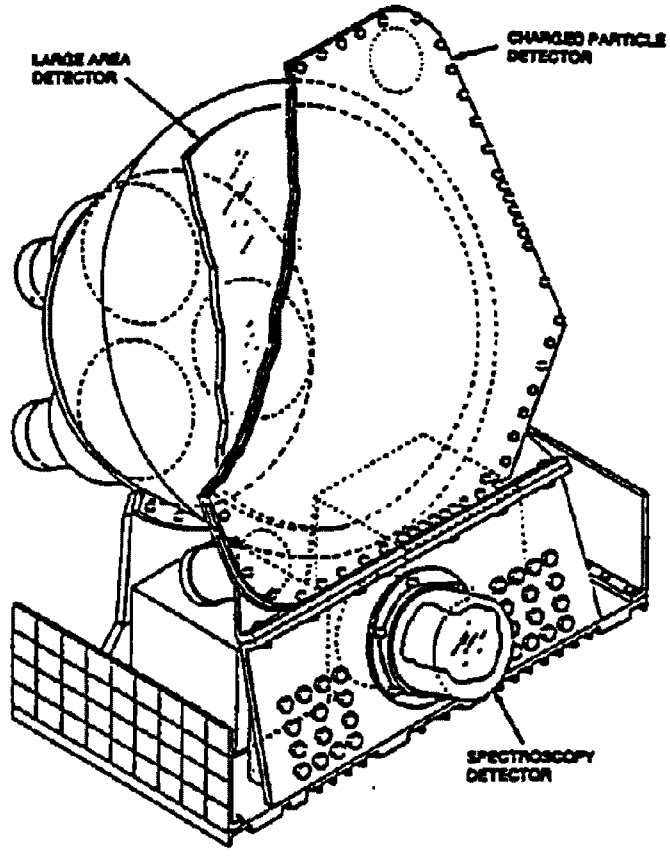

Figure 2.2: A BATSE detector module. The investigations in this thesis all employ data from the large area detectors.

detector (CPD). Our pulsar studies deal entirely with data from the LADs, each of which contains a NaI(Tl) scintillation crystal 1.27 cm thick and 50.8 cm in diameter, viewed in a light collection housing by three 12.7 cm diameter photomultiplier tubes. The LADs are shielded in front by a 1 mm aluminum window and by the CPDs, which are 0.63 cm thick polystyrene scintillators operated in anticoincidence with the LADs to provide a charged particle veto. The LADs have an effective energy range of 20 keV–1.8 MeV. Below 30 keV, the sensitivity is severely attenuated by the aluminum and plastic shielding. The rear of each detector module is protected by a passive lead-tin shield which is opaque to photons below 300 keV.

Scintillation pulses from the LADs are processed in two parallel paths: a fast (1.5 μs deadtime), four-channel discriminator circuit and a slower (2.5–25 μs deadtime, depending on photon energy) multi-channel pulse height analyzer. The nominal energies for

Table 2.1. Energy Channels in BATSE DISCLA and CONT Data

Channel	Energy Range (keV)	Background Rate (count s^{-1})
DISCLA 1	20–60	1500
DISCLA 2	60–110	1200
DISCLA 3	110–320	1000
DISCLA 4	>320	700
CONT 0	20–24	250
CONT 1	24–33	450
CONT 2	33–42	500
CONT 3	42–55	500
CONT 4	55–74	500
CONT 5	74–99	450
CONT 6	99–124	300
CONT 7	124–165	300
CONT 8	165–232	300
CONT 9	232–318	200
CONT 10	318–426	130
CONT 11	426–590	130
CONT 12	590–745	50
CONT 13	745–1103	80
CONT 14	1103–1828	80
CONT 15	>1828	200

NOTE: These channel boundaries are *approximate*, and are averaged over the eight detectors. Each detector has slightly different edges. The CONT edges are programmable; the displayed values are typical.

the upper three discriminators are 60 keV, 110 keV, and 320 keV. The lower level discriminators are programmable and are currently set to approximately 20 keV. The pulse height analyzer constructs 128-channel high energy resolution (HER) spectra from the LAD data. The mapping between HER channel number and energy is calibrated separately for each detector using ground test data and flight observations of the Crab Nebula (Pendleton et al. 1994). The calibration is maintained during flight by an automatic correction scheme which adjusts the detector gain to keep the 511 keV line feature in the gamma-ray background aligned in the correct HER channel.

The BATSE data types fall into four categories.

- **Background data.** These consist of the background DISCLA and CONT products, which are available continuously. The 4-channel LAD discriminator rates (DISCLA data) are sampled every 1.024 s. The 128-channel high energy resolution (HER) spectra are mapped into medium-resolution 16-channel spectra every 2.048 s, called continuous (CONT) data. The mapping of HER channels to CONT channels is programmable, and is occasionally changed temporarily to optimize the tradeoff between energy and time resolutions for a particular science investigation. The typical energy channel boundaries for the DISCLA and CONT data are given in Table 2.1.
- **Housekeeping data.** The HKG product contains information on the spacecraft orientation as well as its geocentric position at 2.048 s intervals. These positions are accurate to $\sim$ 6 km (3σ). The QUAL product contains diagnostic information on data quality, identifying intervals which should be excluded from data analysis due to telemetry errors, spacecraft reorientations, etc. We also use the QUAL information to exclude intervals containing gamma-ray bursts from pulsar timing analysis.
- **Scheduled data.** There are several data products which can be specially scheduled and provide high time or energy resolution. Several pulsar modes are available which can provide time resolution as short 16 ms for limited observation intervals.
- **Burst trigger data.** A variety of special data products are activated with high time and energy resolution when triggered by on-board identification of a gamma-ray burst in the BATSE LAD data stream. These data products are not relevant for pulsar studies.

2.3 Detector Response

The effective area for the LADs at normal incidence as a function of energy is shown in Figure 2.3. The solid curve represents the effective area for any interaction in the detector, while the dashed curve shows the effective area for full energy deposition. Despite the fact that the photoelectric absorption cross-section of NaI increases steeply at low energies, the effective area curve below 100 keV is dropping rapidly. This is due to the attenuation of low energy photons by the aluminum window and the CPD.

Figure 2.4 shows the angular response of the LADs to a monochromatic photon beam at various energies, computed using the detector response matrices of Pendleton et

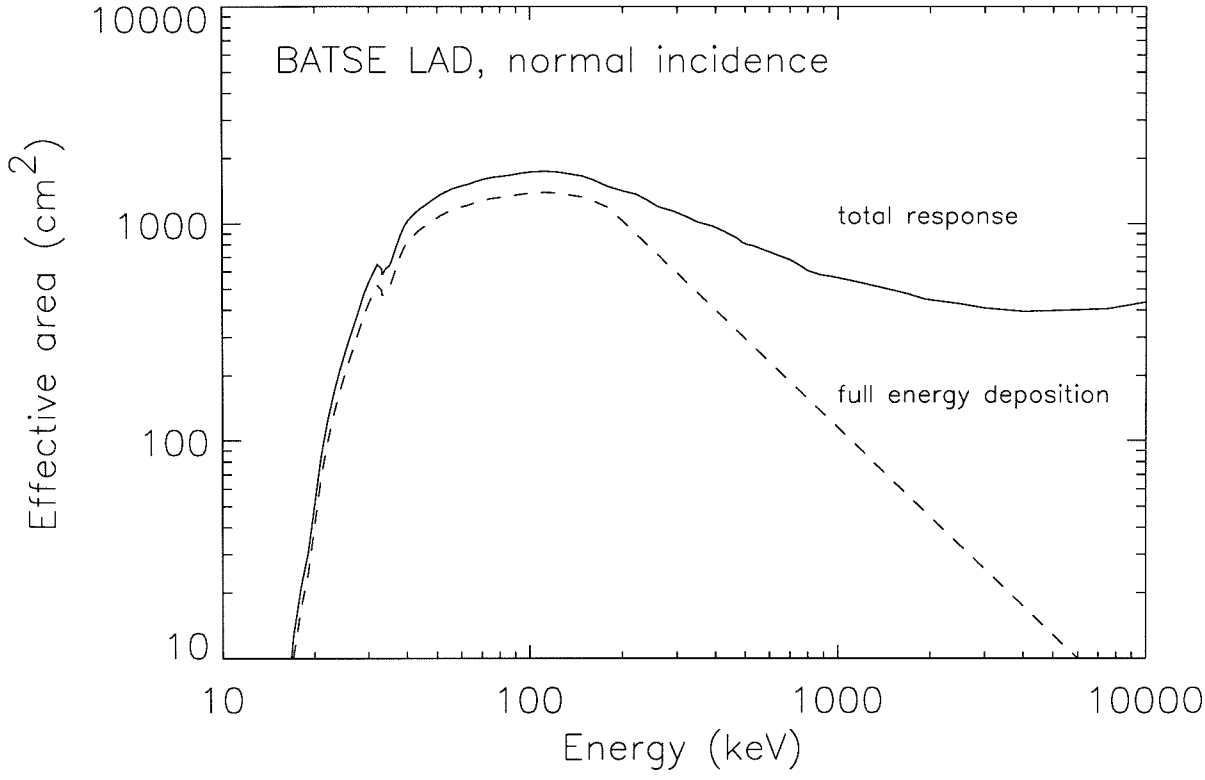

Figure 2.3: Effective area of a BATSE large area detector at normal incidence. The solid curve denotes the total response of the detector, including interactions where the incident photon energy is only partially deposited. The dashed curve denotes the response for full energy deposition in the detector. The feature near 30 keV is due to the iodine K edge. Adapted from Fishman et al. (1989).

al. (1995). The dominant effect governing this response is the projected detector area along the line of sight to the source, which varies as $\cos\theta$ (where θ is the viewing angle between the detector normal and the source). However, while the response to 100 keV photons is approximately $\cos\theta$, the response at energies both above and below 100 keV diverge from this for different reasons. At higher energies, the photon attenuation length in NaI is comparable to the thickness of the crystal, so any interactions tend to occur deep in the crystal. The decrease in projected geometric area with increasing θ is partially offset by the increase in path length through the detector, both of which have a $\cos\theta$ dependence. This results in a relatively flat angular response for $\theta \gtrsim 50°$ at high energies. The response does not fall to zero at 90° incidence due to the finite thickness of the crystal.

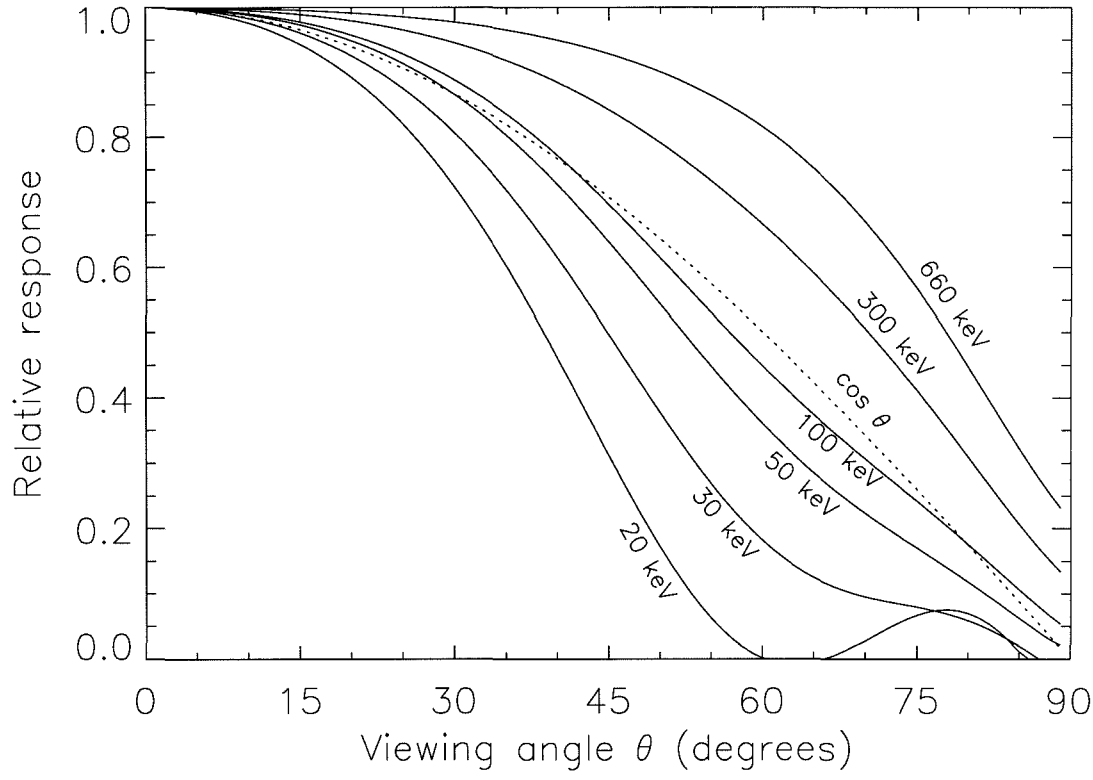

Figure 2.4: Angular response of a BATSE large area detector to photons of various energies. For comparison, a $\cos\theta$ response is indicated by the dotted curve. The secondary maximum in the 20 keV response at large angles is due to a gap in the detector support structure at the edge of the LADs. Computed using the detector response matrices of Pendleton et al. (1995).

At low energies, the attenuation length is very short and the interactions occur near the surface of the crystal, making its effective thickness irrelevant. However, the path length through the shielding in this case increases with θ, and the resulting attenuation of flux incident on the LAD causes the response to fall more steeply than $\cos\theta$. The secondary maximum in the large-angle response for low energies is due to the geometry of the support structure at the edge of the LADs. There is a gap through which low energy photons in that restricted angular range can reach the NaI crystal without passing through most of the shielding. This feature is poorly calibrated and may not be azimuthally symmetric.

A consequence of the variation of angular response with energy is that the integrated angular response to a source is dependent upon its intrinsic energy spectrum. Typical

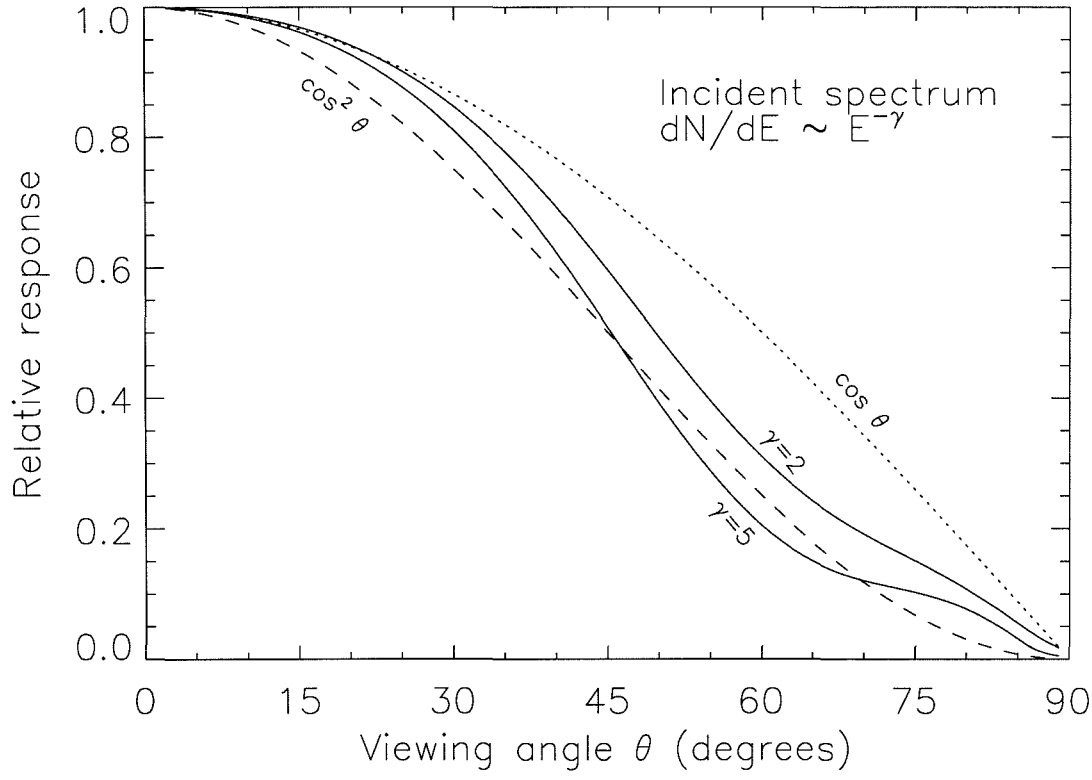

Figure 2.5: BATSE LAD angular response to an incident photon power-law spectrum $dN/dE \propto E^{-\gamma}$, for $\gamma = 2$ and $\gamma = 5$. For comparison, $\cos\theta$ response (*dotted line*) and $\cos^2\theta$ response (*dashed line*) are also shown.

accreting pulsar spectra in the 20–100 keV range can be modeled by a photon power-law of the form $dN/dE \propto E^{-\gamma}$ with photon index $2 < \gamma < 5$. Figure 2.5 shows the angular response to a 20–75 keV photon power law spectrum for the extreme cases of $\gamma = 2$ and $\gamma = 5$. For comparison, $\cos\theta$ and $\cos^2\theta$ responses are also plotted. We see that the predicted response falls off more quickly than $\cos\theta$ because the large number of incident low-energy photons dominate despite the attenuation by the shield. As expected, this effect is more pronounced for the steeper power-law index, where the proportion of incident high-energy photons is even lower. By comparison, Brock et al. (1991) predict an approximately $\cos\theta$ response for gamma-ray bursts, which they model as having a 50–300 keV photon power law with a low-energy cutoff. In general, the integrated response varies approximately as $\cos\theta$ for small angles ($\theta \lesssim 25°$), independent of photon index. At larger angles, $\cos^2\theta$ is a

more conservative general assumption if the source spectrum is unknown.

2.4 Optimal Combination of Detectors

Because of the octahedral arrangement of the BATSE detector planes, an astrophysical source is visible in four BATSE detectors during any given spacecraft pointing. (The spacecraft is typically reoriented at two-week intervals.) We consider here how to optimally combine data from these four detectors in order to maximize the signal-to-noise ratio. For the purposes of this calculation, we will consider background-limited observations of a constant source and will assume that the background noise is constant, isotropic, and governed by Poisson statistics. Then, the signal-to-noise ratio is given by

$$\mathrm{SNR} = \frac{S \sum w(\theta_i)\, r(\theta_i)}{\sqrt{B \sum w(\theta_i)}}, \tag{2.1}$$

where S is the source count rate in a single detector at normal incidence, B is the background count rate in each detector, θ_i is the source viewing angle for ith detector, $r(\theta)$ is the angular response function of the detector, and $w(\theta)$ is the detector weighting function which we are trying to optimize. It is more convenient to work with the signal-to-noise relative to that of a single detector at normal incidence,

$$\text{relative SNR} = \frac{\sum [w(\theta_i)/\max(w)]\, r(\theta_i)}{\sqrt{\sum [w(\theta_i)/\max(w)]}}. \tag{2.2}$$

The optimal choice of weighting function $w(\theta)$ will depend on the form of the detector angular response $r(\theta)$. However, we showed in the previous section that the form of $r(\theta)$ depends upon the intrinsic energy spectrum of the source. In what follows, we will assume that the source of interest is an accreting pulsar with a 20–75 keV photon power law spectrum and that the angular response function as $r(\theta) = \cos^2\theta$.

For a given spacecraft orientation, BATSE is more sensitive to some areas of the sky than others. The highest sensitivity is at the eight points in the sky which lie on the BATSE detector normals (i.e., the direction vector for normal incidence), while the lowest sensitivity is at six points in the sky which lie equidistant from the four incident detector normals. The weighting function for summing detectors which optimizes the tradeoff between maximizing signal and minimizing noise, as parametrized in Equation (2.1), depends upon where in the sky the source is relative to the detector normals. For a source lying *along* one of the detector normals, adding in the data from any of the other three viewing detectors

(which each have 70° incidence) with *any* non-zero weight will reduce sensitivity. On the other hand, the best sensitivity for a source equidistant from the four detector normals is obtained by combining the four detectors with equal weight.

Indeed, it is interesting to note that an unweighted combination of the four incident detectors yields *uniform* sensitivity over the whole sky, under our assumptions. Specifically, this is a consequence of the assumed $\cos^2$ response of the detectors, as we now show. Consider a source at azimuth A and altitude a relative to the spacecraft axes. For definiteness, let us suppose that this source is incident upon detectors 0, 1, 4, and 5. From the altazimuth direction vectors for the corresponding detector normals (see Appendix A), the detector viewing angles are given by

$$\begin{aligned}
\cos\theta_0 &= \frac{1}{\sqrt{3}}(\cos A\cos a + \sin A\cos a + \sin a) \\
\cos\theta_1 &= \frac{1}{\sqrt{3}}(\cos A\cos a + \sin A\cos a - \sin a) \\
\cos\theta_4 &= \frac{1}{\sqrt{3}}(-\cos A\cos a + \sin A\cos a + \sin a) \\
\cos\theta_5 &= \frac{1}{\sqrt{3}}(-\cos A\cos a + \sin A\cos a - \sin a).
\end{aligned}$$

Taking $w(\theta) = 1$ for an unweighted sum and inserting into Equation (2.2), we find that

$$\begin{aligned}
\text{relative SNR} &= \frac{\cos^2\theta_0 + \cos^2\theta_1 + \cos^2\theta_4 + \cos^2\theta_5}{\sqrt{4}} \\
&= \frac{2}{3},
\end{aligned}$$

independent of sky position. However, this isotropic response sacrifices the increased sensitivity possible at certain sky locations.

We have calculated sensitivity as a function of sky position for weighting functions of the form $\cos^n\theta$, with $n = 0, 1, 2, 3, 4$. The results are shown in Figure 2.6 and summarized in Table 2.2. All the results are quoted relative to the sensitivity of a single detector at normal incidence. The best overall sensitivity is achieved by choosing the detector weighting adaptively based on the altazimuth position of the source. The detector weighting used in all the analyses presented in this thesis was $w(\theta) = \cos^2\theta$.

An alternative family of weighting schemes is unweighted sums of *subsets* of the four incident detectors: singles, pairs, triples, and quads. This set of schemes is especially relevant for blind searches, since unweighted combinations can provide good sky coverage and sensitivity without resorting to an inefficient grid search. We have calculated the relative

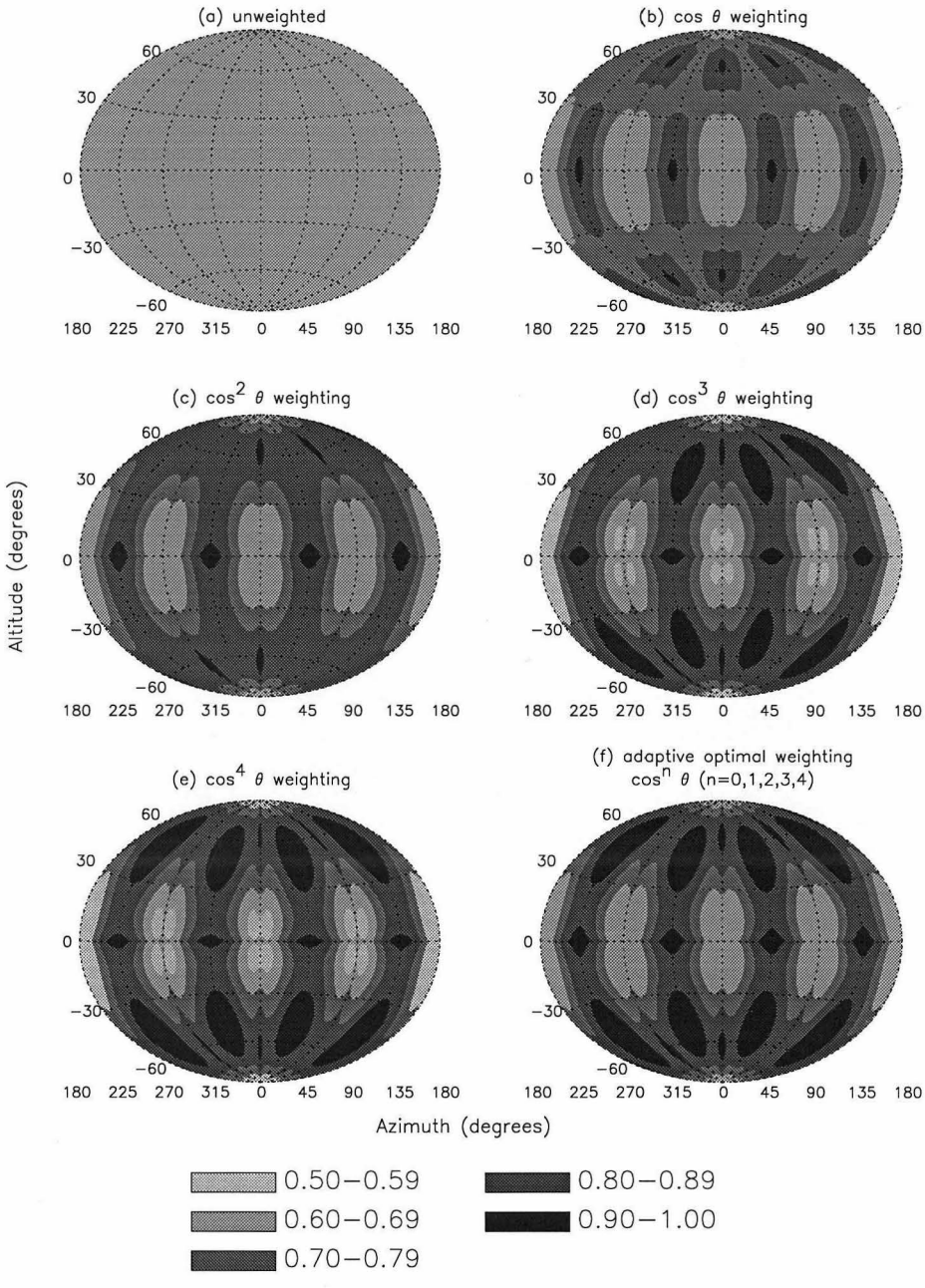

Figure 2.6: Optimal detector weighting for known sky positions. Sky coordinates are shown in the altazimuth system with respect to the spacecraft axes.

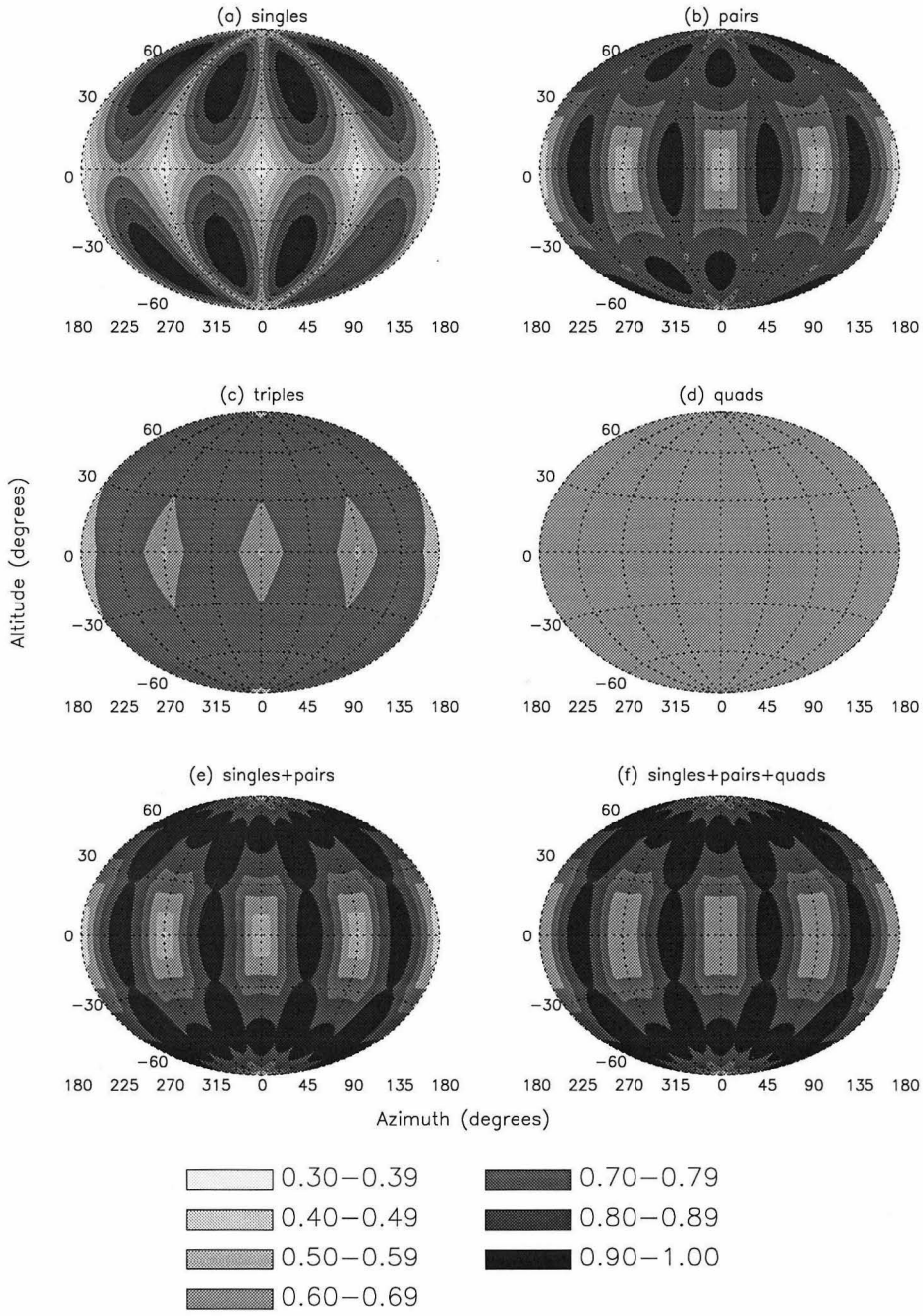

Figure 2.7: Optimal detector combinations for blind searches. Sky coordinates are shown in the altazimuth system with respect to the spacecraft axes.

Table 2.2
Relative sensitivity of various detector weighting schemes

	Sensitivity		
Weighting	Minimum	Maximum	Mean
1	0.67	0.67	0.67
$\cos\theta$	0.63	0.93	0.76
$\cos^2\theta$	0.60	0.94	0.79
$\cos^3\theta$	0.58	0.96	0.80
$\cos^4\theta$	0.56	0.99	0.80
adaptive	0.67	0.99	0.81

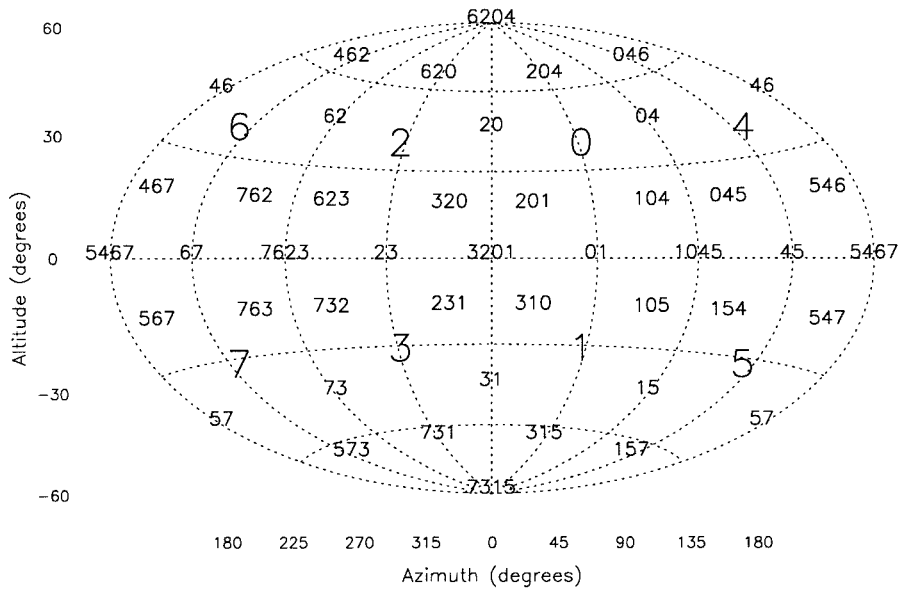

Figure 2.8: View directions for the various BATSE detector combinations. Each digit represents the corresponding detector. Sky coordinates are shown in the altazimuth system with respect to the spacecraft axes.

Table 2.3
Relative sensitivity of various detector combinations

Search pattern	Sensitivity			Efficiency
	Minimum	Maximum	Mean	
singles (8)	0.33	1.00	0.75	9.4%
pairs (12)	0.47	0.94	0.81	6.8%
triples (24)	0.58	0.77	0.74	3.1%
quads (6)	0.67	0.67	0.67	11.0%
singles+pairs+quads (26)	0.67	1.00	0.85	3.2%
all combinations (50)	0.67	1.00	0.85	1.7%
singles+pairs (20)	0.47	1.00	0.84	4.2%

sensitivity of the various unweighted combination schemes, along with the overall efficiency (defined as the mean sensitivity divided by the number of possible combinations). The results are shown in Figure 2.7 and summarized in Table 2.3. For each sky position in a given scheme, the most sensitive combination was chosen; the possibility of correlating information from overlapping combinations was not considered. The altazimuth sky positions for the various detector combinations is shown in Figure 2.8.

In the context of blind searches, we see again that the exclusive use of quads (i.e., unweighted 4-detector sums) provides uniform sky coverage at the expense of some loss in sensitivity. This might be desirable for certain kinds of investigations. The use of unweighted singles+pairs+quads gives better overall sensitivity than the adaptive $\cos^n \theta$ weighting scheme. Adaptive selection of this unweighted scheme (or else the addition of unweighted pairs to the adaptive $\cos^n \theta$ scheme) is the overall best weighting choice.

2.5 Earth Occultation

Viewed from an altitude of 400 km, the Earth covers about 33% of the sky and subtends an angle of 140°. Over the course of a spacecraft orbit at this altitude, 93% of the sky (corresponding to angles $\gtrsim 20°$ from the orbital poles) is subject to occultation. The *Compton* orbital plane is inclined 28.5° with respect to the Earth's equator, and the orbital poles precess around the Earth's polar axis with a ≈ 53 d period due to perturbations by the Earth's equatorial bulge (see Figure 2.12). The entire sky is subject to Earth occultation over at least some portion of the precession period. Bright sources subject to occultation will

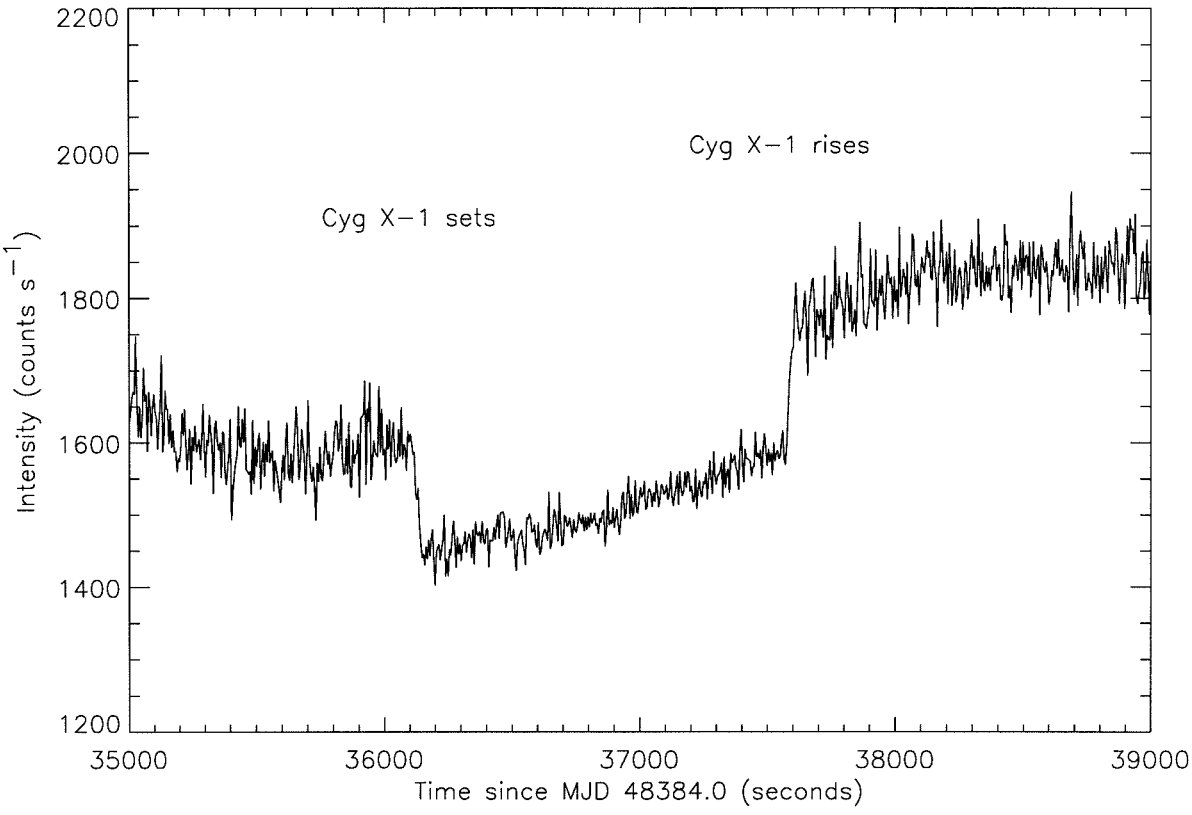

Figure 2.9: Earth occultation of Cygnus X-1, as observed in the 20–60 keV channel of the BATSE large area detector facing the source. (Figure adapted from Zhang et al. 1994.)

be visible as sharp edges in the BATSE data stream as the source passes behind the Earth's limb and then reemerges (see Figure 2.9); the height of these edges is a direct measure of the total (pulsed+unpulsed) instantaneous flux. By timing these edges, one can localize sources along the arc corresponding to the limb of the Earth across the sky. For a given sky region, the orientation of these limbs rotate over the 53-d *Compton* orbital precession period, eventually providing source localization within $\sim 0.1°$, limited by the time resolution of the data and variations in the gamma-ray opacity of the Earth's upper atmosphere (Harmon et al. 1992; Zhang et al. 1994). Fainter sources require averaging of multiple edges; the detection threshold for 1 day of 20–60 keV DISCLA data is ≈ 100 mCrab.

Knowledge of the occultation times for a given sky direction is important for any BATSE data analysis (pulsed or unpulsed), since the signal-to-noise ratio of an observation can always be improved by discarding data during occultations. For most of the analyses

presented in this thesis, occultation times were calculated by assuming the Earth is spherical and modeling its atmosphere as opaque to gamma-rays below an altitude of $h = 70$ km and transparent above this altitude. A source is occulted when the impact parameter of the line of sight with respect to the Earth is less than $R_\oplus + h$. The impact parameter obeys the relation

$$b^2 = r^2 + s^2 + 2\mathbf{r} \cdot \mathbf{s}, \tag{2.3}$$

where b is the impact parameter, $\mathbf{r} = (x, y, z)$ is the geocentric equatorial spacecraft position vector, $\mathbf{s} = s\hat{\mathbf{u}}$ is the line-of-sight vector from the spacecraft to the impact parameter vector, and $\hat{\mathbf{u}} = (\cos\delta\cos\alpha, \cos\delta\sin\alpha, \sin\delta)$ is the equatorial direction vector for a source at right ascension α and declination δ.

We can compute the impact parameter more accurately by accounting for the Earth's oblateness as follows[2]. The surface of an oblate spheroid is given by

$$r = q(1 - f\sin^2\phi) \tag{2.4}$$

where q is the equatorial radius, $f = (q - c)/q$ is the flattening factor, c is the polar radius, and ϕ is the latitude. It is reasonable to assume that atmospheric density is a function of gravitational potential and that the equipotential surfaces are similar oblate spheroids. Given a position vector $\mathbf{r} = (x, y, z)$, the *equatorial* radius of the equipotential passing through that position is given by

$$\begin{aligned} q^2 &= \frac{r^2}{(1 - f\sin^2\phi)^2} \\ &= r^2[1 + 2f\sin^2\phi + O(f^2)] \\ &\approx x^2 + y^2 + z^2(1 + 2f). \end{aligned} \tag{2.5}$$

We can now define an effective impact parameter in terms of

$$b_{\text{eff}}^2 = As^2 + Bs + C, \tag{2.6}$$

with

$$\begin{aligned} A &= u_x^2 + u_y^2 + u_z^2(1 + 2f) \\ B &= 2xu_x + 2yu_y + 2zu_z(1 + 2f) \\ C &= x^2 + y^2 + z^2(1 + 2f). \end{aligned}$$

[2]Based on a suggestion by W. A. Wheaton of JPL.

Minimizing with respect to s, we find that the effective impact parameter is

$$b_{\rm eff} = \left(C - \frac{B^2}{4A} \right)^{1/2}. \tag{2.7}$$

We can achieve additional accuracy by abandoning the step-function model for the occultation edges and instead calculating the relative atmospheric transmission along the line of sight. We will assume an exponential atmosphere with density

$$\rho(q) = \rho(b_{\rm eff}) \exp\left[-\left(\frac{q - b_{\rm eff}}{h} \right) \right], \tag{2.8}$$

where h is the scale height of the atmosphere. The optical depth of the atmosphere along this line of sight is

$$\tau = 2\mu \int_0^\infty \rho(q) ds, \tag{2.9}$$

where μ is the mass attenuation coefficient of air and we have assumed that the spacecraft is well outside the atmosphere. Noting that $s = q \sin\theta$ and making a substitution of variables, we have

$$\tau = 2\mu b_{\rm eff} \rho(b_{\rm eff}) \int_0^{\pi/2} \exp\left[-\frac{b_{\rm eff}}{h} \left(\frac{1}{\cos\theta} - 1 \right) \right] \frac{d\theta}{\cos^2\theta}. \tag{2.10}$$

Assuming $b_{\rm eff} \gg h$, we can effectively make a small angle approximation,

$$\tau \approx 2\mu b_{\rm eff} \rho(b_{\rm eff}) \int_0^\infty \exp\left(\frac{-b_{\rm eff}\theta^2}{2h} \right) d\theta \tag{2.11}$$

$$= \mu \rho(b_{\rm eff}) \sqrt{2\pi b_{\rm eff} h}. \tag{2.12}$$

The occultation transmission function is then given by $e^{-\tau}$, which varies monotonically between zero and one over an occultation step. Typical parameter values are $h = 6$ km, $\rho(70 \text{ km}) = 3 \times 10^{-3}$ g cm^{-3}, and $\mu = 0.3$ cm^2 g^{-1}.

2.6 Detector Background

Gamma-ray observations in low Earth orbit must contend with a low instantaneous signal-to-noise ratio due to the high background count rate. A detailed review of the gamma-ray background for low-Earth orbit instruments in general is given by Dean, Lei, & Knight (1991); a discussion of the background for BATSE in particular is given by Rubin et al. (1996). The typical BATSE background as a function of energy is shown in Figure 2.10. The background count rate in the 20–100 keV range is over two orders of magnitude larger than the count rate for a typical accreting pulsar in BATSE data.

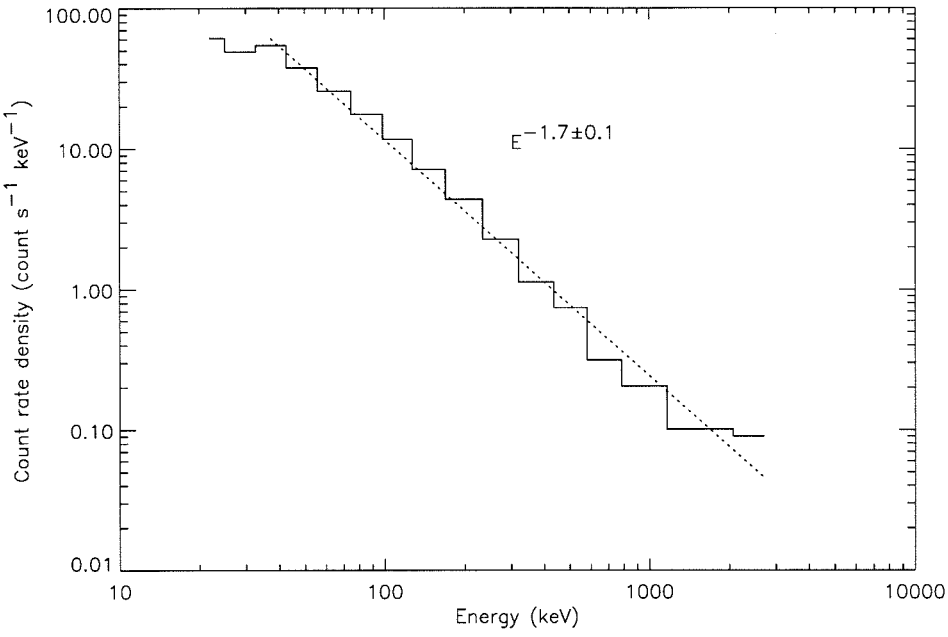

Figure 2.10: Typical count spectrum of the background as a function of energy for a BATSE LAD. The count spectrum is fairly flat in the 20–40 keV range and is well-described by an $E^{-1.7}$ power law above 40 keV. This plot can be used to predict the LAD background rate in an arbitrary energy range.

For pulsar studies, we are mainly interested in energies below 100 keV. In this regime, the dominant background component is diffuse cosmic emission. The raw 20–60 keV BATSE LAD count rates for one day of data are shown in Figure 2.11. The quasi-sinusoidal variations with a $\approx$ 93 min period are due to the spacecraft orbital modulation of sky area visible to the detectors. At these energies, the maximum background occurs when the detector is facing away from Earth, and the minimum occurs when the detector is facing toward Earth. The large gaps in the data occur during passages of the spacecraft through a region of extremely high background known as the South Atlantic magnetic anomaly (SAA; see Tascione 1988). Due to the extremely high flux of trapped charged particles in this region, the detector high voltage is turned off to prevent electrical breakdown damage. Smaller gaps due to brief telemetry errors are also sometimes present.

It is instructive to consider the power spectral properties of the BATSE background in the frequency domain. The mean raw background rate in the 20–60 keV DISCLA data is 1500 counts s^{-1}. A steady, unmodulated photon background of this strength would be a Poisson process and would have a power spectral density of 1500 counts^2 s^{-2} Hz^{-1},

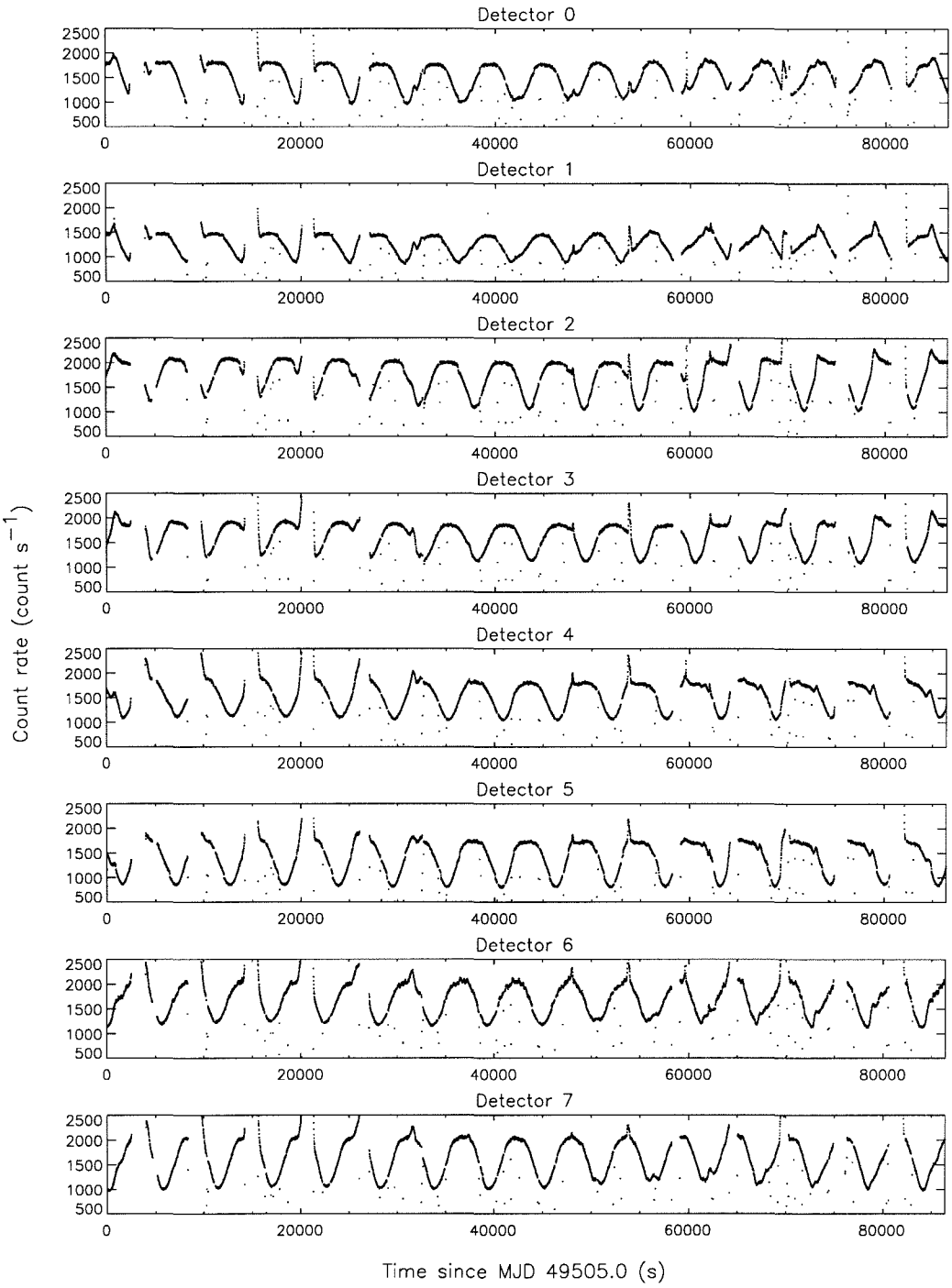

Figure 2.11: Raw DISCLA channel 1 (20–60 keV) count rates from the 8 BATSE LADs on 1994 June 2 (MJD 49505). The data shown are averaged at 50 s intervals. The large off-scale events (e.g., near $t = 15000$ s) occur at the edges of passages through the South Atlantic magnetic anomaly.

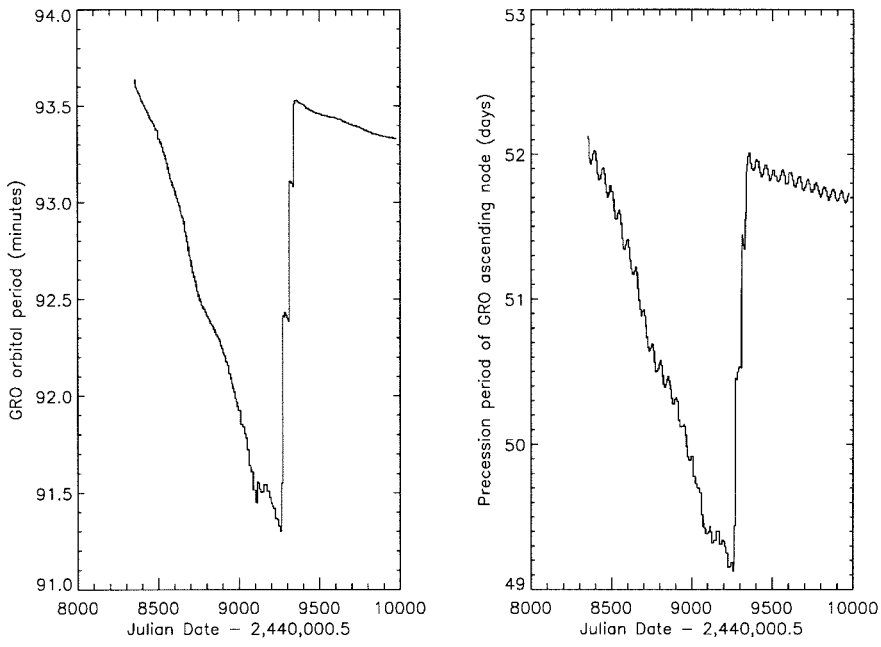

Figure 2.12: Decay of the *Compton* spacecraft orbit. *(Left panel:)* Evolution of the *Compton* orbital period. *(Right panel:)* Evolution of the precession period of *Compton*'s ascending node. The discontinuity of both plots near day MJD 49300 is due to the reboost of the *Compton* spacecraft during that interval.

independent of frequency. However, as is evident in Figure 2.11, the BATSE background is by no means steady and unmodulated. The strong 93 min orbital modulation results in a large excess of power at frequencies near $\nu_{\rm GRO} \approx 2 \times 10^{-4}$ Hz. In addition, the complicated time structure of the SAA gaps and the sharp occultation edges caused by bright astrophysical sources are also modulated at the orbital period, introducing significant power at higher harmonics of $\nu_{\rm GRO}$. There are also power contributions at beat frequencies of $\nu_{\rm GRO}$ and its harmonics with the Earth's daily rotation period. For analysis of long time series of BATSE data, power contributions at harmonics of the precession frequency of the spacecraft orbit, as well as at beats with these frequencies, are also important. Periodic and secular variations in the spacecraft orbital parameters caused by the tidal perturbations and atmospheric drag (see Figure 2.12) result in a modulation of the relevant families of low-frequency noise peaks in the power spectrum.

The complex low-frequency noise contributions to the BATSE background result in a significant departure from Poisson statistics in the raw data, especially at long time scales (top curve of Figure 2.13). We can improve our sensitivity to pulsed signals by attempting

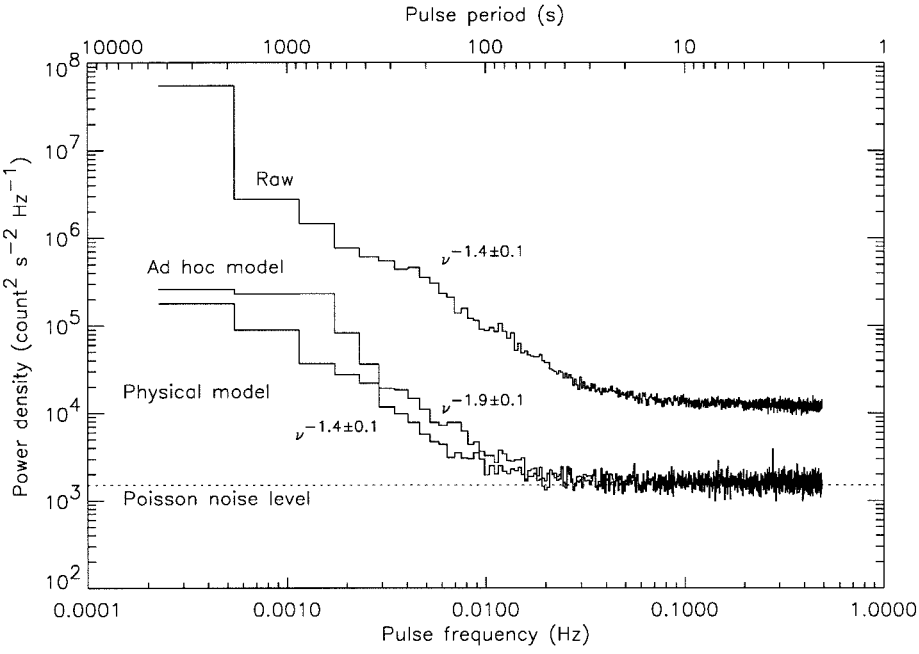

Figure 2.13: Typical pulse frequency dependence of the BATSE LAD background in the 20–60 keV range. The top curve is for the unprocessed raw data. The middle curve is for the raw data after subtraction of an ad hoc background model. The bottom curve is for the raw data after subtraction of the Rubin et al. (1996) physical background model. The dotted line shows the Poisson noise level expected for the raw count rates. For both versions of the background subtraction, the background fluctuations are consistent with the Poisson level on time scales $\lesssim 100$ s. The data shown are for DISCLA channel 1 (20–60 keV) from LAD 0 on 1994 June 2 (MJD 49505). A peak near 0.28 Hz due to the pulsar 4U 0115+63 is visible in the background-subtracted data.

to remove the background contributions. There are two basic approaches to this task:

- **Ad hoc background model.** We can construct an ad hoc model for the background by removing impulsive spikes and interpolating over gaps in the raw data and then smoothing. The resulting time series is a good approximation to the orbital background variation, which can be subtracted from the raw data. Any sort of smoothing or averaging will affect low-frequency signals as well as background. To keep track of this explicitly, we perform the smoothing in the frequency domain by multiplying the Fourier transform of the interpolated raw time series by a frequency-dependent (low pass) filter function

$$R(\nu) = \begin{cases} \frac{1}{2}\left(1 + \cos \pi \frac{\nu}{\nu_0}\right) & \text{for } \nu < \nu_0 \\ 0 & \text{for } \nu_0 < \nu < \nu_{\rm Nyq} \end{cases} \tag{2.13}$$

where ν_0 is the cutoff frequency of the low-pass filter and $\nu_{\rm Nyq}$ is the Nyquist frequency of the time series. (For all of the analysis presented in this thesis, $\nu_0 = 1.6 \times 10^{-3}$ Hz). We then use the inverse Fourier transform of this product as an approximate background model, which we subtract from the raw time series. After this subtraction, we discard the interpolated segments by reintroducing the original gap structure into the background-subtracted time series. The power spectrum of a time series with the ad hoc background model subtracted is shown in the middle curve of Figure 2.13. Most of the noise reduction is from the elimination of broadband "ringing" harmonics introduced by spikes and gaps. We emphasize the explicit side effect of this technique, that real signals with periods $\gtrsim 1/\nu_0 \approx 640$ s are attenuated along with the noise background.

- **Physical background model.** Both the BATSE instrument team (Rubin et al. 1996) and investigators at JPL (Skelton et al. 1993) have developed semi-empirical physical models for the known sources of background in the BATSE data. The Rubin et al. (1996) model includes the diffuse cosmic gamma-ray background, the atmospheric gamma-ray background caused by cosmic ray interactions, the prompt background due to cosmic ray interactions with material on the spacecraft, the delayed internal background caused by activation of spacecraft material by cosmic rays and trapped particles in the SAA, and occultation edges due to bright astrophysical sources. This technique assumes the presence of periodic behavior at harmonics of the orbital period, so some attenuation of low frequency signal as well is inevitable in the fitting process.

For both methods of background subtraction, the noise power is consistent with the Poisson level on time scales $\lesssim 80$ s. However, at longer time scales, a strong noise red-noise component is still present, although at a substantially reduced level compared to the original time series. The physical background model performs somewhat better than the ad hoc model at long time scales, yielding a factor of ~ 3 reduction in the noise power (corresponding to a factor of $\sim \sqrt{3}$ improvement in sensitivity at these pulse frequencies).

2.7 Sensitivity to Pulsed Signals

2.7.1 General Principles

Astrophysical observations with non-imaging instruments require a way to distinguish source emission from background. The usual approach is to split the observation into two adjacent pointings of equal duration: an on-source interval and an off-source interval, with as much overlap in the background regions as possible. This technique is ineffective with BATSE due to its large field of view and highly variable background. Earth occultation measurements provide the only means to make a background-limited observation of a steady source with BATSE. In this case, the occultation step provides the differentiation between on-source and off-source within the same pointing. In a similar vein, pulsations also provide a way to distinguish between source and background within the same pointing. However, in this case, only the pulsed component can be measured; the steady component is indistinguishable from the background. All of the observations described in this thesis fall into this last category.

To compute the signal-to-noise ratio of pulsed signal in the presence of a background which may depend upon pulsed frequency, it is convenient to work in the frequency domain. For a sinusoidal signal with amplitude a and frequency ν_0, the signal strength is characterized by the root-mean-squared amplitude $s = a/\sqrt{2}$. The noise is given by

$$n = \sqrt{\sigma_s^2 + \sigma_b^2(\nu)}, \tag{2.14}$$

where σ_s^2 is the variance of the signal strength and σ_b^2 is the variance of the background level. For a steady pulsed signal, the signal variance is simply given by Poisson statistics,

$$\sigma_s^2 = \frac{a}{\sqrt{2}}\Delta\nu = \frac{a}{T\sqrt{2}}, \tag{2.15}$$

where $\Delta\nu = 1/T$ is the frequency resolution of the observation, T is the duration of the observation, and the result is independent of ν_0. The variance of the background is

$$\sigma_b^2(\nu_0) = \Delta\nu \left[\frac{dP}{d\nu}\right]_{\nu=\nu_0} = \frac{1}{T}\left[\frac{dP}{d\nu}\right]_{\nu=\nu_0}, \tag{2.16}$$

where $dP/d\nu$ is the power spectral density of the background fluctuations. Our pulsar observations are in the background-limited regime ($\sigma_b \gg \sigma_s$), so the signal-to-noise ratio (SNR) is given by

$$\mathrm{SNR} = \frac{aT^{1/2}}{\sqrt{2}}\left[\frac{dP}{d\nu}\right]^{-1/2}_{\nu=\nu_0}. \tag{2.17}$$

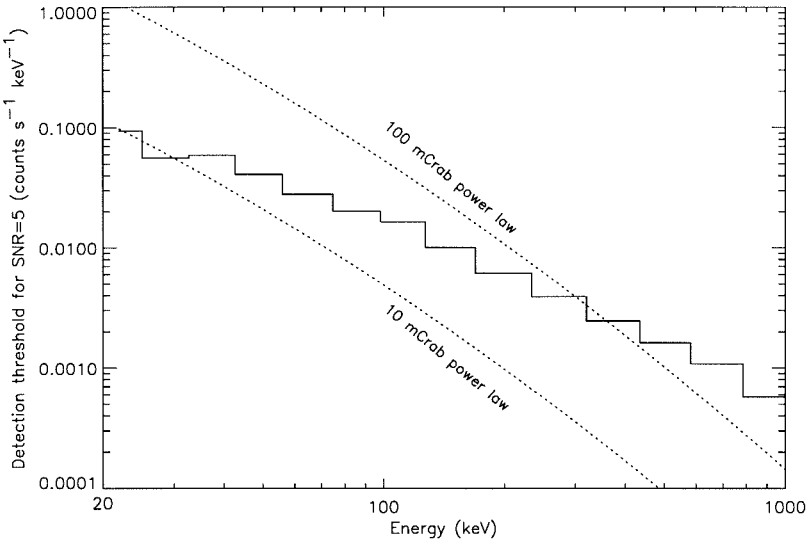

Figure 2.14: Typical BATSE pulsar detection sensitivity as a function of energy, for 1 day of data. The solid line denotes the count flux density required for a signal-to-noise ratio of 5. For comparison, the expected flux densities for a Crab-like source at 15 mCrab and 100 mCrab are shown by the dotted curves.

It is interesting to compare this to the usual (time-domain) expression for SNR in a background-limited observation,

$$\mathrm{SNR} = s\sqrt{\frac{T}{b}}, \tag{2.18}$$

where b is the mean background rate. We can evidently regard $dP/d\nu$ as numerically equivalent to an *effective background rate*. Indeed, we saw in the previous section that $dP/d\nu$ is numerically identical to the mean BATSE background rate at high frequencies where Poisson statistics are operative. We also note the factor of $\sqrt{2}$ reduction in the SNR for a sinusoidally pulsed signal. This is because of the reduced duty cycle of a sinusoid compared to a constant signal. The SNR for a more complicated pulse shape can be computed by superposition of appropriately scaled harmonics. In this case, the background power should be computed separately for each harmonic.

2.7.2 BATSE Sensitivity as a Function of Energy

We can use the count spectrum of the background in Figure 2.10 to estimate the energy dependence of BATSE's pulsed source sensitivity. Let us confine ourselves to pulse periods $P \lesssim 80$ s, so that we can assume Poisson statistics for $dP/d\nu$. The detection

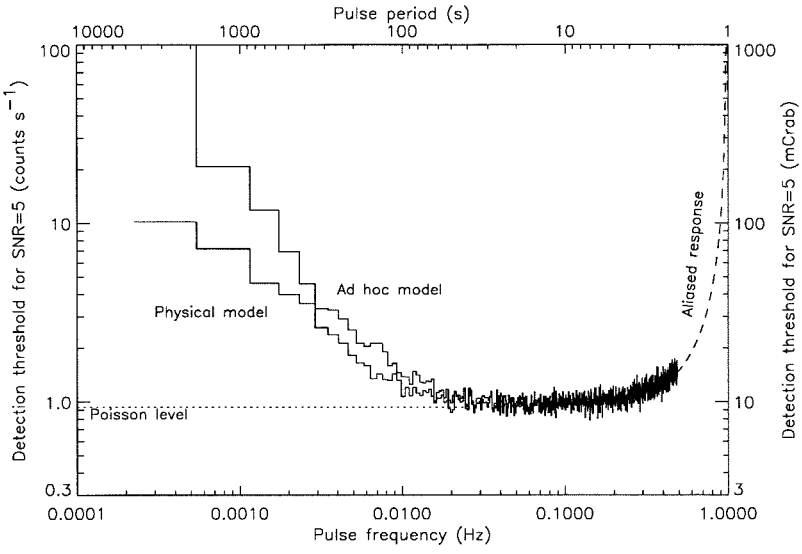

Figure 2.15: Typical BATSE pulsar detection sensitivity as a function of pulse frequency, for 1 day of 20–60 keV DISCLA data. The upturn above 0.2 Hz is due to the 1.024 s binning of the data. At low frequencies, the physical model-subtracted data is at least a factor of 2 more sensitive than the ad hoc model-subtracted data, which has reduced sensitivity below 1.6×10^{-3} Hz due to signal attenuation by the digital filtering process. The low-frequency sensitivity shown for the physical model-subtracted data does not take into account the loss of sensitivity caused by "absorption" of signal power in the background-fitting process. Data shown are from LAD 0 on 1994 June 2 (MJD 49505).

threshold for SNR=5 in 1 day of data is shown with the solid curve in Figure 2.14. The dotted lines represent the expected count spectrum for sources with spectra similar to the Crab Nebula ($\gamma = 2.15$) incident photon power-law spectrum, with intensities of 15 mCrab and 100 mCrab. We see that the 15 mCrab source is only detected below below 30 keV, while the 100 mCrab source can be detected well above 100 keV. Actual accreting pulsars tend to have spectral cutoffs in the 20–40 keV range, with their spectra falling faster than the Crab's above this energy.

2.7.3 BATSE Sensitivity as a Function of Pulse Frequency

Since most of our pulsar detection studies are done with the 20–60 keV DISCLA data, it is of particular interest to determine the pulse frequency dependence of BATSE's sensitivity in this energy range. We have used the frequency-dependent noise background measurement in Figure 2.13 to compute the sensitivity achieved in a 1-day observation of a source at normal incidence using background-subtracted data. The results are plotted in

Table 2.4. Leap Seconds

Starting Epoch Date	MJD	TAI−UTC (s)
1991 Jan 1	48257.0	26.0
1992 Jul 1	48804.0	27.0
1993 Jul 1	49169.0	28.0
1994 Jul 1	49534.0	29.0
1996 Jan 1	50083.0	30.0

New updates of the leap second schedule can be obtained from the U.S. Naval Observatory via WWW (file://maia.usno.navy.mil/ser7/tai-utc.dat).

Figure 2.15. BATSE's sensitivity degrades rapidly for pulse frequencies $\lesssim 0.01$ Hz, although the physical model-subtracted data degrade more slowly than the ad hoc model-subtracted data. Above 0.2 Hz, there is a loss of sensitivity due to binning of the data (see §3.2.3). The expected response for high-frequency (aliased) signals is indicated by the dashed line.

2.8 Time Systems and Reference Frames

The *Compton Observatory* orbits Earth and Earth orbits the Sun. Both these effects will introduce periodic advances and delays in the BATSE measurements of astrophysical pulse arrival times, or equivalently periodic Doppler shifts in measurements of pulse frequencies. These effects are removed by transforming to a reference frame at the solar system barycenter which is inertial with respect to the pulsar[3].

A more subtle correction is necessary as well. Pulsar timing measurements can probe small time variations over long time scales and consequently require extraordinarily careful attention to the terrestrial time standards to which measurements are referred. Indeed, some millisecond radio pulsars have such superb intrinsic temporal stability, and can be timed with such high precision, that they provide an experimental probe of theories of gravity. By contrast, the accreting pulsars studied in this thesis are very noisy clocks. Moreover, their substantially slower rotation periods ease the required timing accuracy of

[3]Of course, there will also be a periodic variation due to the binary motion of the pulsar, but this is one of the things we want to measure! Once the pulsar orbital parameters are known, the observations can be further transformed to a frame which is inertial with respect to the center of mass of the pulsar binary, allowing us to probe the rotation history of the neutron star without orbital contamination.

the observations by three orders of magnitude. Still, it is essential to reduce the observations to an inertial, uniform dynamical time system.

There are several time scale systems which are relevant to our observations[4]. At present, the most precise determination of time available is provided by atomic clocks. International Atomic Time (TAI) is a time scale constructed by averaging a large number of atomic clocks worldwide and provides the basis for the SI second. Coordinated Universal Time (UTC) is the basis of civil timekeeping. It is closely tied to the observationally determined time scale UT1, which is related to the mean apparent motion of the Sun due both to the rotation and the orbit of Earth. Due to irregularities in Earth's rotation, UT1 gradually accumulates discrepancies with respect to TAI. UTC is an artificial time scale which differs from TAI by an exact integer number of seconds, and is maintained within 0.9 s of UT1 by the intermittent introduction of *leap seconds* (see Table 2.4).

The time system which we want to refer our data to is dynamical time. This theoretical time scale is the independent variable in physical equations of motion. Due to relativistic effects, this time scale depends upon the reference frame in which it is measured. Motion referred to a geocentric reference frame can be expressed in terms of Terrestrial Dynamical Time (TDT), while motion referred to the solar system barycenter is expressed in terms of Barycentric Dynamical Time (TDB). TDT is specified with respect to TAI and is currently set as TDT = TAI + 32.184 s (exactly), so that they are identical except for a constant offset. TDB is specified with respect to TDT through a relativistic correction for gravitational redshift and time dilation due to the motion of the Earth with respect to the solar system barycenter. For the analyses in this thesis, a more-than-sufficiently accurate relation (Seidelmann, Guinot, & Doggett 1992) is

$$\mathrm{TDB} = \mathrm{TDT} + (0.001658\ \mathrm{s})\ \sin M + (0.000014\ \mathrm{s})\ \sin 2M, \tag{2.19}$$

where M, the mean anomaly of Earth, is given by

$$M = 357.53^\circ + 0.98560028^\circ\,(\mathrm{MJD} - 51544.5). \tag{2.20}$$

In pulsar astrophysics, this relativistic correction is called the *solar system Einstein delay.*

In summary, there are a series of corrections which must be applied to the BATSE observation times. BATSE data are recorded with UTC measurement times at the spacecraft. By adding the appropriate number of leap seconds (Table 2.4) and a constant 32.184 s

[4]The discussion that follows draws from Seidelmann, Guinot, & Doggett (1992).

offset, we readily obtain TDT at the spacecraft ($t_{\rm GRO}$). To obtain TDB at the solar system barycenter (t_b), we can follow Taylor & Weisberg (1989) by writing

$$t_b = t_{\rm GRO} + \frac{\mathbf{r}\cdot\hat{\mathbf{s}}}{c} + \Delta_{E\odot} + \Delta_{S\odot}. \tag{2.21}$$

The second term on the right-hand side is the projected light travel time correction from the spacecraft to the barycenter along the line of sight to the pulsar, sometimes called the *solar system Römer delay*; $\mathbf{r}$ is the position vector of *Compton* with respect to the solar system barycenter, and $\hat{\mathbf{s}}$ is the unit vector toward the pulsar. The spacecraft barycentric position is calculated as

$$\mathbf{r} = \mathbf{R}_{\rm GRO} + \mathbf{r}_{\oplus}. \tag{2.22}$$

The geocentric spacecraft vector $\mathbf{R}_{\rm GRO}$ is recorded in the BATSE housekeeping data (§2.2), and the barycentric vector for the Earth $\mathbf{r}_{\oplus}$ is computed using the Jet Propulsion Laboratory DE-200 solar system ephemeris (Standish et al. 1992). The third term in Equation (2.21), $\Delta_{E\odot}$, is the solar system Einstein delay given in Equation (2.19). The final term in Equation (2.21), $\Delta_{S\odot}$, is a relativistic correction for the propagation of the pulsar photons through the gravitational field of the Sun. This effect, called the *solar system Shapiro delay*, is of order 5 μs and thus utterly negligible for our purposes.

2.9 Standard Analysis Procedure

The standard pulsed source analysis consists of the following steps (see Figure 2.16):

- **Background-subtraction.** The four detectors viewing the direction of interest are conditioned to remove the orbital background. Timing studies using the DISCLA data were background-subtracted using the ad hoc model technique. Spectral studies using the CONT data were processed with the Rubin et al. 1996 background model.
- **Optimal combination of detectors.** The four detectors are summed using a $\cos^2\theta$ weighting scheme.
- **Mask out bad data and Earth-occulted intervals.** Bad time intervals, as indicated by the QUAL file information, are masked out of the summed time series. Intervals during Earth occultation of the direction of interest are also masked out.

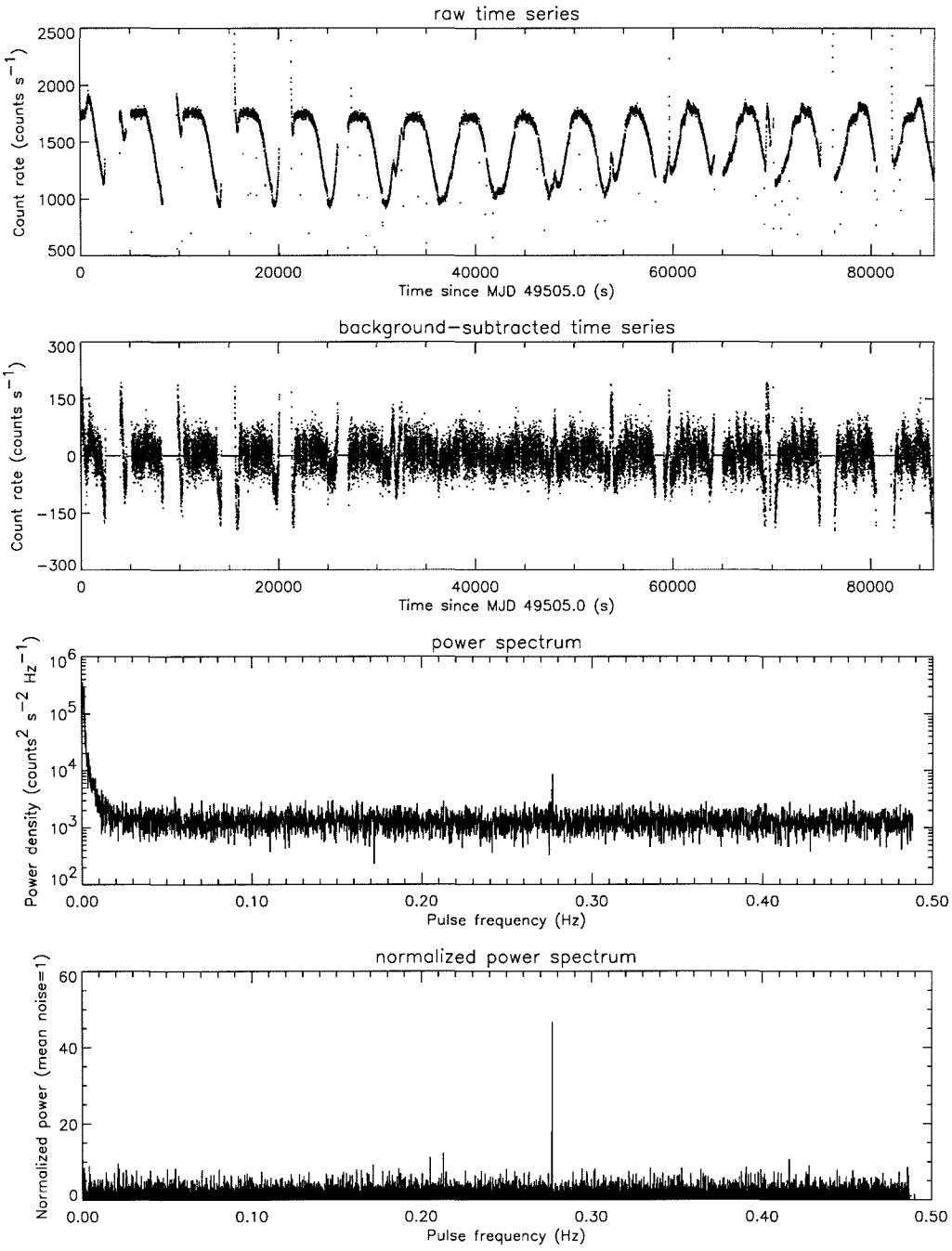

Figure 2.16: Standard BATSE analysis sequence. The data shown are for LAD 0 on 1994 June 2 (MJD 49505). The top panel shows the raw time series. The second panel shows the time series after subtraction of the ad hoc background model. The third panel shows the Fourier power spectrum of the filtered time series. The peak near 0.27 Hz is due to 4U 0115+63. The bottom panel shows the power spectrum renormalized by the local noise power. The pulsed signal due to 4U 0115+63 is evident.

- **Apply barycenter correction.** If the source position is known accurately, then the data are transformed from UTC times at the spacecraft to an inertial frame in terms of TDB times at the solar system barycenter. If the source position is not well known but the observation is long enough that ignoring the barycenter correction would introduce decoherence effects (see Appendix B), then an approximate source position can be used to apply a rough barycenter correction. Operationally, the barycenter correction consists of five steps:

  1. Measure UTC time at *Compton.*
  2. Add appropriate number of leap seconds to obtain TAI time at *Compton.*
  3. Add 32.184 s to obtain TDT at *Compton.*
  4. Add solar system Einstein delay to obtain TDB at *Compton.*
  5. Add light travel time correction to obtain TDB at barycenter.

All pulsar timing parameters in this thesis are referred to TDB at the solar system barycenter. The time series obtained after the above steps is the basic data set used for our pulsar studies at Caltech.

References

Brock, M. N., Meegan, C. A., Roberts, F. E., Fishman, G. J., Wilson, R. B., Paciesas, W. S., & Pendleton, G. N. 1991. Gamma ray burst locations from the Burst and Transient Source Experiment. In *Gamma Ray Bursts*, ed. W. S. Paciesas & G. J. Fishman (New York: AIP), 383.

Dean, A. J., Lei, F., & Knight, P. J. 1991. Background in space-borne low-energy γ-ray telescopes. *Space Sci. Rev.*, **57**, 109.

Fazio, G. G. & Eisenhardt, P. 1990. The Space Infrared Telescope Facility (SIRTF). In *Observatories in Earth Orbit and Beyond*, ed. Y. Kondo (Dordrecht: Kluwer), 193.

Fishman, G. J. et al. 1989. BATSE: the Burst and Transient Source Experiment on the Compton Gamma Ray Observatory. In *Proc. of the GRO Science Workshop*, ed. W. N. Johnson (Greenbelt: NASA/GSFC), 2-39.

Harmon, B. A. et al. 1992. Occultation analysis of BATSE data: operational aspects. In *Compton Observatory Science Workshop*, ed. C. R. Shrader, N. Gehrels, & B. Dennis (Washington: NASA CP-3137), 69.

Horack, J. M. 1991. *Development of the Burst and Transient Source Experiment (BATSE)* (Washington: NASA Reference Publication 1268).

Johnson, W. N. et al. 1993. The Oriented Scintillation Spectrometer Experiment: instrument description. *Astrophys. J. Suppl.*, **86**, 693.

Pendleton, G. N. et al. 1995. The detector response matrices of the Burst and Transient Source Experiment (BATSE) on the Compton Gamma Ray Observatory. *Nucl. Instr. Methods A*, **364**, 567.

Pendleton, G. N., Paciesas, W. S., Briggs, M. S., Harmon, B. A., & Wilson, C. A. 1994. Channel to energy calibration results for the BATSE large area detectors. In *Second Compton Symposium*, ed. C. E. Fichtel, N. Gehrels, & J. P. Norris (New York: AIP), 749.

Rubin, B. C., Lei, F., Fishman, G. J., Finger, M. H., Harmon, B. A., Paciesas, W. S., Pendleton, G. N., & Wilson, R. B. 1996. A model of the gamma-ray background on the BATSE experiment. *Astron. & Astrophys. Suppl.*, in press.

Schönfelder, V. et al. 1993. Instrument description and performance of the imaging gamma-ray telescope COMPTEL aboard the Compton Gamma Ray Observatory. *Astrophys. J. Suppl.*, **86**, 657.

Seidelmann, P. K., Guinot, B., & Doggett, L. E. 1992. Time. In *Explanatory Supplement to the Astronomical Almanac*, ed. P. K. Seidelmann (Mill Valley: University Science Books), 39.

Shrader, C. R. & Gehrels, N. 1995. Recent results from the Compton Gamma Ray Observatory. *Pub. Astron. Soc. Pacific*, **107**, 606.

Skelton, R. T., Ling, J. C., Ling, N. F., Radocinski, R., & Wheaton, W. A. 1993. Status of the BATSE enhanced Earth occultation analysis package for studying point sources. In *Compton Gamma-Ray Observatory*, ed. M. Friedlander, N. Gehrels, & D. J. Macomb (New York: AIP), 1189.

Standish, E. M., Newhall, X. X., Williams, J. G., & Yeomans, D. K. 1992. Orbital ephemerides of the Sun, Moon, and planets. In *Explanatory Supplement to the Astronomical Almanac*, ed. P. K. Seidelmann (Mill Valley: University Science Books), 279.

Tascione, T. F. 1988. *Introduction to the Space Environment* (Malabar: Orbit Book Company).

Taylor, J. H. & Weisberg, J. M. 1989. Further experimental tests of relativistic gravity using the binary pulsar PSR 1913+16. *Astrophys. J.*, **345**, 434.

Thompson, D. J. et al. 1993. Calibration of the Energetic Gamma Ray Experiment (EGRET) for the Compton Gamma Ray Observatory. *Astrophys. J. Suppl.*, **86**, 629.

Weisskopf, M. C. 1988. Astronomy and astrophysics with the Advanced X-Ray Astrophysics Facility. *Space Sci. Rev.*, **47**, 47.

Zhang, S. N., Fishman, G. J., Harmon, B. A., Paciesas, W. S., Meegan, C. A., Wilson, R. B., Finger, M. H., & Rubin, B. C. 1995. A maskless gamma-ray all-sky imager: BATSE/CGRO. *IEEE Trans. Nuc. Sci.*, **41**, 1313.

Chapter 3

Detection and Estimation of Periodic Pulsed Signals

Noise proves nothing.
—Mark Twain (1897)

3.1 Introduction

Detection of a periodic signal in noisy data and estimation of the signal strength are properly treated as distinct questions. The detection problem involves testing the hypothesis of uniformity for the observed data. Only if this null hypothesis can be rejected with reasonable significance is a strength estimate meaningful. In this chapter, we will consider the statistics of these issues.

3.2 Detection of Periodic Pulsed Signals

3.2.1 Time Domain: Epoch Folding

The most intuitive way to search a time series for a periodicity with period P is to fold the data modulo P and look for departures from a uniform distribution. Specifically, we divide P into some number $N_{\rm bins}$ of phase intervals in the range [0, 1] (or, in terms of angular phase, $[0, 2\pi]$), assign each time series datum a phase according to

$$\phi_i = \frac{t_i}{P} \bmod 1, \tag{3.1}$$

and build up a histogram of phases $h_j(\phi)$, where $j = 1, \ldots, N_{\rm bins}$. This is called *epoch folding*. If the time series itself is binned, then the histogram can be constructed in one of two ways. Where a time series bin straddles two or more phase bins, one can split the time series bin and increment each phase bin in proportion to the overlap, making the assumption that the accumulated counts were distributed evenly across the time series bin. Alternatively, one can treat each time series bin as a delta function at the bin center and add it entirely into the single appropriate phase bin. The latter approach has the advantage of keeping the phase bins statistically independent, and it is the approach we favor with the BATSE data[1].

For a uniform background in the absence of a periodic signal, the histogram will be statistically consistent with a flat line. In the presence of a periodic signal component at period P, the histogram will have statistically significant structure. In pulsar timing, such a histogram is called a *pulse profile* and is used to represent the mean pulse shape emitted by the neutron star. Pulse profiles are an example of a class of data variously referred to as *circular*, *directional*, or *angular* due to their intrinsically periodic nature. The statistics of such data are common to a wide variety of applications (see Mardia 1972; Fisher 1993).

The detection of pulsed signals in epoch-folded data was reviewed recently by de Jager (1994). The most commonly employed test for uniformity is the classical Pearson χ^2 test (Leahy et al. 1983). We define the statistic

$$S = \sum_{j=1}^{N} \frac{(x_j - \langle x \rangle)^2}{\sigma_j^2}, \tag{3.2}$$

where x_j is the jth time series bin, $\langle x \rangle$ is the mean value of the time series, and σ_j^2 is the variance of the jth time series bin. In the limit of large count rates (including background), S is a χ^2 random variable with $N-1$ degrees of freedom in the absence of a periodic signal. Values of $S \gg N-1$ thus lead to rejection of the uniform hypothesis and indicate the presence of a pulsed signal. An alternative statistic is the Z_m^2 test of Buccheri et al. (1983) and Buccheri & Sacco (1985), which is constructed from the sum of the Fourier powers of the first m harmonics of the pulse frequency[2].

[1] Our simulations have shown that if the background exhibits large stochastic variations on long time scales (as in the BATSE data), then the introduction of correlations between phase bins can produce fluctuations which falsely mimic a pulsed signal.

[2] Throughout this thesis, we will adopt the convention that the $m\nu = m/P$ is the mth harmonic of the fundamental frequency $\nu = 1/P$. Thus, the fundamental frequency is called the *first* harmonic.

A drawback of both the χ^2 test and the Z_m^2 test is the lack of an objective criterion for selecting the smoothing parameter $N_{\rm bins}$ or m, respectively. The choice of these parameters governs the power of these tests to detect pulses of different shapes, with larger values required for pulse shapes with lower duty cycle (i.e., which are sharper). De Jager et al. (1989) have advocated use of the H-test, a modification of the Z_m^2 test which specifies an objective criterion for selecting m. These issues are of lesser importance in BATSE studies of accreting pulsars, since the pulse shapes tend to be quite broad and sinusoidal.

Epoch folding is an attractively simple method for searching for a signal at a specific period. However, it is an extremely inefficient technique for searching a wide range of periods. The development of the fast Fourier transform (FFT) algorithm makes frequency domain techniques much more attractive for large pulsation searches.

3.2.2 Frequency Domain: Fourier Analysis

A good basic review of Fourier transforms is given by Press et al. (1992), and a detailed review of Fourier analysis techniques in X-ray timing is given by van der Klis (1988). In this section, we summarize the essential results from these reviews and elaborate on certain specific topics relevant to the BATSE analysis.

Consider a uniformly-sampled time series $\{h_j\}$ with mean zero and spacing Δt. The discrete Fourier transform (DFT) of this time series is given by

$$H_k = \sum_{j=0}^{N-1} h_j e^{2\pi i j k/N}. \tag{3.3}$$

The corresponding Fourier power,

$$P_k = |H_k|^2, \tag{3.4}$$

is an estimate of the variance at frequency $\nu = k/T$, where $T = N\Delta t$ is the length of the time series. The power spectrum consists of $N/2$ such estimates up to a maximum, called the *Nyquist frequency*, which is $\nu_{\rm Nyq} = N/2T$. If the background has a flat power spectral density, then it is convenient to renormalize the power spectrum relative to the mean noise power,

$$\bar{P}_k = \frac{P_k}{\langle P \rangle}. \tag{3.5}$$

If the background does not have a flat power spectrum, we can still effectively normalize the power with respect to the *local* noise power in the region of the frequency of interest.

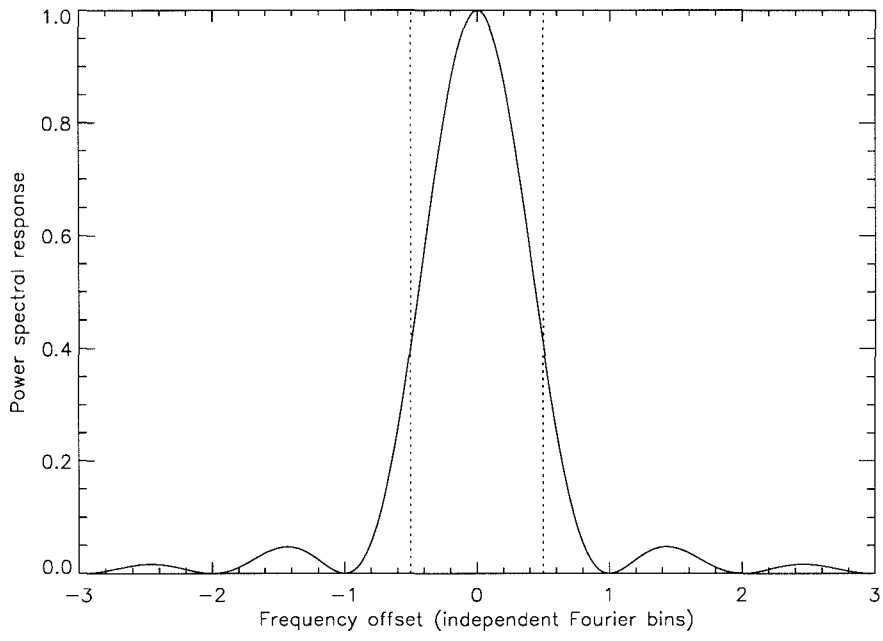

Figure 3.1: Power spectral response of a frequency bin as a function of frequency offset from the bin center. The dotted lines show the boundaries of the frequency bin.

The advantage of this renormalization is that if the power spectrum of the background is at least *locally* flat, then the probability that any given normalized Fourier power bin will exceed a threshold value $\bar{P}_0$ is just

$$\Pr(\bar{P} > \bar{P}_0) = e^{-\bar{P}_0}. \tag{3.6}$$

This relation provides a straightforward way to evaluate the statistical significance of a peak in the power spectrum.

If the discrete Fourier power spectrum were an ideal spectral estimator, it would have a flat frequency response across a frequency bin; that is, the power in bin k would be equally sensitive to any sinusoidal signal in the frequency range $[(k-1/2)/T, (k+1/2)/T]$. Unfortunately, the Fourier power spectrum is less sensitive to signals at frequencies nearly halfway between two Fourier frequencies. Due to the finite length of the time series T, the power spectral response in the kth Fourier frequency bin (where $\nu_k = k/T$) to a periodic signal with frequency ν_0,is given by

$$R(\nu) \approx \left[\frac{\sin \pi(\nu_0 - \nu_k)T}{\pi(\nu_0 - \nu_k)T}\right]^2. \tag{3.7}$$

This response function is plotted in Figure 3.1. We see that the response is not at all flat across the frequency bin.

At first inspection, this loss of sensitivity at intermediate frequencies may seem to contradict the Fourier sampling theorem, which holds that the frequency content of a uniformly-sampled time series is completely determined by the discrete Fourier transform of the time series for all $|\nu| < \nu_{\rm Nyq}$ (see Press et al. 1992). The explanation is that information is lost from the complex-valued DFT in constructing the real-valued power spectrum. We can recover information at intermediate frequencies by shifting our Fourier frequency values by a fraction ϵ of a bin, yielding $f_{k+\epsilon}$ with $0 < \epsilon < 1$. The shifted DFT is given by

$$H_{k+\epsilon} = \sum_{j=0}^{N-1} h_j e^{2\pi i j(k+\epsilon)/N} \tag{3.8}$$

$$= \sum_{j=0}^{N-1} (h_j e^{2\pi i j\epsilon/N}) e^{2\pi i j k/N} \tag{3.9}$$

$$= \sum_{j=0}^{N-1} y_j^{(\epsilon)} e^{2\pi i j k/N} \tag{3.10}$$

where $y_j^{(\epsilon)}$ is just the original time series multiplied by complex phase factors $e^{2\pi i j\epsilon/N}$. Note that while the N shifted power spectrum bins $\{P_{k+\epsilon}\}$ are statistically independent of each other, they are *not* independent of the original power spectrum $\{P_k\}$. Generalizing this process, we can construct an n-times oversampled DFT by interleaving the bins from the original DFT and $n-1$ frequency-shifted DFTs. Operationally, this is equivalent to padding the original N point time series with $(n-1)N$ zeros and taking the nN point DFT of the padded time series. Use of an oversampled power spectrum gives more uniform frequency sensitivity at the expense of independent frequency bins.

The oversampled spectrum also provides a convenient way to make a precise determination of the pulse frequency of a periodic signal. The precision possible depends on the signal-to-noise ratio, and can be much better than the independent Fourier frequency spacing $1/T$ for strong signals. Since we know that a periodic signal will appear in the Fourier power spectrum as Equation (3.7) plus noise, we can use the oversampled powers to calculate the exact position of the peak. If the highest power due to the signal occurs in frequency bin k (where k need not be an integer), then Middleditch (1976) has shown that

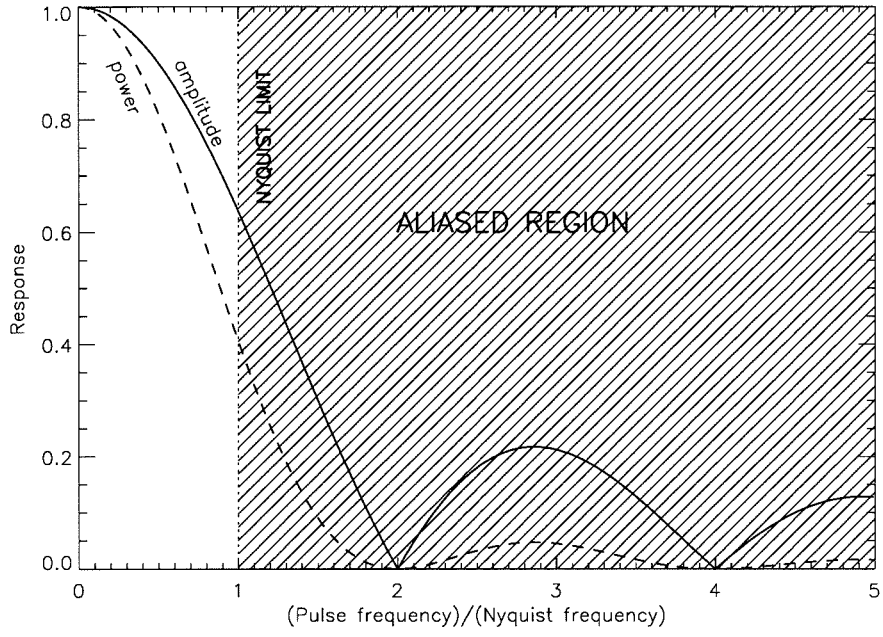

Figure 3.2: Frequency response to pulsed signals in binned data. The solid curve shows the pulsed amplitude response, and the dashed curve shows the Fourier power response. Signals in the shaded region will be aliased.

the best estimate of the signal frequency is given by

$$\hat{\nu}_0 = \nu_k + \frac{3}{4\pi^2 \epsilon T}\left(\frac{\bar{P}_{k+\epsilon} - \bar{P}_{k-\epsilon}}{\bar{P}_k}\right), \tag{3.11}$$

where $\bar{P}$ is normalized power, T is the length of the time series, and $n = 1/\epsilon$ is the oversampling factor. The uncertainty on the frequency determination (Middleditch 1976; Middleditch & Nelson 1976) is given by

$$\sigma_{\hat{\nu}_0} \approx \frac{1}{2\pi T}\sqrt{\frac{6}{\bar{P}_k}}. \tag{3.12}$$

3.2.3 Aliasing and Pulsed Sensitivity in Binned Data

Signals with $\nu > \nu_{\rm Nyq}$ in the power spectrum of a uniformly-sampled time series will be aliased back into range $0 \leq \nu \leq \nu_{\rm Nyq}$ according to

$$\nu_{\rm alias} = \begin{cases} \nu \bmod \nu_{\rm Nyq} & \text{for } (\nu \bmod 2\nu_{\rm Nyq}) \leq \nu_{\rm Nyq} \\ \nu_{\rm Nyq} - \nu \bmod \nu_{\rm Nyq} & \text{for } (\nu \bmod 2\nu_{\rm Nyq}) > \nu_{\rm Nyq} \end{cases}. \tag{3.13}$$

This can be understood as the result of the uniform sampling process, equivalent to multiplying the continuous function by a sum of delta functions $\sum_{j=0}^{N-1} \delta(t - j\Delta t)$. By the Fourier convolution theorem, this is equivalent to convolving the Fourier transform of the continuous function with a sum of delta functions, which results in aliasing in the power spectrum (see, e.g., Brigham 1974; Press et al. 1992). For time series which only samples a continuous function in this way, the aliased power of the signal will not be attenuated. However, binning of photon data *integrates* the flux over intervals of finite duration. This is equivalent to convolving the time series with a rectangular window function with full-width Δt equal to the time spacing of the data. By the Fourier deconvolution theorem, this is equivalent to multiplying the Fourier transform of the continuous flux history by the Fourier transform of the window function. As a result, the DFT will have a *frequency-dependent* response,

$$R(\nu) = \frac{\sin(\pi\nu/2\nu_{\rm Nyq})}{\pi\nu/2\nu_{\rm Nyq}}, \tag{3.14}$$

and the corresponding power spectral response will be $R^2(\nu)$. These curves are shown in Figure 3.2. The aliased frequencies are strongly attenuated and do not contribute significantly for frequencies $\nu \gtrsim 2\nu_{\rm Nyq}$. Note, however, that there is also a frequency dependence for the response below the Nyquist frequency. *This effect applies in both the time domain and the frequency domain and is intrinsic to binned data.* Pulsed flux and sensitivity measurements must take this response into account.

3.3 Estimation of Pulse Strength in Periodic Signals

Pulsed amplitude measurements in noisy data are inherently biased: one will obtain always obtain a positive value even in the absence of a real signal. This bias must be accounted for in order to estimate the true signal strength or to place a meaningful upper limit for a non-detection. Given a weak periodic signal of true amplitude s in the presence of noise with root-mean-squared strength n, the probability distribution for the *measured* amplitude a is given by (Thomas 1969; Goodman 1985)

$$p(a|s,n)da = \frac{2a}{n^2} \exp\left[\frac{-(a^2+s^2)}{n^2}\right] I_0\left(\frac{2as}{n^2}\right) da \qquad (a > 0), \tag{3.15}$$

where I_n is the nth order modified Bessel function of the first kind (Abramowitz & Stegun 1965). This function is plotted in the top panel of Figure 3.3 for several values of the true

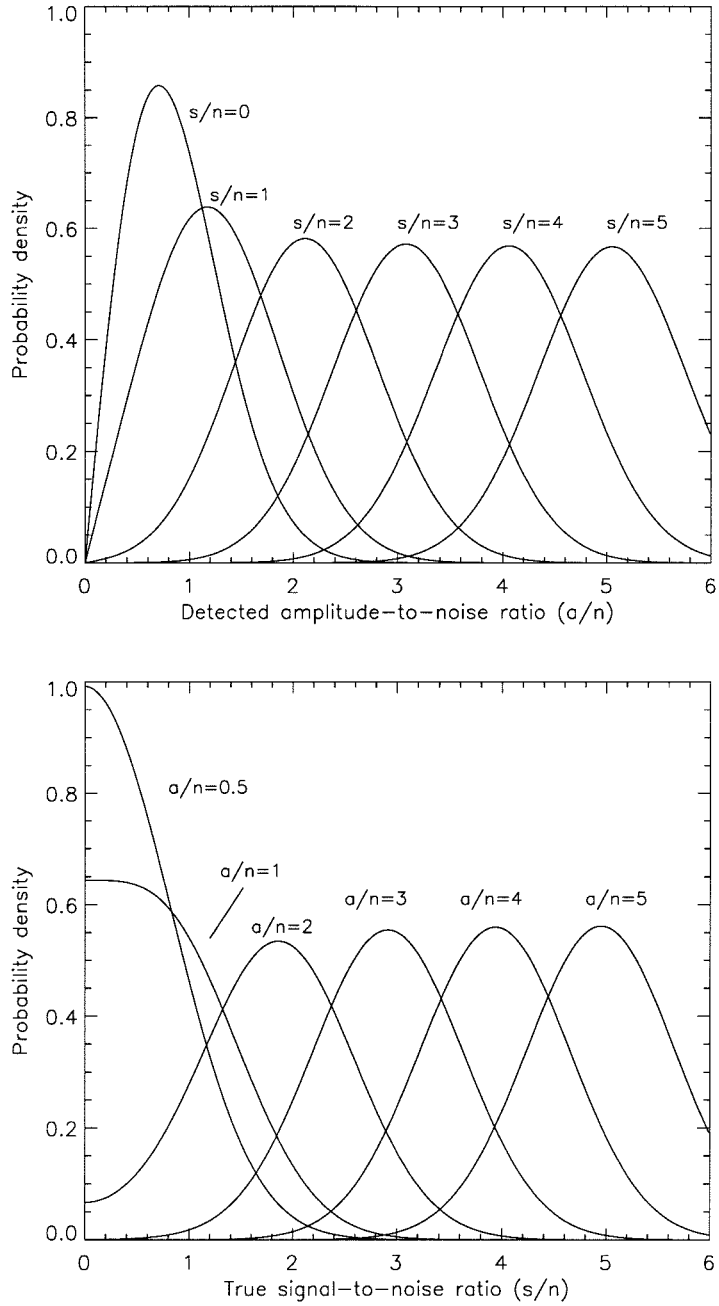

Figure 3.3: *Top panel:* Probability density for detected pulsed amplitude a, given true pulsed signal strength s and RMS noise strength n. Note that even in the absence of a signal ($s = 0$), one will measure a non-zero pulsed amplitude. *Bottom panel:* Probability density for the true pulsed signal amplitude s, given a measured amplitude a and RMS noise strength n. The distribution is highly skewed when $a/n \lesssim 1$, but approaches a Gaussian for strong detections.

signal-to-noise ratio s/n. Note that even in the absence of a signal, the likeliest value for the measured amplitude is $\sim n$. The distribution approaches a Gaussian for large s/n.

To infer the true signal strength from the measured amplitude, we need to know $p(s|a,n)$, which is related to $p(a|s,n)$ by Bayes's theorem (e.g., Eadie et al. 1971),

$$p(s|a,n)ds = \frac{p(s)p(a|s,n)ds}{\int_0^\infty p(s)p(a|s,n)ds}. \tag{3.16}$$

To invert this equation and solve for $p(s|a,n)$, we must make an assumption about the prior distribution of possible signals, $p(s)$. This takes us into the controversial area of Bayesian statistics (see, e.g., Cousins 1995). De Jager (1994) reviews various choices of priors for this problem. For strong signals ($s \gg n$), the inversion is not sensitive to the choice of prior. For weak signals, a conservative assumption is to assign all signal strengths equal prior probability, $p(s) = \text{constant}$. Substituting into Bayes's theorem, we find

$$p(s|a,n)ds = \frac{2}{n}\sqrt{\frac{1}{\pi}}\exp\left[\frac{-(a^2+2s^2)}{2n^2}\right]\frac{I_0\left(\frac{2as}{n^2}\right)}{I_0\left(\frac{a^2}{2n^2}\right)}ds \qquad (a>0). \tag{3.17}$$

This function is plotted in the bottom panel of Figure 3.3. For small values of the measured amplitude ($a/n \lesssim 2$), the distribution is highly skewed towards zero signal. The distribution approaches a Gaussian for large a/n.

We can calculate the relevant moments of these distributions,

$$\langle s|a,n\rangle = \int_0^\infty sp(s|a;n)ds = \sqrt{\frac{1}{\pi}}\frac{n\exp\left(\frac{a^2}{2n^2}\right)}{I_0\left(\frac{a^2}{2n^2}\right)} \tag{3.18}$$

$$\langle s^2|a,n\rangle = \int_0^\infty s^2p(s|a;n)ds = \frac{n^2}{2}\frac{\exp\left(\frac{a^2}{2n^2}\right)}{I_0\left(\frac{a^2}{2n^2}\right)}L_{1/2}\left(\frac{-a^2}{n^2}\right) \tag{3.19}$$

$$= \frac{n^2}{2}\left[\left(1+\frac{a^2}{n^2}\right)+\frac{a^2}{n^2}\frac{I_1\left(\frac{a^2}{2n^2}\right)}{I_1\left(\frac{a^2}{2n^2}\right)}\right], \tag{3.20}$$

where L_n is a Laguerre polynomial (Abramowitz & Stegun 1965). Similarly,

$$\langle a|s,n\rangle = \frac{\sigma\sqrt{\pi}}{2}\exp\left(\frac{-s^2}{2\sigma^2}\right)\left[\left(1+\frac{s^2}{n^2}\right)I_0\left(\frac{s^2}{2n^2}\right)+\frac{s^2}{n^2}I_1\left(\frac{s^2}{2n^2}\right)\right] \tag{3.21}$$

$$\langle a^2|s,n\rangle = s^2+n^2. \tag{3.22}$$

For a strong signal, we can use an asymptotic expansion for the modified Bessel functions (Abramowitz & Stegun 1965) to show

$$p(a|s,n) \approx p(s|a,n) \approx \frac{1}{\sqrt{\pi n^2}}\exp\left[\frac{-(a-s)^2}{n^2}\right] \qquad \text{for } s,a \gg n. \tag{3.23}$$

As expected, the distribution in the strong signal limit is a Gaussian with variance $\sigma^2 = n^2/2$.

Equation (3.17) is used to calculate confidence intervals for measurement of a pulsed signal in BATSE data. The resulting signal amplitude must be corrected for the frequency-dependent response in Equation (3.14). For a non-sinusoidal pulse shape, the pulse can be decomposed into harmonics. Unless the noise background has a flat power spectrum, the root-mean-squared noise strength n will depend on the harmonic frequency.

3.4 Flux and Spectral Estimation

Photons incident on a detector may fail to deposit their full energy. The difficulty of inferring the incident photon spectrum from a measured count spectrum arises from this simple fact. In the discussion that follows (which is equally applicable to pulsed and unpulsed measurements), we will distinguish between incident (*input*) energy E' and measured (*output*) energy E. For an idealized detector (one with perfect energy resolution), we can write

$$\underbrace{\frac{dC}{dE}(E)}_{[\text{count s}^{-1}\ \text{keV}^{-1}]} = \int_0^\infty dE' \quad \underbrace{\frac{\partial^2 N}{\partial E' \partial A}(E')}_{[\text{ph cm}^{-2}\ \text{s}^{-1}\ \text{keV}^{-1}]} \times \underbrace{\frac{dA}{dE}(E, E')}_{[\text{cm}^2\ \text{keV}^{-1}]}, \tag{3.24}$$

where dC/dE is the measured count flux density, $\partial^2 N/\partial E' \partial A$ is the incident source photon spectrum, and dA/dE is the detector resolution (response) kernel. Conceptually, the incident spectrum is convolved with the non-diagonal detector response to yield the observed spectrum. Mathematically, this is called a Fredholm integral equation of the first kind,

$$g(y) = \int_a^b f(x)\, K(x, y)\, dx, \tag{3.25}$$

with $f(x)$ consisting of both a homogeneous and a particular solution

$$f(x) = f_{\rm h}(x) + f_{\rm p}(x), \tag{3.26}$$

where

$$0 = \int_a^b f_{\rm h}(x) K(x, y). \tag{3.27}$$

One cannot solve such equations generally for $f(x)$ without making an assumption about its functional form (see Jeffrey & Rosner 1986 for a discussion). For the particular problem of spectral fitting, this means that we must make a choice of spectral model before trying

to fit the data. There is a substantial literature discussing numerical approaches to this issue, often referred to as the *inverse problem* in astronomy (see Craig & Brown 1986 for a review).

We can parametrize the problem for BATSE as follows. BATSE data are count rates in discrete output energy channels (16 in the case of the CONT data). For each BATSE detector, Pendleton et al. (1995) have computed the effective area of output channel i as a function of incident photon energy E' and viewing angle θ,

$$A_i(E') = A(E_i < E < E_{i+1}, E') = \int_{E_i}^{E_{i+1}} dE \frac{dA}{dE}(E, E'). \tag{3.28}$$

Operationally, a numerical integration is performed to compute a detector response matrix which gives the mean response of the detector to a series of narrow ranges of incident energy,

$$A_{ij} = \frac{1}{E'_{j+1} - E'_j} \int_{E'_j}^{E'_{j+1}} dE' \int_{E_i}^{E_{i+1}} dE \frac{dA}{dE}(E, E'). \tag{3.29}$$

Thus, the measured count rate in output channel i is modeled as

$$c_i = \frac{1}{E'_{j+1} - E'_j} \int_0^\infty dE' \int_{E_i}^{E_{i+1}} dE \frac{\partial^2 N}{\partial E' \partial A} \frac{dA}{dE}(E, E') \tag{3.30}$$

$$\approx \sum_j A_{ij} \int_{E'_j}^{E'_{j+1}} dE' \frac{\partial^2 N}{\partial E' \partial A}. \tag{3.31}$$

In this thesis, two different choices of spectral model are employed. The first is a photon power law,

$$\frac{dN}{dE'} = C_0 E'^{-\gamma}, \tag{3.32}$$

where γ is the photon index and C_{30} is a normalization constant. The second uses the functional form for optically-thin thermal bremsstrahlung,

$$\frac{dN}{dE'} = \frac{C_0}{E'} \bar{g}_{\rm ff}(E', kT) \exp(-E'/kT), \tag{3.33}$$

where kT is a characteristic thermal energy and $\bar{g}_{\rm ff}(E', kT)$ is the velocity-averaged free-free Gaunt factor (Rybicki & Lightman 1979). For most of our observations, the spectral quality is not high enough to detect curvature of the photon spectrum on a logarithmic scale, so we employ the power-law model as the simplest description. However, for the long-duration GX 1+4 spectra in Chapter 7, a power-law fit is clearly inadequate. It should be emphasized that the choice of a bremsstrahlung model is made because it is a convenient parametrization and is in wide use by observers of this source. The BATSE spectra are not of sufficient quality to distinguish between this model and other exponential forms.

References

Abramowitz, M. & Stegun, I. A., eds. 1965. *Handbook of Mathematical Functions* (New York: Dover).

Brigham, E. O. 1974. *The Fast Fourier Transform* (Englewood Cliffs, NJ: Prentice-Hall).

Buccheri, R. & Sacco, B. 1985. Time analysis in astronomy: tools for periodicity searches. In *Data Analysis in Astronomy*, ed. V. Di Gesu et al. (New York: Plenum), 15.

Cousins, R. D. 1995. Why isn't every physicist a Bayesian? *Am. J. Phys.*, **63**, 398.

Craig, I. J. D. & Brown, J. C. 1986. *Inverse Problems in Astronomy* (Bristol: Adam Hilger).

de Jager, O. C. 1994. On periodicity tests and flux limit calculations for gamma-ray pulsars. *Astrophys. J.*, **436**, 239.

de Jager, O. C., Swanepoel, J. W. H., & Raubenheimer, B. C. 1989. A powerful test for weak periodic signals with unknown light curve shape in sparse data. *Astron. & Astrophys.*, **221**, 180.

Eadie, W. T., Dryard, D., James, F. E., Roos, M., & Sadoulet, B. 1971. *Statistical Methods in Experimental Physics* (Amsterdam: North-Holland).

Fisher, N. I. 1993. *Statistical Analysis of Circular Data* (Cambridge: Cambridge U. Press).

Goodman, J. W. 1985. *Statistical Optics* (New York: Wiley).

Jeffrey, W. & Rosner, R. 1986. On strategies for inverting remote sensing data. *Astrophys. J.*, **310**, 463.

Leahy, D. A., Darbro, W., Elsner, R. F., Weisskopf, M. C., Sutherland, P. G., Kahn, S., & Grindlay, J. E. 1983. On searches for pulsed emission with application to four globular cluster X-ray sources: NGC 1851, 6441, 6624, and 6712. *Astrophys. J.*, **266**, 160.

Mardia, K. V. 1972. *Statistics of Directional Data* (London: Academic Press).

Middleditch, J. 1976. The measurement of the masses of the neutron star, Her X-1, and its binary companion, HZ Her, as derived from the study of 1.24-second optical pulsations from the HZ Her-Her X-1 binary system and the X-ray-to-optical reprocessing reflection and transmission mechanisms. Ph.D. thesis. University of California, Berkeley (Lawrence Berkeley Laboratory Report LBL-3639).

Middleditch, J. & Nelson, J. 1976. Studies of optical pulsations from HZ Herculis/Hercules X-1: a determination of the mass of the neutron star. *Astrophys. J.*, **208**, 567.

Pendleton, G. N. et al. 1995. *Nucl. Instr. Methods A*, **364**, 567.

Press, W. H., Teukolsky, S. A., Vetterling, W. T., & Flannery, B. P. 1992. *Numerical Recipes in C: The Art of Scientific Computing*, 2nd ed. (Cambridge: Cambridge U. Press).

Rybicki, G. J. & Lightman, A. P. 1979. *Radiative Processes in Astrophysics* (New York: Wiley).

Thomas, J. B. 1969. *An Introduction to Statistical Communication Theory* (New York: Wiley).

van der Klis, M. 1988. Fourier techniques in X-ray timing. In *Timing Neutron Stars*, ed. H. Ogelman & E. P. J. van den Heuvel (Dordrecht: Kluwer), 27.

Chapter 4

Discovery of the Orbit of the Accreting X-Ray Pulsar OAO 1657–415*

Something hidden. Go and find it. Go and look behind the Ranges—
Something lost behind the Ranges. Lost and waiting for you. Go!
—Rudyard Kipling (1903)

4.1 Introduction

There are currently six known eclipsing X-ray binary pulsars with well-determined orbits and optical spectroscopy, all of which yield important constraints on the neutron star mass range (see Nagase 1989). These measurements are complementary to the more accurate ones made in binary radio pulsar systems and might point out any evolutionary differences between these two types of systems. This chapter reports the detection of orbital motion and X-ray eclipses for a seventh X-ray binary pulsar, OAO 1657–415. Optical identification of the undiscovered companion followed by orbital phase spectroscopy and photometry will provide constraints on the neutron star mass.

The X-ray source OAO 1657–415 ($l = 344°, b = 0°.3$) was first detected by the *Copernicus* satellite (Polidan et al. 1978) in the 4–9 keV range and was initially misidentified as the companion to the massive spectroscopic binary V861 Sco. Subsequent observations by the *HEAO 1* satellite (Byrne et al. 1979; Armstrong et al. 1980) and the *Einstein*

*Adapted with changes from "Discovery of the Orbit of the X-Ray Pulsar OAO 1657–415" in *The Astrophysical Journal*, **403**, L33–L37 (1993 January 20), by D. Chakrabarty, J. M. Grunsfeld, T. A. Prince, L. Bildsten, M. H. Finger, R. B. Wilson, G. J. Fishman, C. A. Meegan, & W. S. Paciesas. Used by permission of the authors.

Observatory (Parmar et al. 1980) yielded a position error box which excludes V861 Sco. *HEAO 1* observations also showed 38.22 s pulsations in the 1–40 keV (White & Pravdo 1979) and 40–80 keV (Byrne et al. 1981) X-ray flux. More recent observations have shown both spin-up and spin-down of the pulse period (Kamata et al. 1990; Gilfanov et al. 1991; Mereghetti et al. 1991; Sunyaev et al. 1991).

We have made daily pulse period measurements of OAO 1657–415 with the Burst and Transient Source Experiment (BATSE) on the *Compton Gamma Ray Observatory (GRO)* since 1991 April as part of a joint MSFC/Caltech pulsar detection program. These observations show clear evidence of binary motion and eclipses of the X-ray source by its companion. Preliminary results of a pulse period analysis were given by Finger et al. (1992). In this chapter, we report on an accurate determination of the orbital parameters using an arrival time analysis. The implications for the stellar type of the still-unidentified companion are outlined.

4.2 Observations and Timing Analysis

BATSE consists of eight identical uncollimated detector modules arranged on the corners of the *Compton* spacecraft, providing an all-sky monitor of hard X-ray and γ-ray flux (Fishman et al. 1989). Except for source occultation by Earth, the instrument provides nearly continuous observations of discrete sources. We are reporting on observations with the BATSE large-area detectors (LADs), each of which contains a NaI(Tl) scintillation crystal 1.27 cm thick and 50.8 cm in diameter, viewed in a light collection housing by three 12.7 cm diameter photomultiplier tubes. The LADs have an effective energy range of 20 keV–1.8 MeV. In our analysis, only the data in the approximate range 20-60 keV were used, where each LAD has an effective area of ≈ 1000 cm^2.

A number of standard data types are generated from the LADs at various time and energy resolutions. The DISCLA data contain the photon count rate from the discriminators of each LAD in four energy channels at 1.024 s resolution. Our analysis of OAO 1657–415 is based on the lowest DISCLA energy channel data from 1991 April 23–1992 March 3 (MJD 48370–48685). DISCLA data are available for this entire period except for short segments during South Atlantic Anomaly crossings when the high voltage to the detectors was turned off, and for occasional data gaps due to telemetry and onboard tape recorder errors.

The DISCLA data were processed to construct, for each day, a single time series

at 1.024 s resolution on which a timing analysis was performed. For any given spacecraft orientation, OAO 1657–415 is visible in four detectors except when occulted by Earth (once each orbit). Only data from those detectors were analyzed, using intervals when the source was not occulted. A model of the background in each of the four detectors was generated by passing the data through a low pass filter; this was subtracted from the detector signals to remove the large (factor of 2) variations in count rate due to the changing background in the $\approx$ 93 min orbit of the spacecraft around Earth. The signals from the four detectors were then optimally weighted for the view direction of OAO 1657–415 and combined to form a single time series. The spacecraft times of the count rate bins were transformed to arrival times at the solar system barycenter using corrections based on the Jet Propulsion Laboratory DE200 solar system ephemeris (see §2.8).

Preliminary timing analysis was performed by producing a Fourier power spectrum for each one day time series and searching a small period range near the previously observed pulse period of OAO 1657–415. Since the LADs are uncollimated, and other bright X-ray sources are in the large field of view, this analysis used only the pulsed flux information contained in the data. Having optimized the time series for the view direction of OAO 1657–415 and searched a narrow range of periods near 38 s, we attributed any statistically significant signal to OAO 1657–415. A strong signal was detected on approximately 2/3 of the days, and the resulting period history was used to derive a preliminary orbit.

Using the preliminary orbit as a provisional ephemeris, a pulse profile template was constructed by folding data from 71 days when the signal was strong. We selected these days from an interval (MJD 48370–48460) where the source showed roughly linear spin-up. We then folded 0.2 day segments of our time series at the pulsar ephemeris period and cross-correlated with the template to obtain pulse times of arrival (TOAs) for each segment. These TOAs were fit over short intervals using a Taylor expansion for intrinsic changes in the pulse period and a standard model for the orbital Doppler delays. Writing the pulse emission times as (e.g., Deeter, Boynton, & Pravdo 1981)

$$t'_n = t'_0 + nP_0 + \frac{1}{2}n^2\dot{P}P_0 \tag{4.1}$$

where t'_0 is the emission time epoch and P_0 and $\dot{P}$ are the pulse period and its derivative at t'_0, the arrival times can be represented by

$$t_n = t'_n + f(t'_n) \tag{4.2}$$

where $f(t'_n)$, the orbital Doppler delay, is parametrized by five Keplerian orbital parameters: projected semi-major axis $a_x \sin i$ (where i is the inclination angle between the line of sight and the orbital angular momentum vector, defined to lie in the first quadrant), orbital period $P_{\rm orb}$, eccentricity e, longitude of periastron ω, and orbital epoch[1] $T_{\pi/2}$ (defined as the epoch where the mean longitude is 90°). The orbit parametrization is discussed in more detail in Appendix D.

Determination of the neutron star orbital elements from the observed pulse history is complicated by the need to decouple the effects of the orbital Doppler delays and intrinsic changes in the neutron star rotation rate. Preliminary fits indicated that $\dot{P}$ changed over orbital time scales. Thus, we have employed a "hybrid" approach to determining the orbit. The gaps in our data caused by eclipses of the X-ray source over its 10.4 day orbit naturally divide our TOA data into $\sim$ 8 day segments separated by $\sim$ 2 days. The five orbital parameters were fit simultaneously for all the segments, along with an independent t'_0, P_0 and $\dot{P}$ for each segment. This approach is especially attractive because it does not require an unambiguous pulse count to be maintained across eclipse intervals. To minimize the effect of rotation fluctuations on the orbital parameters, we confined our analysis to an interval where the pulse period history could be approximately represented by a single $\dot{P}$ term (MJD 48370 – 48460).

4.3 Results

Table 4.1 presents our best fit orbital elements, measured eclipse information, and several derived quantities. Figure 4.1 shows the best-fit Doppler delay curve for OAO 1657–415 with our best model of the intrinsic spin period variations removed. The fit residuals are plotted on a 5× expanded scale. Figure 4.2 shows the spin period history of OAO 1657–415 for days MJD 48370–48685, where our best-fit orbital Doppler delays have been removed. OAO 1657–415 exhibited both spin-up at $\dot{P}/P \approx -8 \times 10^{-3}$ yr^{-1} and spin-down at $\dot{P}/P \approx 2 \times 10^{-3}$ yr^{-1}. The long term trend since 1979 has been for secular spin-up with $\dot{P}/P \approx -10^{-3}$ yr^{-1}.

A Monte Carlo analysis was used to estimate the single-parameter 1σ confidence limits for the orbital elements by generating simulated data with $\sigma_{\rm sim} = 2$ s Gaussian errors in the TOAs. We chose $\sigma_{\rm sim}$ to be larger than the RMS arrival time fit residual

[1]See Deeter et al. (1981) for a discussion of the advantages of this particular choice of orbital epoch.

Table 4.1
OAO 1657–415 Parameters

Parameter	Symbol	Value[a]
Best-fit orbital parameters and eclipse measurements		
Orbital period	$P_{\rm orb}$	10.4436[b] $\pm$ 0.0038 d
Projected semi-major axis	$a_{\rm x} \sin i$	106.0 $\pm$ 0.5 lt-sec
Eccentricity	e	0.104 $\pm$ 0.005
Longitude of periastron ..	ω	93° $\pm$ 5°
Orbital epoch	$T_{\pi/2}$	JD 2448516.49 $\pm$ 0.05 TDB
Eclipse ingress[c]	$l_{\rm e,in}$	57°.1 $\pm$ 1°.8
Eclipse egress[c]	$l_{\rm e,out}$	116°.5 $\pm$ 1°.8
Derived quantities		
Pulsar mass function	$f_{\rm x}(M)$	11.7 $\pm$ 0.2 $M_\odot$
Eclipse half-angle	$\theta_{\rm e}$	29°.7 $\pm$ 1°.3
Inferred constraints [d]		
Orbital inclination	i	$\gtrsim$ 60°
Companion mass	$M_{\rm c}$	14–18 $M_\odot$
Companion radius	$R_{\rm c}$	25–32 $R_\odot$
$R_{\rm c}$-Roche radius ratio	$R_{\rm c}/R_{\rm L}$	$\gtrsim$ 0.85

[a] Quoted uncertainties are single-parameter 1σ confidence limits.

[b] A recent analysis of additional BATSE data measured $P_{\rm orb} = 10.44809 \pm 0.00030$ d (Finger 1995, personal communcation).

[c] Mean longitude.

[d] For $M_{\rm x} = 1.4\,M_\odot$ and the companion inside its critical lobe at periastron.

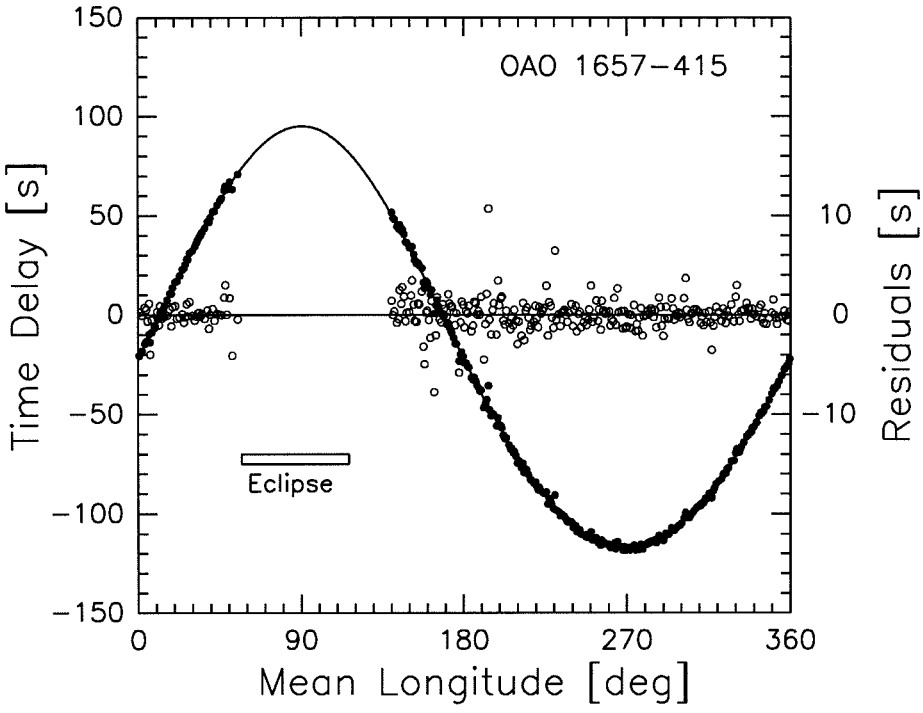

Figure 4.1: Doppler delays for the pulse arrival times as a function of the 10.4436 day orbit of OAO 1657-415 after removing our best model for the intrinsic variations in spin period. The data plotted are from the interval MJD 48370–48460. The solid circles are the delay times, the solid curve is the best-fit orbital model, and the open circles are the residuals (5× expanded scale).

$\sigma_{\rm rms} = 1.5$ s and the typical TOA measurement uncertainty $\sigma_{\rm toa} \sim 1$ s in order to allow for the possibility that red noise fluctuations in the pulsar rotation may have contributed to the parameter uncertainties. We believe this ad hoc approach correctly bounds the parameter uncertainties even though an explicit red-noise model was not included in our simulations. A more detailed study of red noise fluctuations in the rotation of OAO 1657–415 will be presented elsewhere. Boynton et al. (1986) have modeled such variability in Vela X-1 as a random walk (red noise) in spin frequency due to white noise torque fluctuations and found that torque noise was the dominant contribution to the orbital parameter uncertainties.

An eclipse centered near periastron ($\omega = 93° \pm 5°$) is evident in Figure 4.1. We have measured the eclipse duration by dividing our entire data set into 100 orbital phase bins and folding each phase bin at the pulsar spin period. Each of these light curves was correlated with our template to determine in which orbital phase bins no signal was seen.

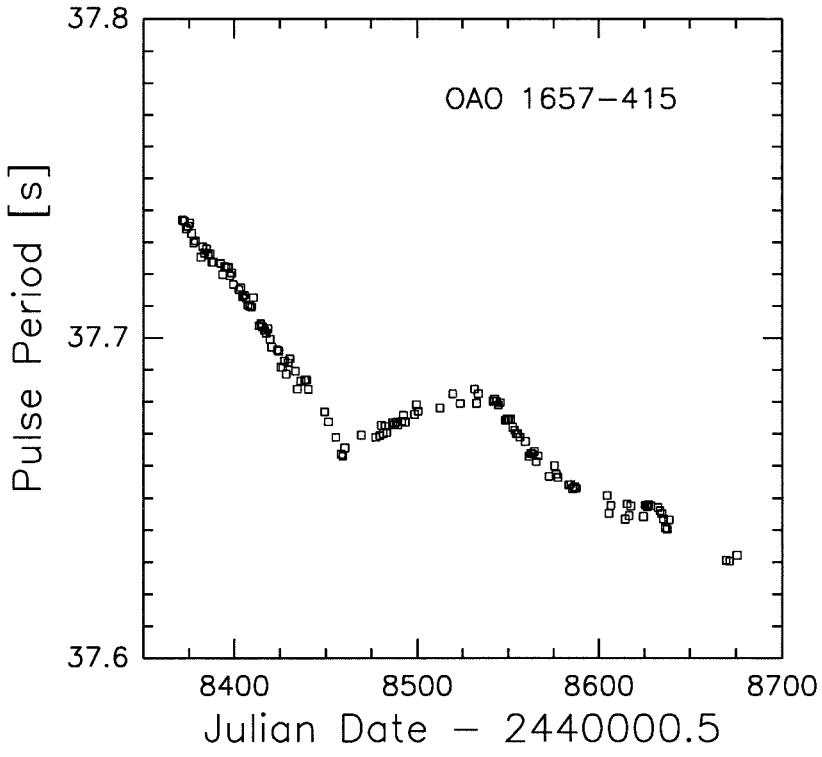

Figure 4.2: Spin period history for OAO 1657–415 derived from BATSE data with the orbital Doppler shifts removed. Only data for which a significant signal was detected are shown.

To obtain further precision, we then repeated the process, shifting the orbital phase "zero" by 1/2 phase bin. We measured eclipse ingress at mean longitude $l_{\rm e,in} = 57°.1 \pm 1°.8$ and eclipse egress at $l_{\rm e,out} = 116°.5 \pm 1°.8$, yielding an eclipse half-angle $\theta_{\rm e} = 29°.7 \pm 1°.3$. A comparison of the BATSE-derived eclipse ephemeris with the orbital phase (assuming our values of $P_{\rm orb}$ and $T_{\pi/2}$) for the ten previous observations[2] of pulsed flux from OAO 1657–415 (White & Pravdo 1979; Parmar et al. 1980; Kamata et al. 1990; Mereghetti et al. 1991; Gilfanov et al. 1991; Sunyaev et al. 1991) shows that none of these detections lies inside a predicted eclipse interval, providing an additional consistency check on our orbit fit. In particular, the 1983 July *Tenma* detections of pulsed flux (Kamata et al. 1990) restrict the allowed values of orbital period consistent with our data to the interval 10.4420 d $\lesssim P_{\rm orb} \lesssim$ 10.4450 d. The previous observations provide a weak limit on the orbital evolution rate, $|\dot{P}_{\rm orb}/P_{\rm orb}| \lesssim 10^{-5}$ yr^{-1}.

[2]We included a 1983 detection by the *EXOSAT* ME experiment using data from the High Energy Astrophysics Science Archive Research Center at NASA Goddard Space Flight Center.

We can use the derived orbital parameters to constrain the undiscovered companion's mass and radius. For a particular choice of neutron star mass M_x, the X-ray mass function

$$f_{\rm x}(M) \equiv \frac{4\pi^2(a_{\rm x}\sin i)^3}{GP_{\rm orb}^2} = \frac{(M_{\rm c}\sin i)^3}{(M_{\rm x}+M_{\rm c})^2} = 11.7 \pm 0.2\,M_\odot \tag{4.3}$$

(derived from our measured values of $a_{\rm x}\sin i$ and $P_{\rm orb}$) yields a lower limit for the companion mass $M_{\rm c}$, for which $\sin i = 1$. Choosing a value for $M_{\rm c}$, we calculate $\sin i$ and the mean orbital separation $a = a_{\rm x} + a_{\rm c}$. We can then use the measured eclipse angle to estimate the radius of the companion. (See Appendix E.1 for a detailed discussion.) For an eclipse centered at periastron of an eccentric orbit, we have

$$R_{\rm c} \approx \frac{a(1-e^2)}{1+e\cos\phi_{\rm e}}(\cos^2 i + \sin^2 i \sin^2\phi_{\rm e})^{1/2}, \tag{4.4}$$

where $\phi_{\rm e}$, the eclipse half-angle in *true* longitude, can be written in terms of the usual eclipse half-angle $\theta_{\rm e}$ using the standard elliptic expansion for true anomaly in terms of mean anomaly[3] (Brouwer & Clemence 1961),

$$\phi_{\rm e} = \theta_{\rm e} + 2e\sin\theta_{\rm e} + \frac{5}{4}e^2\sin 2\theta_{\rm e} + O(e^3). \tag{4.5}$$

By requiring that $R_{\rm c}$ be less than the radius of the critical potential lobe $R_{\rm L}$ at periastron, we obtain an upper limit on the companion mass. To show the largest possible parameter space, we only consider slow rotation of the companion ($P_{\rm c} \gg P_{\rm orb}$), in which case the Joss & Rappaport (1984) parameterization of $R_{\rm L}$ simply scales to the separation at periastron (Avni 1976).

Figure 4.3 shows the resulting $M_{\rm c}$-$R_{\rm c}$ curves under this constraint and the assumption that $M_{\rm x} > 1.0\,M_\odot$. The dark solid lines bound the allowed region while the light solid lines indicate the $M_{\rm c}$-$R_{\rm c}$ relations for different neutron star masses with varying inclinations. The allowed region for co-rotating (i.e., $P_{\rm c} = P_{\rm orb}$) companions is extremely small. The dark solid line on the left corresponds to inclination $i = 90°$, while the dark solid curve at the top is the boundary for $R_{\rm c} < R_{\rm L}$. The dark solid curve at the bottom corresponds to $M_{\rm x} = 1.0\,M_\odot$. If we assume a neutron star mass of $M_{\rm x} = 1.4\,M_\odot$, then a non-rotating companion has $14\,M_\odot \lesssim M_{\rm c} \lesssim 18\,M_\odot$ and $25\,R_\odot \lesssim R_{\rm c} \lesssim 32\,R_\odot$. These estimates are based on the smallest eclipse angle consistent with our measurements ($\theta_{\rm e} \approx 28°$), which places the

[3]For an eclipse centered at periastron, $\theta_{\rm e}$ and $\phi_{\rm e}$ are identical to the eclipse egress values of the mean and true anomalies, respectively.

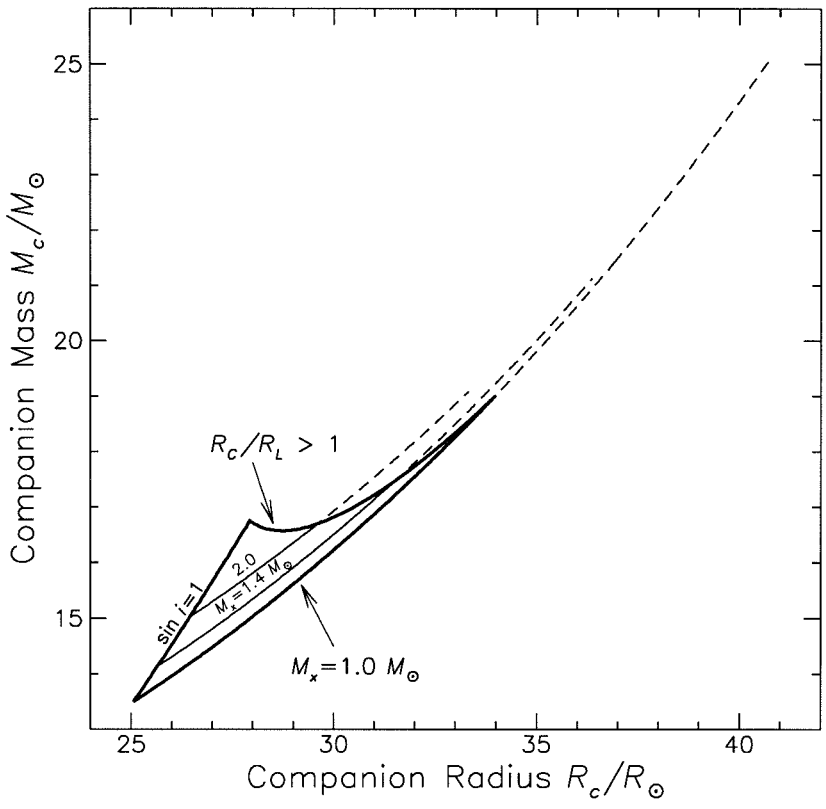

Figure 4.3: Constraints on the mass and radius of the companion of OAO 1657–415, based on the measured orbital parameters and assuming an eclipse half-angle $\theta_e = 28°$. The region inside of the dark solid curves shows the allowed M_c-R_c values for inclination $i < 90°$ (*left curve*), for a companion that does not overfill its critical lobe at periastron (*top curve*), and for neutron star mass $M_x > 1\,M_\odot$ (*bottom curve*). The light solid lines indicate the M_c-R_c relation for neutron star mass $M_x = 1.4\,M_\odot$ and $2.0\,M_\odot$. The dashed lines show the extended M_c-R_c relations if the star is allowed to overflow the critical lobe at periastron.

weakest limits. If the star is inside of the critical lobe at periastron, then our measurements also constrain $i \gtrsim 60°$, and $R_c/R_L \gtrsim 0.85$. Since the question of overflow at periastron is a dynamical one when the star is close to filling the critical lobe, we have arbitrarily extended the M_c-R_c relations to the point where $R_c = R_L$ at $0.95a$ (dashed lines). This provides an extreme upper limit since it implies that $R_c > R_L$ for $\sim 40\%$ of the orbit.

The constraints on M_c and R_c allow us to locate the star on the theoretical Hertzsprung-Russell diagram (see Maeder & Meynet 1989), yielding a blue supergiant of stellar type B0–B6 with absolute visual magnitude $M_v \approx -6.3$, corresponding to luminosity

class Ia–Iab.

4.4 Discussion

We have measured the eccentric binary orbit and eclipse duration of the accretion-powered X-ray pulsar OAO 1657–415. Our measurements imply that the mass-giving companion is a blue supergiant of mass 14–18 $M_\odot$. Optical identification of the companion followed by a measurement of its orbital velocity and accurate orbital phase photometry would place important constraints on the neutron star mass.

The distance to OAO 1657–415 is still unknown. However, we can set a lower limit to the distance from our observation of steady spin-up (see Appendix C). Accretion is difficult, if not impossible, when the Alfvén radius (where the kinetic energy density of the accreting matter is equal to the magnetic energy density) lies outside the co-rotation radius $r_{\rm co}$ (where the spin period is equal to the Keplerian period). The maximum torque exerted on the neutron star, $N_{\rm max} = \dot{M}(GM_{\rm x}r_{\rm co})^{1/2}$, occurs when the Alfvén radius and the co-rotation radius are equal. The observed values of the pulsar spin period and its derivative during the steady spin-up interval (MJD 48370–48460) then imply

$$L_{\rm x} \approx \frac{GM_{\rm x}\dot{M}}{R_{\rm x}} \gtrsim 1.6 \times 10^{37}\,{\rm erg\ s^{-1}} \left(\frac{M_{\rm x}}{1.4\,M_\odot}\right)^{4/3} \left(\frac{R_{\rm x}}{10\,{\rm km}}\right), \tag{4.6}$$

where we have used $I_{\rm x} = (2/5)M_{\rm x}R_{\rm x}^2$. A preliminary analysis of the 16 channel CONT data from BATSE for the spin-up interval indicates that the spectral index and hard X-ray pulsed flux were similar to the values measured during the 1978 September observation by *HEAO 1* (Byrne et al. 1981). Assuming the same pulsed fraction, we can use the total X-ray flux measured during the *HEAO 1* pointing, $Fx \approx 10^{-9}$ erg s^{-1} cm^{-2} (White & Pravdo 1979), to obtain the limit

$$d \gtrsim 11\,{\rm kpc} \left(\frac{M_{\rm x}}{1.4\,M_\odot}\right)^{2/3} \left(\frac{R_{\rm x}}{10\,{\rm km}}\right)^{1/2} \left(\frac{F_{\rm x}}{10^{-9}\,{\rm erg\ s^{-1}\ cm^{-2}}}\right)^{-1/2}, \tag{4.7}$$

consistent with the source's low galactic latitude.

Corbet (1986) showed that massive X-ray binaries fall into three separate groups when the pulse period is plotted versus the orbital period (see Figure 1.2). Those systems with unevolved Be companions have a strong correlation between the orbital and spin periods (see Waters & van Kerkwijk 1989 for an updated discussion), while systems with OB supergiant companions fall into two separate broad regions of the diagram. Systems

with optical photometric evidence for accretion disks (LMC X-4, Cen X-3, and SMC X-1; see van Paradijs 1991) and nearly steady spin-up have the shortest spin and orbital periods, while those without such evidence have much longer spin periods ($\gtrsim$ 100 s) and show torque reversals characteristic of accretion from the wind of the supergiant (Blondin et al. 1990). Interestingly, OAO 1657–415 falls between these two groups, both on the Corbet diagram and in terms of its observed spin period history. Its short spin period relative to the wind accreters probably results from the long intervals ($\sim$ 100 d) of steady spin-up which we observe. Whether these spin-up episodes are due to transient disk accretion can be resolved through optical photometry, which is sensitive to emission from an accretion disk.

References

Armstrong, J. T., Johnston, M. D., Bradt, H. V., Cowley, A. P., Doxsey, R. E., Griffiths, R. E., Hesser, J. E., & Schwartz, D. A. 1980. Precise positions and optical search for the 38 second X-ray pulsar near OAO 1653–40 and upper limit on X-ray emission from V861 Scorpii. *Astrophys. J.*, **236**, L131.

Avni, Y. 1976. The eclipse duration of the X-ray pulsar 3U 0900–40. *Astrophys. J.*, **209**, 574.

Blondin, J. M., Kallman, T. R., Fryxell, B. A., & Taam, R. E. 1990. Hydrodynamic simulations of stellar wind disruption by a compact X-ray source. *Astrophys. J.*, **356**, 591.

Boynton, P. E., Deeter, J. E., Lamb, F. K., & Zylstra, G. 1986. Vela X-1 pulse timing. I. Determination of the neutron star orbit. *Astrophys. J.*, **307**, 545.

Brouwer, D. & Clemence, G. M. 1961. *Methods of Celestial Mechanics* (New York: Academic Press).

Byrne, P. et al. 1979. OAO 1653–40. *IAU Circ.*, No. 3368.

Byrne, P. F. et al. 1981. High energy X-ray observations of the 38-second pulsar. *Astrophys. J.*, **246**, 951.

Corbet, R. H. D. 1986. The three types of high-mass X-ray pulsator. *Mon. Not. R. Astron. Soc.*, **220**, 1047.

Deeter, J. E., Boynton, P. E., & Pravdo, S. H. 1981. Pulse timing observations of Hercules X-1. *Astrophys. J.*, **247**, 1003.

Finger, M. H., Chakrabarty, D., Grunsfeld, J. M., Prince, T. A., Wilson, R. B., Fishman, G. J., Meegan, C. A., & Paciesas, W. S. 1992. OAO 1657–415. *IAU Circ.*, No. 5430.

Fishman, G. J. et al. 1989. BATSE: the Burst and Transient Source Experiment on the Compton Gamma Ray Observatory. In *Proc. of the GRO Science Workshop*, ed. W. N. Johnson (Greenbelt: NASA/GSFC), 2-39.

Gilfanov, M., Sunyaev, R., Churazov, E., Babalyan, G., Pavlinskii, M., Yamburenko, N., & Khavenson, N. 1991. First results of X-ray pulsar observations by the ART-P telescope on the Granat observatory. *Soviet Astron. Lett.*, **17**, 46.

Joss, P. C. & Rappaport, S. A. 1984. Neutron stars in interacting binary systems. *Ann. Rev. Astron. Astrophys.*, **22**, 537.

Kamata, Y., Koyama, K., Tawara, Y., Makishima, K., Ohashi, T., Kawai, N., & Hatsukade, I. 1990. X-ray observations of OAO 1657–415 with Tenma and Ginga. *Pub. Astron. Soc. Japan*, **42**, 785.

Maeder, A. & Meynet, G. 1989, Grids of evolutionary models from 0.85 $M_{\odot}$ to 120 $M_{\odot}$: observational tests and the mass limits. *Astron. & Astrophys.*, **210**, 155.

Mereghetti, S. et al. 1991. SIGMA observation of the pulsar OAO 1657–415: precise localization at hard X-ray energy and discovery of spin-down. *Astrophys. J.*, **366**, L23.

Nagase, F. 1989. Accretion-powered X-ray pulsars. *Pub. Astron. Soc. Japan*, **41**, 1.

Parmar, A. N. et al. 1980. X-ray observations of the OAO 1653–40 field. *Mon. Not. R. Astron. Soc.*, **193**, 49P.

Polidan, R. S., Pollard, G. S. G., Sanford, P. W., & Locke, M. C. 1978. X-ray emission from the companion to V861 Sco. *Nature*, **275**, 296.

Sunyaev, R., Gilfanov, M., Goldurm, A., & Schmitz-Frayesse, M. C. 1991. GX 340-0 region. *IAU Circ.*, No. 5342.

van Paradijs, J. 1991. In *Neutron Stars: Theory and Observation*, ed. J. Ventura & D. Pines (Dordrecht: Kluwer), 289.

Waters, L. B. F. M. & van Kerkwijk, M. H. 1989. The relation between orbital and spin periods in massive X-ray binaries. *Astron. & Astrophys.*, **223**, 196.

White, N. E. & Pravdo, S. H. 1979. The discovery of 38.22 second X-ray pulsations from the vicinity of OAO 1653–40. *Astrophys. J.*, **233**, L121.

Chapter 5

Discovery of the 18.7-Second Accreting X-Ray Pulsar GRO J1948+32*

Ships that pass in the night, and speak each other in passing,
Only a signal shown and a distant voice in the darkness;
—Henry Longfellow (1874)

5.1 Introduction

Since the discovery of pulsations from Centaurus X-3 over twenty years ago (Giacconi et al. 1971), more than thirty accretion-powered X-ray pulsars have been detected (see Nagase 1989). Nearly half of these pulsars are transient sources which were discovered during bright outbursts. However, due to incomplete and non-uniform sky coverage, the population and recurrence history of these transients is poorly determined. The Burst and Transient Source Experiment (BATSE) on the *Compton Gamma Ray Observatory (GRO)* has provided a nearly continuous all-sky monitor of pulsed hard X-ray ($\gtrsim$ 20 keV) emission since its launch in 1991 April (Prince et al. 1994). On 1994 April 6 BATSE first detected 18.7 s pulsed hard X-ray emission from a previously unknown source in the Cygnus region of the Galactic plane (Finger, Wilson, & Fishman 1994). The source was detected at energies as high as 75 keV and reached phase-averaged pulsed intensities $\approx$ 50 mCrab in the 20–75 keV band during the 33 day outburst. BATSE data taken prior to 1994 April fail to

*Adapted with changes from "Discovery of the 18.7 Second Accreting X-Ray Pulsar GRO J1948+32" in *The Astrophysical Journal*, **446**, 826–831 (1995 June 20), by D. Chakrabarty, T. Koh, L. Bildsten, T. A. Prince, M. H. Finger, R. B. Wilson, G. N. Pendleton, & B. C. Rubin. Used by permission of the authors.

show any pulsed emission near 18.7 s from this region of the sky, indicating that the new source is transient or at least highly variable.

In this chapter, we present a detailed analysis of the BATSE observations of GRO J1948+32 as well as a refined estimate (10 $\deg^2$ solid angle with 99% confidence) for its position. The approximate Galactic coordinates of the source are $l \sim 65°$, $b \sim 2°$. A preliminary position estimate for the source (originally designated GRO J2014+34) yielded a 68% confidence error circle with 8° radius, corresponding to a solid angle of 200 $\deg^2$ (Finger, Wilson, & Fishman 1994). Further observations yielded an improved position with a 90% confidence error box covering a solid angle of 15 $\deg^2$ and led to a redesignation of the source as GRO J1948+32 (Chakrabarty et al. 1994; see Appendix I). A preliminary search of the brightest sources in this region in archival data from the *ROSAT*/PSPC soft X-ray (0.1–2.4 keV) all-sky survey failed to detect any sources with a similar pulse period (Kahabka et al. 1994). A 6° × 6° optical *R*-band plate of the region was obtained during the X-ray outburst, using the Palomar Observatory 1.2-m Oschin Schmidt telescope (I. N. Reid 1994, private communication). Comparison of the 10 $\deg^2$ source error box on this plate with archival plates from the Palomar sky survey (Reid et al. 1991) may aid in the identification of the optical companion.

5.2 Observations and Analysis

BATSE is an all-sky monitor of 20 keV–1.8 MeV γ-ray flux (see Fishman et al. 1989 for a description). Our standard detection and timing analysis uses the 20–60 keV channel of the 1.024 s resolution DISCLA data type (see Chapter 2). GRO J1948+32 was initially detected in a routine search of the Fourier power spectra of these data for 1994 April 7. Once the source was discovered, a systematic search of the entire BATSE DISCLA data archive from 1991 April 22 to 1994 November 9 (MJD 48369–49665) was made. The Fourier power spectrum of the data for each day (optimized for the source direction) was searched for a statistically significant pulsed signal with a pulse period in the range 18.6 s$\leq P_{\rm pulse} \leq$ 18.8 s. The only detections were during the outburst, from 1994 April 6 to May 12 (MJD 49448–49482). The detection threshold for this analysis was $\approx$ 25 mCrab (20–60 keV).

For those days where a significant signal was detected in the DISCLA data, the CONT data (20 keV–2 MeV count rates, in 16 energy channels at 2.048 s resolution) were also analyzed. The raw data were pre-processed using the orbital background and bright

source occultation model developed by Rubin et al. (1993). Pulse profiles for each of the 16 channels in the background-subtracted CONT data were generated from two-day folds of the time series corresponding to the outburst. Only data from the detector with the smallest viewing angle to the source were used.

In order to simplify estimation of the measurement uncertainties, we used a single-harmonic model for the pulse to obtain phase-averaged pulsed-component count rates from these pulse profiles (see §3.3). For GRO J1948+32, a single-harmonic model systematically underestimates the pulsed intensity by 25%, due to the small but significant non-sinusoidal component of the pulse shape. We corrected all of the measured pulsed count rates for this factor. Goodman (1985) gives the probability distribution $p(a|s,n)$ for the measured harmonic amplitude a given a signal amplitude s and noise strength n. We used Bayes's theorem to invert this function to obtain the probability distribution $p(s|a,n)$ for the signal amplitude, allowing an estimate of the pulsed count rate in a noisy pulse profile.[1] These count rates are well fit by assuming a power-law photon spectrum of the form $dN/dE = C_{30}(E/30\ \mathrm{keV})^{-\gamma}$ and accounting for the BATSE instrumental response. Fluxes for the individual channels are obtained by folding the best-fit values of C_{30} and γ through the BATSE instrumental response. (See Heindl et al. 1993 for a detailed discussion of the procedure for converting count rates to fluxes.) The unpulsed flux of GRO J1948+32 was too faint ($\lesssim$ 100 mCrab) to be detected using the standard Earth occultation technique described by Harmon et al. (1993).

All the two-day folds of the background-subtracted CONT data over the outburst yielded statistically significant pulse flux detections in channels 1–4 (approximately 20–75 keV), and several folds yielded detections in channel 5 (approximately 75–100 keV). Figure 5.1 shows the 20–75 keV pulsed flux history of the outburst. (If significant channel 5 contributions were to be included in this plot for the appropriate segments, the quoted fluxes would change by $< 10\%$.) The pulsed flux increased from $(2.2 \pm 0.5) \times 10^{-10}$ erg cm^{-2} s^{-1} to $(4.9 \pm 0.5) \times 10^{-10}$ erg cm^{-2} s^{-1} over 10 days before decaying to the minimum detectable level over 25 days. The photon spectral index for these two-day fits had a mean value

[1]We assumed a prior probability $p(s) =$constant; see de Jager (1994) for a discussion of the strengths and weaknesses of this choice. For $a \gg n$, $p(s|a,n)$ is approximately a Gaussian distribution centered at $s = a$, with an associated 1 σ error defined by the symmetrical 68% confidence interval of the distribution. In this case, the computed flux is not sensitive to the choice of prior, and the Bayesian result is identical to that obtained with other methods commonly employed at high signal-to-noise. However, for $a \lesssim n$, the distribution is highly skewed and peaks near $s = 0$. In such cases, we quote a 2σ upper limit s_{ul} on the count rate, implicitly defined by $\int_0^{s_{\mathrm{ul}}} p(s|a,n)ds = 0.95$. See §3.3 for a more detailed discussion.

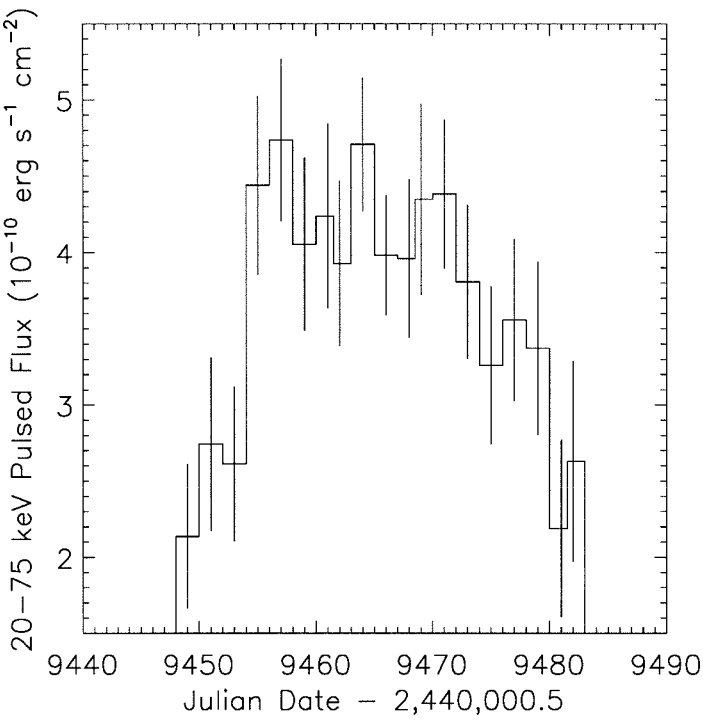

Figure 5.1: Pulse-phase-averaged 20–75 keV pulsed flux history of GRO J1948+32. The vertical bars show the 1 σ uncertainties in the flux measurements.

$\langle\gamma\rangle = 2.29 \pm 0.08$, with individual values varying between 1.25 ± 0.35 and 2.82 ± 0.39. There was not a statistically significant correlation of the spectral index with either time or pulsed intensity.

It is advantageous to phase-connect longer intervals of data in order to probe the high-energy spectrum of the source. However, as the spacecraft orientation is changed (which happens at ~10 day intervals), different detectors will have the best source viewing angle. Because the effective area of the BATSE detectors is a very sensitive function of energy and viewing angle in the 20–100 keV range and since each detector has slightly different energy channel edges, it is difficult to produce count spectra from data combined over more than one pointing. There were three different *Compton* pointings during the outburst, each with a different best viewing angle to the source: 22.8° for detector 7 on MJD 49448–49461, 3.6° for detector 0 on MJD 49462–49468, and 26° for detector 6 on MJD 49468-49482. There was no statistically significant change in the source spectral index during these three pointings. Figure 5.2 shows the measured spectrum during the bright

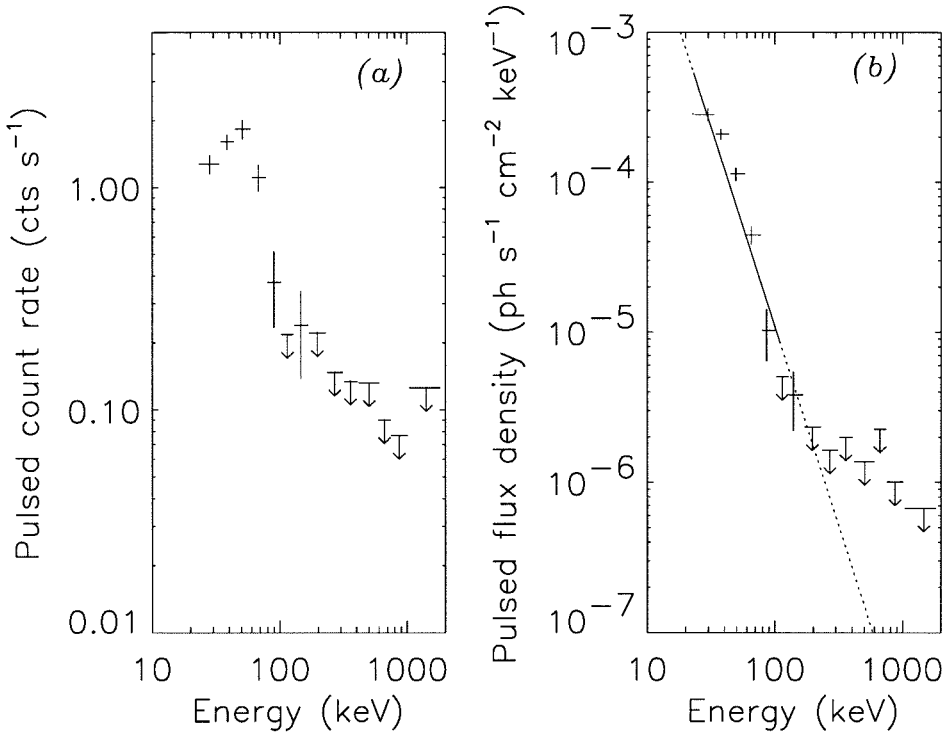

Figure 5.2: Pulsed energy spectrum of GRO J1948+32. *(a)* The phase-averaged pulsed count rate spectrum of GRO J1948+32 for MJD 49462-49468, measured with BATSE large area detector 0. The viewing angle to the source was 3°. The vertical bars show the 1 σ statistical uncertainties, while the horizontal bars show the widths of the energy channels. Upper limits are quoted at 95% confidence. *(b)* The corresponding phase-averaged pulsed photon spectrum, corrected for the BATSE instrumental response and the source viewing angle. The solid line shows the best-fit power law photon spectral model ($\gamma = 2.65$, $C_{30} = 3.4 \times 10^{-4}$ photons cm^{-2} s^{-1} keV^{-1}).

pointing with the most favorable viewing angle, MJD 49462–49468. The left panel shows the measured pulsed count spectrum from a 7-day fold across this interval, and the right panel shows the inferred source photon spectrum assuming a power-law spectral model. In determining upper limits for the flux in the higher channels, no assumption was made about the phase relationship with the pulse component in the lower channels. The pulse profiles for this interval as a function of energy are shown in Figure 5.3. For display purposes, these profiles are about twice-overresolved. The best-fit 20–120 keV power-law spectral parameters for the phase-averaged pulsed component during this interval are $\gamma = 2.65 \pm 0.15$ and $C_{30} = (3.4 \pm 0.2) \times 10^{-4}$ photons cm^{-2} s^{-1} keV^{-1}.

The crosses in Figure 5.4 denote the pulse frequency history observed by BATSE.

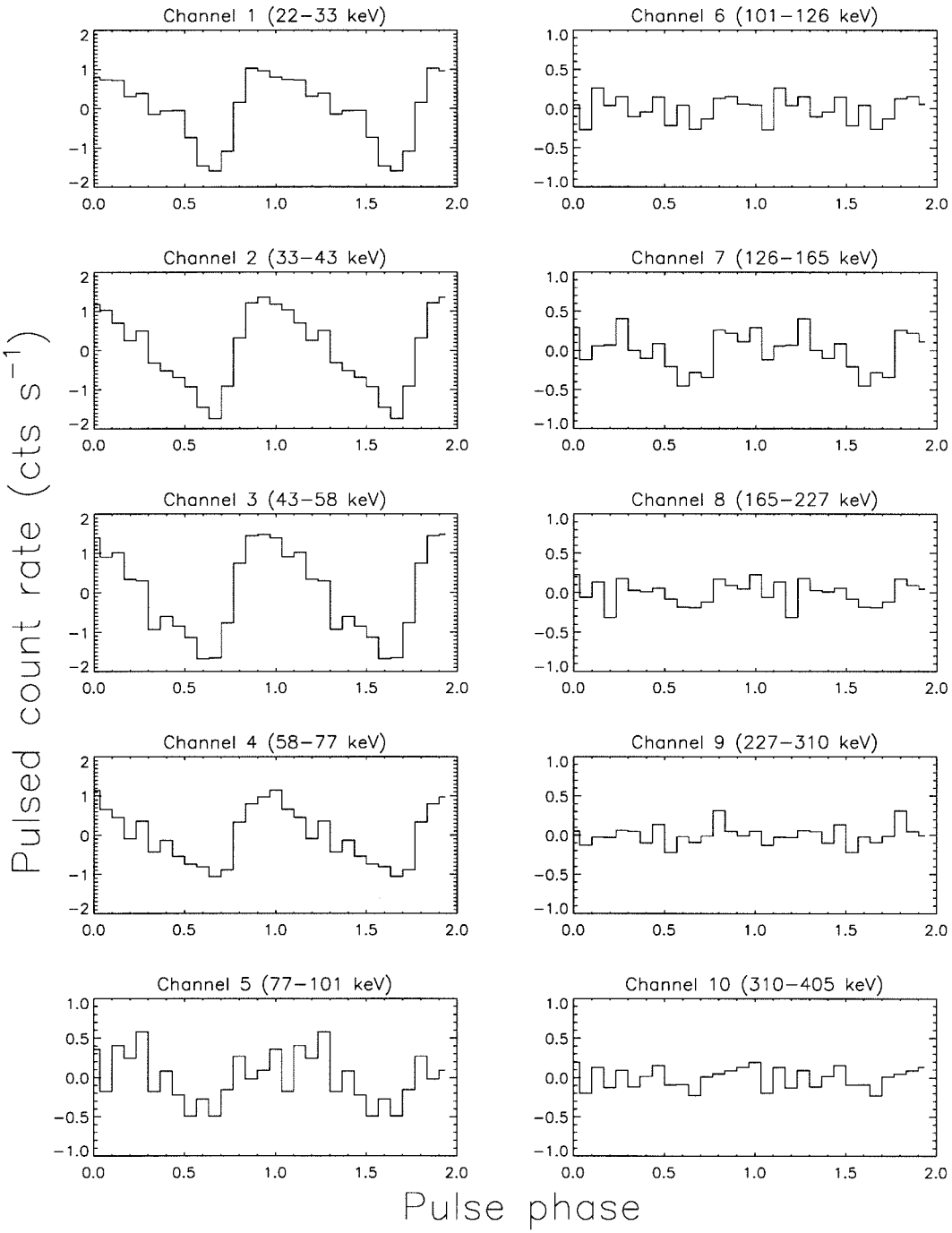

Figure 5.3: Pulse profiles as a function of energy for GRO J1948+32, during the interval MJD 49462–49468. Two pulses are shown for each channel. The energy edges for each CONT channel of BATSE detector 0 are indicated. These pulse profiles are overresolved by a factor of 1.7. Note that the pulse shapes are uncorrected for the rapid change in detector response as a function of energy in the 20–100 keV range.

The quasi-sinusoidal variation may be due to orbital motion of the source; if so, a complete orbital cycle has not yet been observed. Consequently, it is not possible to reliably decouple orbital effects from variations in the intrinsic spin period due to accretion torques, and the orbital parameter estimates remain highly correlated. A wide range of degenerate solutions exist which provide a good fit to the data (solid curve in Figure 5.4). However, it is possible to constrain the allowed parameter space (see Appendix F for details). If we assume a circular orbit and a constant spin frequency derivative, then the following 95%-confidence limits can be placed: orbital period 35 d $< P_{\rm orb} <$ 44 d; orbital radius 95 lt-s $< a_{\rm x} \sin i <$ 165 lt-s; spin frequency derivative 2×10^{-12} Hz s^{-1} $< \dot{\nu} < 6 \times 10^{-12}$ Hz s^{-1}, X-ray mass function $0.7\,M_\odot < f_{\rm x}(M) < 2.3\,M_\odot$. If we permit eccentric solutions, the allowed 95%-confidence parameter ranges are broader: eccentricity $e < 0.25$; orbital period 35 d $< P_{\rm orb} <$ 70 d; orbital radius 75 lt-s $< a_{\rm x} \sin i <$ 300 lt-s; spin frequency derivative 5×10^{-13} Hz s^{-1} $< \dot{\nu} < 2.5 \times 10^{-11}$ Hz s^{-1}; X-ray mass function $0.5\,M_\odot < f_{\rm x}(M) < 5\,M_\odot$. It should be noted that these ranges are the individual confidence regions for each of the parameters separately, computed by allowing all the other parameters to vary.

A revised position estimate for GRO J1948+32 was made using the method described in Appendix G with the 20–60 keV DISCLA data for MJD 49448–49482. The frequency, amplitude, and phase of the pulsed signal were assumed constant for each day but were allowed to vary from day to day. We computed the likelihood function for an $8^\circ \times 12^\circ$ grid of positions, spaced by 0.5° and centered at an earlier position estimate (Chakrabarty et al. 1994; see Appendix I). The formal confidence contours were calculated by interpolation between the grid points. These are shown in Figure 5.5, along with the earlier estimate by Chakrabarty et al. (1994) for comparison.

5.3 Discussion

GRO J1948+32 is certainly a neutron star; the lower limit on the spin frequency derivative exceeds, by an order of magnitude, the maximum possible spin-up rate for a white dwarf pulsar (6×10^{-14} Hz s^{-1} for accretion at the Eddington critical rate, assuming radius $R_{\rm x} = 10^9$ cm, mass $M_{\rm x} = 1.4 M_\odot$, and spin period $P_{\rm spin} = 18.7$ s). If we assume steady spin-up over the outburst duration, we can further exploit our lower limit on $\dot{\nu}$ to infer that the total X-ray luminosity $L_{\rm x} \gtrsim 10^{36}$ erg s^{-1} (see Appendix C). The upper limit on $\dot{\nu}$, which is within a factor of 3 of the maximum spin-up rate for a neutron star

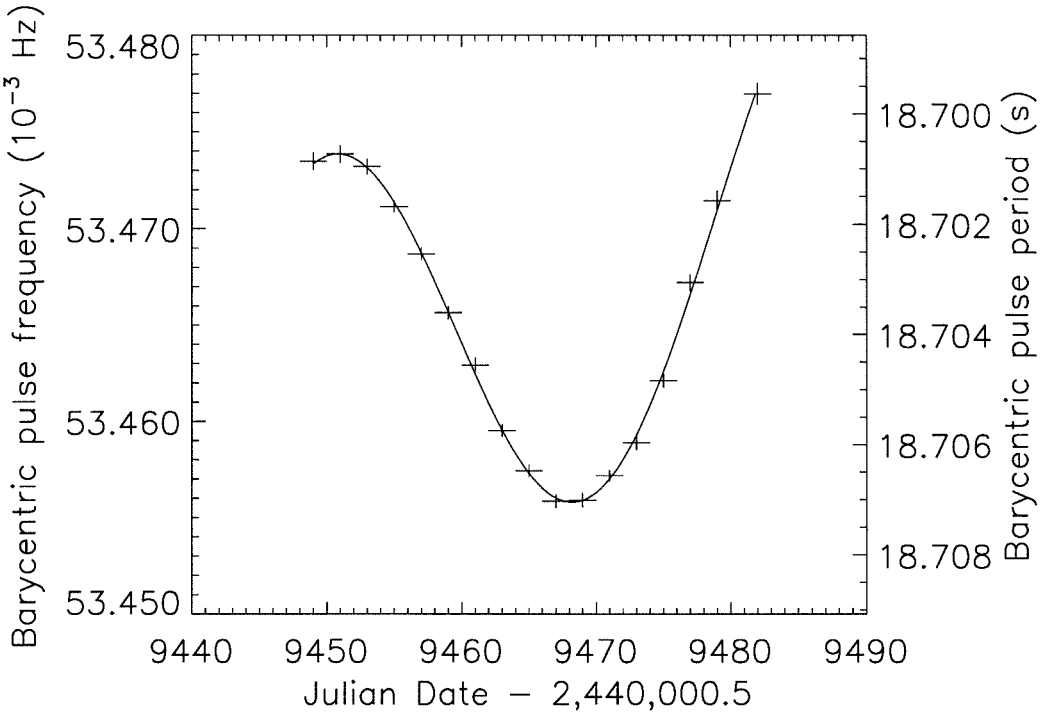

Figure 5.4: Pulse frequency history of GRO J1948+32 from BATSE observations. The vertical bars show the 1 σ statistical uncertainties in the frequency measurements, while the horizontal bars show the time interval over which each measurement was integrated. A wide range of orbital parameters can produce a nearly identical model curve (*solid curve*).

(6×10^{-11} Hz s^{-1} assuming $R_x = 10^6$ cm, $M_x = 1.4 M_\odot$, and $P_{spin} = 18.7$ s), corresponds to $L_x \lesssim 8 \times 10^{37}$ erg s^{-1}. Since we have no measure of the bolometric X-ray flux, we are unable to place useful limits on the distance to the source.

The nature of the mass transfer in this system is not clear. The values of P_{spin} and P_{orb} are consistent with the correlation generally observed in Be/X-ray binaries (Corbet 1986; Waters & van Kerkwijk 1989; see also Figure 1.2), and the inferred mass function range is also consistent with this classification. Unlike GRO J1948+32, the known Be/X-ray binary systems are typically in highly eccentric orbits ($e \gtrsim 0.3$), but this may be an observational selection effect. The system has some similarities to the 12.3 s transient X-ray pulsar GS 0834-430, which has a wide, mildly eccentric ($e = 0.128 \pm 0.063$), 112 d orbit with a small mass function (Wilson et al. 1994). Both systems exhibit transient outbursts which last for a large fraction of the orbital period, but both systems also go for multiple orbital cycles without any detectable emission. (BATSE has observed only one outburst from

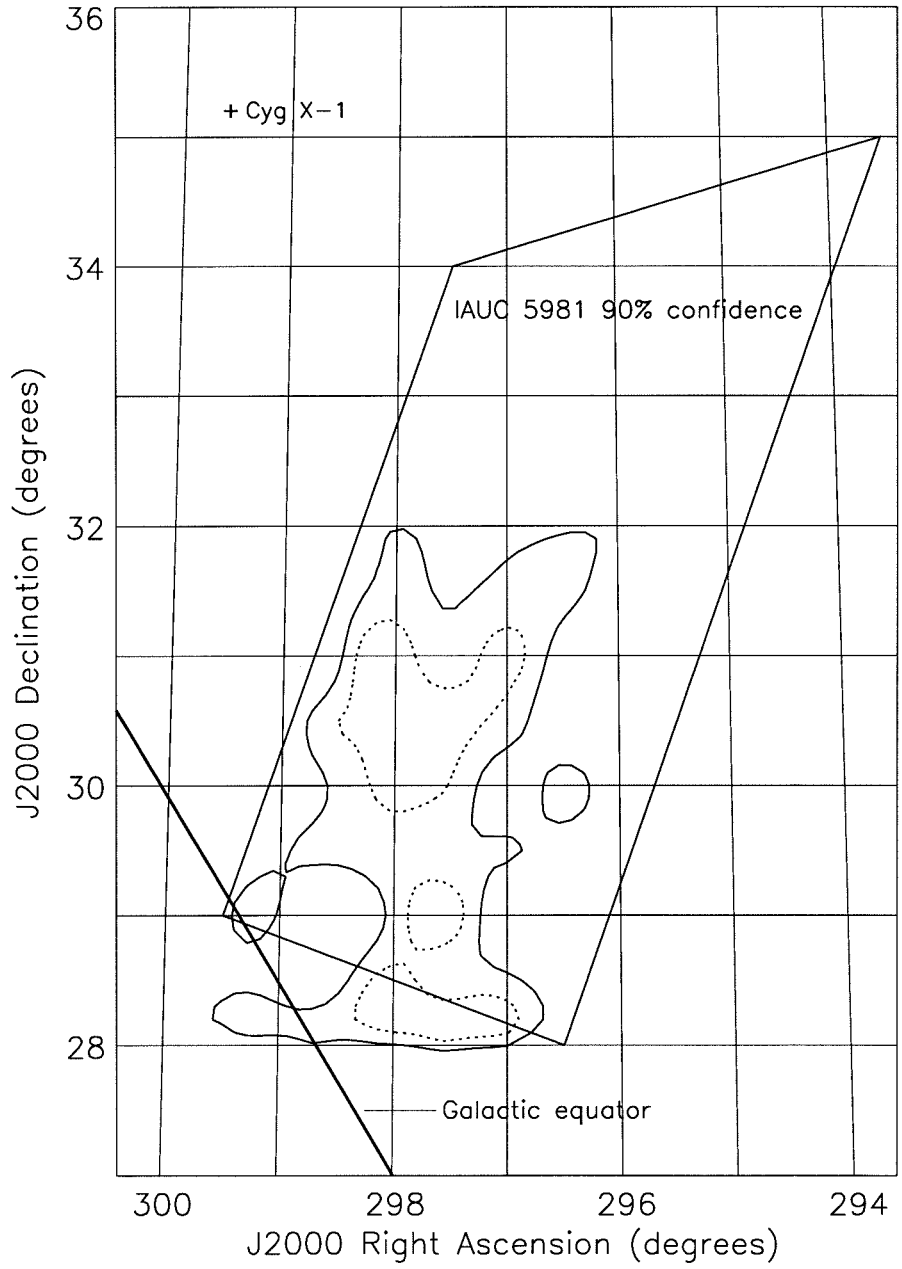

Figure 5.5: Position estimate for GRO J1948+32 ($l \sim 65°$, $b \sim 2°$). The broken contours show the formal 90% confidence region, while the solid contours show the formal 99% confidence region. These contours do not include the systematic uncertainty (see text). For comparison, the large quadrilateral is the earlier 90% confidence estimate by Chakrabarty et al. (1994) (see Appendix I).

GRO J1948+32 despite > 18 orbital cycles of the pulsar since the launch of the *Compton Observatory.*)

References

Chakrabarty, D., Prince, T. A., Finger, M. H., Wilson, R. B., & Pendleton, G. N. 1994. GRO J1948+32 = GRO J2014+34. *IAU Circ.*, No. 5981. [see Appendix I]

Corbet, R. H. D. 1986. The three types of high-mass X-ray pulsator. *Mon. Not. R. Astron. Soc.*, **220**, 1047.

de Jager, O. C. 1994. On periodicity tests and flux limit calculations for gamma-ray pulsars. *Astrophys. J.*, **436**, 239.

Finger, M. H., Stollberg, M., Pendleton, G. N., Wilson, R. B., Chakrabarty, D., Chiu, J., & Prince, T. A. 1994. GRO J2014+34. *IAU Circ.*, No. 5977.

Fishman, G. J. et al. 1989. BATSE: the Burst and Transient Source Experiment on the Compton Gamma Ray Observatory. In *Proc. of the GRO Science Workshop*, ed. W. N. Johnson (Greenbelt: NASA/GSFC), 2-39.

Giacconi, R., Gursky, H., Kellogg, E. M., Schreier, E., & Tananbaum, H. 1971. Discovery of periodic X-ray pulsations from Centaurus X-3 from Uhuru. *Asrophys. J.*, **167**, L67.

Goodman, J. W. 1985. *Statistical Optics* (New York: Wiley).

Harmon, B. A. et al. 1993. Earth occultation measurements of Galactic hard X-ray/gamma-ray sources: a survey of BATSE results. In *Compton Gamma-Ray Observatory*, ed. M. Friedlander, N. Gehrels, & D. J. Macomb (New York: AIP Press), 314.

Heindl, W. A., Cook, W. R., Grunsfeld, J. M., Palmer, D. M., Prince, T. A., Schindler, S. M., & Stone, E. C. 1993. An observation of the Galactic center hard X-ray source 1E 1740.7–2942 with the Caltech coded aperture telescope. *Asrophys. J.*, **408**, 507.

Kahabka, P. et al. 1994. Search for the newly discovered accreting pulsar GRO J1948+32. *Astron. & Astrophys.*, in preparation.

Nagase, F. 1989. Accretion-powered X-ray pulsars. *Pub. Astron. Soc. Japan*, **41**, 1.

Prince, T. A., Bildsten, L., Chakrabarty, D., Wilson, R. B., & Finger, M. H. 1994. Observations of accreting pulsars. In *Evolution of X-Ray Binaries*, ed. S. S. Holt & C. S. Day (New York: AIP Press), 235.

Reid, I. N. et al. 1991. The second Palomar sky survey. *Pub. Astron. Soc. Pacific*, **103**, 661.

Rubin, B. C. et al. 1993. Modeling the gamma-ray background on BATSE. In *Compton Gamma-Ray Observatory*, ed. M. Friedlander, N. Gehrels, & D. J. Macomb (New York: AIP Press), 1127.

Waters, L. B. F. M. & van Kerkwijk, M. H. 1989. The relation between orbital and spin periods in massive X-ray binaries. *Astron. & Astrophys.*, **223**, 196.

Wilson, C. A., Harmon, B. A., Wilson, R. B., Fishman, G. J., & Finger, M. H. 1994. BATSE observations of GS 0834–430. In *Evolution of X-Ray Binaries*, ed. S. S. Holt & C. S. Day (New York: AIP Press), 259.

Chapter 6

Extended Spin-Down of the Accreting X-Ray Pulsar 4U 1626–67*

What goes up must come down.
—American proverb

6.1 Introduction

Early studies of X-ray pulsars accreting from disks found that the observed long-term spin-up time scale ($\tau_{\rm su} = |\nu_{\rm spin}/\dot{\nu}_{\rm spin}| \lesssim 10^4$ yr) was much less than the X-ray emitting lifetime ($\tau_{\rm x} \gtrsim 10^6$ yr), implying that long-term spin-up cannot be the steady-state behavior of these systems (Elsner, Ghosh, & Lamb 1980). The discovery of prolonged spin-down (Makishima et al. 1988) and subsequent additional torque reversals (see Chapter 7) in GX 1+4 was a dramatic illustration of this for the source with the shortest spin-up time ($\tau_{\rm su} \approx 40$ yr). At the same time, it raised questions about what sets the time scale of ~years for these torque sign reversals. In this chapter, we report the discovery of a torque reversal and extended spin-down in a second pulsar, 4U 1626–67.

The X-ray source 4U 1626–67 ($l = 321°$, $b = -13°$) was discovered in the 2–20 keV band by *Uhuru* (Giacconi et al. 1972). Subsequent 1.5–30 keV observations with *SAS-3* revealed 7.68 s pulsations (Rappaport et al. 1977) and provided a sufficiently accurate position (Bradt et al. 1977) to identify the optical counterpart, KZ TrA (McClintock et al. 1977). Optical pulsations with 2% amplitude were detected at the same frequency as the

*Adapted from a manuscript in preparation for *The Astrophysical Journal* by D. Chakrabarty, L. Bildsten, J. M. Grunsfeld, T. Koh, T. A. Prince, B. Vaughan, M. H. Finger, D. M. Scott, & R. B. Wilson.

X-ray pulsations (Ilovaisky, Motch, & Chevalier 1978) and are understood as reprocessing of the pulsed X-ray flux by the accretion disk (Chester 1979). The system shows strong, correlated X-ray/optical flares every $\approx$ 1000 s that are of undetermined origin (Joss, Avni, & Rappaport 1978; McClintock et al. 1980; Li et al. 1980) and show no X-ray spectral changes (Kii et al. 1986). A $\approx$ 40 mHz quasi-periodic oscillation was detected in X-ray observations by *Ginga* and *ASCA* (Shinoda et al. 1990; Angelini et al. 1995), and has been recently detected in optical observations as well (see Appendix H).

Further timing of the optical pulsations detected weak, persistent pulsations in a sidelobe of the "direct" (X-ray) pulse frequency, which were attributed to a beat frequency with a ~40 min binary orbit arising from reprocessing on the companion surface (Middleditch et al. 1981; see also Appendix H). X-ray timing measurements place an upper limit of $a_{\rm x} \sin i < 10.5$ lt-ms on a neutron star orbit with this binary period, giving an upper limit on the X-ray mass function of $f_{\rm x}(M) \leq 1.3 \times 10^{-6} M_{\odot}$ (Levine et al. 1988). The most likely Roche-lobe filling companion consistent with these limits is a low mass (0.02–0.06 $M_{\odot}$) degenerate helium or carbon-oxygen dwarf; more massive stars require very unlikely inclination angles (see Verbunt, Wijers & Burm 1990 for a complete discussion). Recent *ASCA* observations detected a strong complex of neon emission lines near 1 keV (Angelini et al. 1995).

For more than a decade after its discovery, accretion was steadily spinning up 4U 1626–67 at the rate $\tau_{\rm su} \approx 5000$ yr. However, long-term 20–60 keV monitoring of the source with the Burst and Transient Source Experiment (BATSE) on the *Compton Gamma Ray Observatory* found that the accretion torque changed sign, causing spin-down at nearly the same rate (Wilson et al. 1993; Bildsten et al. 1994). This change of state has been subsequently confirmed in 3–60 keV observations with the ART-P instrument on *Granat* (Lutovinov et al. 1994), 0.2–2.4 keV observations with *ROSAT*/PSPC (Angelini, Ghosh, & White 1994), and 0.5–10 keV observations with *ASCA* (Angelini et al. 1995). In this chapter we report on four years of continuous BATSE timing and spectral data.

6.2 Observations and Analysis

6.2.1 Pulse Timing

BATSE is a nearly continuous all-sky monitor of 20 keV–1.8 MeV hard X-ray/γ-ray flux (see Fishman et al. 1989 for a description). Our standard BATSE pulsed source detection and timing analysis uses the 20–60 keV channel of the 4 channel/1.024 s resolution DISCLA data type (see Chapter 2). The barycentric pulse frequency history of 4U 1626–67 from 1991 April to 1995 November was determined by dividing the BATSE data into short (~few days) segments and searching the Fourier power spectrum of each segment for the strongest signal in a small range around a pulse period of 7.7 s. The length of data used was always much shorter than the time scale for signal decoherence caused by the large pulse frequency derivative ($\tau_{\rm decoh} = \sqrt{1/|\dot{\nu}|} \approx 13$ days; see Appendix B).

Figure 6.1 shows the pulse frequency history of 4U 1626–67. During 1977–1989, the source underwent steady spin-up at a mean rate $\dot{\nu} = 8.54(7) \times 10^{-13}$ Hz s^{-1}. Levine et al. (1988) found a significant quadratic term in the pulse period history ($|\dot{P}/\ddot{P}| \approx 40$ yr) when doing an unweighted fit of a subset of these data. However, we find that a polynomial model of fourth order or higher is necessary to obtain an acceptable weighted fit to the pre-1990 data. The *ROSAT* and ART-P observations show a clear decrease in the spin-up rate and suggest that the torque reversal occurred during 1990 (see bottom panel of Figure 6.1).

The pulse frequency history observed by BATSE from 1991 April to 1995 November (MJD 48360–50030) shows a significant quadratic component and is well fit (reduced χ^2=1.46 with 320 degrees of freedom) by

$$\nu(t) = \nu_0 + \dot{\nu}_0(t - t_0) + \frac{1}{2}\ddot{\nu}(t - t_0)^2, \tag{6.1}$$

with $\nu_0 = 0.13048862(2)$ Hz, $\dot{\nu}_0 = -7.1795(41) \times 10^{-13}$ Hz s^{-1}, and $\ddot{\nu} = 9.41(16) \times 10^{-22}$ Hz s^{-2}, referenced to the epoch t_0 = MJD 49000 TDB. Thus, the spin-down torque is decreasing in magnitude on the time scale $|\dot{\nu}/\ddot{\nu}| \approx$12 yr, similar to the e-folding scale for the spin-up rate which was reported by Levine et al. (1988). Higher order terms do not significantly improve the fit. We can probe the rotation history of the pulsar more sensitively using a pulse arrival time (phase) analysis; a description of this technique is given in Chapter 4. The pulsar's behavior is very stable, and we can maintain an unambiguous pulse count over the entire BATSE observation history. In the absence of a clear binary

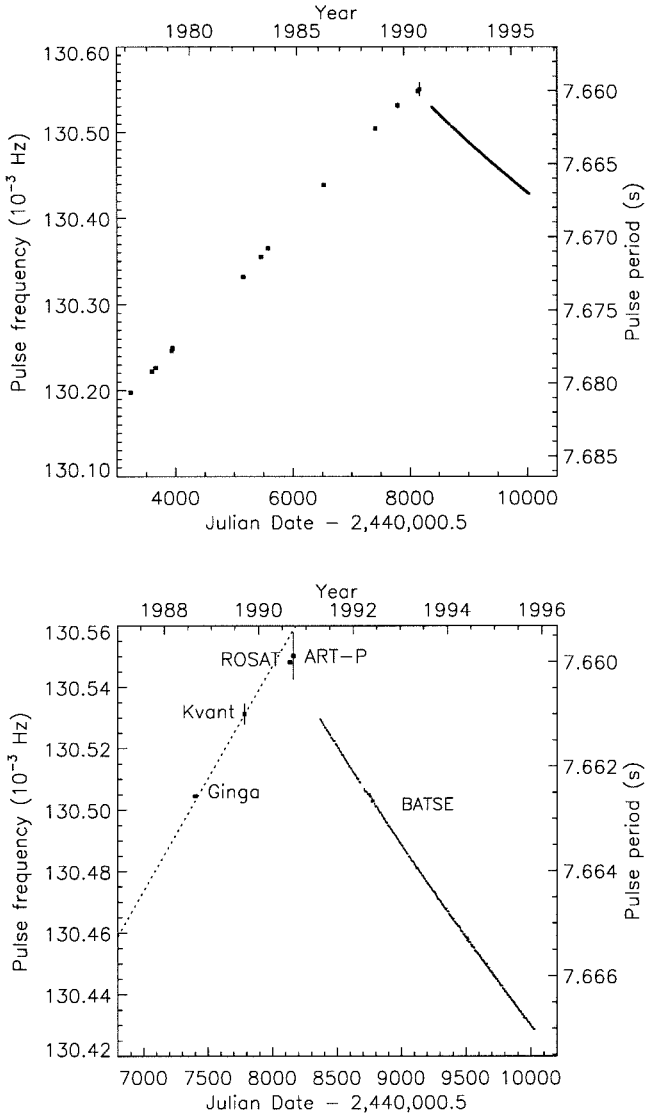

Figure 6.1: Pulse frequency history of 4U 1626–67, reduced to the solar system barycenter. The top panel shows the historical data, which are mostly taken from Nagase (1989), with some typographical errors corrected and several measurements omitted due to particularly large uncertainties. Also shown are a 1983 measurement with *EXOSAT*/ME (Mavromatakis 1994), a 1989 measurement with *Mir*/Kvant (Gilfanov et al. 1989), 1990 measurements with *ROSAT*/PSPC (Mavromatakis 1994) and *Granat*/ART-P (Lutovinov et al. 1994), and our 1991–1994 measurements with BATSE. The bottom panel is an expanded view of the interval around the torque reversal and the BATSE observations. The dashed line shows the best linear fit to the 1977–1989 spin-up data (see text).

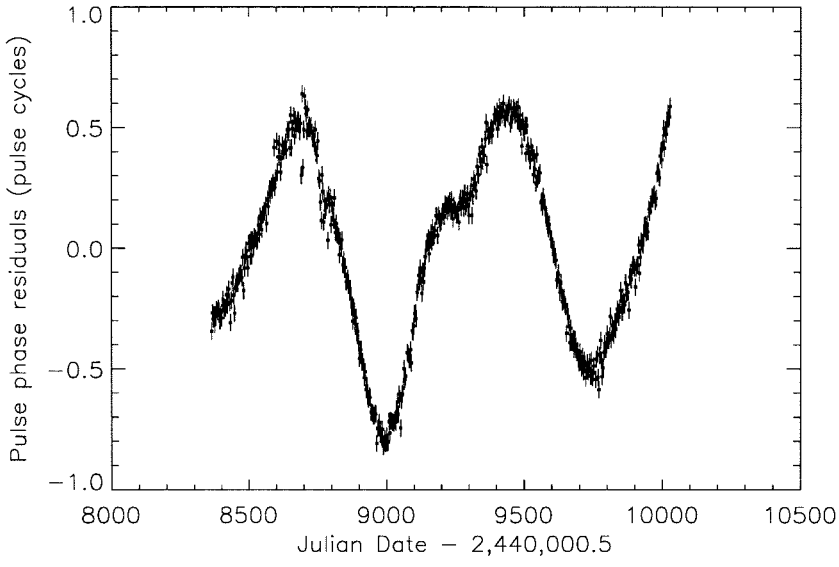

Figure 6.2: Pulse phase residuals of 4U 1626–67 relative to the best-fit quartic phase model (Equation 6.2). The phase measurements were obtained from three-day folds of the 20–60 keV BATSE DISCLA data. The typical measurement uncertainty is ±0.035 pulse cycles.

orbital signature, we fit the resulting pulse phase history to a descriptive model of the form

$$\phi(t) = \phi_0 + \nu_0(t - t_0) + \frac{1}{2}\dot{\nu}_0(t - t_0)^2 + \frac{1}{6}\ddot{\nu}_0(t - t_0)^3 + \frac{1}{24}\dddot{\nu}\,(t - t_0)^4, \qquad (6.2)$$

where pulse phase is defined relative to the maximum of the fundamental harmonic of the 20–60 keV pulse profile. (The pulse shape is dominated by this harmonic.) The resulting best-fit parameters are: $\phi_0 = 0.864(28)$, $\nu_0 = 0.1304884979(13)$ Hz, $\dot{\nu}_0 = -7.18492(56) \times 10^{-13}$ Hz s^{-1}, $\ddot{\nu}_0 = 1.119(4) \times 10^{-21}$ Hz s^{-2}, and $\dddot{\nu} = 5.8(2) \times 10^{-30}$ Hz s^{-3}, referenced to the epoch t_0 = MJD 49000 TDB.

The pulse phase residuals with respect to the fit to Equation 6.2 are shown in Figure 6.2. Slowly varying excursions from the model on time scales of a few hundred days are evident. These variations are not periodic and thus cannot arise from a binary orbit.[1] We can use the Fourier amplitude spectrum of the pulse phase residuals to set an upper limit on the possible size of a long-period orbit (Levine et al. 1988). (Because BATSE requires ~1 d to acquire a significant detection of 4U 1626–67, we cannot constrain the size of orbits with $P_{\rm orb} \lesssim 2$ d with our data.) Combining our results with earlier measurements

[1]We note that while the size and aperiodicity of the phase residuals limit the utility of Equation 6.2 as a predictive pulse phase ephemeris, Equation 6.1 is an excellent (0.0002% RMS) ephemeris for the pulse *frequency*.

by *SAS-3* and *Ginga* (Rappaport et al. 1977; Joss, Avni, & Rappaport 1978; Shinoda et al. 1990), we can set following upper limits on the projected orbital radius:

$$a_x \sin i \lesssim \begin{cases} 8 \text{ lt-ms } (3\sigma) & \text{for } 10 \text{ min} \lesssim P_{\rm orb} \lesssim 1 \text{ d} \quad (\textit{Ginga}) \\ 100 \text{ lt-ms } (2\sigma) & \text{for } 1 \text{ d} \lesssim P_{\rm orb} \lesssim 2 \text{ d} \quad (\textit{SAS-3}) \\ 60 \text{ lt-ms } (2\sigma) & \text{for } 2 \text{ d} \lesssim P_{\rm orb} \lesssim 60 \text{ d} \quad (\text{BATSE}) \\ 150 \text{ lt-ms } (2\sigma) & \text{for } 60 \text{ d} \lesssim P_{\rm orb} \lesssim 1300 \text{ d} \quad (\text{BATSE}). \end{cases} \tag{6.3}$$

The limit for orbital periods longer than ~60 d is less stringent due to a substantial increase in noise power fluctuations at low frequencies. Nevertheless, these limits effectively rule out the possibility of a long-period orbit.

6.2.2 Phase Residual Analysis

Since the phase residuals in Figure 6.2 cannot be explained by a binary orbit, it is useful to characterize the statistical properties of the pulse frequency fluctuations. The strong correlations evident on long time scales indicate the presence of a strong "red noise" component (a power spectral component which rises with decreasing frequency) in the pulse frequency fluctuations. The presence of red noise can bias an unwindowed Fourier analysis of the power spectrum continuum due to power leakage through the broad sidelobe response of sinusoidal basis functions (Deeter & Boynton 1982). Spectral leakage can be suppressed (at a cost in frequency resolution) by judicious use of data windowing (Harris 1978). Before computing the power spectrum, we multiplied the pulse frequency residuals by a window function of the form $w_j = \cos^4(j\pi/N)$ with $j = -N/2, \cdots, N/2$, substantially suppressing the sidelobe response of the Fourier transform (Harris 1978). To preserve the proper normalization, we rescaled the power spectrum by a factor $N/\sum w$.

The resulting power spectral density of the pulse frequency fluctuations P_ϕ is shown in the left panel of Figure 6.3. The spectrum at analysis frequencies $f < 10^{-7}$ Hz varies as $P_\phi \propto f^{-3.99\pm0.52}$. The power spectrum for $f > 10^{-7}$ Hz is dominated by the white noise process caused by the statistical uncertainties in the pulse phase measurements. (The measurement noise level indicated in the figure is not a fit to the power spectrum data but was calculated from the phase measurement uncertainties.) Although our measurements were made of pulse phases, it is of physical interest to study the fluctuations in pulse frequency derivative, since this quantity is proportional to the net torque on the neutron star. The power spectral density of fluctuations in pulse frequency derivative $P_{\dot\nu}$ is simply

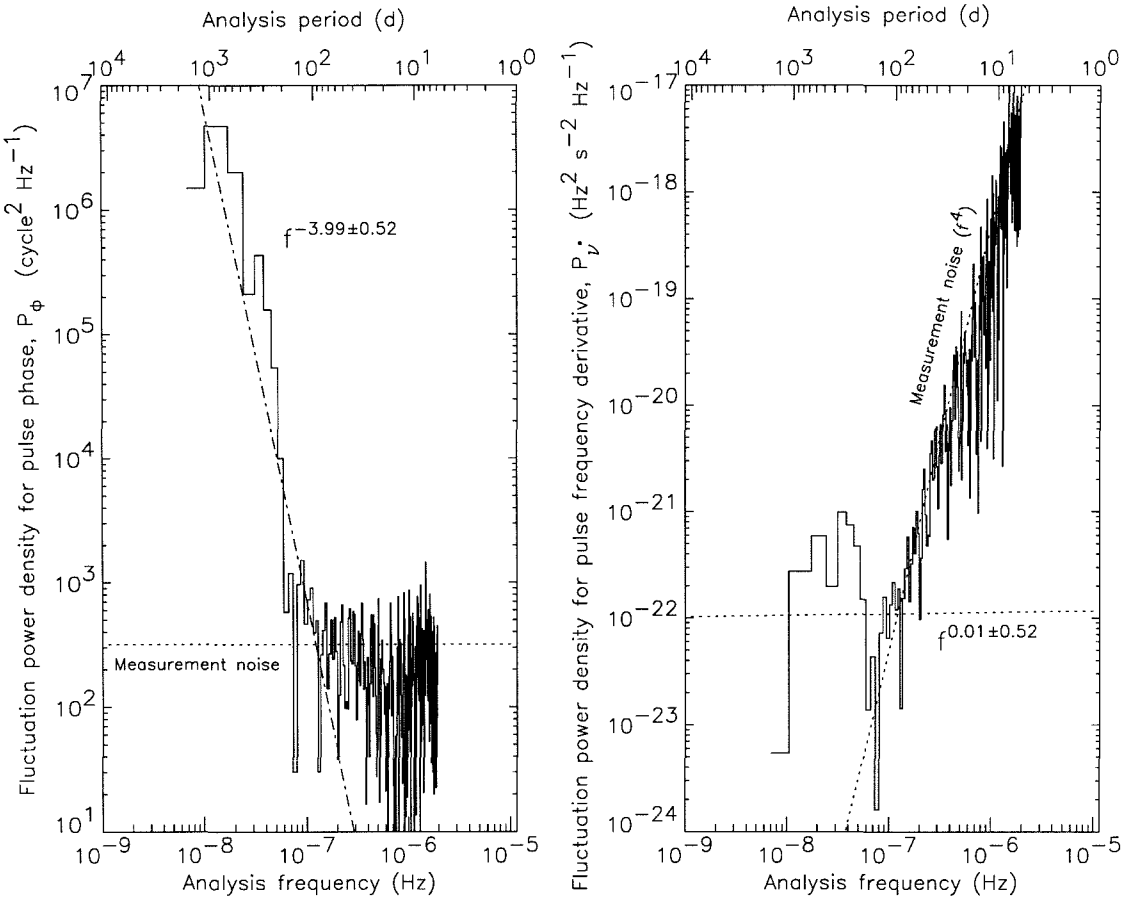

Figure 6.3: Fluctuation analysis of pulse phase residuals of 4U 1626–67. *Left panel:* Power spectrum of fluctuations in pulse phase 4U 1626–67. The white noise level expected for the measurement uncertainties is shown, as is the best fit to the low-frequency spectrum. *Right panel:* Corresponding power spectrum of fluctuations in the pulse frequency derivative $\dot\nu$. The spectrum below 10^{-7} Hz is consistent with a random walk in pulse frequency (*dotted line*), while the high frequency spectrum is consistent with measurement noise.

related to P_ϕ by $P_{\dot\nu} = (2\pi f)^4 P_\phi$ (see, e.g., Boynton 1981). This spectrum is shown in the right panel of Figure 6.3. At low frequencies, we see that the $P_{\dot\nu}$ is well described by white noise in the torque fluctuations, which is equivalent to a random walk in pulse frequency. Thus, the pulse phase variations are entirely consistent with phase measurement noise plus a random walk process in pulse frequency of strength $S_\nu \equiv R\langle(\delta\nu)^2\rangle = P_{\dot\nu} \approx 1 \times 10^{-22}$ Hz^2 s^{-1}, where R is the rate at which random walk steps of magnitude $\delta\nu$ occur.

A random walk in pulse frequency is capable of inducing apparent high-order terms in the pulse timing model. Since the root-mean-squared variation in the pulse frequency induced by the random walk in a time T is just $\sqrt{S_\nu\, T}$, the apparent pulse frequency second

derivative induced over our 1600 d observation is

$$\ddot{\nu}_{\rm rw} \sim \frac{2\sqrt{S_\nu T}}{T^2} \approx 10^{-23} \text{ Hz s}^{-2}. \quad (6.4)$$

This is two orders of magnitude smaller than the observed $\ddot{\nu} \approx 10^{-21}$ Hz s^{-2}, suggesting that the rapid $\dot{\nu}$ evolution does not arise from the random walk but is due to some different process. The apparent pulse frequency third derivative induced is

$$\dddot{\nu}_{\rm rw} \sim \frac{6\sqrt{S_\nu T}}{T^3} \approx 3 \times 10^{-31} \text{ Hz s}^{-3}. \quad (6.5)$$

This is within an order of magnitude of the measured value $\dddot{\nu} \approx 6 \times 10^{-30}$ Hz s^{-3}. Given the uncertainties in our measurement of the random walk strength, the observed $\dddot{\nu}$ is consistent with the random walk.

6.2.3 Pulse Spectroscopy

In order to measure the photon energy spectrum of the pulsed emission, we folded segments of the BATSE CONT data (16 energy channels, 2.048 s resolution) using the pulse frequency model of Equation 6.1. Spectral measurement of this source is difficult because it is usually only detected in the two lowest CONT energy channels (roughly 20–30 keV and 30–45 keV). We selected the data interval 1993 August 16–21 (MJD 49217–49222), during which the source was also detected in the next highest channel (45–60 keV). A single-harmonic pulse model was employed to measure the pulsed count rates in the pulse profiles (see Chapter 5). The inferred phase-averaged pulsed photon spectrum, assuming a power-law spectral model $dN/dE = C_{30}(E/30 \text{ keV})^{-\gamma}$, is shown in Figure 6.4. The best-fit spectral parameters are $\gamma = 4.76(20)$ and $C_{30} = 1.50(3) \times 10^{-4}$ photons cm^{-2} s^{-1} keV^{-1}. The pulse profiles from the CONT data are shown in Figure 6.5; no pulsed signal was detected in channel 4. The 20–60 keV pulsed intensity of 4U 1626–67 was relatively steady at 1.5×10^{-10} erg cm^{-2} s^{-1} over the entire BATSE observation interval, varying by less than 50%.

6.3 Discussion

The accretion torque exerted on the neutron star in 4U 1626–67 is very steady and smooth, most likely a sign of disk accretion. Our observations have found that the neutron star is now steadily spinning down as it accretes, in contrast to the spin-up

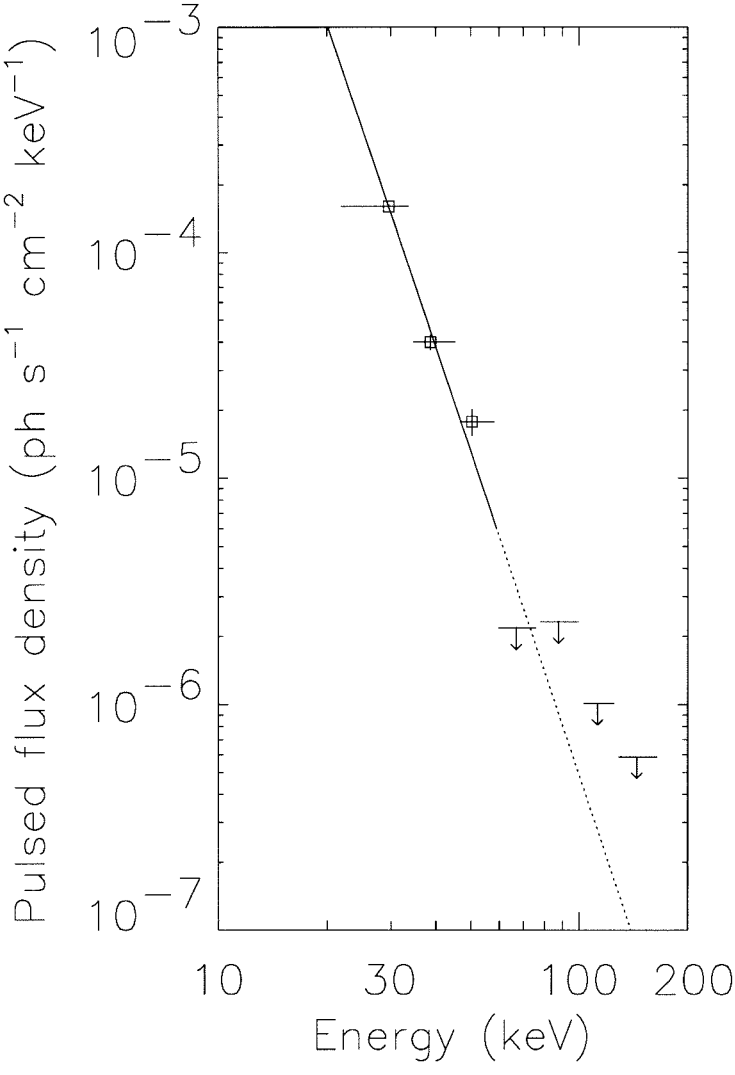

Figure 6.4: The phase-averaged pulsed photon spectrum of 4U 1626–67 during the interval MJD 49217–49222. The vertical bars show the 1 σ statistical uncertainties, while the horizontal bars show the widths of the energy channels. Upper limits are quoted at 95% confidence. The solid line shows the best-fit power law photon spectral model ($\gamma = 4.76$, $C_{30} = 1.50 \times 10^{-4}$ photons cm^{-2} s^{-1} keV^{-1}) in the detected energy range. The dashed line indicates the extrapolation of this model to higher energies.

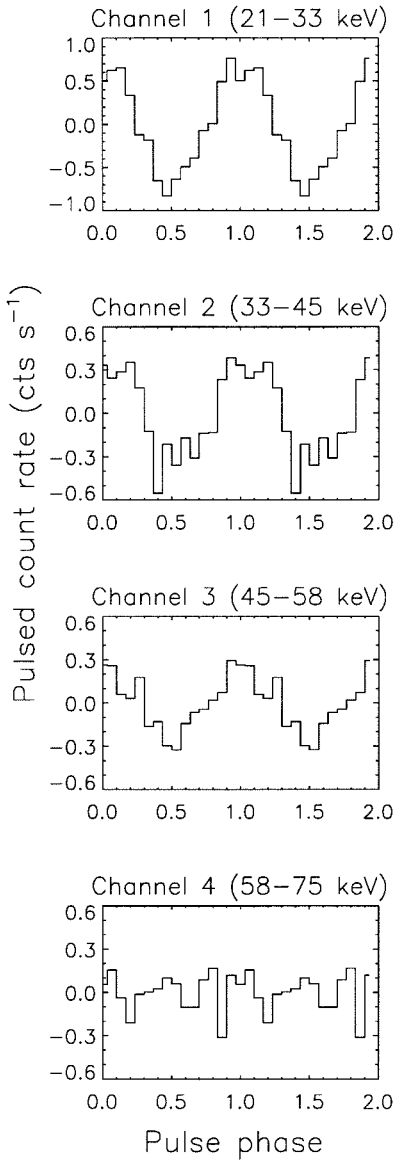

Figure 6.5: Pulse profiles as a function of energy for 4U 1626–67, during the interval MJD 49217–49222. Two pulses are shown for each channel, and all channels are displayed relative to the same pulse phase. The energy edges for each CONT channel of BATSE detector 6 are indicated. These pulse profiles are overresolved by a factor of 4. Note that the pulse shapes are uncorrected for the rapid change in detector response as a function of energy in the 20–75 keV range. No pulse was detected in channel 4.

previously observed. This probably indicates that the pulsar is spinning near its equilibrium period, where the magnetospheric radius is comparable to the co-rotation radius $r_{co} = (GM_x/4\pi^2\nu^2)^{1/3} = 6.5 \times 10^8$ cm (assuming neutron star mass $M_x = 1.4M_\odot$). The characteristic torque $N_{char} = \dot{M} l_{co}$ is set by the mass accretion rate $\dot{M}$ and the specific angular momentum $l_{co} = (GM_x r_{co})^{1/2}$ of matter at the co-rotation radius. This torque would give a spin evolution rate of $|\dot{\nu}| = N/2\pi I \approx 3.5 \times 10^{-13}$ Hz s^{-1}, assuming $\dot{M} = 10^{-10} M_\odot$ yr^{-1} and moment of inertia $I = 10^{45}$ g cm^2. As the actual torque might be less than N_f, we can use our measured value of $\dot{\nu}$ to place a lower limit on the mass accretion rate, $\dot{M} \gtrsim 2 \times 10^{-10} M_\odot$ yr^{-1} (see Appendix C). The source must then be further than 3 kpc away to give a flux consistent with Pravdo et al. (1978), implying that the system lies > 600 pc above the Galactic plane.

As Levine et al. (1988) have already noted, mass accretion rates of this order are consistent with a low-mass degenerate helium or carbon-oxygen companion whose evolution is driven by gravitational radiation. The surface magnetic field strength needed to place the magnetosphere at the co-rotation radius is $B \gtrsim 10^{12}$ G for these accretion rates. Though the magnetic field for this system has never been measured, previous authors have suggested a magnetic field strength of 6–8$\times 10^{12}$ G on the basis of the cutoff energy in the X-ray spectrum (Pravdo et al. 1979) and the energy dependence of the pulse shape (Kii et al. 1986).

The various theories of magnetic accretion torques (Ghosh & Lamb 1979; Arons et al. 1984; Wang 1987) all agree that lower values of accretion rate will move the magnetosphere to larger radii and eventually lead to spin-down. The accretion luminosity has been measured during both spin-up and spin-down for this system. The best measurement during spin-up was $F_x \approx 2.4 \times 10^{-9}$ erg cm^{-2} s^{-1} (0.7–60 keV; Pravdo et al. 1979). Our measurements found a 20–60 keV pulsed spectrum with the same power-law slope as the Pravdo et al. measurement (for the same bandpass), but with a factor of 3–4 reduction in overall normalization. This is not a bolometric measurement, as BATSE is only sensitive to the pulsed flux above 20 keV. However, a contemporaneous 0.5–10 keV *ASCA* observation found that the total flux in this bandpass was a factor of 3 lower than a 1979 (spin-up) measurement in the same bandpass (Angelini et al. 1995). In addition, a 0.5–2.4 keV *ROSAT* observation made near the torque reversal also measured a total flux lower than the spin-up value in the same bandpass (Mavromatakis 1994). There is thus evidence for a reduction in the accretion rate onto the neutron star during the spin-down.

In the broader context of all the disk-fed accreting pulsars, a wide range of behavior is seen (Prince et al. 1994). As noted earlier, disk-fed pulsars with a characteristic spin-up time much shorter than their lifetime should be at or near their equilibrium spin period. These systems evidently oscillate about this equilibrium through alternating episodes of spin-up and spin-down. This scenario was checked by comparing the observed long-term ($\gtrsim$ years) mean torque $N_{\rm avg}$ to the characteristic torque $N_{\rm char}$. For both 4U 1626–67 and GX 1+4 (and also SMC X-1 and 1E 2259+586, both of which have exhibited long-term spin-up and/or spin-down episodes), the observed long-term average torque always satisfies $N_{\rm avg} \gtrsim 0.2N_{\rm char}$, which (within the uncertainties) is consistent with accretion from matter near the co-rotation radius. In contrast, the disk-fed source Her X-1 exhibits $N_{\rm avg} \sim 0.01N_{\rm char}$. Some of these systems have frequency histories that are consistent with a random walk (Baykal & Ögelman 1993) that could arise if the torque had a value $\sim N_{\rm char}$, but changed signs on a shorter time scale. Recent short time scale ($\lesssim$10–20 d) torque measurements for Her X-1 and Cen X-3 by BATSE always find torques well in excess of $N_{\rm avg}$, but never in excess of $N_{\rm char}$ (Wilson, Finger, & Scott 1994; Finger, Wilson, & Fishman 1994).

This suggests that all disk-fed accreting pulsars show torques with magnitudes $\lesssim N_{\rm char}$ on short time scales and differentiate themselves by the torque switching time. This raises two new questions which need to be addressed:

- **Why is the magnitude of the torque during spin-up nearly the same as during spin-down?** Ghosh & Lamb (1979) predicted that the torque would smoothly pass through zero before the magnetospheric radius moves outside of the co-rotation radius (the point where accretion might be halted by centrifugal effects), in which case one would expect a wide range of possible spin-down torque magnitudes. It is thus puzzling that the magnitude of the spin-up and spin-down torques in 4U 1626–67 are nearly identical.

- **What physics sets the time scale for the torque reversals?** It seems unlikely to be set by the viscous time in the accretion disk, as this time scale (for an $\alpha = 1$ Shakura-Sunyaev accretion disk) is $\sim 10^4$ seconds at the magnetosphere and a few days at the outer edge of the accretion disk. It might well arise from long-term cycles in the supply of matter from the companion, in which case the time scale is similar to the long-term cycles seen in other low-mass X-ray binaries (Smale & Lochner 1992).

The neutron star in accreting X-ray pulsars is subject to both external and internal torques. The external torques arise from both the accretion of matter from the binary

companion and the interaction of the pulsar magnetosphere with the accretion disk. The internal torques arise from the response of the neutron star to these external torques and depend on the detailed interior structure of neutron stars. The pulse phase and its time derivatives provide a probe of these torque components. Among the accretion-powered pulsars, detailed statistical studies have been made of the disk-fed systems Her X-1 (Boynton 1981) and Cen X-3 (Finger, Wilson, & Fishman 1994), and the wind-fed system Vela X-1 (Deeter et al. 1989; Finger et al. 1996). Her X-1 and Vela X-1 both exhibit fluctuations consistent with a random walk in pulse frequency of strength 2×10^{-19} Hz^2 s^{-1} and 2×10^{-20} Hz^2 s^{-1}, respectively. The power density of torque fluctuations for Cen X-3 exhibits a $1/f$ spectrum of strength $> 10^{-18}$ Hz^2 s^{-1} below 10^{-6} Hz. By comparison, the frequency random walk of strength 10^{-22} Hz^2 s^{-1} observed in 4U 1626–67 is a very quiet process. These contrasts may simply reflect differences in the stability of the accretion flows in these systems.

It is also interesting to compare the torque noise in 4U 1626–67 with the timing irregularities seen in radio pulsars. Both timing noise and glitches are seen in many young radio pulsars (see Lyne 1993 for a review). For most of these pulsars, the timing noise can be described by a random walk in frequency (Cordes & Helfand 1980). The Crab pulsar, one of the youngest and noisiest radio pulsars, exhibits a random walk in frequency of strength 7×10^{-23} Hz^2 s^{-1} (Boynton et al. 1972; Cordes & Helfand 1980), only a factor of 2 weaker than what we observe in 4U 1626–67. Observations of glitches and timing noise in radio pulsars has motivated much theoretical work on the interactions between the crustal neutron superfluid and the charged component of the crust (see Alpar 1995 for a recent summary). Internal torques might be the source of the noise process we observe in 4U 1626–67 (Lamb, Pines, & Shaham 1978).

A comparison of the interior conditions of accreting X-ray pulsars and young radio pulsars is instructive. The neutron star's response to an external torque should depend mainly on the strength of the torque and the interior temperature of the star; whether the torque is caused by accretion or by radiative losses is most likely irrelevant. The torques in noisy radio pulsars are generally larger than what we see in 4U 1626–67 ($\dot{\nu} = 3.6\times10^{-10}$ Hz s^{-1} in the Crab pulsar). However, the core temperature (which is important to most models of the glitching mechanisms and may be for timing noise as well) is comparable. Most of the noisiest radio pulsars are young ($\lesssim 10^4$ yr) and still have relatively hot cores from their birth ($T_c \gtrsim 2\times10^8$ K) for a standard cooling curve (Nomoto & Tsuruta 1987).

The core temperatures in accreting neutron stars are also $\gtrsim 10^8$ K, as the nuclear burning of the freshly accreted matter on the surface heats the interior to these temperatures in $< 10^6$ yr (Fujimoto et al. 1984). The steady-state core temperature of an accreting system is found by balancing the thermal heating from the hot blanket of burning matter with internal neutrino cooling. Ayasli and Joss (1982) showed that a system accreting at the 10^{-10} $M_\odot$ yr^{-1} rate relevant to 4U 1626–67 would equilibrate at $T_c \approx 1 \times 10^8$ K. These similarities in temperatures might prove important in our eventual understanding of the torque noise in 4U 1626–67.

References

Alpar, M. A. 1995. Model for pulsar glitches. In *The Lives of Neutron Stars*, ed. M. A. Alpar et al. (Dordrecht: Kluwer), 185.

Angelini, L., Ghosh, P., & White, N. E. 1994. 4U 1626–67: the ROSAT PSPC observtation. In *New Horizon of X-Ray Astronomy*, ed. F. Makino & T. Ohashi (Tokyo: Univ. Acad. Press), 411.

Angelini, L., White, N. E., Nagase, F., Kallman, T. R., Yoshida, A., Takeshima, T., Becker, C. M., & Paerels, F. 1995. Neon line emission in the X-ray spectrum of the pulsar 4U 1626–67. *Astrophys. J.*, **449**, L41.

Arons, J., Burnard, D., Klein, R. I., McKee, C. F., Pudritz, R. E., & Lea, S. M. 1984. Accretion onto magnetized neutron stars: magnetospheric structure and stability. In *High Energy Transients in Astrophysics*, ed. S. E. Woosley (New York: AIP Press), 215.

Ayasli, S. & Joss, P. C. 1982. Thermonuclear processes on accreting neutron stars: a systematic study. *Astrophys. J.*, **256**, 637.

Baykal, A. & Ögelman, H. 1993. An empirical torque noise and spin-up model for accretion-powered X-ray pulsars. *Astron. & Astrophys.*, **267**, 119.

Bildsten, L., Chakrabarty, D., Chiu, J., Finger, M. H., Grunsfeld, J. M., Koh, T., Prince, T. A., & Wilson, R. B. 1994. Change in the accretion torque in the binary accreting pulsar 4U 1626–67. In *Second Compton Symposium*, ed. C. E. Fichtel, N. Gehrels, & J. P. Norris (New York: AIP Press), 290.

Boynton, P. E. 1981. Pulsar timing and neutron star structure. In *Pulsars*, ed. W. Sieber & R. Wielebinski (Dordrecht: Reidel), 279.

Boynton, P. E., Groth, E. J., Hutchinson, D. P., Nanos, G. P., Patridge, R. B., & Wilkinson, D. T. 1972. Optical timing of the Crab pulsar, NP 0532. *Astrophys. J.*, **175**, 217.

Bradt, H. V., Apparao, K. M. V., Dower, R., Doxsey, R. E., Jernigan, J. G., & Markert, T. H. 1977. Positions of Galactic X-ray sources Cir X-1, TrA X-1, and 3U 1626–67. *Nature*, **269**, 496.

Chakrabarty, D., Koh, T., Prince, T. A., Vaughan, B., Finger, M. H., Scott, M., & Wilson, R. B. 1995b. GX 1+4. *IAU Circ.*, No. 6153.

Chakrabarty, D., Prince, T. A., Finger, M. H., & Wilson, R. B. 1994. GX 1+4. *IAU Circ.*, No. 6105.

Chester, T. J. 1979. Continuum optical pulsation from the companions of binary X-ray pulsars. *Astrophys. J.*, **227**, 569.

Cordes, J. M. & Helfand, D. J. 1980. Pulsar timing. III. Timing noise of 50 pulsars. *Astrophys. J.*, **239**, 640.

Deeter, J. E. 1984. Techniques for the estimation of red power spectra. II. Evaluation of alternative methods. *Astrophys. J.*, **281**, 482.

Deeter, J. E. & Boynton, P. E. 1982. Techniques for the estimation fo red power spectra. I. Context and methodology. *Astrophys. J.*, **261**, 337.

Deeter, J. E., Boynton, P. E., Lamb, F. K., & Zylstra, G. 1989. Vela X-1 pulse timing. II. Variations in pulse frequency. *Astrophys. J.*, **336**, 376.

Elsner, R. F., Ghosh, P., & Lamb, F. K. 1980. On the origin and persistence of long-period pulsating X-ray sources. *Astrophys. J.*, **241**, L155.

Finger, M. H., Vaughan, B., van der Klis, M., Berger, M., & Wilson, R. B. 1996. Fourier power spectral characterization of the rotational history of the X-ray pulsar Vela X-1. *Astrophys. J.*, in preparation.

Finger, M. H., Wilson, R. B., & Fishman, G. J. 1994. Observations of accretion torques in Cen X-3. In *Second Compton Symposium*, ed. C. E. Fichtel, N. Gehrels, & J. P. Norris (New York: AIP Press), 304.

Fishman, G. J. et al. 1989. BATSE: the Burst and Transient Source Experiment on the Compton Gamma Ray Observatory. In *Proc. of the GRO Science Workshop*, ed. W. N. Johnson (Greenbelt: NASA/GSFC), 2-39.

Fujimoto, M. Y., Hanawa, T., Iben, I., & Richardson, M. B. 1984. Thermal evolution of accreting neutron stars. *Astrophys. J.*, **278**, 813.

Ghosh, P. & Lamb, F. K. 1979. Accretion by rotating magnetic neutron stars. III. Accretion torques and period changes in pulsating X-ray sources. *Astrophys. J.*, **234**, 296.

Giacconi, R., Murray, S., Gursky, H., Kellogg, E., Schreier, E. & Tananbaum, H. 1972. The Uhuru catalog of X-ray sources. *Astrophys. J.*, **178**, 281.

Gilfanov, M. et al. 1989. Observations of the X-ray pulsars from the Kvant module. In *Proceedings of the 23rd ESLAB Symposium on Two Topics in X-ray Astronomy*, Vol. 1 (Noordwijk: ESA SP–196), 71.

Harris, F. J. 1978. On the use of windows for harmonic analysis with the discrete Fourier transform. *Proc. IEEE*, **66**, 51.

Ilovaisky, S. A., Motch, C., & Chevalier, C. 1978. Discovery of optical pulsations from 4U 1626–67. *Astron. & Astrophys.*, **70**, L19.

Joss, P. C., Avni, Y., & Rappaport, S. 1978. Accreting neutron stars in highly compact binary systems and the nature of 4U 1626–67. *Astrophys. J.*, **221**, 645.

Kii, T., Hayakawa, S., Nagase, F., Ikegami, T., & Kawai, N. 1986. Anisotropic X-ray transfer in a strongly magnetized plasma of the X-ray pulsar 4U 1626–67. *Pub. Astron. Soc. Japan*, **38**, 751.

Lamb, F. K., Pines, D., & Shaham, J. 1978. Period variations in pulsating X-ray sources. I. Accretion flow parameters and neutron star structure from timing observations. *Astrophys. J.*, **224**, 969.

Levine, A., Ma, C. P., McClintock, J., Rappaport, S., van der Klis, M., & Verbunt, F. 1988. 4U 1626–67: the binary with the smallest known mass function. *Astrophys. J.*, **327**, 732.

Li, F. K., Joss, P. C., McClintock, J. E., Rappaport, S., & Wright, E. L. 1980. 4U 1626–67 and the character of highly compact binary X-ray sources. *Astrophys. J.*, **240**, 628.

Lutovinov, A. A., Grebenev, S. A., Sunyaev, R. A., & Pavlinsky, M. N. 1994. Timing of X-ray pulsars from data obtained with the ART-P telescope of the Granat space observatory in 1990–1992. *Astron. Lett.*, **20**, 538.

Lyne, A. G. 1993. Glitches as probes of neutron star interiors. In *Pulsars as Physics Laboratories*, ed. R. D. Blandford et al. (Oxford: Oxford U. Press), 29.

Makishima, K. et al. 1988. Spin-down of the X-ray pulsar GX 1+4 during an extended low state. *Nature*, **333**, 746.

Mavromatakis, F. 1994. Soft and hard X-ray observations of 4U 1626–67. *Astron. & Astrophys.*, **285**, 503.

McClintock, J. E., Canizares, C. R., Bradt, H. V., Doxsey, R. E., Jernigan, J. G., & Hiltner, W. A. 1977. Optical candidates for two X-ray bursters and an X-ray pulsar. *Nature*, **270**, 320.

McClintock, J. E., Canizares, C. R., Li, F. K., & Grindlay, J. E. 1980. Simultaneous X-ray and optical observations of the 7.7 second X-ray pulsar 4U 1626–67. *Astrophys. J.*, **235**, L81.

Middleditch, J., Mason, K. O., Nelson, J. E., & White, N. E. 1981. 4U 1626–67: a prograde spinning X-ray pulsar in a 2500 s binary system. *Astrophys. J.*, **244**, 1001.

Nagase, F. 1989. Accretion-powered X-ray pulsars. *Pub. Astron. Soc. Japan*, **41**, 1.

Nomoto, K. & Tsuruta, S. 1987. Cooling of neutron stars: effects of the finite time scale of thermal conduction. *Astrophys. J.*, **312**, 711.

Pravdo, S. H. et al. 1979. HEAO-1 observations of the X-ray pulsar 4U 1626–67. *Astrophys. J.*, **231**, 912.

Prince, T. A., Bildsten, L., Chakrabarty, D., Wilson, R. B., & Finger, M. H. 1994. Observations of accreting pulsars. In *Evolution of X-Ray Binaries*, ed. S. S. Holt & C. S. Day (New York: AIP Press), 235.

Rappaport, S., Markert, T., Li, F. K., Clark, G. W., Jernigan, J. G., & McClintock, J. E. 1977. Discovery of a 7.68 second X-ray periodicity in 3U 1626–67. *Astrophys. J.*, **217**, L29.

Shinoda, K., Kii, T., Mitsuda, K., Nagase, F., Tanaka, Y., Makishima, K., & Shibazaki, N. 1990. Discovery of the quasi-periodic oscillations from the X-ray pulsar X1627–673. *Pub. Astron. Soc. Japan*, **42**, L27.

Smale, A. P. & Lochner, J. C. 1992. Long-term variability in low-mass X-ray binaries: a study using data from Vela 5B. *Astrophys. J.*, **395**, 582.

Verbunt, F., Wijers, R. A. M. J., & Burm, H. M. G. 1990. Evolutionary scenarios for the X-ray binary pulsars 4U 1626–67 and Hercules X-1, and their implications for the decay of neutron star magnetic fields. *Astron. & Astrophys.*, **234**, 195.

Wang, Y. M. 1987. Disc accretion by magnetized neutron stars: a reassessment of the torque. *Astron. & Astrophys.*, **183**, 257.

Wilson, R. B., Finger, M. H., Pendleton, G. N., Briggs, M., & Bildsten, L. 1994. BATSE observations of Her X-1: the 35 day cycle, orbit determination, and torque studies. In *Second Compton Symposium*, ed. C. E. Fichtel, N. Gehrels, & J. P. Norris (New York: AIP Press), 235.

Wilson, R. B., Fishman, G. J., Finger, M. H., Pendleton, G. N., Prince, T. A., & Chakrabarty, D. 1993. Observations of isolated pulsars and disk-fed X-ray binaries. In *Compton Gamma Ray Observatory*, ed. M. Friedlander, N. Gehrels, & D. J. Macomb (New York: AIP Press), 291.

Chapter 7

Torque-Luminosity Anticorrelation in the Accreting Pulsar GX 1+4*

A fine wind is blowing the new direction of Time.
—D. H. Lawrence (1920)

7.1 Introduction

The torque exerted on an accreting star is of great interest in astrophysics, with relevance to binary evolution, star formation, neutron star structure, and the origin of millisecond radio pulsars. A widely studied scenario is disk accretion onto a rotating, magnetized star, usually a neutron star, white dwarf, or T Tauri star (see King 1995 for a recent review). As first discussed by Pringle & Rees (1972) and Lamb, Pethick, & Pines (1973), the Keplerian disk flow will be disrupted at the magnetospheric radius $r_{\rm m}$ (where the Keplerian kinetic stress is equal to the magnetic stress), attaching matter to the magnetic field lines. If $r_{\rm m}$ lies beyond the corotation radius $r_{\rm co}$ (where the presumably corotating magnetic field lines are moving at the local Kepler velocity), then matter attached to the field lines will be centrifugally inhibited from accreting, potentially being expelled as in a propeller (Illarionov & Sunyaev 1975). Matter can easily accrete if $r_{\rm m} < r_{\rm co}$ and flows along the field lines onto a restricted surface near the magnetic poles of the star, spinning up the star with specific angular momentum $N = (GM_{\rm x}r_{\rm m})^{1/2}$ and giving rise to pulsed emission at the star's spin period. This phenomenon is seen in both accreting neutron stars (X-ray

*Adapted from a manuscript in preparation for *The Astrophysical Journal* by D. Chakrabarty, L. Bildsten, J. M. Grunsfeld, T. Koh, T. A. Prince, B. Vaughan, M. H. Finger, R. B. Wilson, & B. C. Rubin.

pulsars; see White, Nagase, & Parmar 1995) and accreting white dwarfs (DQ Her systems; see Patterson 1994).

Accreting neutron stars are the ideal laboratory for the study of accretion torques, since the bolometric X-ray intensity is proportional to the mass accretion rate, and the low moment of inertia permits torque measurements on short time scales. Early observations of X-ray pulsars found that the simple dimensional model for steady spin-up sketched above is inadequate; some X-ray pulsars are observed to spin up at rates smaller than predicted, or even to spin down for extended intervals while continuing to accrete matter. This led to the suggestion of mechanisms for a spin-down torque during accretion which could compete with or even dominate the spin-up torque. These suggestions fall into two categories. In the first, the magnetic field penetrates the accretion disk beyond $r_{\rm m}$ (Ghosh & Lamb 1979a, 1979b; Wang 1987, 1995). In this *magnetically-threaded disk* (MTD) model, the spin-down torque arises from magnetic coupling of the neutron star with material beyond $r_{\rm co}$, where the disk rotates more slowly than the pulsar. In the second category, the spin-down torque arises from the loss of angular momentum via matter outflow from some parts of the disk while accretion continues from other parts (Arons et al. 1984; Lovelace, Romanova, & Bisnovatyi-Kogan 1995). In the *centrifugally-driven wind* (CDW) model of Arons et al. (1984), the magnetic field does not thread the disk but penetrates a narrow boundary layer. Kelvin-Helmholtz instabilities load the magnetosphere with disk material, causing some field lines to be broken open by centrifugal stresses. A magnetohydrodynamic wind outflow results, which carries away angular momentum.

The two scenarios differ dramatically in the topology of the magnetic field beyond $r_{\rm m}$. The principal observational distinction is the outflow predicted by the CDW model, which would probably be supersonic. Otherwise, both scenarios share a number of features. They both predict an equilibrium spin period where the spin-up and spin-down torques balance, which occurs when $r_{\rm m} \approx r_{\rm co}$. At this equilibrium, there is no net torque on the star, but accretion continues to occur. They both predict that a higher mass accretion rate $\dot{M}$ should yield a smaller magnetospheric radius $r_{\rm m}$, resulting in a larger spin-up torque. They both predict that a reduced value of $\dot{M}$ increases $r_{\rm m}$, reducing the spin-up torque until a net spin down occurs and eventually leading to centrifugal inhibition of matter due to the propeller effect (Illarionov & Sunyaev 1975).

The sparse, intermittent observations of X-ray pulsars during the 1970s and 1980s were generally consistent with either scenario (see Nagase 1989 and references therein).

Presently, the Burst and Transient Source Experiment (BATSE) on the *Compton Gamma Ray Observatory* (*GRO*) has made daily measurements of a large sample of X-ray pulsars over a long ($\gtrsim$ 5 yr) time baseline available for the first time, allowing investigations on a wide variety of time scales. In some cases [e.g., A0535+26 (Finger, Wilson, & Harmon 1996); 4U 1626–67 (Chapter 5)], the BATSE observations have also been compatible with both the MTD and CDW models of magnetic disk accretion. However, in this paper, we describe observations of a disk-fed X-ray pulsar which is not readily understood in these terms.

The $\approx$ 2 min accretion-powered binary pulsar GX 1+4 was discovered in an 18–50 keV hard X-ray balloon experiment a quarter century ago (Lewin, Ricker, & McClintock 1971) and was later identified with the 2–10 keV *Uhuru* source 4U 1728–247 (Forman et al. 1978). It was found to have the hardest X-ray spectrum among the persistent X-ray pulsars, well fit by a broken power law photon spectrum with soft index $\gamma_1 \approx 1.3$ (2–20 keV; Becker et al. 1976) and hard index $\gamma_2 \approx 2.5$ (20-60 keV; Ricker et al. 1976). Several authors reported evidence that the true pulse period was $\sim$ 4 min. However, Doty et al. (1981) found that there is a significant excess of aperiodic variability in the source on time scales near 4 min, and that this excess noise was capable of explaining the apparent 4 min period in their *SAS-3* observation[1].

Armed with the 1 arcmin *Uhuru* X-ray position, Glass & Feast (1973) tentatively identified GX 1+4 with the bright infrared star V2116 Oph. This association was strengthened by an improved 25 arcsec X-ray position circle centered within 8 arcsec of V2116 Oph (Doxsey et al. 1977). Optical spectroscopy found that V2116 Oph was the cool component of a symbiotic binary (see Kenyon 1986 for a review of symbiotic stars), with bright emission lines of H I (especially Hα) and He I superimposed on the cool continuum spectrum of a highly reddened ($A_V \approx 5$) M6 III giant (Davidsen, Malina, & Bowyer 1977). In addition, the optical spectrum also contained emission lines of several highly ionized species, notably [Fe VII] and [Fe X], requiring the presence of $\gtrsim$ 100 eV ionizing photons and suggesting that the hot secondary component is an X-ray source. A recent improved position (8 arcsec radius) for GX 1+4 lies within 2 arcsec of the optical position of V2116 Oph (Predehl, Friedrich, & Staubert 1995). This latest position must be viewed with some caution as it is derived from only 15 detected photons in a 22 arcsec radius. Nevertheless, the optical

[1]Viewed in hindsight, this may be evidence for a weak quasi-periodic oscillation, a phenomenon which was not known to exist in X-ray pulsars until 1988. See van der Klis (1995) for a recent review.

identification seems secure, making this system the only known neutron star symbiotic.

Throughout the 1970s, GX 1+4 was repeatedly detected as a persistent source (see McClintock & Leventhal 1989 and references therein) and was spinning up rapidly on a time scale $|\nu/\dot{\nu}| \approx 40$ yr. However, a series of deep observations by *EXOSAT* in 1983 September and 1984 August–September failed to detect the source, establishing an upper limit two orders of magnitude below the previously observed intensity (Hall & Davelaar 1983; Dotani et al. 1989). Optical spectroscopy of V2116 Oph acquired during the X-ray low state in GX 1+4 found variability in the emission line features: strong Hα emission was detected in 1983 August, *no* emission lines were detected in 1983 November, and strong Balmer emission had resumed in 1984 February (Whitelock, Menzies, & Feast 1983; Whitelock 1984).

In 1987, observations with *Ginga* found the X-ray source at a low intensity and spinning down rapidly (Makishima et al. 1988). In order to interpret this torque reversal as the oscillation between spin-up and spin-down of a pulsar at its equilibrium spin period, an unusually high surface magnetic field of $B \sim 7 \times 10^{13}$ G is required. As an alternative, Makishima et al. suggested that the spin-down may be due to accretion from the dense, slow wind of the M giant after disruption of an earlier accretion disk during spin-up. Subsequent observations found the source brightening somewhat over the next few years. Optical spectroscopy of V2116 Oph found strong H I and He I emission features, but the highly ionized [Fe] features observed during the 1970s were notably absent (Gotthelf, Halpern, & Szentgyorgyi 1988; Sood et al. 1991; Chakrabarty & Roche 1996).

Our daily observations of GX 1+4 with the *Compton*/BATSE all-sky monitor began in 1991 April. These observations found relatively steady, persistent quiescent emission along with intermittent bright flares, most notably the widely observed 1993 September flare (Finger et al. 1993; Staubert et al. 1995). Several authors have claimed that this X-ray flare was accompanied by enhanced Hα emission (Manchanda et al. 1995; Greenhill et al. 1995), although optical spectroscopic measurements do not support this (Chakrabarty & Roche 1996). In 1994 November, after several months of gradually increasing in intensity, GX 1+4 underwent a smooth torque reversal and began spinning up for several months (Chakrabarty et al. 1994; see Appendix I). By 1995 March, the X-ray flux had dropped back to its quiescent level and the source underwent another smooth torque reversal into a spin-down state (Chakrabarty et al. 1995; see Appendix I). In this chapter, we present a detailed analysis of the BATSE monitoring data.

7.2 Observations and Analysis

7.2.1 Timing

BATSE is a nearly continuous all-sky monitor of 20 keV–1.8 MeV hard X-ray/γ-ray flux, consisting of eight identical uncollimated detectors arranged on the corners of the *Compton* spacecraft (see Fishman et al. 1989 for a description). Because the detectors are uncollimated, steady sources are indistinguishable from the background except when occulted by Earth's limb. Bright impulsive transients (e.g., solar flares and gamma ray bursts) are detected because their high intensity and short duration make them easily discriminated from the background. Periodic pulsed sources are also readily detectable. Our standard BATSE pulsed source detection and timing analysis uses the 20–60 keV channel of the 4 channel/1.024 s resolution DISCLA data type (see Chapter 2). The barycentric pulse frequency history of GX 1+4 from 1991 April to 1995 November (MJD 48362–50031) was determined by dividing the BATSE data into five-day segments and searching the Fourier power spectrum of each segment for the strongest signal in the pulse period range 110 s$\lesssim P_{\rm pulse} \lesssim$ 130 s.

Figure 7.1 shows the long-term pulse frequency history of GX 1+4, including both previous observations by various instruments as well as our BATSE observations (see Appendix J). During the 1970s, GX 1+4 was spinning up with mean rate $\dot{\nu} \approx 6.0 \times 10^{-12}$ Hz s^{-1}. From 1984 to date, the source has spun down at a mean rate $\dot{\nu} \approx -3.7 \times 10^{-12}$ Hz s^{-1}, similar in magnitude to the previous spin-up rate. A close inspection of the pulse frequency data shows significant deviations from simple linear trends. During the spin-up era, the post-1975 measurements were of high precision and show excursions from steady spin-up.

The spin-down data during 1987–1991 (see bottom panel of Figure 7.1) show a clear quadratic trend, with the spin-down torque decreasing on a time scale $|\dot{\nu}/\ddot{\nu}| \approx 10$ yr. Our BATSE observations (shown in detail in Figure 7.2) also display a significant quadratic trend with a similar time scale $|\dot{\nu}/\ddot{\nu}| \approx 10$ yr. However, the two quadratic trends are not consistent. Instead, they meet in a cusp around MJD 48300, indicating that a discontinuous change in the torque history occurred around this time. The SIGMA observations are approximately consistent with both trends. We observed a transition from spin-down to spin-up in 1994 November (Figure 7.3). Steady spin-up was observed for about 100 d followed by a gradual transition back to spin-down. About 20 d after the resumption

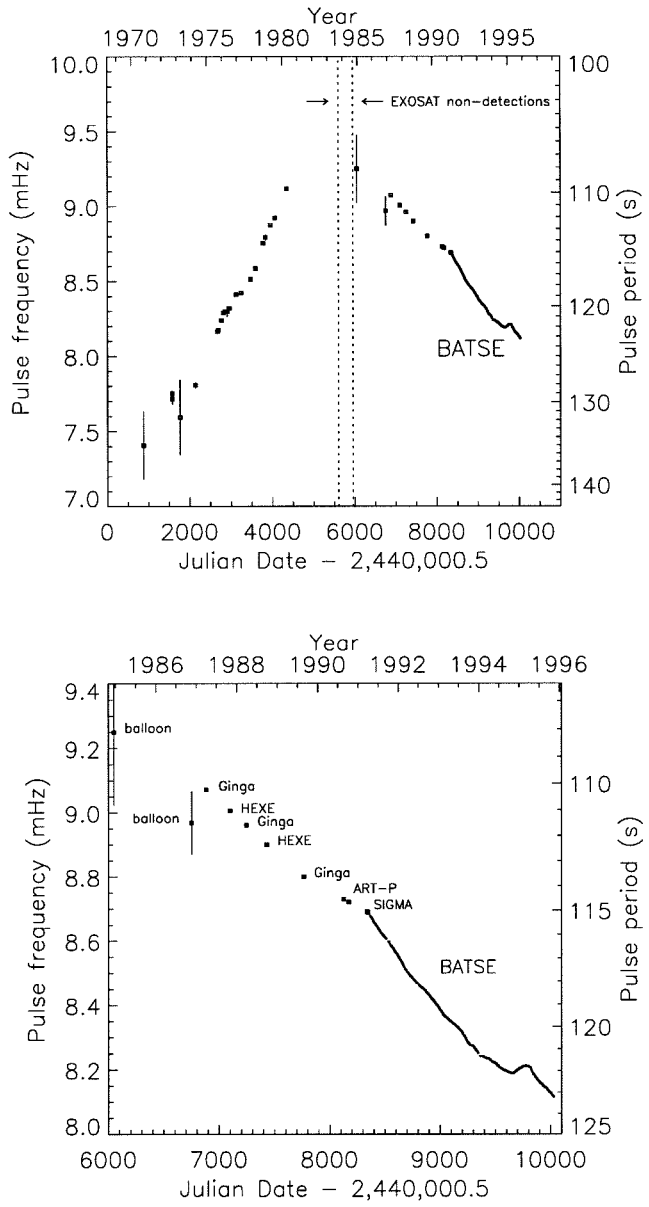

Figure 7.1: Pulse frequency history of GX 1+4 at the solar system barycenter. *Top panel:* Long-term history of the source since its discovery. *Bottom panel:* Detailed spin-down history. The data for both panels are collected in Appendix J. Observations taken by other instruments after the start of BATSE monitoring have been omitted from this figure for clarity, but are also included in Appendix J. These measurements agree with the BATSE data.

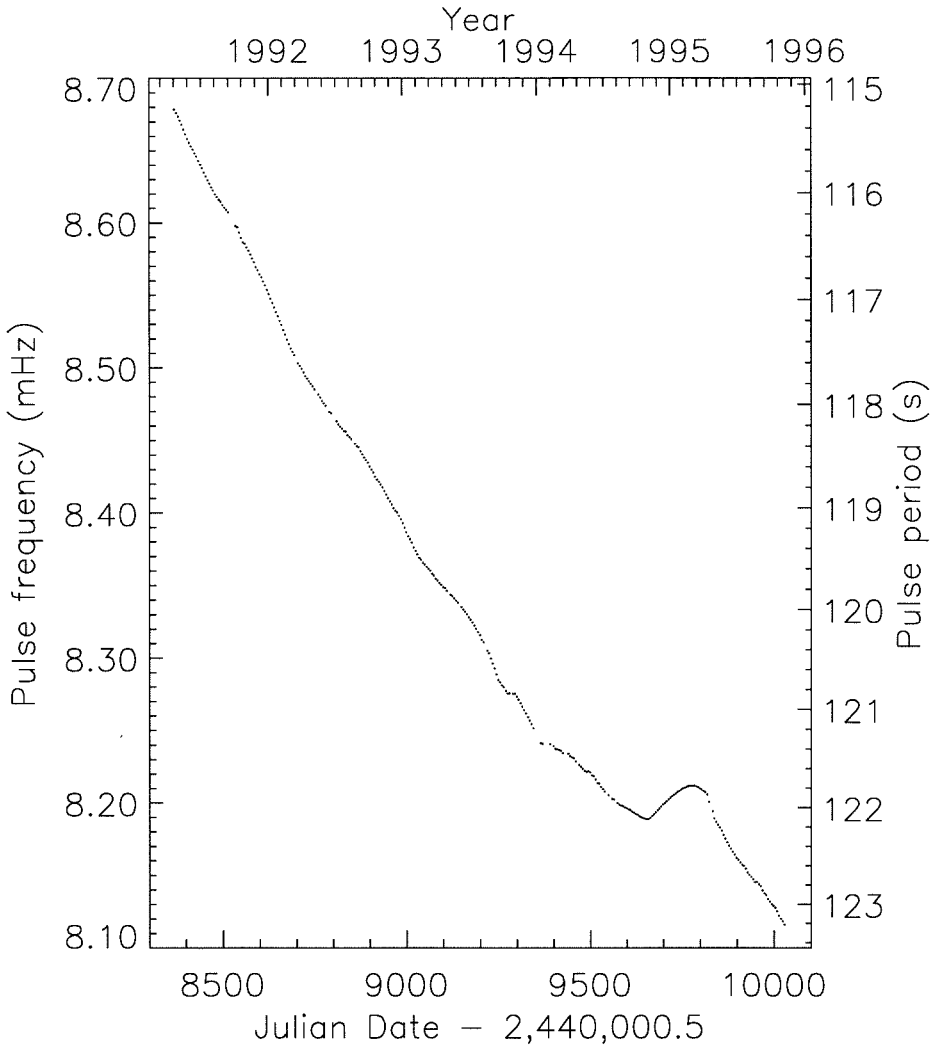

Figure 7.2: Detailed view of the BATSE pulse frequency history of GX 1+4.

of spin-down, there was a dramatic increase in the spin-down rate which then gradually relaxed over the next 100 d.

Despite the overall strong quadratic trend in the BATSE data, our pulse frequency measurements display significant systematic excursions. The BATSE pulse frequency residuals with respect to the best-fit quadratic frequency model are shown in Figure 7.4. The oscillatory excursions evident on a $\sim$ 300 d time scale are too large to be attributed to orbital Doppler shifts. If we take $\Delta\nu \sim 5\,\mu$Hz to be the Doppler amplitude of a $\sim$ 300 d

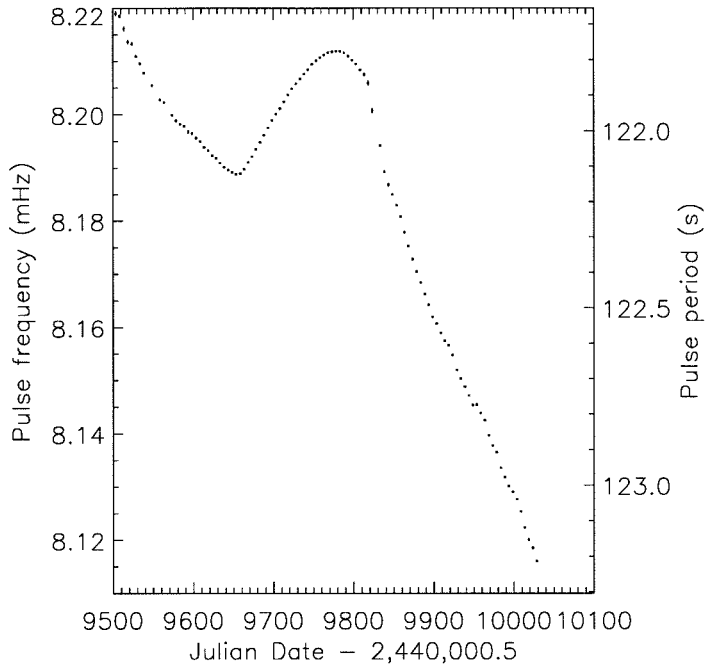

Figure 7.3: Pulse frequency history of two recent torque reversals in GX 1+4.

orbit, we obtain for the mass function

$$f_{\rm x}(M) \approx 200\ M_\odot \left(\frac{\Delta\nu}{5\ \mu{\rm Hz}}\right)^3 \left(\frac{P_{\rm orb}}{300\ {\rm d}}\right), \tag{7.1}$$

too massive for any stellar companion, let alone a red giant. The excursions are most likely due to variations in accretion torque. It is possible that the torques exhibit an orbital modulation, in which case the orbital period may still be $\sim$ 300 d. We note that Cutler et al. (1986) suggested the presence of a 304 d periodicity in the torque history of the 1970s spin-up era.

It is useful to characterize the statistical properties of the pulse frequency fluctuations. The strong correlations evident on long time scales indicate the presence of a strong "red noise" component (a power spectral component which rises with decreasing frequency) in the pulse frequency fluctuations. The presence of red noise can bias an unwindowed Fourier analysis of the power spectrum continuum due to power leakage through the broad sidelobe response of sinusoidal basis functions (Deeter & Boynton 1982). Spectral leakage can be suppressed (at a cost in frequency resolution) by judicious use of data windowing

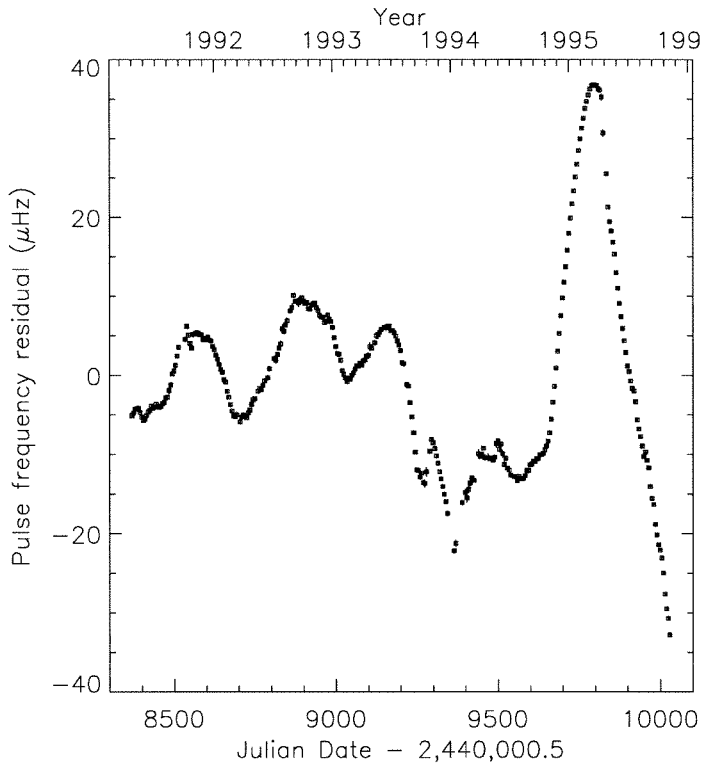

Figure 7.4: Pulse frequency residuals of GX 1+4 with respect to a best-fit quadratic frequency model.

(Harris 1978). Before computing the power spectrum, we multiplied the pulse frequency residuals by a window function of the form $w_j = \cos^4(j\pi/N)$ with $j = -N/2, \cdots, N/2$, substantially suppressing the sidelobe response of the Fourier transform (Harris 1978). To preserve the proper normalization, we rescaled the power spectrum by a factor $N/\sum w$.

The resulting power spectral density of the pulse frequency fluctuations P_ν is shown in the left panel of Figure 7.5. The spectrum at analysis frequencies $f < 4 \times 10^{-7}$ Hz varies as $P_\nu \propto f^{-2.80\pm0.17}$. The power spectrum for $f > 4 \times 10^{-7}$ Hz is dominated by the white noise process caused by the statistical uncertainties in the frequency measurements. (The measurement noise level indicated in the figure is not a fit to the power spectrum data but was calculated from the frequency measurement uncertainties.) Although our measurements were made with pulse frequencies, it is of physical interest to study the fluctuations in pulse frequency derivative since this quantity is proportional to the net torque on the neutron star. The power spectral density of fluctuations in pulse frequency derivative $P_{\dot\nu}$ is simply related to P_ν by $P_{\dot\nu} = (2\pi f)^2 P_\nu$ (see, e.g., Boynton 1981). This spectrum is shown in the

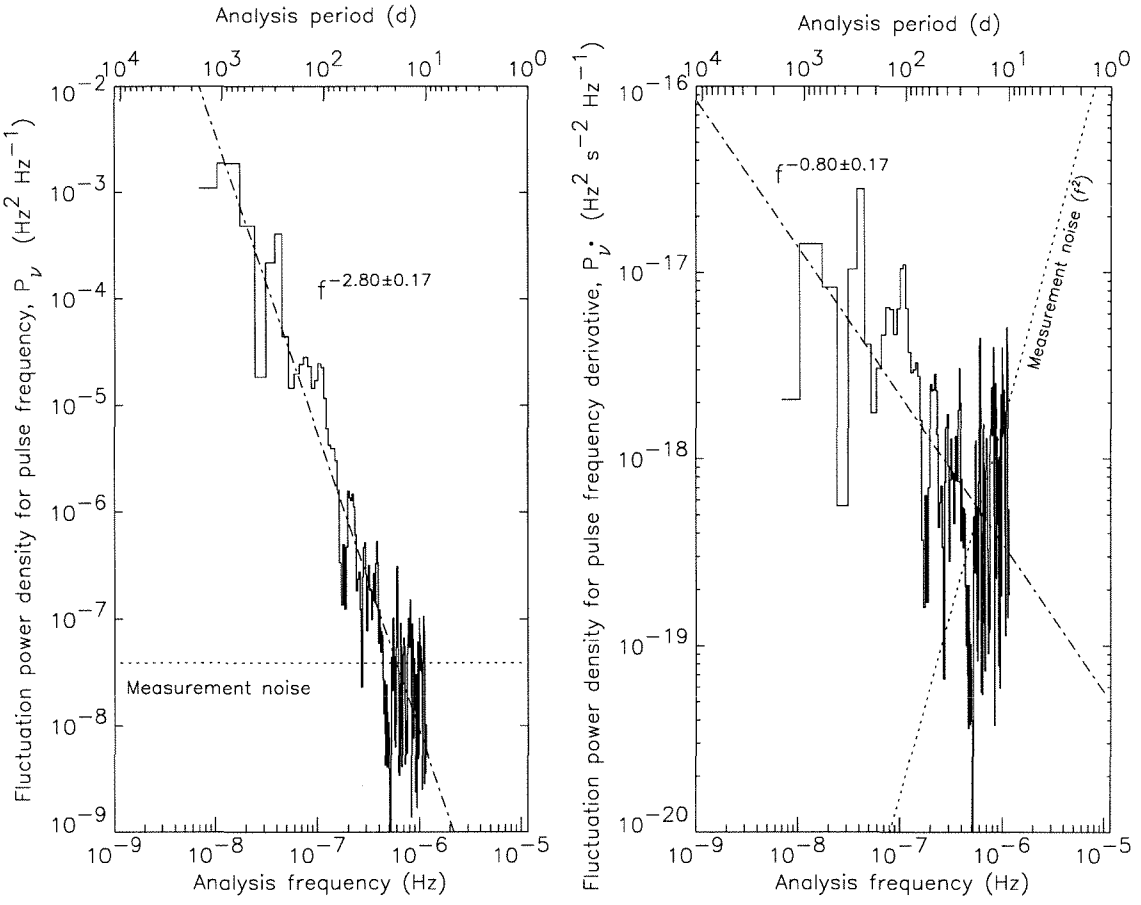

Figure 7.5: *Left panel:* Power spectrum of fluctuations in the pulse frequency. The white noise level expected for the frequency measurement uncertainties is indicated. *Right panel:* Corresponding power spectrum of fluctuations in the pulse frequency derivative $\dot{\nu}$. Our measurements are consistent with $1/f$ noise in the torque fluctuations.

right panel of Figure 7.5. There is evidently a $1/f$ red noise process in the torque fluctuation power for GX 1+4. This is similar to (although an order of magnitude weaker than) the torque fluctuations observed in Cen X-3 (Finger, Wilson, & Fishman 1994), but it is in marked contrast to the white noise torque processes observed in Her X-1 (Boynton 1981), Vela X-1 (Deeter et al. 1989), and 4U 1626–67 (Chapter 6). These systems are the only X-ray pulsars for which a detailed characterization of the torque noise process has been made.

7.2.2 Pulse Profiles and Spectroscopy

We measured the pulse-phase-averaged pulsed photon spectra for several different intensity states using the BATSE CONT data (16 energy channels at 2.048 s resolution).

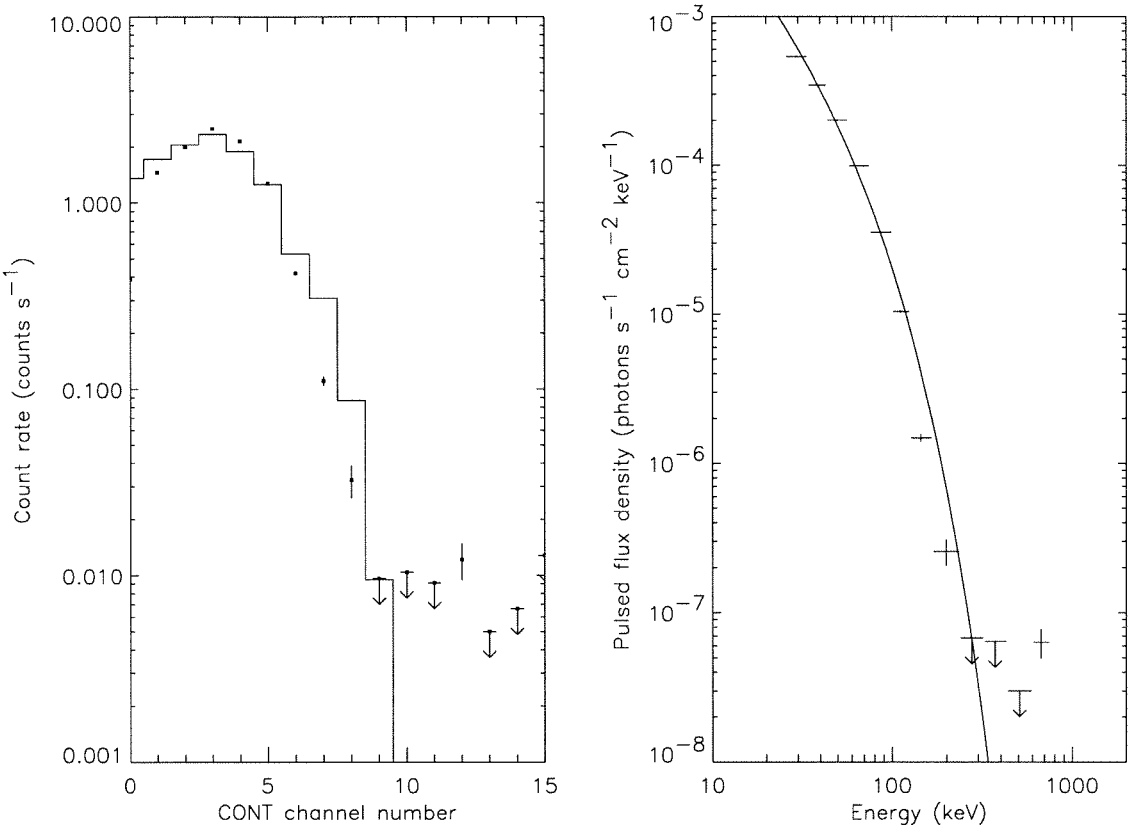

Figure 7.6: *Left panel:* The phase-averaged pulsed count spectrum of GX 1+4 during the bright spin-up state. *Right panel:* The corresponding photon spectra of GX 1+4. The vertical bars show the 1 σ statistical uncertainties, while the horizontal bars show the widths of the energy channels. Upper limits are quoted at 95% confidence. The solid curve shows the best-fit thermal bremsstrahlung spectrum. The data shown are for MJD 49618–49798 (1994 September 23–1995 March 22).

These data were background-subtracted using the BATSE background model of Rubin et al. 1996 (Rubin et al. 1996). Three intervals were chosen: the bright extended spin-up state during 1994 November–1995 March (MJD 49618–49798), a part of the bright 1993 September flare (MJD 49239–49251), and a relatively quiescent interval during 1993 January–April (MJD 49010–49100). The phase-averaged pulsed count rates were fit with

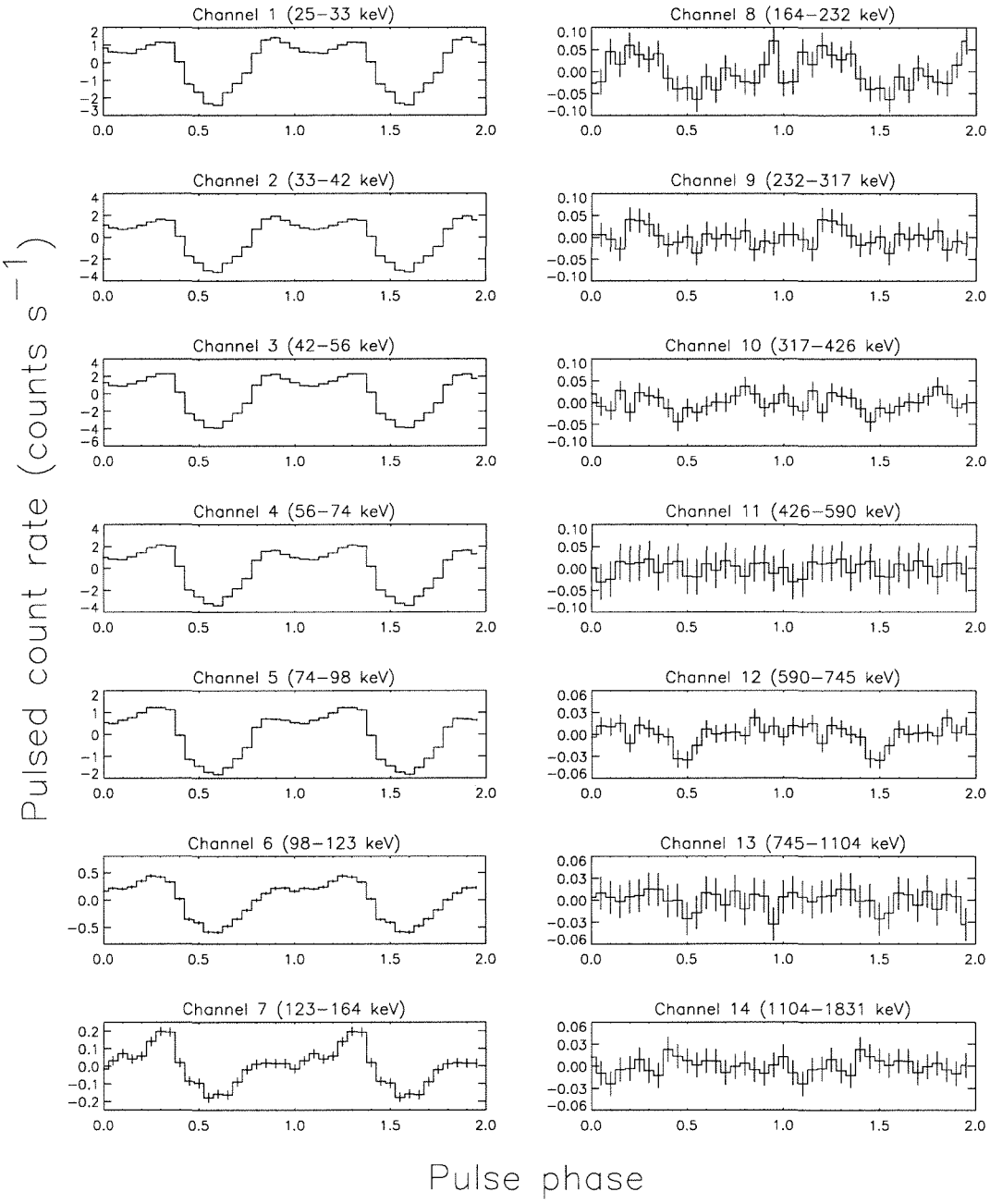

Figure 7.7: The pulse profile of GX 1+4 as a function of energy. Data shown are for the same dates as the previous figure.

Table 7.1. BATSE Pulsed Spectrum Fits for GX 1+4

Interval		kT	dN/dE at 70 keV	
Dates	MJD	(keV)	(ph cm^{-2} s^{-1} keV^{-1})	Remarks
1993 Jan 23–Apr 23	49010–49100	45.2 ± 1.3	$(1.86 \pm 0.06) \times 10^{-5}$	spin-down, low
1993 Sep 9–21	49239–49251	48.8 ± 2.1	$(6.9 \pm 0.3) \times 10^{-5}$	spin-down, flare
1994 Sep 23–1995 Mar 22	49618–49798	44.1 ± 0.2	$(7.19 \pm 0.04) \times 10^{-5}$	spin-up, high

NOTE: These fits assume optically-thin thermal bremsstrahlung pulsed emission.

an optically-thin thermal bremsstrahlung spectrum[2] of the form

$$\frac{dN}{dE} = \frac{C_0}{E}\,\bar{g}_{\rm ff}(E, kT)\,\exp(-E/kT), \tag{7.2}$$

where kT is a characteristic thermal energy and $\bar{g}_{\rm ff}$ is the velocity-averaged free-free Gaunt factor (Rybicki & Lightman 1979). The best-fit spectral parameters are given in Table 7.1. The spectral shape did not change appreciably between the different intensity states. The spectrum for the bright spin-up interval is shown in Figure 7.6. The corresponding pulse profiles are shown in Figure 7.7. Pulsed emission is clearly detected at energies up to 160 keV. An additional detection in the 590–745 keV channel has a formal significance of only 2.6σ.

The spectrum for the 1993 September flare is shown in Figure 7.8. A simultaneous measurement of the total (pulsed+unpulsed) spectrum of GX 1+4 in the 40–200 keV range was made with *Compton*/OSSE (Staubert et al. 1995). Before comparing the BATSE and OSSE spectra, two adjustments are required. First, a recent recalibration of the low-energy response of the OSSE detectors has found that observations reduced with the previous calibration underestimated the low-energy flux by an energy-dependent factor. The necessary correction factor is ≈ 1.2 at 50 keV and falls to unity at 100 keV (J. E. Grove 1995, personal communication). In addition, an intercomparison of BATSE and OSSE observations of the Crab Nebula has found that the BATSE fluxes are systematically $\approx$20% higher than the OSSE fluxes (Much et al. 1996). Note that this is the discrepancy *after* applying the low-energy correction to the OSSE data; the discrepancy would be worse without the

[2]A power-law model did not produce an acceptable fit; the photon spectrum falls too quickly at high energies. We adopted the bremsstrahlung model because it is a convenient parametrization which is in wide use by other observers of this source. However, we emphasize that our data are of insufficient quality to discriminate between thermal bremsstrahlung and other exponential spectra.

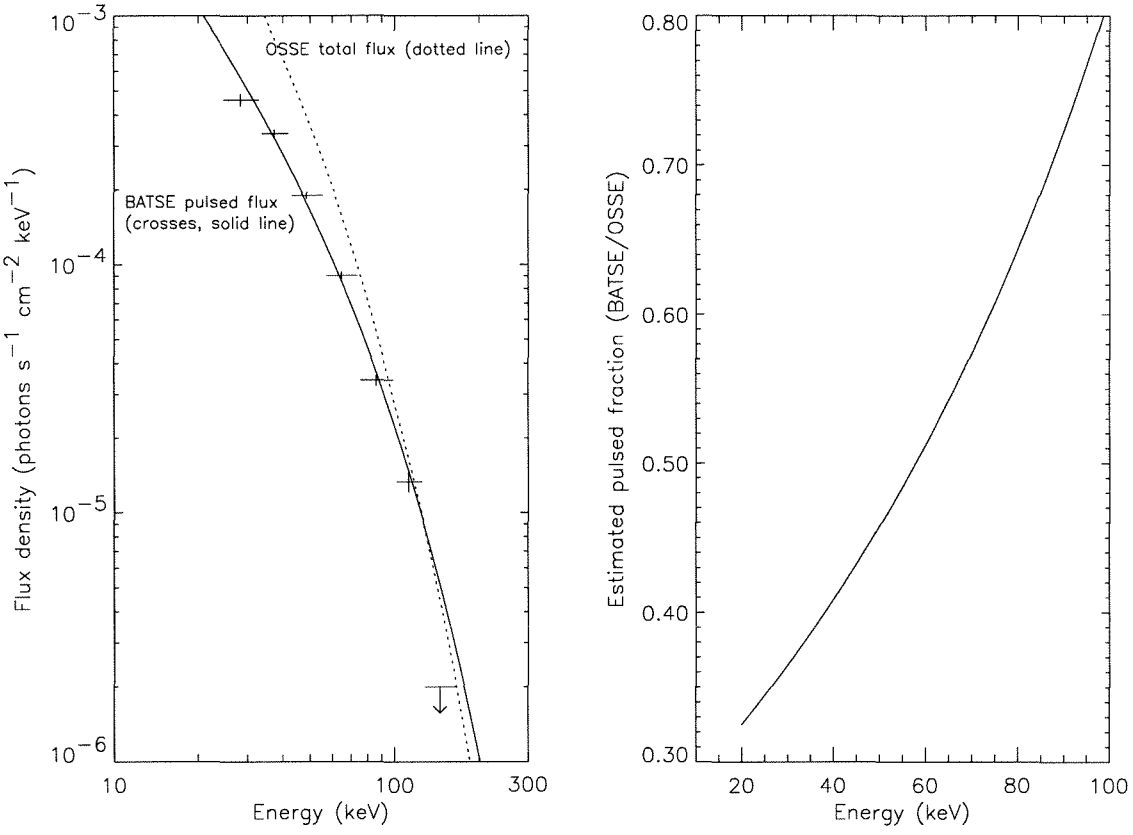

Figure 7.8: *Left panel:* Photon spectrum of the 1993 September flare of GX 1+4. The crosses show the BATSE measurements of the pulsed flux. The solid curve shows the best-fit thermal bremsstrahlung model for the BATSE observations. The dotted curve shows the best-fit model for simultaneous OSSE observations of the *total* (pulsed+unpulsed) flux, with corrections applied (see text for details). *Right panel:* Inferred pulsed fraction of GX 1+4 as a function of energy. This curve was computed by dividing the best-fit BATSE pulsed spectrum for the 1993 September flare by the best-fit OSSE total spectrum.

correction. The origin of this difference in overall normalization is unclear. However, to allow an intercomparison of the GX 1+4 spectra from the two instruments, we applied the low-energy correction to the Staubert et al. (1995) OSSE spectrum and then multiplied the entire OSSE spectrum by 1.2. This should place both spectra on the same scale, although the overall normalization may be 20% too large.

The best-fit thermal bremsstrahlung model for the OSSE data, corrected as described, is plotted as a dotted curve in the left panel of Figure 7.8. The BATSE and OSSE fits agree at 120 keV but diverge at lower energies, differing by more than a factor of 2 at 20 keV. (We cannot infer anything from the divergence above 100 keV since the BATSE

spectrum is unconstrained in this region.) The difference between the two spectra is consistent with previous observations which showed that pulsed fraction increases with energy for most X-ray pulsars, including GX 1+4 (see Frontera & Dal Fiume 1989). Since OSSE is not an imaging instrument, part of the discrepancy may be due to a problem in the subtraction of the low energy background from the Galactic center region. BATSE, a wide field instrument which is also non-imaging, suffers from the same problem for observations of the total flux. However, by restricting the BATSE analysis to the pulsed flux, we obtain a proper background subtraction automatically. If we assume that the OSSE background is properly subtracted in the Staubert et al. observation, then we can estimate the pulsed fraction of GX 1+4 as a function of energy by simply dividing the BATSE spectral fit by the corrected OSSE spectral fit. The resulting estimate for the 20–100 keV pulsed fraction, shown in the right panel of Figure 7.8, should be viewed with caution due to the several possible sources of systematic uncertainty.

7.2.3 Flux and Torque

We obtained a 20–60 keV pulsed flux history by folding five-day intervals of the DISCLA channel 1 data and correcting the resulting pulsed count rates for the BATSE instrumental response. Given that the spectrum of GX 1+4 does not change shape significantly (see above), we assumed a fixed 20–60 keV power law photon spectrum of the form $dN/dE \propto E^{-\gamma}$ with $\gamma = 2.5$. The resulting hard X-ray pulsed flux history is given in Appendix J and is shown in the top panel of Figure 7.9. For most of the *Compton* mission, the pulsed flux history can be described by a quiescent level of $\approx 2 \times 10^{-10}$ erg cm^{-2} s^{-1} with intermittent bright flares of $\sim$ 20 d duration superimposed. The centers or edges of some of these bright events are indicated by the vertical dotted lines in Figure 7.9. Around MJD 49638, GX 1+4 entered an extended bright state which lasted nearly 200 d, substantially longer than the usual flaring activity.

Flux measurements with BATSE suffer from the limitation that we measure only the pulsed component in a restricted energy range. The bolometric total X-ray flux is related to the BATSE pulsed flux by $F_{\rm bol} = \eta_1 \eta_2 F_{\rm BATSE}$, where η_1 and η_2 are bolometric correction factors. The first factor is the 20–60 keV inverse pulsed fraction,

$$\eta_1 = \frac{F_{\rm x}(\text{20–60 keV total})}{F_{\rm x}(\text{20–60 keV pulsed})}. \tag{7.3}$$

The second factor is an inverse hardness ratio,

$$\eta_2 = \frac{F_{\rm x}(\text{2–60 keV total})}{F_{\rm x}(\text{20–60 keV total})}. \tag{7.4}$$

Both η_1 and η_2 may vary with time. Repeated timing and spectroscopy with a broadband mission like the forthcoming *X-Ray Timing Explorer*[3] (Bradt, Swank, & Rothschild 1990) will be necessary to settle this question. However, if we assume that both factors are roughly constant, then we can estimate the bolometric correction for the BATSE data. Taking the pulsed fraction from Figure 7.8 and assuming that the incident 20–60 keV total photon spectrum is a power law with photon index 2.5, we find $\eta_1 \approx 2.7$. If we further assume that the incident 2–20 keV total photon spectrum is a power law with photon index 1.3, then we find $\eta_2 \approx 2.3$. Thus, we estimate that the bolometric correction factor for our BATSE pulsed flux measurements is $(\eta_1\eta_2) \approx 6$. This suggests that the brightest flux levels observed with BATSE are comparable to the bright states observed during spin-up in the 1970s.

In order to study the torque history of GX 1+4, we computed a running 3-point numerical derivative of the pulse frequency history. The resulting history of the pulse frequency derivative (i.e., the spin-up rate), which is proportional to the net torque applied to the neutron star if we can neglect orbital Doppler shifts, is shown in the middle panel of Figure 7.9. It is apparent that most of the bright flares were accompanied by enhanced spin down. We can write the net angular momentum transferred to the neutron star per unit mass of accreting matter as

$$\tilde{l}_{\rm net} = \frac{2\pi I\dot{\nu}}{\dot{M}} \tag{7.5}$$

$$= \frac{2\pi I\dot{\nu}GM_{\rm x}}{R_{\rm x}L_{\rm x}} \tag{7.6}$$

$$\approx 10^{18}\ {\rm cm^2\ s^{-1}} \left(\frac{\dot{\nu}}{10^{-12}\ {\rm Hz\ s^{-1}}}\right) \left(\frac{F_{\rm BATSE}}{10^{-10}\ {\rm erg\ cm^{-2}\ s^{-1}}}\right)^{-1} \left(\frac{\eta_1\eta_2}{6}\right)^{-1} \times \left(\frac{d}{4\ {\rm kpc}}\right)^{-2} \left(\frac{I}{10^{45}\ {\rm g\ cm^2}}\right) \left(\frac{M_{\rm x}}{1.4\,M_\odot}\right) \left(\frac{R_{\rm x}}{10\ {\rm km}}\right)^{-1}. \tag{7.7}$$

This quantity is plotted in the bottom panel of Figure 7.9. For comparison, the Keplerian specific angular momentum at the corotation radius is $\tilde{l}_{\rm co} = \sqrt{GM_{\rm x}r_{\rm co}} = 8.7\times10^{17}\ {\rm cm^2\ s^{-1}}$. The net angular momentum per unit mass transferred to the neutron star during spin-down maintained a remarkably stable mean value $\langle\tilde{l}_{\rm net}\rangle \approx -2\times10^{18}\ {\rm cm^2\ s^{-1}}$, even during the

[3]Launched on 1995 December 30.

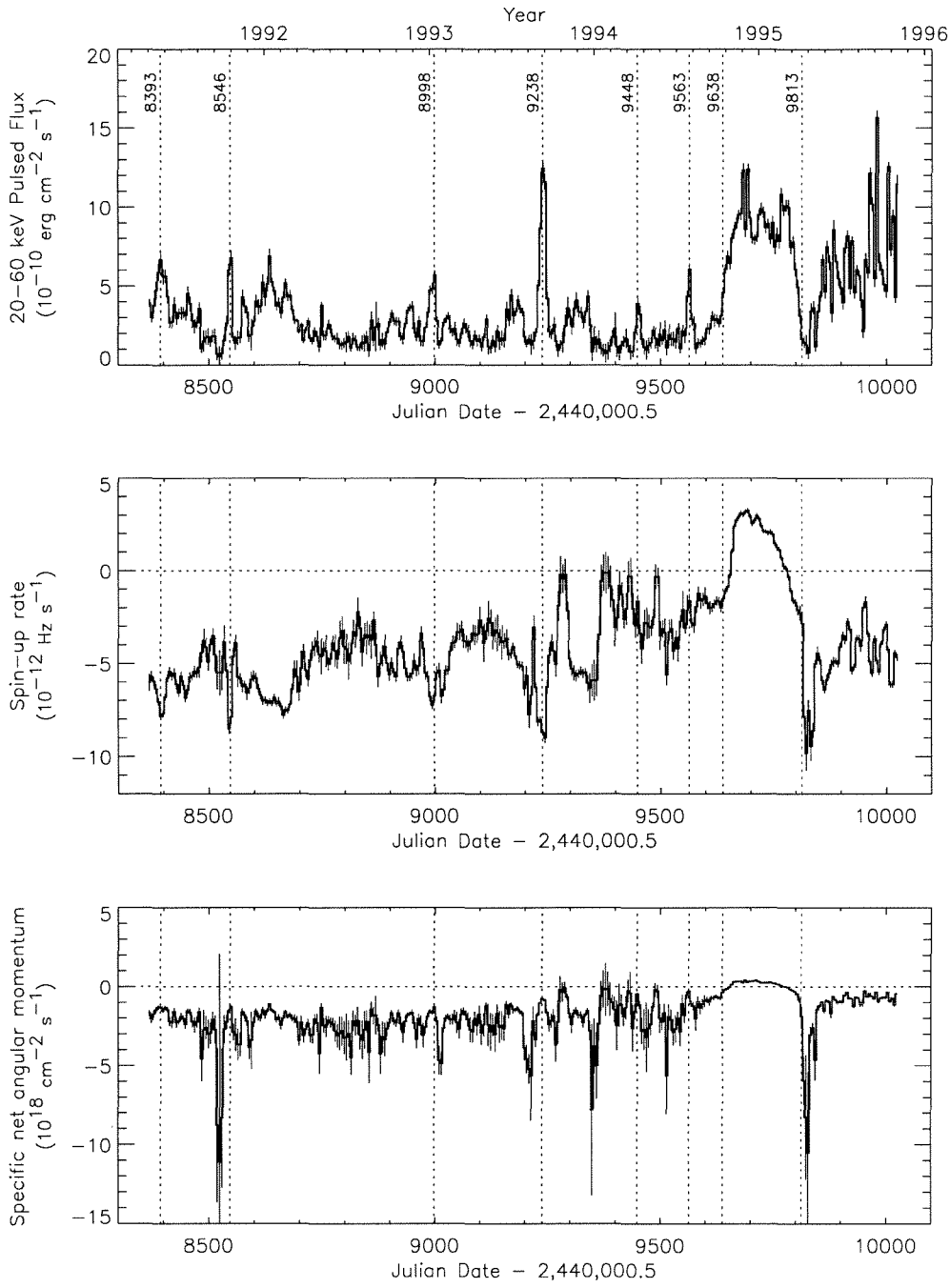

Figure 7.9: *Top panel:* BATSE 20–60 keV pulsed flux history for GX 1+4, averaged at 5-day intervals. *Middle panel:* Spin-up rate history of GX 1+4. *Bottom panel:* Net angular momentum transferred to GX 1+4 per unit accreted mass, using our estimated bolometric correction for the flux and assuming the source is 4 kpc distant.

bright spin-down flares. Most of the excursions from this mean have large uncertainties due to a low flux level. A few of the excursions, particularly the one around MJD 49813, have high statistical significance and are consistent with "propeller" expulsion of matter (Illarionov & Sunyaev 1975).

We can formalize the correlation between torque and luminosity by computing the cross-correlation of the two time series. We have done this separately for the long spin-down interval (MJD 48370–49610) and the spin-up interval (MJD 49620–49820). The resulting cross-correlation functions are shown in Figure 7.10. The spin-down data show a strong anticorrelation (i.e., negative correlation) of torque and luminosity with zero lag. Figure 7.11 plots the magnitude of the spin-down torque as a function of the observed flux during MJD 48370–49610. The correlation is clearly visible, but is evidently more complex than a power-law relationship. In contrast to the spin-down interval, the spin-up data show a strong *positive* correlation, also with zero lag (bottom panel of Figure 7.10).

7.3 Discussion

7.3.1 Accretion

There are several indications that the mass transfer in GX 1+4 is mediated by an accretion disk. The long ($\sim$ years) intervals of steady spin-up and spin-down are more typical of disk-fed accreters rather than of the more erratic wind-fed X-ray pulsars (see Nagase 1989; Prince et al. 1994). Also, optical emission line diagnostics indicate that there is an 8×10^4 K photoionization source in the system (Chakrabarty & Roche 1996). This is too cool to be the neutron star's emission and much too hot to be the M giant; however, it is consistent with emission from the outer parts of an accretion disk. Finally, the possible presence of a 4 mHz quasi-periodic oscillation (QPO) (Doty, Hoffman, & Lewin 1981) can be understood in the context of a magnetosphere-disk beat frequency QPO model (see van der Klis 1995). This evidence, along with our observation of a steady, uninterrupted transition between spin-down and spin-up and then back again, allows us to rule out the suggestion of Makishima et al. (1988) that the spin-down results from the disruption and reformation of accretion disks with opposite senses of rotation. There are no observational constraints, however, on whether GX 1+4 is a Roche-lobe-overflow system. It is plausible that the dense, subsonic wind of the M giant could form an accretion disk and supply enough matter to

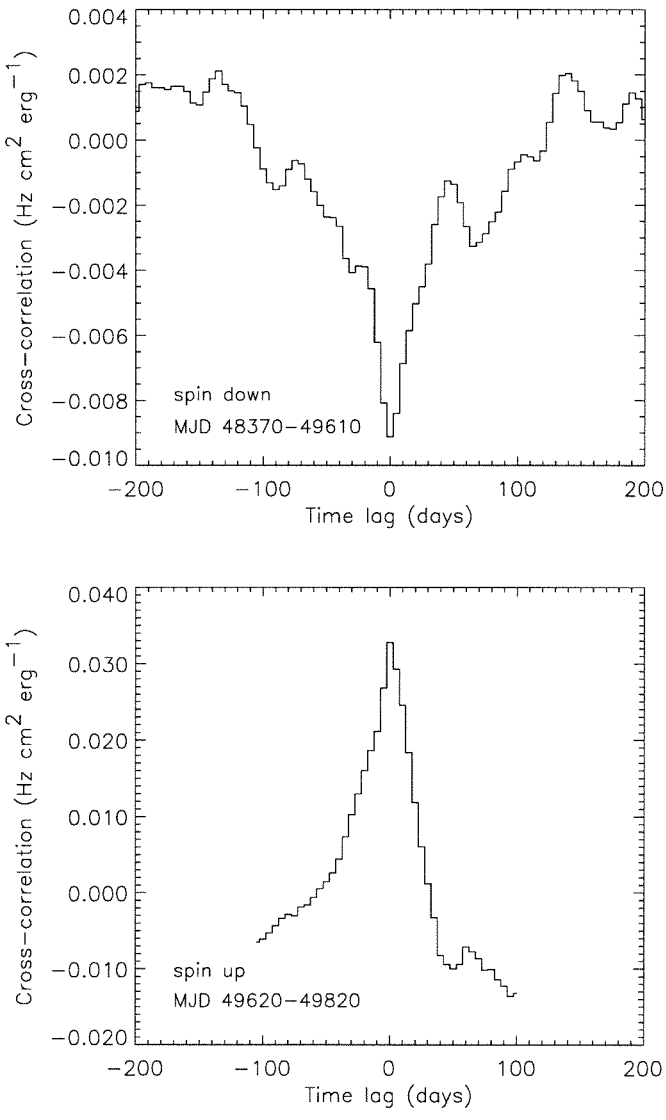

Figure 7.10: *Top panel:* Cross-correlation of $\dot{\nu}$ and pulsed flux during spin-down. There is a strong anticorrelation at zero lag. Data shown are from MJD 48370–49610. *Bottom panel:* Same cross-correlation, computed during the bright spin-up interval (MJD 49620–49820). There is a strong correlation at zero lag.

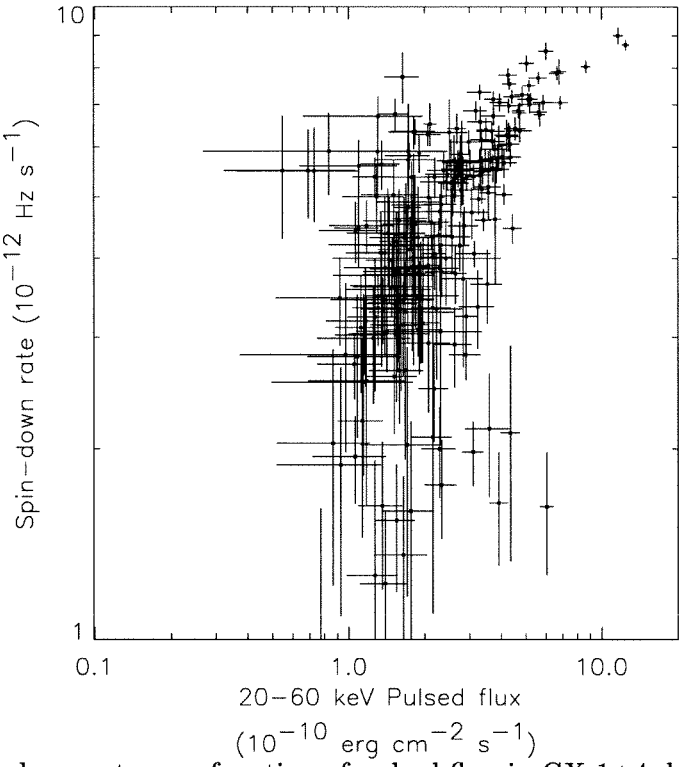

Figure 7.11: Spin-down rate as a function of pulsed flux in GX 1+4 during spin-down.

generate the observed luminosities.

In the context of magnetic disk accretion, our observations raise two major questions:

- **What triggers the torque reversals in GX 1+4?** Both the MTD and CDW accretion models predict that a sufficiently increased mass transfer rate can cause a transition from spin-down to spin-up, consistent with our observations of the sustained bright state around MJD 49600. Yet the bright flare centered at MJD 49238 reached similar luminosities without triggering a torque reversal from spin-down to spin-up; indeed, it was accompanied by enhanced spin-*down*, even though the duration of the flare was much longer than the time scale required for $r_{\rm m}$ to readjust to the higher mass accretion rate. Moreover, comparison of the BATSE flux history (with our estimated bolometric correction applied) with the 1970s flux monitoring from *Uhuru* and *Ariel-5* suggest that the mean bolometric luminosity we observe now is close to the value observed in the 1970s during spin-up.

- **Why are torque and luminosity anticorrelated in GX 1+4 during spin-down?** Except for the sustained bright state during MJD 49600–49800, all of the BATSE data display this anticorrelation, both during gradual intensity variations and during impulsive flares. This behavior is exactly the opposite of what the MTD and CDM models predict. Also, the start of the sustained bright spin-up state does not appear different in flux history from the start of the spin-down flares, and yet for the MJD 49600 brightening the transition toward spin-up began immediately. For consistency with the other data, we would expect at least an initial enhancement of the spin-down torque.

Both the MTD and CDW models are steady-state theories, so they may be unsuitable for explaining time-dependent behavior. A qualitatively different spin-down model may be required for this system. In trying to understand the relationship between torque and luminosity in accreting pulsars, however, it is important to bear in mind that GX 1+4 may be an exceptional rather than a typical case. Certainly, the red giant companion and the presence of a dense, subsonic stellar wind set it apart from other systems, and so the torque-luminosity anticorrelation may also be unique this system. However, there are some indications of similar anticorrelation in GX 301–2 occurring as a regular function of orbital phase (Koh et al. 1996).

7.3.2 System Parameters

GX 1+4 has been widely assumed to lie near the Galactic center at a distance of ≈ 10 kpc. However, the estimated visual extinction of the companion, $A_V \approx 5$ (Davidsen, Malina, & Bowyer 1977), suggests that the source is not quite so distant. We can place a lower limit on the distance and the X-ray luminosity from the steady spin-up of the source during the 1970s (see Appendix C). From the observed spin-up rate, we can infer

$$L_{\rm x} = \frac{GM_{\rm x}\dot{M}}{R_{\rm x}} \gtrsim 9 \times 10^{36}\ {\rm erg\ s^{-1}} \left(\frac{\dot{\nu}}{6 \times 10^{-12}\ {\rm Hz\ s^{-1}}}\right) \left(\frac{\nu}{8.5\ {\rm mHz}}\right)^{1/3}. \tag{7.8}$$

We can combine this with the bolometric X-ray flux measurement made during spin-up by *SAS-3*, $F_{\rm x} = 8 \times 10^{-9}$ erg cm^{-2} s^{-1} (1.5–55 keV; Doty, Hoffman, & Lewin 1981), to obtain

$$d \gtrsim 3\ {\rm kpc} \left(\frac{F_{\rm x}}{8 \times 10^{-9}\ {\rm erg\ cm^{-2}\ s^{-1}}}\right)^{-1/2}. \tag{7.9}$$

Moreover, a distance of ≈ 4 kpc is required to make the observed infrared colors of V2116 Oph (Glass 1979) consistent with those of a reddened M6 III giant. This implies that the

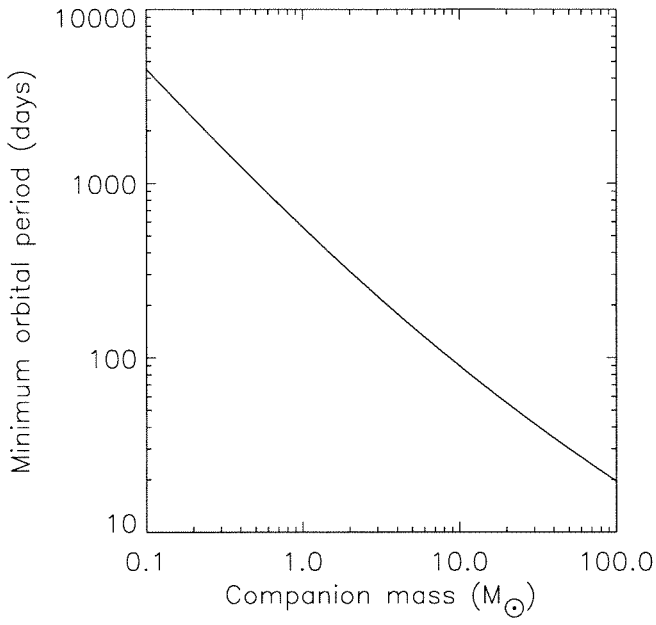

Figure 7.12: The minimum orbital period of GX 1+4 as a function of companion mass, assuming a distance of 4 kpc and that the red giant companion has radius 100 $R_\odot$ and fills its Roche lobe. If it is smaller than its Roche lobe, then the orbital period will exceed this minimum.

peak luminosity of GX 1+4 during the extended spin-up interval was $\sim 1.4 \times 10^{37}$ erg s^{-1} and that the quiescent luminosity during spin-down is $\sim 3 \times 10^{36}$ erg s^{-1}. The corresponding mass accretion rates are $1 \times 10^{-9}\, M_\odot$ yr^{-1} and $2.5 \times 10^{-10}\, M_\odot$ yr^{-1}, respectively. As other authors have pointed out previously (e.g., Makishima et al. 1988), the assumption that GX 1+4 is near its equilibrium spin frequency leads to a very high value for the surface magnetic field,

$$B \approx 10^{13}\ \mathrm{G} \left(\frac{\nu_{\mathrm{eq}}}{8.3\ \mathrm{mHz}}\right)^{6/7} \left(\frac{L_{\mathrm{x}}}{10^{37}\ \mathrm{erg\ s^{-1}}}\right)^{1/2}. \tag{7.10}$$

Our observations tend to support the equilibrium assumption.

We can use the observed infrared magnitudes (Glass 1979) and the spectroscopic classification (Davidsen, Malina, & Bowyer 1977) of V2116 Oph to parametrize the red giant's radius as

$$R_{\mathrm{c}} \approx 100 R_\odot \left(\frac{d}{4\ \mathrm{kpc}}\right) \left(\frac{T_{\mathrm{eff}}}{3200\ \mathrm{K}}\right)^{-2}, \tag{7.11}$$

where T_{eff} is the effective temperature of the red giant. If we assume that the companion is no larger than its Roche lobe, then we can calculate a lower limit on the orbital period

as a function of the companion's mass. Eggleton (1983) has computed an approximate relationship between Roche lobe radius $R_{\rm L}$ for a corotating star, orbital separation a, and the binary mass ratio $q = M_{\rm c}/M_{\rm x}$:

$$\frac{R_{\rm L}}{a} \approx \frac{0.49q^{2/3}}{0.6q^{2/3} + \ln(1+q^{1/3})}. \tag{7.12}$$

By taking $R_{\rm L} = R_{\rm c}$, we can use this to solve for the minimum allowed orbital separation and hence show that the orbital period must obey

$$P_{\rm orb} \gtrsim \left[\frac{4\pi^2 a_{\rm min}^3}{G(M_{\rm x}+M_{\rm c})}\right]^{1/2}. \tag{7.13}$$

For neutron star mass $M_{\rm x} = 1.4\ M_\odot$ and a companion mass range typical of M giants, the minimum allowed orbital period is ~years (see Figure 7.12). If the mass transfer is not occurring via Roche lobe overflow, the orbital period for a given companion mass could be higher than what we calculated.

Because the size of the torque fluctuations on time scales $\gtrsim$ 100 d is much larger than the expected orbital Doppler shifts, it is unlikely that X-ray timing observations will be able to determine the orbit of GX 1+4. On the other hand, if the accretion torque or the mass transfer rate has an orbitally-modulated component, a sufficiently long-term X-ray flux and/or torque history might be able to establish the orbital period. The $\sim$ 300 d time scale we observe in the pulse frequency residuals is intriguing, but will require a longer time baseline to check its coherence.

The red giant companion may be a more accessible target for orbital period studies. Some symbiotics show systematic variations in the Hα emission line profile as a function of orbital phase (Kenyon 1986). Sood et al. (1995) have established a high-resolution spectroscopy program monitoring the bright Hα emission from V2116 Oph to search for this effect. Another possible approach would be a radial velocity study in the infrared, where the V2116 Oph is bright and its absorption spectrum relatively uncontaminated by emission lines.

References

Arons, J., Burnard, D., Klein, R. I., McKee, C. F., Pudritz, R. E., & Lea, S. M. 1984. Accretion onto magnetized neutron stars: magnetospheric structure and stability. In *High Energy Transients in Astrophysics*, ed. S. E. Woosley (New York: AIP Press), 215.

Becker, R., Boldt, E., Holt, S., Pravdo, S., Rothschild, R., Serlemitsos, P., & Swank, J. 1976. Spectral variability in the X-ray pulsar GX 1+4. *Astrophys. J.*, **207**, L167.

Boynton, P. E. 1981. Pulsar timing and neutron star structure. In *Pulsars*, ed. W. Sieber & R. Wielebinski (Dordrecht: Reidel), 279.

Bradt, H. V., Swank, J. H., & Rothschild, R. E. 1990. The X-Ray Timing Explorer. *Adv. Space Res.*, **10**, (2)297.

Chakrabarty, D., Koh, T., Prince, T. A., Vaughan, B., Finger, M. H., Scott, M., & Wilson, R. B. 1995. GX 1+4. *IAU Circ.*, No. 6153. [see Appendix I]

Chakrabarty, D., Prince, T. A., Finger, M. H., & Wilson, R. B. 1994. GX 1+4. *IAU Circ.*, No. 6105. [see Appendix I]

Chakrabarty, D. & Roche, P. 1996, in preparation.

Cutler, E. P., Dennis, B. R., & Dolan, J. F. 1986. An elliptical binary orbit model of GX 1+4. *Astrophys. J.*, **300**, 551.

Davidsen, A., Malina, R., & Bowyer, S. 1977. The optical counterpart of GX 1+4: a symbiotic star. *Astrophys. J.*, **211**, 866.

Deeter, J. E. & Boynton, P. E. 1982. Techniques for the estimation of red power spectra. I. Context and methodology. *Astrophys. J.*, **261**, 337.

Deeter, J. E., Boynton, P. E., Lamb, F. K., & Zylstra, G. 1989. Vela X-1 pulse timing. II. Variations in pulse frequency. *Astrophys. J.*, **336**, 376.

Dotani, T., Kii, T., Nagase, F., Makishima, K., Ohashi, T., Sakao, T., Koyama, K., & Tuohy, I. R. 1989. Peculiar pulse profile of GX 1+4 observed in the spin-down phase. *Pub. Astron. Soc. Japan*, **41**, 427.

Doty, J., Hoffman, J., & Lewin, W. H. G. 1981. SAS-3 observations of GX 1+4. *Astrophys. J.*, **243**, 257.

Doxsey, R. E., Apparao, K. M. V., Bradt, H. V., Dower, R. G., & Jernigan, J. G. 1977. Positions of Galactic X-ray sources: $0° < l^{II} < 20°$. *Nature*, 270, 586.

Eggleton, P. P. 1983. Approximations to the radii of Roche lobes. *Astrophys. J.*, **268**, 368.

Finger, M. H. et al. 1993. GX 1+4. *IAU Circ.*, No. 5859.

Finger, M. H., Wilson, R. B., & Fishman, G. J. 1994. Observations of accretion torques in Cen X-3. In *Second Compton Symposium*, ed. C. E. Fichtel, N. Gehrels, & J. P. Norris (New York: AIP Press), 304.

Finger, M. H., Wilson, R. B., & Harmon, B. A. 1996. Quasi-periodic oscillations during a giant outburst of A0535+26. *Astrophys. J.*, in press.

Fishman, G. J. et al. 1989. BATSE: the Burst and Transient Source Experiment on the Compton Gamma Ray Observatory. In *Proc. of the GRO Science Workshop*, ed. W. N. Johnson (Greenbelt: NASA/GSFC), 2-39.

Forman, W., Jones, C., Cominsky, L., Julien, P., Murray, S., Peters, G., Tananbaum, H., & Giacconi, R. 1978. The fourth Uhuru catalog of X-ray sources. *Astrophys. J. Suppl.*, **38**, 357.

Frontera, F. & Dal Fiume, D. 1989. High energy properties of X-ray pulsars. In *Proc. 23rd ESLAB Symp. of Two Topics in X-Ray Astronomy*, Vol. 1, ed. N. White (Paris: ESA), 57.

Ghosh, P. & Lamb, F. K. 1979a. Accretion by rotating magnetic neutron stars. II. Radial and vertical structure in the transition zone in disk accretion. *Astrophys. J.*, **232**, 259.

Ghosh, P. & Lamb, F. K. 1979b. Accretion by rotating magnetic neutron stars. III. Accretion torques and period changes in pulsating X-ray sources. *Astrophys. J.*, **234**, 296.

Glass, I. S. 1979. Infrared observations of Galactic X-ray sources. *Mon. Not. R. Astron. Soc.*, **187**, 807.

Glass, I. S. & Feast, M. W. 1973. Peculiar object near GX 2+5. *Nature Phys. Sci.*, **245**, 39.

Gotthelf, E., Halpern, J., & Szentgyorgyi, A. 1988. GX 1+4. *IAU Circ.*, No. 4635.

Greenhill, J. G., Watson, R. D., Tobin, W., Pritchard, J. D., & Clark, M. 1995. Hα monitoring of the X-ray pulsar GX 1+4 during an X-ray flare. *Mon. Not. R. Astron. Soc.*, **274**, L59.

Hall, R. & Davelaar, J. 1983. GX 1+4. *IAU Circ.*, No. 3872.

Harris, F. J. 1978. On the use of windows for harmonic analysis with the discrete Fourier transform. *Proc. IEEE*, **66**, 51.

Illarionov, A. F. & Kompaneets, D. A. 1990. A spin-down mechanism for accreting neutron stars. *Mon. Not. R. Astron. Soc.*, **247**, 219.

Illarionov, A. F. & Sunyaev, R. A. 1975. Why the number of Galactic X-ray stars is so small? *Astron. & Astrophys.*, **39**, 185.

Kendziorra, E., Staubert, R., Reppin, C., Pietsch, W., Voges, W., & Trumper, J. 1982. The pulsating X-ray source GX 1+4 (4U 1728–24). In *Galactic X-Ray Sources*, ed. P. Sanford, P. Laskarides, & J. Salton (New York: Wiley), 205.

Kenyon, S. J. 1986. *The Symbiotic Stars* (Cambridge: Cambridge Univ. Press).

King, A. 1995. Accretion in close binaries. In *X-Ray Binaries*, ed. W. H. G. Lewin, J. van Paradijs, & E. P. J. van den Heuvel (Cambridge: Cambridge U. Press), 419.

Koh, T. et al. 1996. BATSE observations of the accreting X-ray pulsar GX 301–2. *Astrophys. J.*, in preparation.

Lamb, F. K., Pethick, C. J., & Pines, D. 1973. A model for compact X-ray sources: accretion by rotating magnetic stars. *Astrophys. J.*, **184**, 271.

Lewin, W. H. G., Ricker, G. R., & McClintock, J. E. 1971. X-rays from a new variable source GX 1+4. *Astrophys. J.*, **169**, L17.

Lovelace, R. V. E., Romanova, M. M., & Bisnovatyi-Kogan, G. S. 1995. Spin-up/spin-down of magnetized stars with accretion discs and outflows. *Mon. Not. R. Astron. Soc.*, **275**, 244.

Makishima, K. et al. 1988. Spin-down of the X-ray pulsar GX 1+4 during an extended low state. *Nature*, **333**, 746.

Manchanda, R. K., James, S. D., Lawson, W. A., Sood, R. K., Grey, D. J., & Sharma, D. P. 1995. An X-ray correlated Hα flare in GX 1+4. *Astron. & Astrophys.*, **293**, L29.

McClintock, J. E. & Leventhal, M. 1989. Is GX 1+4 the compact 511 keV Galactic center source? *Astrophys. J.*, **346**, 143.

Much, R. et al. 1996. The Crab total gamma-ray emission as seen by CGRO. *Astron. & Astrophys.*, in press.

Nagase, F. 1989. Accretion-powered X-ray pulsars. *Pub. Astron. Soc. Japan*, **41**, 1.

Patterson, J. 1994. The DQ Herculis stars. *Pub. Astron. Soc. Pacific*, **108**, 209.

Predehl, P., Friedrich, S., & Staubert, R. 1995. ROSAT observation of GX 1+4. *Astron. & Astrophys.*, **295**, L33.

Prince, T. A., Bildsten, L., Chakrabarty, D., Wilson, R. B., & Finger, M. H. 1994. Observations of accreting pulsars. In *Evolution of X-Ray Binaries*, ed. S. S. Holt & C. S. Day (New York: AIP Press), 235.

Pringle, J. E. & Rees, M. J. 1972. Accretion disc models for compact X-ray sources. *Astron. & Astrophys.*, **21**, 1.

Ricker, G. R., Gerassimenko, M., McClintock, J. E., Ryckman, S. G., & Lewin, W. H. G. 1976. High energy X-ray observations of the southern sky. *Astrophys. J.*, **207**, 333.

Rybicki, G. J. & Lightman, A. P. 1979. *Radiative Processes in Astrophysics* (New York: Wiley).

Sood, R. K. et al. 1991. GX 1+4. *IAU Circ.*, No. 5381.

Sood, R. K., James, S. D., Lawson, W. A., Sharma, D. P., & Manchanda, R. K. 1995. The orbital period of the X-ray binary GX 1+4. *Adv. Space Res.*, **16**, (3)131.

Staubert, R., Maisack, M., Kendziorra, E., Draxler, T., Finger, M. H., Fishman, G. J., Strickman, M. S., & Starr, C. H. 1995. Observations of a large flare in GX 1+4 with the Compton Gamma Ray Observatory. *Adv. Space Res.*, **15**, (5)119.

van der Klis, M. 1995. Rapid aperiodic variability in X-ray binaries. In *X-Ray Binaries*, ed. W. H. G. Lewin, J. van Paradijs, & E. P. J. van den Heuvel (Cambridge: Cambridge U. Press), 252.

Wang, Y. M. 1987. Disc accretion by magnetized neutron stars: a reassessment of the torque. *Astron. & Astrophys.*, **183**, 257.

Wang, Y. M. 1995. On the torque exerted by a magnetically threaded accretion disk. *Astrophys. J.*, **449**, L153.

White, N. E., Nagase, F., & Parmar, A. N. 1995. The properties of X-ray binaries. In *X-Ray Binaries*, ed. W. H. G. Lewin, J. van Paradijs, & E. P. J. van den Heuvel (Cambridge: Cambridge U. Press), 1.

Whitelock, P. A. 1984. GX 1+4. *IAU Circ.*, No. 3919.

Whitelock, P. A., Menzies, J. W., & Feast, M. W. 1983. GX 1+4. *IAU Circ.*, No. 3885.

Appendix A

Spacecraft Coordinates and Sky Coordinates

The fundamental coordinate system for *Compton* observations is defined by the spacecraft xyz-axes (see Figure A.1). The orientation of the spacecraft with respect to the sky is specified in terms of the right ascension (α) and declination (δ) of the x and z-axes of the spacecraft. Let us denote the J2000.0 celestial equatorial direction vector of a celestial source as $\mathbf{r}$ and the spacecraft direction vector of the same source as $\mathbf{r}'$. We can transform between these systems using

$$\mathbf{r} = \begin{bmatrix} x \\ y \\ z \end{bmatrix} = \begin{bmatrix} \lambda_1 & \lambda_2 & \lambda_3 \\ \mu_1 & \mu_2 & \mu_3 \\ \nu_1 & \nu_2 & \nu_3 \end{bmatrix} \begin{bmatrix} x' \\ y' \\ z' \end{bmatrix} \tag{A.1}$$

$$\mathbf{r}' = \begin{bmatrix} x' \\ y' \\ z' \end{bmatrix} = \begin{bmatrix} \lambda_1 & \mu_1 & \nu_1 \\ \lambda_2 & \mu_2 & \nu_2 \\ \lambda_3 & \mu_3 & \nu_3 \end{bmatrix} \begin{bmatrix} x \\ y \\ z \end{bmatrix}, \tag{A.2}$$

where the direction cosines for the spacecraft x and z axes are given by

$$\begin{aligned} \lambda_1 &= \cos\delta_x \cos\alpha_x & \lambda_3 &= \cos\delta_z \cos\alpha_z \\ \mu_1 &= \cos\delta_x \sin\alpha_x & \mu_3 &= \cos\delta_z \sin\alpha_z \\ \nu_1 &= \sin\delta_x & \nu_3 &= \sin\delta_z, \end{aligned} \tag{A.3}$$

and the direction cosines for the y-axis are given by

$$\lambda_2 = \mu_3\nu_1 - \nu_3\mu_1 \tag{A.4}$$

$$\mu_2 = \nu_3\lambda_1 - \lambda_3\nu_1$$

$$\nu_2 = \lambda_3\mu_1 - \mu_3\lambda_1. \tag{A.5}$$

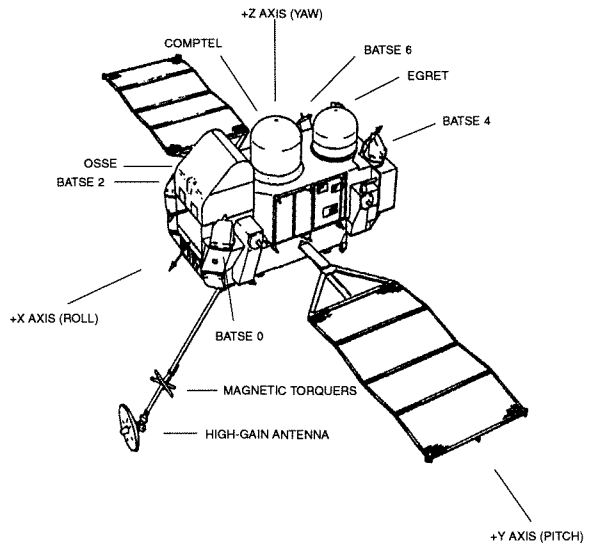

Figure A.1: Spacecraft axes for the *Compton Gamma Ray Observatory*. The 8 BATSE detector modules are situated on the corners of the spacecraft's main body. Modules 0, 2, 4, and 6 are visible in this diagram.

Table A.1. Spacecraft Direction Vectors for BATSE Detector Normals

Detector	$\hat{\mathbf{x}}$	$\hat{\mathbf{y}}$	$\hat{\mathbf{z}}$
0	$1/\sqrt{3}$	$1/\sqrt{3}$	$1/\sqrt{3}$
1	$1/\sqrt{3}$	$1/\sqrt{3}$	$-1/\sqrt{3}$
2	$1/\sqrt{3}$	$-1/\sqrt{3}$	$1/\sqrt{3}$
3	$1/\sqrt{3}$	$-1/\sqrt{3}$	$-1/\sqrt{3}$
4	$-1/\sqrt{3}$	$1/\sqrt{3}$	$1/\sqrt{3}$
5	$-1/\sqrt{3}$	$1/\sqrt{3}$	$-1/\sqrt{3}$
6	$-1/\sqrt{3}$	$-1/\sqrt{3}$	$1/\sqrt{3}$
7	$-1/\sqrt{3}$	$-1/\sqrt{3}$	$-1/\sqrt{3}$

The relations between (x, y, z) and (α, δ) are

$$\begin{aligned} x &= \cos\delta\cos\alpha \qquad \alpha = \tan^{-1}(y/x) \\ y &= \cos\delta\sin\alpha \qquad \delta = \tan^{-1}(z/\sqrt{x^2+y^2}) \\ z &= \sin\delta. \end{aligned} \tag{A.6}$$

The vectors for the BATSE detector normals in spacecraft coordinates are given in Table A.1. The sky coordinates for the spacecraft axes for each of the *Compton Observatory* pointings are given in Table A.2.

Table A.2. *Compton Observatory* Pointing Table

Viewing Period	Starting Epoch Date	MJD	Pointed Target	z-axis α_z (°)	z-axis δ_z (°)	x-axis α_x (°)	x-axis δ_x (°)
Verification							
0.1	1991 Apr 15	48361	Testing	108.12	−6.52	19.04	8.05
Phase 1							
0.2	1991 Apr 22	48368	Crab pulsar	86.76	22.09	357.03	−0.66
0.3	1991 Apr 28	48374	Crab pulsar	89.77	15.24	342.47	47.50
0.4	1991 May 1	48377	Crab pulsar	89.77	15.24	12.32	−38.58
0.5	1991 May 4	48380	Crab pulsar	83.52	22.02	354.10	−1.42
0.6	1991 May 7	48383	N. Gal hole	162.44	57.26	68.08	2.80
0.7	1991 May 10	48386	Vela pulsar	135.19	−45.11	81.50	30.54
1	1991 May 16	48392	Crab pulsar	88.07	17.14	339.12	46.48
2	1991 May 30	48406	Cyg X-1	301.39	36.58	60.31	33.09
2.5	1991 Jun 8	48415	Sun	87.83	12.47	338.68	56.03
3	1991 Jun 15	48422	SN 1991T	191.54	2.62	101.49	1.04
4	1991 Jun 28	48435	NGC 4151	179.84	41.52	57.38	31.23
5	1991 Jul 12	48449	Gal center	270.39	−30.96	196.56	24.91
6	1991 Jul 26	48463	SN 1987A	91.28	−67.97	153.97	10.52
7.0	1991 Aug 8	48476	Cyg X-1	310.05	28.06	143.74	61.25
7.5	1991 Aug 15	48483	Gal plane 25	291.98	−13.27	208.11	24.38
8	1991 Aug 22	48490	Vela pulsar	124.96	−46.35	198.99	14.71
9.0	1991 Sep 5	48504	GX 339–4	8.34	−32.31	244.20	−41.58
9.5	1991 Sep 12	48511	Her X-1	251.28	36.89	142.05	23.69
10	1991 Sep 19	48518	N Mus	30.91	−60.66	190.28	−27.75
11	1991 Oct 3	48532	3C 273	189.02	1.06	278.42	−29.71
12	1991 Oct 17	48546	Cen A	202.29	−40.09	221.48	48.29
13.0	1991 Oct 31	48560	Gal plane 25	291.98	−13.27	208.11	24.38
13.5	1991 Nov 7	48567	GX 339–4	8.34	−32.31	244.20	−41.58
14	1991 Nov 14	48574	Gal center	156.83	−58.51	274.30	−15.78
15	1991 Nov 28	48588	NGC 1275	52.00	40.24	293.36	29.53
16	1991 Dec 12	48602	Gal center	248.36	−17.20	351.62	−36.55
17	1991 Dec 27	48617	SN 1987A	83.48	−72.27	266.22	−17.72
18	1992 Jan 10	48631	M82	154.61	72.04	292.51	13.52
19	1992 Jan 23	48644	Gal plane	331.40	−1.93	242.82	36.31
20	1992 Feb 6	48658	SS 433	285.28	6.37	12.01	−27.04
21	1992 Feb 20	48672	Gal center	39.09	−1.24	308.14	−37.66
22	1992 Mar 5	48686	N Cyg 1992	216.00	70.74	329.43	7.91
23	1992 Mar 19	48700	Cir X-1	227.43	−54.62	11.72	−29.97
24.0	1992 Apr 2	48714	Gal center	223.34	11.03	302.52	−43.94
24.5	1992 Apr 9	48721	Gal plane 5	223.34	11.03	304.56	−38.07
25	1992 Apr 16	48728	Gal center	229.85	4.47	315.25	−45.69
26	1992 Apr 23	48735	Mrk 335	1.59	20.20	73.89	−39.58
27	1992 Apr 28	48740	4U 1543–47	241.11	−49.06	348.99	−14.92
28	1992 May 7	48749	Mrk 335	1.59	20.20	73.89	−39.58
29	1992 May 14	48756	3C 390.3	68.97	−25.09	53.03	64.04
30	1992 Jun 4	48777	NGC 2992	149.50	−14.73	61.41	7.22
31	1992 Jun 11	48784	MCG +8-11-11	88.87	49.44	86.22	−40.53
32	1992 Jun 25	48798	NGC 3783	171.17	−36.81	92.97	15.28

Table A.2—Continued

Viewing Period	Starting Epoch Date	MJD	Pointed Target	z-axis α_z (°)	z-axis δ_z (°)	x-axis α_x (°)	x-axis δ_x (°)
33	1992 Jul 2	48805	NGC 2992	149.50	−14.73	61.41	7.22
34	1992 Jul 16	48819	Cas A	345.77	57.49	100.24	14.79
35	1992 Aug 6	48840	ESO 141–55	287.12	−61.21	144.32	−23.64
36.0	1992 Aug 11	48845	GRO J0422+32	68.99	30.42	141.11	−27.60
36.5	1992 Aug 12	48846	GRO J0422+32	69.39	32.90	168.57	13.86
37	1992 Aug 20	48854	GRO J0422+32	358.75	18.82	98.42	26.22
38	1992 Aug 27	48861	ESO 141–55	287.12	−61.21	144.32	−23.64
39	1992 Sep 1	48866	GRO J0422+32	68.87	33.82	168.45	13.95
40	1992 Sep 17	48882	NGC 4388	140.88	30.40	224.38	−10.90
41	1992 Oct 8	48903	MCG -6-30-15	112.43	−12.05	210.43	−33.09
42	1992 Oct 15	48910	PKS 2155-304	319.72	−41.67	189.66	−35.87
43	1992 Oct 29	48924	Mrk 509	307.83	−13.95	204.08	−43.75
44	1992 Nov 3	48929	MCG -6-30-15	112.43	−12.05	210.43	−33.09
Phase 2							
201	1992 Nov 17	48943	Her X-1	253.15	42.26	266.02	−47.01
202	1992 Nov 24	48950	Her X-1	251.55	45.40	270.04	−43.08
203.0	1992 Dec 01	48957	Cygnus	306.59	39.34	258.44	−39.15
203.3	1992 Dec 08	48964	Cygnus	306.59	39.34	264.05	−41.96
203.6	1992 Dec 15	48971	Cygnus	306.59	39.34	258.44	−39.15
204	1992 Dec 22	48978	3C 273	188.99	−0.74	279.50	−34.03
205	1992 Dec 29	48985	3C 273	188.84	−1.03	279.32	−24.79
206	1993 Jan 05	48992	3C 273	188.99	−0.74	279.50	−34.30
207	1993 Jan 12	48999	IC 4329A	203.86	−30.41	293.35	0.86
208	1993 Feb 02	49020	NGC 4507	198.47	−41.93	296.86	−9.24
209	1993 Feb 09	49027	2CG 010-31	305.69	−40.81	297.95	48.93
210	1993 Feb 22	49040	Gal center	257.65	−29.10	351.03	−6.03
211	1993 Feb 25	49043	Gal 123-05	18.38	58.05	8.08	−31.53
212	1993 Mar 09	49055	WR 140	298.65	50.54	341.61	−31.07
213	1993 Mar 23	49069	Crab pulsar	80.30	22.29	348.47	4.44
214	1993 Mar 29	49075	Gal center	257.65	−29.10	351.03	−6.03
215	1993 Apr 01	49078	Cen A	203.26	−39.28	53.56	−46.55
216	1993 Apr 06	49083	SN 1993J	143.64	71.46	3.37	14.47
217	1993 Apr 12	49089	Cen A	203.26	−39.28	53.56	−46.55
218	1993 Apr 20	49097	NGC 4151	180.75	43.09	31.04	42.71
219.1	1993 May 04	49111	REBOOST THRUSTER TESTING				
219.4	1993 May 05	49112	Gal center	245.35	−27.22	341.26	−11.31
219.7	1993 May 07	49114	REBOOST CALIBRATION BURN				
220	1993 May 08	49115	SMC	24.11	−72.07	69.97	12.70
221	1993 May 13	49120	Crab pulsar	85.21	19.46	326.68	53.49
222	1993 May 24	49131	NGC 4151	178.02	42.25	60.65	26.85
223	1993 May 31	49138	Gal center	265.98	−29.72	316.33	48.19
224	1993 Jun 03	49141	SMC	24.11	−72.07	69.97	12.70
225	1993 Jun 15	49153	REBOOST				
226	1993 Jun 19	49157	Gal 355+05	258.44	−30.35	189.52	31.57
227	1993 Jun 28	49166	SN 1993J	143.64	65.00	116.97	−22.62
228	1993 Jul 13	49181	SN 1993J	145.33	63.18	131.74	−26.16
230	1993 Jul 27	49195	Vela region	143.03	−54.64	127.10	34.31

Table A.2—Continued

Viewing Period	Starting Epoch Date	MJD	Pointed Target	z-axis α_z (°)	z-axis δ_z (°)	x-axis α_x (°)	x-axis δ_x (°)
230.5	1993 Jul 30	49198	Vela region	149.86	−53.17	131.53	35.41
231	1993 Aug 03	49202	NGC 6814	289.94	−15.33	186.93	−39.38
229	1993 Aug 10	49209	Gal 5+05	264.60	−22.06	188.59	30.82
229.3	1993 Aug 11	49210	PERSEID METEOR SHOWER				
229.5	1993 Aug 12	49211	Gal 5+05	264.60	−22.06	188.59	30.82
Phase 3							
301	1993 Aug 17	49216	Vela pulsar	128.92	−45.18	161.94	39.80
232	1993 Aug 24	49223	Gal 348+0	258.02	−39.35	188.46	23.07
232.5	1993 Aug 26	49225	Gal 348+0	258.02	−39.35	182.10	16.48
302.0	1993 Sep 07	49237	N Cyg 1992	307.63	52.63	202.99	10.92
302.3	1993 Sep 09	49239	GX 1+4	258.64	−22.70	180.21	25.63
303.0	1993 Sep 21	49251	GRS 1009–45	157.58	−42.88	217.43	28.41
303.2	1993 Sep 22	49252	N Cyg 1992	307.63	52.63	202.99	10.92
303.4	1993 Oct 01	49261	Cyg X-1	270.79	37.87	182.17	−1.77
303.5	1993 Oct 04	49264	REBOOST				
303.7	1993 Oct 17	49277	N Cyg 1992	307.63	52.63	202.99	10.92
304	1993 Oct 19	49279	Virgo 278+67	183.29	5.68	271.03	−21.61
305	1993 Oct 25	49285	Virgo 278+63	181.58	2.06	270.59	−25.79
306	1993 Nov 02	49293	Virgo 278+59	180.01	−1.62	270.91	−28.89
307	1993 Nov 09	49300	Virgo 269+69	181.19	9.53	267.48	−21.06
308.0	1993 Nov 16	49307	Virgo 283+75	187.61	12.59	261.40	−51.35
308.3	1993 Nov 19	49310	REBOOST				
308.6	1993 Nov 23	49314	Virgo 283+75	187.61	12.59	261.40	−51.35
310	1993 Dec 01	49322	Geminga	98.48	17.77	201.46	35.02
311.0	1993 Dec 13	49334	Virgo 284+75	187.69	12.41	272.61	−21.93
311.3	1993 Dec 15	49336	Virgo 284+75	187.69	12.41	272.61	−21.93
312	1993 Dec 20	49341	Virgo 281+71	185.52	9.12	265.95	−46.00
313	1993 Dec 27	49348	Virgo 289+79	190.10	16.12	270.42	−30.20
314	1994 Jan 03	49355	PSR 1259–63	195.69	−63.83	277.5	53.99
315	1994 Jan 16	49368	PSR 1259–63	195.69	−63.83	282.8	31.41
316	1994 Jan 23	49375	Cen A	201.37	−43.02	310.35	−19.21
318.1	1994 Feb 01	49384	Cyg X-1	301.26	30.92	332.98	−54.85
321.1	1994 Feb 08	49391	1A 0535+262	84.73	26.32	10.50	−28.79
321.5	1994 Feb 15	49398	1A 0535+262	84.73	26.32	9.37	−27.06
317	1994 Feb 17	49400	3C 120	37.41	10.61	306.0	67.18
319.0	1994 Mar 01	49412	QSO 0716+714	110.48	71.34	341.13	12.08
320	1994 Mar 08	49419	NGC 7469	345.81	8.87	76.4	54.13
319.5	1994 Mar 15	49426	Mrk 3	105.20	68.99	343.89	11.28
323	1994 Mar 22	49433	1H 1822–371	276.44	−37.11	349.25	21.35
322	1994 Apr 05	49447	QSO 1028+313	157.07	31.09	65.0	23.39
324	1994 Apr 19	49461	Gal plane 15	269.39	−13.15	356.64	11.62
325	1994 Apr 26	49468	GT 0236+610	49.07	46.94	67.24	−41.60
326	1994 May 10	49482	QSO 1028+313	156.69	31.65	47.37	28.24
327	1994 May 17	49489	NGC 7469	348.06	5.44	81.57	32.73
328	1994 May 24	49496	Cyg X-3	298.76	28.07	69.89	50.97
329	1994 May 31	49503	PSR J0437–47	69.26	−47.25	88.04	41.18
331.0	1994 Jun 07	49510	Cyg X-3	298.76	28.07	69.89	50.97

Table A.2—Continued

Viewing Period	Starting Epoch Date	MJD	Pointed Target	z-axis α_z (°)	z-axis δ_z (°)	x-axis α_x (°)	x-axis δ_x (°)
330	1994 Jun 10	49513	Gal plane 18	275.93	–13.26	341.41	60.41
331.5	1994 Jun 14	49517	Cyg X-3	298.76	28.07	69.89	50.97
332	1994 Jun 18	49521	Gal plane 18	275.93	–13.26	341.41	60.41
333	1994 Jul 05	49538	Cyg X-3	298.76	28.07	69.89	50.97
335.0	1994 Jul 12	49545	PSR J0437–47	69.26	–47.25	107.01	36.16
334	1994 Jul 18	49551	Gal plane 16	279.49	–25.06	235.26	56.88
335.5	1994 Jul 25	49558	PSR J0437–47	69.26	–47.25	107.01	36.16
336	1994 Aug 01	49565	NGC 7469	349.67	9.72	106.56	69.25
336.5	1994 Aug 04	49568	GRO J1655–40	249.14	–43.04	135.68	–23.09
337	1994 Aug 09	49573	PSR 0656+14	87.70	0.98	178.49	39.05
338.0	1994 Aug 29	49593	GRO J1655–40	253.50	–39.85	149.06	–16.64
338.5	1994 Aug 31	49595	Vela pulsar	128.92	–45.18	200.60	17.34
339	1994 Sep 20	49615	PG 1416–129	234.71	–1.82	143.62	–30.89
Cycle 4							
401	1994 Oct 04	49629	Cas A	348.90	67.40	195.74	20.38
402.0	1994 Oct 18	49643	Gal plane 310	211.71	–66.78	190.16	21.75
402.5	1994 Oct 25	49650	Gal plane 310	202.34	–66.37	237.14	19.76
403	1994 Nov 01	49657	Her X-1	254.46	35.34	205.10	–42.56
403.5	1994 Nov 09	49665	OJ 287	133.70	20.11	217.85	–15.56
404	1994 Nov 15	49671	S Gal pole	354.98	–33.17	257.34	–11.49
405	1994 Nov 29	49685	3C 279	194.93	–6.27	288.32	–28.32
405.5	1994 Dec 07	49693	GRO J1655-40	194.93	–6.27	290.58	–41.85
406	1994 Dec 13	49699	Virgo	205.27	7.64	285.17	–52.56
407	1994 Dec 20	49706	Virgo	206.58	3.50	293.10	–44.73
408	1995 Jan 03	49720	3C 279	194.05	–5.79	288.35	–36.50
409	1995 Jan 10	49727	LMC	68.52	–63.61	311.85	–12.56
410	1995 Jan 24	49741	Gal 082-33	337.33	18.83	256.57	–25.23
411.1	1995 Feb 14	49762	QSO 0716+714	98.49	69.75	328.38	13.37
411.5	1995 Feb 21	49769	QSO 0716+714	93.91	71.03	344.06	6.65
412	1995 Feb 28	49776	Gal anticenter	90.09	24.68	9.86	–20.28
413	1995 Mar 07	49783	Gal anticenter	89.78	17.10	8.21	–25.49
414	1995 Mar 21	49797	Vela	132.83	–65.69	11.02	–13.40
414.3	1995 Mar 29	49805	GRO J1655-40	257.28	–39.14	337.80	11.44
419.1	1995 Apr 04	49811	Orion	83.40	–3.84	352.77	–9.19
415	1995 Apr 11	49818	LMC	104.00	–65.30	11.78	–1.02
418	1995 Apr 25	49832	Mrk 421	173.20	45.55	53.92	25.64
419.5	1995 May 09	49846	Orion	86.68	–6.99	7.94	57.87
420	1995 May 23	49860	Orion	79.91	4.12	343.16	58.49
421	1995 Jun 06	49874	Gal center	263.13	–32.68	54.66	–53.87
422	1995 Jun 13	49881	Gal center	263.93	–33.02	165.35	–12.93
423	1995 Jun 20	49888	Gal center	268.12	–26.82	142.45	–49.07
423.5	1995 Jun 30	49898	PKS 1622-297	244.01	–31.94	127.51	–35.60
424	1995 Jul 10	49908	Cen A	205.46	–42.88	112.68	–2.98
425	1995 Jul 25	49923	Gal 137-47	22.90	14.43	113.29	1.50
426	1995 Aug 08	49937	Gal anticenter	83.52	22.02	179.93	15.44
427	1995 Aug 22	49951	Gal 154–10	55.91	42.35	160.61	15.55
428	1995 Sep 07	49967	S Gal pole	17.68	–33.41	147.58	–44.21

Table A.2—Continued

Viewing Period	Starting Epoch Date	MJD	Pointed Target	z-axis α_z (°)	δ_z (°)	x-axis α_x (°)	δ_x (°)
429	1995 Sep 20	49980	Gal 018+04	272.51	−11.07	180.03	−12.47
429.5	1995 Sep 27	49987	GRO J2058+42	326.22	36.72	215.19	25.69
Cycle 5							
501	1995 Oct 03	49993	Gal 28+4	277.41	−2.77	187.15	−5.25
502	1995 Oct 17	50007	PKS 0528+134	81.92	13.85	175.85	15.55
505	1995 Oct 31	50021	Cas A-4	2.81	60.49	207.29	27.26
506	1995 Nov 07	50028	Cas A-1	343.55	65.12	215.42	15.98
503	1995 Nov 14	50035	Cas A-3	337.80	55.63	228.39	12.81
504	1995 Nov 21	50042	Cas A-2	353.94	51.11	248.98	11.76
507	1995 Nov 28	50049	CTA 102	338.15	11.73	248.10	0.25
507.5	1995 Dec 07	50058	CTA 102	338.15	11.73	260.96	−46.86
508	1995 Dec 14	50065	Gal 5+0	269.71	−24.29	145.76	−51.04

Coordinates for more recent pointings are available from the *Compton Observatory* Science Support Center via WWW (http://cossc.gsfc.nasa.gov/cossc/cossc.html).

Appendix B

Decoherence Time Scales in Pulse Timing

In low signal-to-noise situations, it is necessary to integrate weak signals over long observations in order to obtain a significant detection. For pulse timing observations of a source whose pulse frequency is not constant, this can lead to signal decoherence as later pulses are added in out of phase with earlier pulses; it does not matter whether the measurement is in the time domain (epoch folding) or in the frequency domain (power spectra). In this Appendix, we calculate the time scale on which a signal will begin to become decoherent. Observation lengths much longer than this time scale will suffer loss of sensitivity due to pulse smearing. Pulse shapes with short duty cycles are considerably more susceptible to this problem. For X-ray pulsars, there are two common causes of signal decoherence: accretion torques and orbital Doppler shifts.

B.1 Decoherence Due to Accretion Torque

Let us consider the effect of a constant frequency derivative $\dot{\nu}$ on a pulse timing observation. The pulse phase is given by

$$\phi = \phi_0 + \dot{\phi}t + \frac{1}{2}\ddot{\phi}t^2 + \cdots \tag{B.1}$$

$$= \phi_0 + \nu t + \frac{1}{2}\dot{\nu}t^2 + \cdots. \tag{B.2}$$

We will define decoherence as a phase residual of 180° ($\Delta\phi = \frac{1}{2}$) with respect to a constant frequency model. Then, the decoherence condition can be written

$$\Delta\phi = \frac{1}{2}\dot{\nu}\tau^2 = \frac{1}{2}, \tag{B.3}$$

and the decoherence time scale is

$$\tau = \sqrt{\frac{1}{\dot{\nu}}} = \sqrt{\frac{P^2}{\dot{P}}}. \tag{B.4}$$

For longer observations, phase coherence can be recovered by "accelerating" the time series to compensate for the phase drift, essentially stretching or squeezing the size of the time bins (Middleditch 1989; Anderson et al. 1990; Wood et al. 1991; Johnston & Kulkarni 1991).

B.2 Decoherence Due to Orbital Motion

A second cause of signal decoherence is periodic Doppler shifting of the pulse frequency due to a binary orbit. We will restrict our discussion to the case of a circular orbit. For this case, the pulse phase can be written

$$\phi = \phi_0 + \dot{\phi}t + \frac{(a_x/c)\sin i}{P_{\rm pulse}} \cos\left(\frac{2\pi t}{P_{\rm orb}} + \psi\right) \tag{B.5}$$

$$= \phi_0 + \nu t + \frac{(a_x/c)\sin i}{P_{\rm pulse}} \left[1 - \frac{1}{2}\left(\frac{2\pi t}{P_{\rm orb}} + \psi\right)^2 + \frac{1}{4!}\left(\frac{2\pi t}{P_{\rm orb}} + \psi\right)^4 + \cdots\right], \tag{B.6}$$

and the corresponding decoherence condition is given by

$$\Delta\phi = \frac{(a_x/c)\sin i}{P_{\rm pulse}} \left[1 - \cos\left(\frac{2\pi\tau}{P_{\rm orb}} + \psi\right)\right] = \frac{1}{2}. \tag{B.7}$$

Since we are interested in the *minimum* decoherence time scale, we set the orbital phase $\psi = 0$. Then, the orbital decoherence time scale is

$$\tau = P_{\rm orb}\frac{1}{2\pi}\cos^{-1}\left[1 - \frac{1}{2}\frac{P_{\rm pulse}}{(a_x/c)\sin i}\right]. \tag{B.8}$$

This expression can be simplified for two special cases. If the light travel time across the orbit is long compared to the pulse period, then

$$\tau \approx \frac{P_{\rm orb}}{2\pi}\left[\frac{P_{\rm pulse}}{(a_x/c)\sin i}\right]^{1/2} \quad \text{for} \frac{(a_x/c)\sin i}{P_{\rm pulse}} \gtrsim \frac{1}{2}. \tag{B.9}$$

However, for sufficiently small orbits ($(a_x/c)\sin i < P_{\rm pulse}/4$), the signal will not suffer from decoherence at all ($\tau = \infty$). Note that these calculations are not accurate for highly eccentric orbits. A plot of orbital decoherence time scale as a function of orbital size is shown in Figure B.1. The decoherence time scales for a number of systems is given in Table B.1.

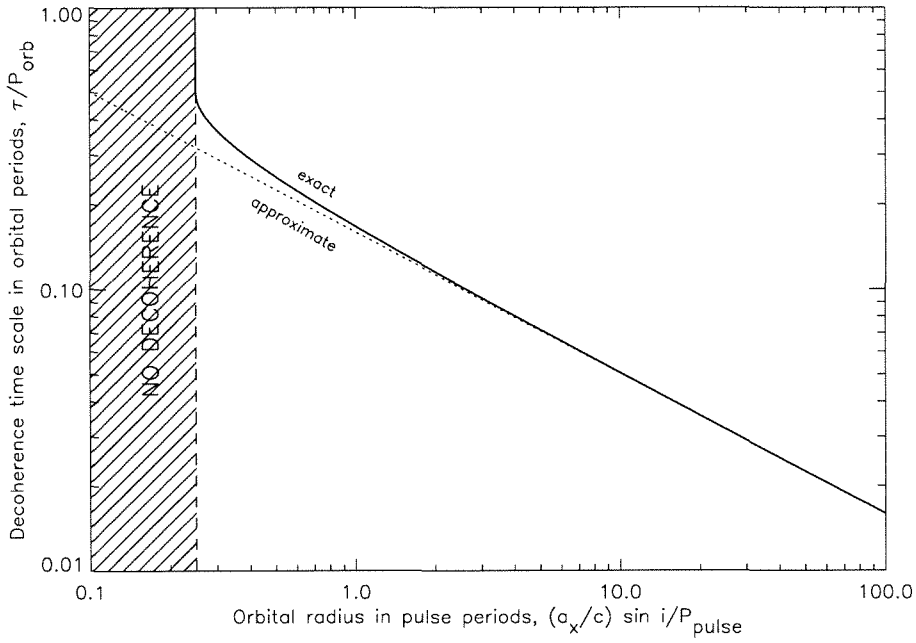

Figure B.1: Decoherence time scale due to orbital motion as a function of projected orbital radius.

Table B.1. Orbital Decoherence Time Scales

System	$a_x \sin i$ (lt-s)	P_{pulse} (s)	P_{orb} (d)	$(a_x/c)\sin i/P_{pulse}$	τ_{decoh}
SMC X-1	53.5	0.7	3.89	76.4	1.70 h
GS 0834–430	205.7	12.3	111	16.7	4.3 d
Her X-1	13.2	1.2	1.7	11	1.96 h
Cen X-3	39.6	4.8	2.09	8.2	2.79 h
OAO 1657–415	106	37.7	10.4	2.8	1.0 d
LMC X-4	26.3	13.5	1.408	1.9	3.94 h
Vela X-1	113.6	141	8.96	0.8	1.7 d
4U 1907+09	113.6	438	8.38	0.26	3.7 d
4U 1538–52	52.8	530	3.73	0.1	∞
4U 1626–67	< 0.008	7.7	0.02	< 0.001	∞

References

Anderson, S. B. et al. 1990. Discovery of two radio pulsars in the globular cluster M15. *Nature*, **346**, 42.

Johnston, H. M. & Kulkarni, S. R. 1991. On the detectability of pulsars in close binary systems. *Astrophys. J.*, **368**, 504.

Middleditch, J. 1989. Searches for millisecond pulsars in binary systems. In *Supercomputing '89*, Vol. 2, ed. L. P. Kartashev & S. I. Kartashev (St. Petersberg, FL: Intl. Supercomp. Inst.), 303.

Wood, K. S. et al. 1991. Searches for millisecond pulsations in low-mass X-ray binaries. *Astrophys. J.*, **379**, 295.

Appendix C

Limits on Luminosity and Distance from Steady Spin-Up

When a bolometric X-ray flux measurement is available for an accreting pulsar undergoing steady spin-up, a lower limit can be placed on the distance to the source. The angular momentum of a rotating neutron star is given by

$$l = 2\pi I \nu, \tag{C.1}$$

where ν is the spin frequency and I is the moment of inertia of the neutron star. Differentiating, we can write the torque on the neutron star as

$$N = \dot{l} = 2\pi I \dot{\nu}. \tag{C.2}$$

In an accreting pulsar undergoing steady spin-up, the torque applied to the neutron star is set by the mass accretion rate and the specific angular momentum of the accreting matter at the magnetospheric radius $r_{\rm m}$ (where the magnetic stress forces the matter to move along the magnetic field lines), and can be written

$$N_{\rm max} = \dot{M}\sqrt{GM_{\rm x} r_{\rm m}}. \tag{C.3}$$

For a given mass accretion rate $\dot{M}$ in a disk-fed system, the *maximum* possible torque will occur when $r_{\rm m} \approx r_{\rm co}$, where the corotation radius $r_{\rm co}$ is given by

$$r_{\rm co} = \left(\frac{GM_{\rm x}}{4\pi^2\nu^2}\right)^{1/3}. \tag{C.4}$$

For $r_{\rm m} > r_{\rm co}$, matter will be centrifugally inhibited from accreting via the propeller effect.

Thus, setting $N \leq N_{\max}$, we find that the mass accretion rate must obey

$$\dot{M} \geq I\dot{\nu}\left(\frac{16\pi^4\nu}{G^2M_{\rm x}^2}\right)^{4/3}, \tag{C.5}$$

and hence

$$L_{\rm x} = \frac{GM_{\rm x}\dot{M}}{R_{\rm x}} \geq \frac{I\dot{\nu}}{R_{\rm x}}(16\pi^4 GM_{\rm x}^4\nu)^{1/3}. \tag{C.6}$$

Since $L_{\rm x} = 4\pi d^2 F_{\rm x}$, we can use the observed bolometric X-ray flux $F_{\rm x}$ to set a lower limit on the distance to the source

$$d \geq \left(\frac{\pi GM_{\rm x}\nu I^3\dot{\nu}^3}{4F_{\rm x}^3R_{\rm x}^3}\right)^{1/6}. \tag{C.7}$$

Inserting typical values, we have

$$\begin{aligned} d \geq\ & 1.8 \text{ kpc} \\ & \times \left(\frac{\nu}{0.1 \text{ Hz}}\right)^{1/6} \left(\frac{\dot{\nu}}{10^{-13} \text{ Hz s}^{-1}}\right)^{1/2} \left(\frac{F_{\rm x}}{10^{-9} \text{ erg cm}^{-2} \text{ s}^{-1}}\right)^{-1/2} \\ & \times \left(\frac{M_{\rm x}}{1.4\,M_\odot}\right)^{2/3} \left(\frac{R_{\rm x}}{10 \text{ km}}\right)^{1/2} \left(\frac{I/M_{\rm x}R_{\rm x}^2}{0.2}\right)^{1/2}, \end{aligned} \tag{C.8}$$

or, in terms of spin period $P_{\rm spin}$ and its derivative $\dot{P}$,

$$\begin{aligned} d \geq\ & 1.8 \text{ kpc} \\ & \times \left(\frac{P}{10 \text{ s}}\right)^{-7/6} \left(\frac{\dot{P}}{10^{-11} \text{ s s}^{-1}}\right)^{1/2} \left(\frac{F_{\rm x}}{10^{-9} \text{ erg cm}^{-2} \text{ s}^{-1}}\right)^{-1/2} \\ & \times \left(\frac{M_{\rm x}}{1.4\,M_\odot}\right)^{2/3} \left(\frac{R_{\rm x}}{10 \text{ km}}\right)^{1/2} \left(\frac{I/M_{\rm x}R_{\rm x}^2}{0.2}\right)^{1/2}. \end{aligned} \tag{C.9}$$

Appendix D

Binary Orbits

D.1 Basic Concepts

Consider the bound binary star system shown in Figure D.1, with component masses M_1 and M_2. Both components are in an elliptical orbit, with their center of mass as a common focus F for the two orbits. The orbit of M_1 has semimajor axis a_1 and semiminor axis b_1, and the orbit of M_2 has semimajor axis a_2 and semiminor axis b_2. The two orbits have a common eccentricity given by $e = \sqrt{a_1^2 - b_1^2}/a_1 = \sqrt{a_2^2 - b_2^2}/a_2$. The dimensions of the two orbits are related by $M_1 a_1 = M_2 a_2$. The separation between the center of mass and the point of closest approach of M_1 (called *periastron* or, more generally, *periapse*) is $a_1(1-e)$, and is denoted in Figure D.1 as P_1. The separation to the most distant point in the orbit, called *apastron* or *apoapse*, is $a_1(1+e)$, and is denoted by A_1. The corresponding points for M_2 are labelled as P_2 and A_2. The line joining periastron and apastron is called the *line of apsides.*

We will restrict our attention to the orbit of M_2; symmetry considerations immediately give the corresponding results for M_1. The physical phase angle $v = M_2 F P_2$ of M_2, measured along the orbit from periastron, is called the *true anomaly.* The instantaneous separation between F and M_2 is given by

$$r_2 = \frac{a_2(1-e^2)}{1+e\cos v}. \tag{D.1}$$

It is not possible to write the time-dependence of v in closed form. Instead, we introduce an auxiliary angle E (see Figure D.1), called the *eccentric anomaly*, such that

$$r_2 = a_2(1 - e\cos E). \tag{D.2}$$

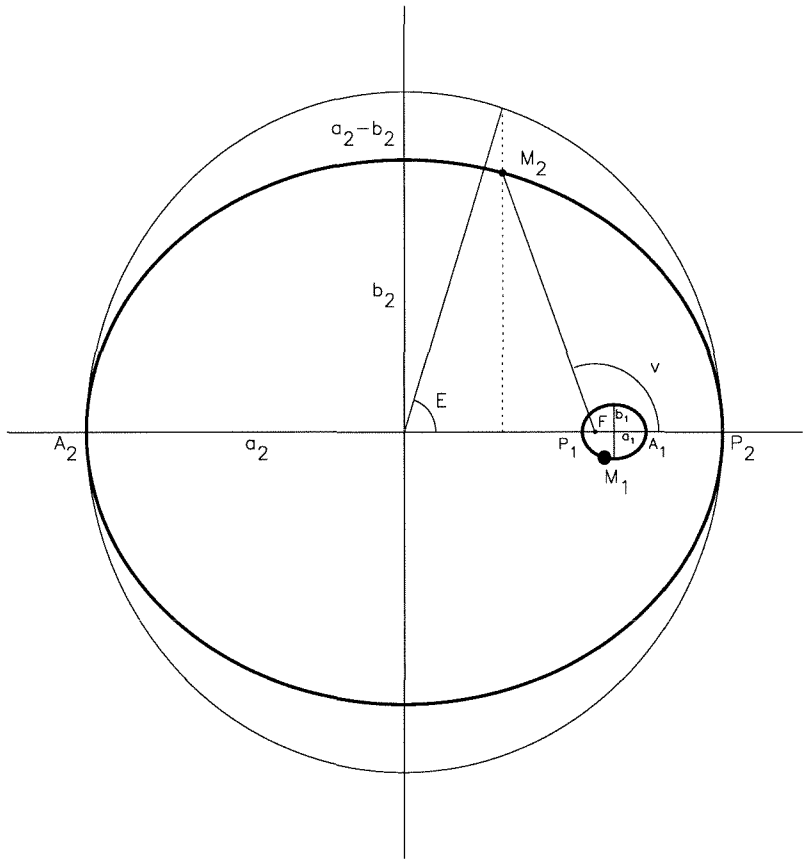

Figure D.1: Binary geometry for two masses ($M_1 > M_2$) orbiting their common center-of-mass F. The bold ellipses show the orbital paths. P_1 and A_1 are the periastron and apastron for M_1, and P_2 and A_2 are the corresponding points for M_2. The true anomaly v, measured along the orbit from periastron, is angle M_2FP_2 (or M_1FP_1). The circumscribed circle used to construct the auxiliary quantity E (eccentric anomaly) is also shown.

True anomaly v and eccentric anomaly E are related by

$$\sin v = \frac{\sqrt{1-e^2}\sin E}{1-e\cos E} \tag{D.3}$$

$$\cos v = \frac{\cos E - e}{1-e\cos E}, \tag{D.4}$$

and E can then be related to a third quantity M (called the *mean anomaly*), which varies linearly with time and is defined as

$$M \equiv \frac{2\pi(t-T_0)}{P} = E - e\sin E, \tag{D.5}$$

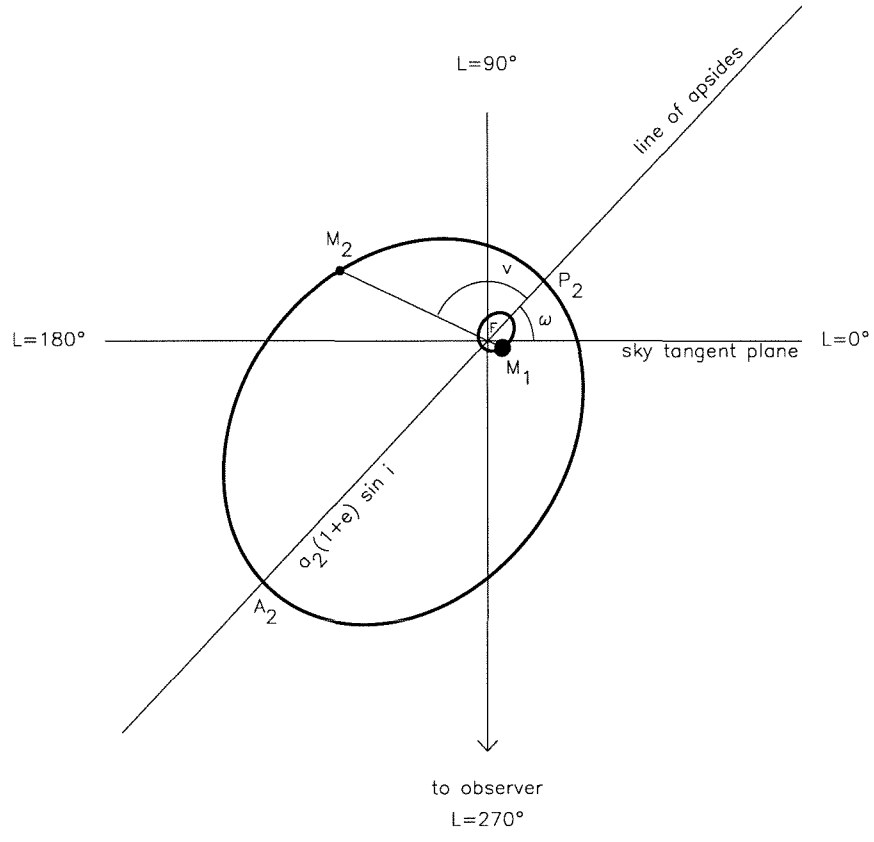

Figure D.2: Binary orbit geometry, projected along the observer's line of sight. The sense of orbital motion is this diagram is taken to be counterclockwise. Axes of true longitude L are shown. The orientation of the line of apsides with respect to the line of sight is specified through the longitude of periastron ω. The semimajor axis of the projected orbit of M_2 is $a_2 \sin i$.

where P is the orbital period and T_0 is a time of periastron passage. This is called *Kepler's equation.* Note that mean anomaly is *not* a physical angle for any non-zero value of e. It is equal to 2π times the fraction of the orbital period elapsed since periastron.

In using the Doppler shifts of a binary pulsar to measure an orbit, we are only sensitive to motion projected along the line of sight. In general, the orbit plane will have some inclination angle i, defined as the angle between the orbital angular momentum vector and our line of sight. The observed orbital motion is then scaled by $\sin i$; if $i = 0$, then we will observe no motion at all. To specify the orientation of the orbit with respect to the line

of sight, we introduce an angular coordinate L, called the *true longitude* (see Figure D.2), which is measured along the orbit from the *ascending node* (the point in the orbit where the plane tangent to the sky is crossed, moving away from the observer). We see that $L = 90°$ is the point of maximum distance from the observer. If $\sin i$ is sufficiently close to 1 to allow an eclipse of M_2 by M_1, then $L = 90°$ will roughly correspond to the mid-point of the eclipse (see Deeter et al. 1981 for some subtleties related to this point). Since L is a physical phase angle, it is easily related to true anomaly by

$$L = v + \omega, \tag{D.6}$$

where ω is the longitude of periastron. In analogy to the mean anomaly, we can define *mean longitude* by

$$l = M + \omega. \tag{D.7}$$

Like M, l is proportional to time but is *not* a physical angle (unless the orbit is circular).

As $e \to 0$, the concept of periastron becomes ill-defined, and thus so do ω, T_0, v, E, and M. In this case, Deeter et al. (1981) have pointed out that it is convenient to parametrize binary orbits in terms of quantities which remain equally well-defined for both elliptical and circular orbits. Instead of $a \sin i$, P, e, ω, and T_0, they suggest using $a \sin i$, P, $g = e \sin \omega$, $h = e \cos \omega$, and $T_{\pi/2}$, where this last quantity is an epoch when mean longitude $l = 90°$. Some authors refer to $T_{\pi/2}$ as the *mid-eclipse time*. However, as we have noted, mean longitude is not a physical angle except for circular orbits, and $l = 90°$ can lie far from mid-eclipse for eccentric orbits (depending upon the value of ω).

D.2 Orbit-Fitting Equations

D.2.1 Auxiliary Chain Rule Quantities

In fitting binary orbit models to observations, it is convenient to know the partial derivatives of the observed quantity with respect to the orbital parameters. Because the equations of motion are implicit in time, we must calculate some auxiliary derivatives for chain rule manipulations. Note that $E = E(t; e, P, T_0)$ and $v = v(t; e, P, T_0)$ are both functions not only of t, but also of the orbital parameters e, P, and T_0. It is therefore necessary to compute the partial derivatives of these quantities with respect to the orbital

parameters. For eccentric anomaly,

$$\frac{\partial E}{\partial e} = \frac{\sin E}{1 - e\cos E} \tag{D.8}$$

$$\frac{\partial E}{\partial P} = \frac{-2\pi(t - T_0)}{P^2(1 - e\cos E)} \tag{D.9}$$

$$\frac{\partial E}{\partial T_0} = \frac{-2\pi}{P(1 - e\cos E)}. \tag{D.10}$$

Similarly, for true anomaly,

$$\frac{\partial v}{\partial e} = \frac{\sin^2 E(2 - e\cos E - e^2)}{(1 - e\cos E)^3 \sin v} \tag{D.11}$$

$$\frac{\partial v}{\partial P} = \frac{-2\pi(t - T_0)(1 - e^2)\sin E}{P^2(1 - e\cos E)^3 \sin v} \tag{D.12}$$

$$\frac{\partial v}{\partial T_0} = \frac{-2\pi(1 - e^2)\sin E}{P(1 - e\cos E)^3 \sin v}. \tag{D.13}$$

If using the alternate parameterization for low-eccentricity orbits, the partial derivatives with respect to T_0 are replaced by those with respect to $T_{\pi/2}$,

$$\frac{\partial E}{\partial T_{\pi/2}} = \frac{-2\pi}{P(1 - e\cos E)} \tag{D.14}$$

$$\frac{\partial v}{\partial T_{\pi/2}} = \frac{-2\pi(1 - e^2)\sin E}{P(1 - e\cos E)^3 \sin v}. \tag{D.15}$$

Also, since

$$T_{\pi/2} = T_0 - \frac{P}{2\pi}(\omega - \pi/2), \tag{D.16}$$

E and v will have an ω-dependence as well:

$$\frac{\partial E}{\partial \omega} = \frac{-1}{1 - e\cos E} \tag{D.17}$$

$$\frac{\partial v}{\partial \omega} = \frac{(1 - e^2)\sin E}{(1 - e\cos E)^3 \sin v}. \tag{D.18}$$

D.2.2 Pulse Frequency Measurements

For a pulsar with constant spin frequency ν_0, the observed pulse frequency history, including orbital effects (see, e.g., Green 1985), will be given by

$$\nu = \nu_0 \left\{ 1 - \frac{2\pi a \sin i}{P\sqrt{1 - e^2}} \left[\cos(v + \omega) + e\cos\omega \right] \right\}. \tag{D.19}$$

The partial derivatives with respect to the orbital parameters are

$$\frac{\partial \nu}{\partial \nu_0} = 1 - \frac{2\pi a \sin i}{P\sqrt{1-e^2}}[\cos(v+\omega) + e\cos\omega] \tag{D.20}$$

$$\frac{\partial \nu}{\partial (a \sin i)} = \frac{2\pi \nu_0}{P\sqrt{1-e^2}}[\cos(v+\omega) + e\cos\omega] \tag{D.21}$$

$$\frac{\partial \nu}{\partial \omega} = \frac{2\pi \nu_0 a \sin i}{P\sqrt{1-e^2}}[\sin(v+\omega) + e\sin\omega] \tag{D.22}$$

$$\begin{aligned}\frac{\partial \nu}{\partial e} = {} & \frac{-4\pi\nu_0 e a \sin i}{P\sqrt{1-e^2}}[\cos(v+\omega) + e\cos\omega] + \\ & \frac{-2\pi\nu_0 a \sin i}{P\sqrt{1-e^2}} \times \\ & \left\{\cos\omega - \frac{\sin^2 E(2 - e\cos E - e^2)[\sin(v+\omega) + e\sin\omega]}{(1-e\cos E)^3 \sin v}\right\}\end{aligned} \tag{D.23}$$

$$\begin{aligned}\frac{\partial \nu}{\partial P} = {} & \frac{-4\pi^2\nu_0\sqrt{1-e^2} a \sin i \sin E \sin(v+\omega)}{P^3(1-e\cos E)^3 \sin v} + \\ & \frac{2\pi\nu_0 a \sin i}{P^2\sqrt{1-e^2}}[\cos(v+\omega) + e\cos\omega]\end{aligned} \tag{D.24}$$

$$\frac{\partial \nu}{\partial T_0} = \frac{-4\pi^2\nu_0\sqrt{1-e^2} a \sin i \sin E \sin(v+\omega)}{P^2(1-e\cos E)^3 \sin v}. \tag{D.25}$$

A slightly different set of derivatives will be necessary if the orbit is parametrized in terms of $T_{\pi/2}$ instead of T_0.

D.2.3 Pulse Arrival Time Measurements

The line-of-sight time delay associated with a binary orbit (see, e.g., Green 1985) is given by

$$z(t) = a \sin i[\sin\omega(\cos E - e) + \sqrt{1-e^2}\cos\omega \sin E]. \tag{D.26}$$

The partial derivatives with respect to the orbital parameters are

$$\frac{\partial \nu}{\partial (a \sin i)} = \sin\omega(\cos E - e) + \sqrt{1-e^2}\cos\omega\sin E \tag{D.27}$$

$$\frac{\partial \nu}{\partial \omega} = a\sin i[\cos\omega(\cos E - e) + \sqrt{1-e^2}\sin\omega\sin E] \tag{D.28}$$

$$\begin{aligned}\frac{\partial \nu}{\partial e} = {} & -a\sin i\left[\sin\omega\left(1 + \frac{\sin^2 E}{1-e\cos E}\right) + \right. \\ & \left. \sin E\cos\omega\left(\frac{e}{\sqrt{1-e^2}} - \frac{\sqrt{1-e^2}\cos E}{1-e\cos E}\right)\right]\end{aligned} \tag{D.29}$$

$$\frac{\partial \nu}{\partial P} = \frac{2\pi(t-T_0)a\sin i}{P^2(1-e\cos E)}[\sin\omega\sin E - \sqrt{1-e^2}\cos\omega\cos E] \tag{D.30}$$

$$\frac{\partial \nu}{\partial T_0} = \frac{2\pi a \sin i}{P(1 - e\cos E)}[\sin\omega \sin E - \sqrt{1-e^2}\cos\omega\cos E]. \quad \text{(D.31)}$$

A slightly different set of derivatives will be necessary if the orbit is parametrized in terms of $T_{\pi/2}$ instead of T_0.

References

Deeter, J. E., Boynton, P. E., & Pravdo, S. H. 1981. Pulse timing observations of Hercules X-1. *Astrophys. J.*, **247**, 1003.

Green, R. M. 1985. *Spherical Astronomy* (Cambridge: Cambridge U. Press).

Appendix E

Eclipse Constraints in OAO 1657–415

This appendix reviews the geometric constraints placed on the companion radius and system inclination of OAO 1657–415 by the presence of an X-ray eclipse with half-angle θ_e. Note that the half-angle is defined as π times the duration of the eclipse; it is not a physical angle unless the orbit is circular. We will begin by assuming a circular orbit and a spherical companion. It is convenient to adopt a rotating coordinate system similar to that of Chanan, Middleditch, & Nelson (1976). We place the neutron star at the origin and the companion on the x-axis with coordinates (a, 0, 0), where a is the binary separation, and take the orbital angular momentum to be parallel to the z-axis. We then let the coordinate system rotate at the orbital period. In this coordinate system, the vector from the neutron star to an observer fixed in space will have a fixed angle $\psi_{\rm obs} = i$ with the z-axis (where i is the inclination angle of the system), while the projection of this vector in the x-y plane will make an angle $\phi_{\rm obs}$ with the x-axis which varies linearly with time over [0, 2π]. Mid-eclipse occurs when $\phi_{\rm obs} = 0$. We model the companion as a sphere with radius R_c, whose surface is given in terms of spherical coordinates (r, ψ, ϕ) by

$$r^2 + a^2 - 2aru\sin\psi = R_c^2, \tag{E.1}$$

where we have defined $u \equiv \cos\phi$. For a circular orbit, the eclipse half-angle θ_e is equal to the maximum value of $\phi_{\rm obs}$ for which the observer vector intersects the surface. To find this value, we set $\psi = i$ in Equation (E.1) and solve for the extreme values of $u = \cos\phi$ by differentiating with respect to r and setting $\partial u/\partial r = 0$, from which we find the constraint

$$r = au\sin i. \tag{E.2}$$

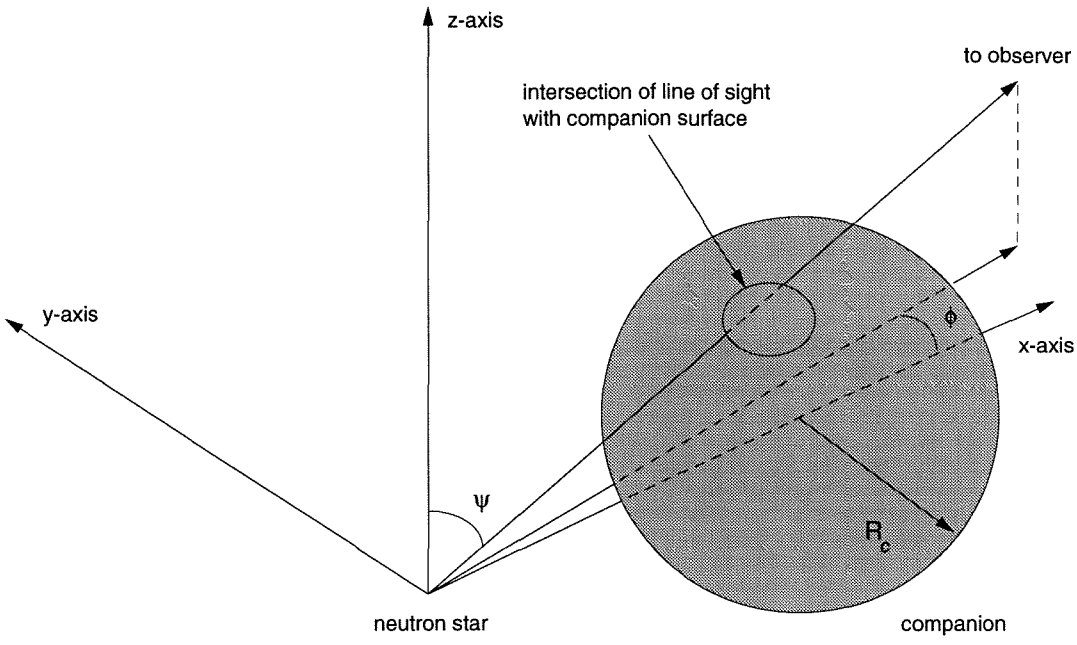

Figure E.1: Eclipse angle geometry. The coordinate system rotates about the z-axis in the ϕ, with one revolution per orbital period, so that the companion always lies on the x-axis with the neutron star at the origin. A fixed observer at infinity has a fixed polar angle $\psi_{\rm obs} = i$, and an azimuthal angle $\phi_{\rm obs}$ which varies through $[0, 2\pi]$ over the orbital period. Mid-eclipse occurs when $\phi_{\rm obs} = 0$. The line of sight from the neutron star to the observer will intersect the companion surface on the closed curve shown. Eclipse ingress and egress occur at the extreme values of $\phi_{\rm obs}$, when the line of sight is tangent to this curve.

Substituting into Equation (E.1), we find

$$R_c = a(1 - \cos^2 \phi_{\rm max} \sin^2 i)^{1/2} \quad \text{(E.3)}$$

$$= a(\cos^2 i + \sin^2 \phi_{\rm max} \sin^2 i)^{1/2}, \quad \text{(E.4)}$$

where $\phi_{\rm max}$ is the measured eclipse half-angle $\theta_{\rm e}$.

For an eccentric orbit, this relation is inaccurate for two reasons: the binary separation varies with orbital phase, and eclipse half-angle generally differs from the physical angle $\phi_{\rm max}$. In the case of OAO 1657-415, we can exploit the fact that mid-eclipse occurs at periastron (within the uncertainties) to note that ϕ is identical to the true anomaly of the relative binary orbit. Thus, the orbital separation in our coordinate system is just

$$\rho = \frac{a(1 - e^2)}{1 + eu}. \quad \text{(E.5)}$$

Replacing a with ρ in Equation (E.1) and setting $\partial u/\partial r = 0$, we find the new constraint

$$r = \frac{au(1-e^2)\sin i}{1+eu}, \tag{E.6}$$

and thus

$$R_c = \frac{a(1-e^2)}{1+e\cos\phi_{\max}}(\cos^2 i + \sin^2\phi_{\max}\sin^2 i)^{1/2}. \tag{E.7}$$

However, since for an eccentric orbit the coordinate system is no longer rotating at a uniform rate, we no longer have $\theta_e = \phi_{\max}$. To relate the observed quantity θ_e to Equation (E.7), we can again exploit the location of periastron at mid-eclipse ($\phi = 0$). The distinction, in this case, between $\phi_{\max}$ and θ_e is identical to the distinction between true anomaly and mean anomaly (see Appendix D). Thus, we can use standard elliptic expansions (e.g., Brouwer & Clemence 1961, Taff 1985) to write

$$\phi_{\max} = \theta_e + 2e\sin\theta_e + \frac{5}{4}e^2\sin 2\theta_e + O(e^3). \tag{E.8}$$

A further improvement in accuracy could be obtained by replacing the spherical companion with one which fills its Roche lobe. Chanan et al. (1976) have derived a formalism for computing eclipses by a Roche-lobe-filling companion numerically.

References

Brouwer, D. & Clemence, G. M. 1961. *Methods of Celestial Mechanics* (New York: Academic Press).

Chanan, G. A., Middleditch, J., & Nelson, J. E. 1976. The geometry of the eclipse of a pointlike star by a Roche-lobe-filling companion. *Astrophys. J.*, **208**, 512.

Taff, L. G. 1985. *Celestial Mechanics* (New York: Wiley).

Appendix F

Limits on the Orbit of GRO J1948+32

When you have eliminated the impossible, whatever remains, however improbable, must be the truth.

—Arthur Conan Doyle (1890)

Since many transient accreting pulsars do not remain active over their entire binary orbit, one frequently is faced with the problem of determining the binary parameters from incomplete sampling of the orbit. As an example of how to proceed in these circumstances, let us assume that the quasi-sinusoidal variation in the observed pulse frequency history of GRO J1948+32 (Figure F.1) is due to a binary orbit plus a constant spin frequency derivative. What can we then infer about the orbital parameters? Because the observations clearly span less than one entire orbital cycle, the allowed parameter solutions are highly correlated; that is, a wide range of different parameter values can provide an acceptable fit to the data. The only way to remove this degeneracy is to observe multiple orbital cycles. We can see this degeneracy as follows. If we fit the most conservative model, a circular orbit with constant $\dot{\nu}$, we obtain the following best-fit parameters:

$P_{\rm orb}$	=	38.5 ± 0.7 d
$a_{\rm x} \sin i$	=	116.0 ± 2.5 lt-s
$T_{\pi/2}$	=	MJD 49478.8 ± 0.3
$\dot{\nu}$	=	$(3.4 \pm 0.2) \times 10^{-12}$ Hz s^{-1}
Reduced χ^2	=	0.758 (12 degrees of freedom)

This model, along with the data, is shown in Figure F.1. If we now fit an eccentric orbit to the data, we obtain virtually the *same* model curve, with $e = 0.026 \pm 0.014$ and reduced $\chi^2 = 0.69$ with 10 degrees of freedom.

Since we cannot determine a unique solution, the best we can do is to identify

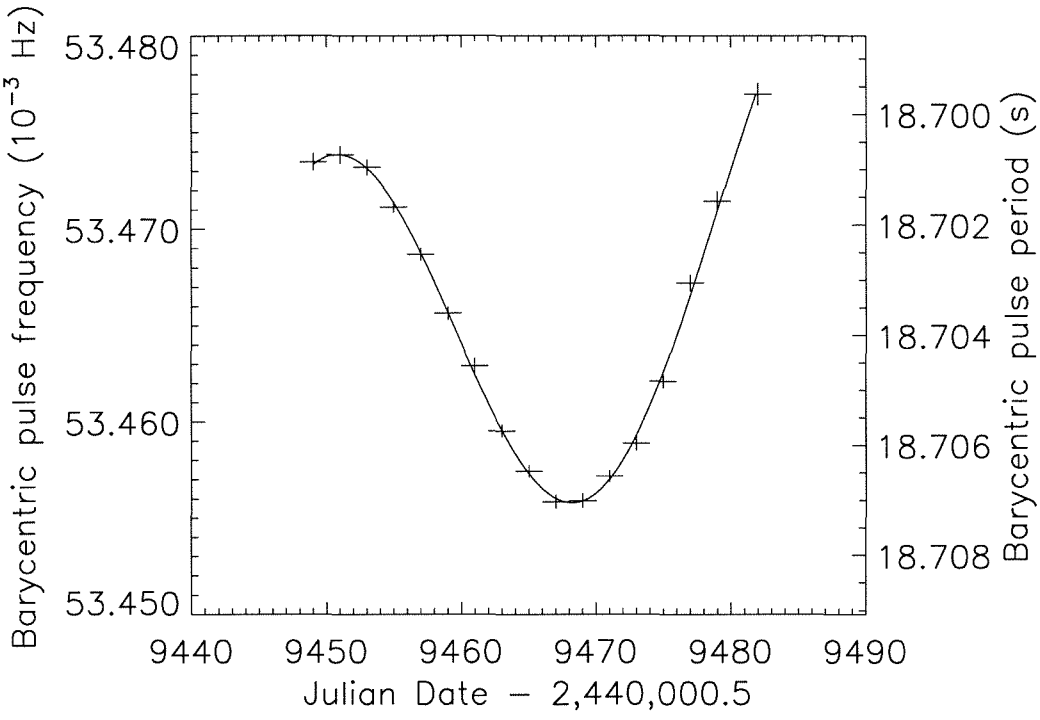

Figure F.1: Pulse frequency history of GRO J1948+32 from BATSE observations. The vertical bars show the 1 σ statistical uncertainties in the frequency measurements, while the horizontal bars show the time interval over which each measurement was integrated. A wide range of orbital parameters can produce a nearly identical model curve (*solid curve*).

confidence intervals for the orbital parameters. We do this for a given parameter by holding it fixed at some value and then varying all the *other* parameters to find the best fit to the data, being careful to avoid local minima in the multidimensional χ^2 space. By doing this for a grid of fixed parameter values, we can compute the allowed region of parameter space corresponding to a given confidence level by excluding parameter values for which χ^2 is too high. That is, for a given confidence level C, we can set an maximum allowed χ^2 value,

$$\int_{\chi^2_{\rm max}}^{\infty} p(\chi^2_\nu) d\chi^2_\nu = 1 - C, \tag{F.1}$$

where $\nu = N_{\rm data} - N_{\rm param}$ is the number of degrees of freedom, $N_{\rm data}$ is the number of data points, $N_{\rm param}$ is the number of model parameters, and the χ^2_ν probability density (e.g., Eadie et al. 1971) is

$$p(\chi^2_\nu) = \frac{(\chi^2)^{\nu/2-1} e^{-\chi^2/2}}{\Gamma(\nu/2) 2^{\nu/2}}. \tag{F.2}$$

Table F.1. Circular Orbit Limits for GRO J1948+32

Parameter	Value
Orbital period	$36 \text{ d} < P_{\text{orb}} < 44 \text{ d}$
Projected orbital radius	$95 \text{ lt-s} < a_x \sin i < 165\text{-lt-s}$
Spin frequency derivative	$2 \times 10^{-12} \text{ Hz s}^{-1} < \dot{\nu} < 6 \times 10^{-12} \text{ Hz s}^{-1}$
Mass function	$0.7\ M_\odot < f_x(M) < 2.3\ M_\odot$

Upper limits are quoted at the 95%-confidence level.

Table F.2. Eccentric Orbit Limits for GRO J1948+32

Parameter	Value
Eccentricity	$e < 0.25$
Orbital period	$36 \text{ d} < P_{\text{orb}} < 70 \text{ d}$
Projected semimajor axis	$75 \text{ lt-s} < a_x \sin i < 300 \text{ lt-s}$
Spin frequency derivative	$5 \times 10^{-13} \text{ Hz s}^{-1} < \dot{\nu} < 2.5 \times 10^{-11} \text{ Hz s}^{-1}$
Mass function	$0.5\ M_\odot < f_x(M) < 5\ M_\odot$

Upper limits are quoted at the 95%-confidence level.

For example, for our eccentric orbit fits we have $N_{\text{data}} = 17$, $N_{\text{param}} = 6$, and $\nu = 11$. Then, for $C = 0.95$, we have reduced $\chi^2_{\text{max}} = 1.789$. Model with reduced χ^2 above this value are inconsistent with the data at the 95%-confidence level.

The results of such an analysis for circular orbit models are summarized in Table F.1 and shown in Figure F.2. The corresponding results for eccentric orbit models are summarized in Table F.2 and shown in Figure F.3.

References

Eadie, W. T., Dryard, D., James, F. E., Roos, M., & Sadoulet, B. 1971. *Statistical Methods in Experimental Physics* (Amsterdam: North-Holland).

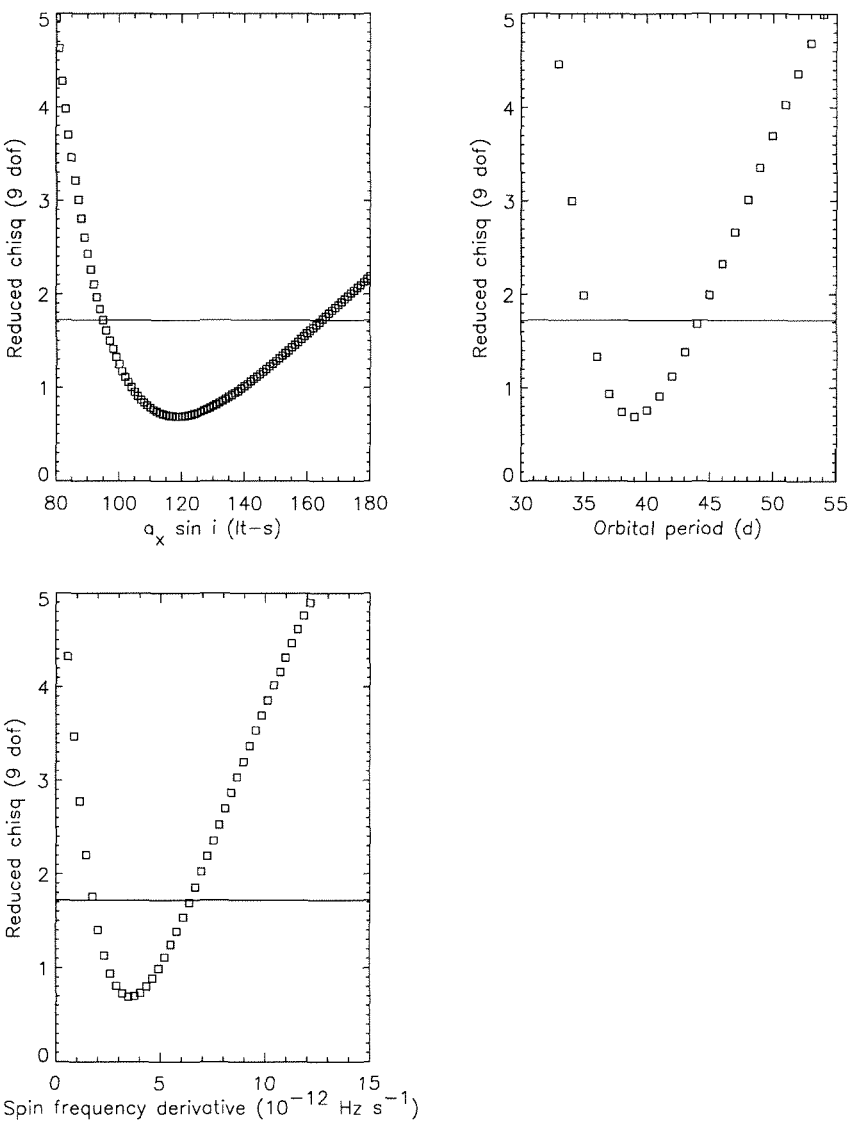

Figure F.2: Allowed parameter ranges for a GRO J1948+32 circular orbit. The 95%-confidence region for each parameter corresponds to reduced $\chi^2 < 1.72$.

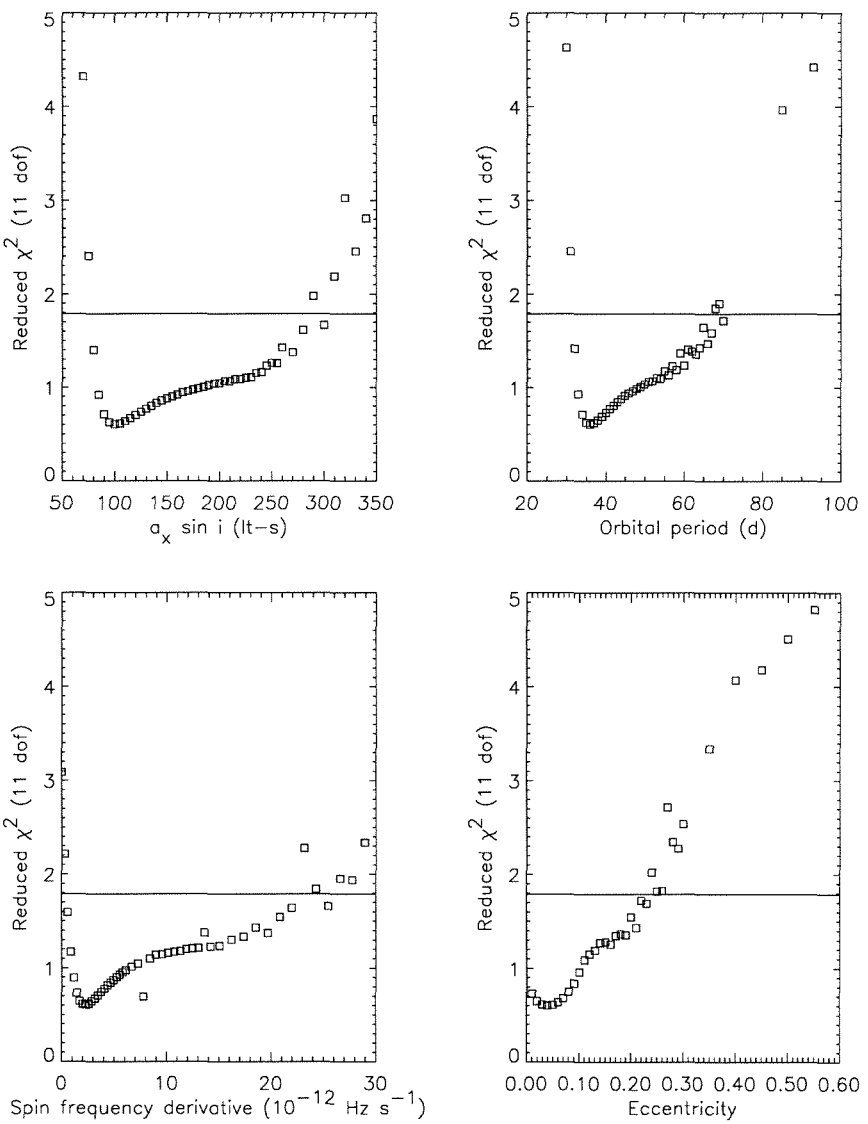

Figure F.3: Allowed parameter ranges for a GRO J1948+32 eccentric orbit. The 95%-confidence region for each parameter corresponds to reduced $\chi^2 < 1.79$.

Appendix G

BATSE Localization of Faint Pulsed Sources*

BATSE can localize intense transient sources (e.g., gamma-ray bursts) to within $\approx 5^\circ$ accuracy by using the ratios of measured intensities in the various incident detectors (Brock et al. 1992; Fishman et al. 1994). Bright persistent sources are localized more precisely ($\sim 0.1^\circ$) using Earth occultation edge measurements (Harmon et al. 1993; Zhang et al. 1994). Neither of these techniques is directly applicable to sources like GRO J1948+32 which are too faint ($\lesssim 100$ mCrab) to localize using standard occultation edge techniques, even though their pulsed flux is detectable by integrating the data over some interval. For such sources, it is still possible to extract spatial information from Earth occultations by using them to define the time intervals over which the pulsed signal is integrated. The maximum Fourier power is used to determine the maximum-likelihood sky location, subject to the assumptions discussed below.

For an assumed sky position (α, δ) and pulse frequency ν_0, we first construct a sinusoidal model time series

$$M_j(A, \phi, \alpha, \delta) = A \cos(2\pi\nu_0 t_j + \phi) W_j(\alpha, \delta), \tag{G.1}$$

where A and ϕ are the amplitude and phase of the sinusoid, and $W_j(\alpha, \delta)$ is a visibility window function whose value is taken to be zero or unity depending upon the assumed source location and the spacecraft position with respect to the Earth. If we assume Gaussian statistics for the observed data, then the probability of model $\{M_j\}$ given an observed time

*Adapted from the appendix of "Discovery of the 18.7 Second Accreting X-Ray Pulsar GRO J1948+32" in *The Astrophysical Journal*, **446**, 826–831 (1995 June 20), by D. Chakrabarty, T. Koh, L. Bildsten, T. A. Prince, M. H. Finger, R. B. Wilson, G. N. Pendleton, & B. C. Rubin. Used by permission of the authors.

series $\{S_j\}$ is

$$\Pr = \prod_{j=1}^{N} \frac{e^{-(S_j - M_j)^2/2\sigma^2}}{\sqrt{2\pi\sigma^2}}, \tag{G.2}$$

where σ is the standard deviation of the background noise level, assumed to be constant over the integration. We can then write the likelihood function

$$L = 2\ln\Pr = -\frac{1}{\sigma^2}\sum_{j=1}^{N}(S_j - M_j)^2 + \text{constant} \tag{G.3}$$

$$= \frac{2A}{\sigma^2}\sum_{j=1}^{N} S_j W_j \cos(2\pi\nu_0 t_j + \phi) - \frac{A^2}{\sigma^2}\sum_{j=1}^{N} W_j^2 \cos^2(2\pi\nu_0 t_j + \phi), \tag{G.4}$$

where we have dropped the constant terms. Defining the duty fraction $\epsilon \equiv \sum W_j^2/N = \sum W_j/N$ and the trial time series $Q_j = S_j W_j$, Equation (G.4) becomes

$$L = \frac{2A}{\sigma^2}\sum_{j=1}^{N} Q_j e^{2\pi i\nu_0 t_j + i\phi} - \frac{A^2}{2\sigma^2}\sum_{j=1}^{N} W_j e^{4\pi i\nu_0 t_j + 2i\phi} - \frac{\epsilon N A^2}{2\sigma^2} \tag{G.5}$$

$$= \frac{2A}{\sigma^2}\widetilde{Q}_k e^{i\phi} - \frac{A^2}{2\sigma^2}\widetilde{W}_{2k} e^{2i\phi} - \frac{\epsilon N A^2}{2\sigma^2}, \tag{G.6}$$

where $\widetilde{Q}$ and $\widetilde{W}$ are the discrete Fourier transforms of Q and W respectively, and k is the frequency index corresponding to ν_0. Since $\widetilde{W}$ is dominated by harmonics of the spacecraft orbital frequency $\nu_{\rm GRO} \ll 2\nu_0$ (where $1/\nu_{\rm GRO} \approx 93$ min), we can generally assume $|\widetilde{W}_{2k}| \ll \epsilon N$ and neglect the second term in Equation (G.6).

For a given sky position (α, δ), the maximum-likelihood value is obtained by maximizing L with respect to A, ϕ, and ν_0,

$$L_{\rm opt}(\alpha,\delta) = \frac{2|\widetilde{Q}_k|^2}{\epsilon N\sigma^2} = 2P_k(\alpha,\delta), \tag{G.7}$$

where $P_k = |\widetilde{Q}_k|^2/\epsilon N\sigma^2$ is the unity-normalized Fourier power at frequency ν_0. (The factor of ϵ in the denominator of this definition appears because a fraction $1-\epsilon$ of the time series $\{Q_j\}$ has been set to zero.) If we define $L_{\rm opt}$ as the maximum value of L found by varying all five parameters (A, ϕ, ν_0, α, δ) and define $L_{\rm true}$ as the maximum value of L found by varying only A, ϕ, and ν_0 but holding α and δ fixed at the (unknown) true coordinates of the source, then Cash (1979) has shown that the likelihood ratio statistic

$$\Delta L = L_{\rm opt} - L_{\rm true} \tag{G.8}$$

$$= 2P_{\rm opt} - 2P_{\rm true} \tag{G.9}$$

$$= 2\Delta P \tag{G.10}$$

is distributed as a χ^2 variable with two degrees of freedom, where we have assumed that the optimum and true coordinates are within $\sim 10^\circ$ of each other so that $\epsilon_{\rm true} \approx \epsilon_{\rm opt} \approx \epsilon$.

We now estimate the celestial coordinates of a periodic pulsed source of known frequency by computing L for a grid of trial positions (α, δ). The maximum-likelihood estimate for the source position is the grid point with the optimum L value. Confidence intervals can be constructed using contours of $\Delta\chi^2_2 = \Delta L = L_{\rm opt} - L$. A 90% confidence region corresponds to a contour of $\Delta\chi^2_2 = 4.6$ while a 99% confidence region corresponds to a contour of $\Delta\chi^2_2 = 9.2$ (Lampton, Margon, & Bowyer 1976). Multiple time series can be treated in the same way. Each time series contributes an additional product series in Equation (G.2), or equivalently additional terms in Equation (G.7). Thus, despite a larger aggregate value of L, the ratio statistic ΔL will still be distributed as χ^2_2.

This method implicitly assumes a constant sinusoidal signal and a constant Gaussian background over the entire interval of interest. Since real data depart from this idealization, we expect that systematic errors will eventually limit the precision of the technique. To estimate this limit, we studied DISCLA data from the recent bright outburst of the 3.6 s accreting pulsar 4U 0115+63 (Wilson, Finger, & Scott 1994). For the 20–60 keV channel, the background level varied between 1000–2000 cts s^{-1} over the spacecraft orbit. Using a location grid spacing of 0.25° and 25 days of data, our estimated 99% confidence region was $\approx 1^\circ$ across, centered on the true position of the source (which is known to within several arc seconds from optical astrometry of the companion). Given the strength of the signal in these data, we will adopt 0.5° as the systematic precision limit of this technique with DISCLA data.

References

Brock, M. N., Meegan, C. A., Roberts, F. E., Fishman, G. J., Wilson, R. B., Paciesas, W. S., & Pendleton, G. N. 1991. Gamma ray burst locations from the Burst and Transient Source Experiment. In *Gamma Ray Bursts*, ed. W. S. Paciesas & G. J. Fishman (New York: AIP), 383.

Cash, W. 1979. Parameter estimation in astronomy through application of the likelihood ratio. *Astrophys. J.*, **228**, 939.

Fishman, G. J. et al. 1994. The first BATSE gamma-ray burst catalog. *Astrophys. J. Suppl.*, **92**, 229.

Harmon, B. A. et al. 1993. Earth occultation measurements of Galactic hard X-ray/gamma-ray sources: a survey of BATSE results. In *Compton Gamma-Ray Observatory*, ed. M. Friedlander, N. Gehrels, & D. J. Macomb (New York: AIP Press), 314.

Lampton, M., Margon, B., & Bowyer, S. 1976. Parameter estimation in X-ray astronomy. *Astrophys. J.*, **208**, 177.

Wilson, R. B., Finger, M. H., & Scott, D. M. 1994. 4U 0115+63. *IAU Circ.*, No. 5999.

Zhang, S. N., Fishman, G. J., Harmon, B. A., & Paciesas, W. S. 1994. Imaging high-energy astrophysical sources using Earth occultation. *Nature*, **366**, 245.

Appendix H

Optical Pulse Timing of 4U 1626–67*

Here comes a pair of very strange beasts
—Shakespeare, *As You Like It* (1599)

H.1 Introduction

Binary stellar systems comprising a collapsed primary and a hydrogen-depleted low-mass secondary can evolve to extraordinarily short ($\lesssim$1 hr) orbital periods while maintaining high mass transfer rates. Only a handful of these systems are currently known. These include the six AM CVn cataclysmic variables (see Warner 1995) and the X-ray burst sources 4U 1820–30 and 4U 1916–05 (see Nelson et al. 1986). The accreting pulsar 4U 1626–67 is also thought to belong to this class of systems, based on the detection of weak optical pulsations interpreted as a beat with a 42-min binary orbital period (Middleditch et al. 1981). In this Appendix, I present the preliminary results of recent optical pulse timing observations. A more detailed analysis of these observations will be presented elsewhere (Chakrabarty 1996).

H.2 Observations

These observations were made during new moon on UT 1995 May 26–29, using the ASCAP single-channel photometer at the $f/8$ Ritchey-Chretien focus of the 4-m telescope

*Based on observations made at the Cerro Tololo Inter-American Observatory, National Optical Astronomy Observatories, which are operated by the Association of Universities for Research in Astronomy, under contract to the National Science Foundation.

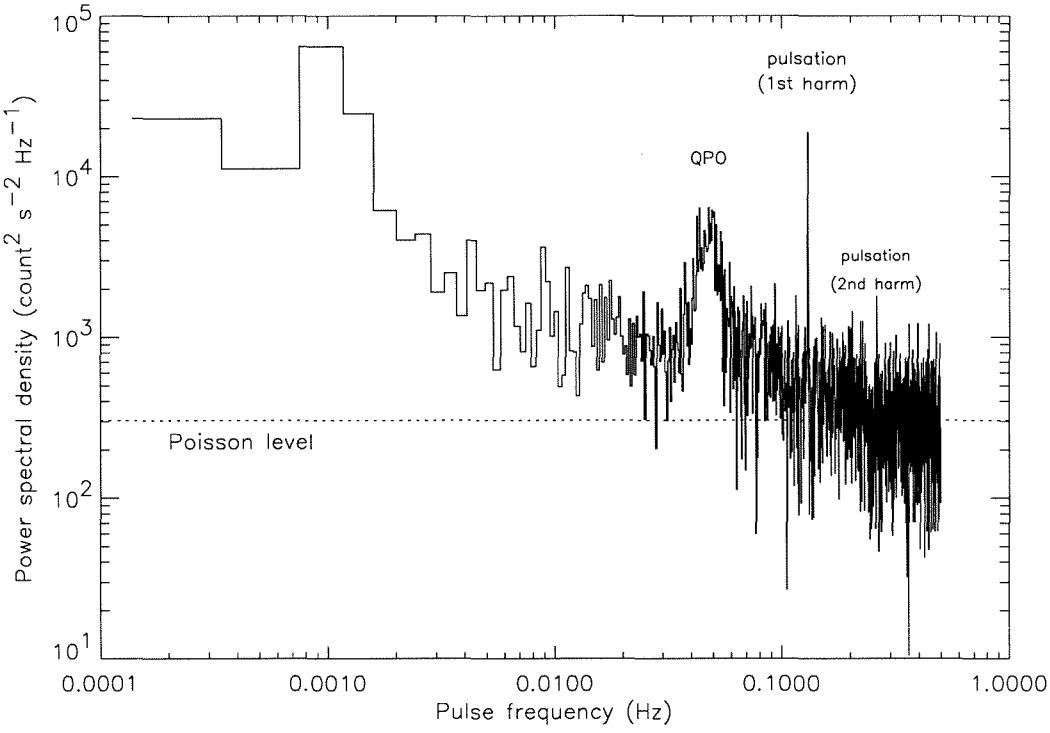

Figure H.1: Power spectral density of a 2-hr U-band (3600 Å) pulse timing observation of 4U 1626–67 on 1995 May 26 from CTIO. The fundamental and second harmonic of the optical pulsations, seen near 0.13 Hz and 0.26 Hz, are in good agreement with the BATSE pulse frequency ephemeris. A strong quasi-periodic oscillation near 0.048 Hz is also present.

at the Cerro Tololo Inter-American Observatory (CTIO) in La Serena, Chile. The detector, a Varian VPM-159A photomultiplier tube cooled with dry ice, had good sensitivity from the ultraviolet out to 10000 Å. The detected count rate was integrated every 1 ms. Absolute time accuracy within ±1.5 ms of UTC-NIST was maintained using a Kinemetrics/Truetime model 468-DC satellite-synchronized clock in conjunction with the *GOES-West* satellite operated by the National Oceanographic and Atmospheric Administration.

H.3 Results

Figure H.1 shows the power spectral density of a 1.8 hr observation made on May 26, using a Johnson U-band (3650 Å) filter. At low analysis frequencies, the spectrum is dominated by red noise fluctuations in the sky background. At high analysis frequencies,

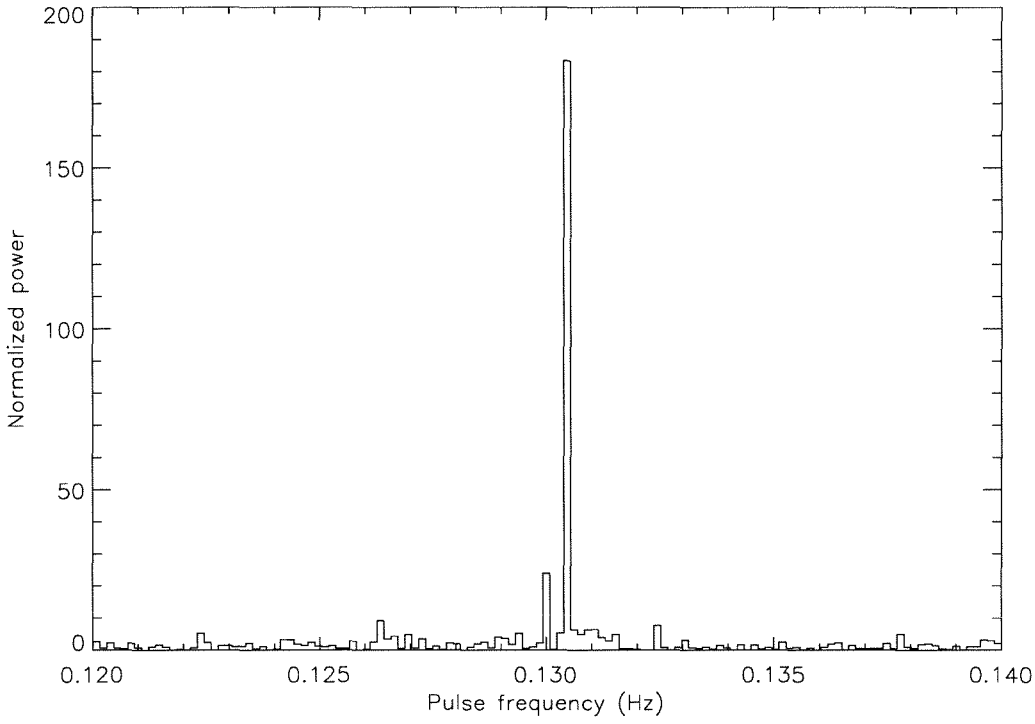

Figure H.2: Optical power spectrum of 4U 1626–67 in the vicinity of the fundamental, normalized with respect to the local noise power. In addition to the main pulsation peak at 130.4378(42) mHz, a significant lower sidelobe is evident at 130.0358(113) mHz.

the spectrum is consistent with white noise (Poisson) counting statistics. A strong coherent pulsation is visible at a topocentric pulse frequency of 130.4378(42) mHz. When corrected to the solar system barycenter, this is in good agreement with the BATSE epmeheris for the X-ray pulsations (see Chapter 6). The second harmonic of this pulsation is visible as well. Also present is a strong quasi-periodic oscillation (QPO) near 0.048 Hz, consistent with the frequency at which an X-ray QPO was recently observed by *ASCA* (Angelini et al. 1995). This is the first detection of an optical QPO from an X-ray pulsar system.

Figure H.2 shows a detailed view of the same power spectrum near the coherent pulsation frequency, normalized with respect to the local noise power level. In addition to the main pulsation, a significant lower-frequency sidelobe is also present with topocentric frequency 130.0358(113) mHz. The spacing between the main peak and the sidelobe, 0.4020(121) mHz, is nearly identical to the sidelobe spacing reported by Middleditch et al. (1981) and attributed to a binary orbit.

Additional observations were made in the B (4400 Å), V (5500 Å), R (7000 Å), and I (9000 Å) bands. The main pulsation was clearly detected in the B, V, and R bands, and was marginally detected in the I band. All these detections were at reduced significance compared to the U-band observation; this was at least partially due to worsening sky conditions. Unambiguous detections of the sidelobe feature were not obtained in the other observations.

References

Angelini, L., White, N. E., Nagase, F., Kallman, T. R., Yoshida, A., Takeshima, T., Becker, C. M., & Paerels, F. 1995. Neon line emission in the X-ray spectrum of the pulsar 4U 1626–67. *Astrophys. J.*, **449**, L41.

Chakrabarty, D. 1996. *Astrophys. J.* In preparation.

Middleditch, J., Mason, K. O., Nelson, J. E., & White, N. E. 1981. 4U 1626–67: a prograde spinning X-ray pulsar in a 2500 s binary system. *Astrophys. J.*, **244**, 1001.

Nelson, L. A., Rappaport, S. A., and Joss, P. C. 1986. The evolution of ultrashort period binary systems. *Astrophys. J.*, **304**, 231.

Warner, B. 1995. The AM Canum Venaticorum stars. *Astrophys.& Space Sci.*, **225**, 249.

Appendix I

IAU Circulars

I.1 Position of GRO J1948+32

IAU Circular, No. 5981, 1994 April 29

GRO J1948+32 = GRO J2014+34

D. Chakrabarty and T. A. Prince, California Institute of Technology; M. H. Finger, Universities Space Research Association; R. B. Wilson, Marshall Space Flight Center, NASA; and G. N. Pendleton, University of Alabama, Huntsville, report for the Compton Gamma Ray Observatory BATSE team: "Further observations of the recently-discovered, 18.7-s, transient hard X-ray pulsar in Cygnus (originally designated GRO J2014+34; see IAUC 5977) have yielded a more precise position. The estimated 90%-confidence error box is approximately a 2°.5 x 5°.5 quadrilateral, with corners at R.A. = 19h58m, Decl. = +29°.0; 19h50m, +34°.0; 19h34m, +35°.0; 19h46m, +28°.0 (equinox 2000.0). In accordance with the substantially improved position, we have redesignated the source as GRO J1948+32. The pulsed emission was first detectable on Apr. 6 UT and continues to be visible as of April 28. Optical and soft-X-ray observations of the error box are strongly encouraged in order to further constrain the X-ray position and identify the accreting companion."

I.2 Spin-Up of GX 1+4

IAU Circular, No. 6105, 1994 November 16

GX 1+4

D. Chakrabarty and T. A. Prince, California Institute of Technology; M. H. Finger,

Universities Space Research Association; and R. B. Wilson, Marshall Space Flight Center, NASA, report for the Compton Gamma Ray Observatory BATSE team: "The accreting X-ray pulsar GX 1+4 has resumed spinning up, reversing the steady spin- down trend that had been observed since 1987. We observed a smooth decrease in the spin-down rate, from $(3.8 \pm 0.1) \times 10^{-12}$ s^{-2} on June 20 to zero on about October 30. During the interval November 8–11, the spin-up rate was $(2.7 \pm 0.3) \times 10^{-12}$ s^{-2}, with a mean barycentric pulse frequency of $(8.19033 \pm 0.00003) \times 10^{-3}$ s^{-1}. The pulsed flux has increased by a factor of three since October 17, when the spin-down rate was $(1.5 \pm 0.2) \times 10^{-12}$ s^{-2}. On November 10, the 20–100 keV phase-averaged pulsed flux was 95 ± 10 mCrab, with a spectrum well fit by an optically-thin thermal bremsstrahlung model $F(E) = (A/E)\exp(-E/kT)$, with temperature $kT = 35 \pm 2$ keV and $F(50\text{ keV}) = (2.6 \pm 0.1) \times 10^{-4}$ photons cm^{-2} s^{-1} keV^{-1}. The pulsed emission is brighter and harder than observed during a previous outburst (IAUC 5859), and is continuing to increase in intensity."

I.3 Spin-Down of GX 1+4

IAU Circular, No. 6153, 1995 March 27

GX 1+4

D. Chakrabarty, T. Koh, T. A. Prince, and B. Vaughan, California Institute of Technology; M. H. Finger and M. Scott, Universities Space Research Association; and R. B. Wilson, Marshall Space Flight Center, NASA, report for the Compton Gamma Ray Observatory BATSE team: "The accreting X-ray pulsar GX 1+4 has undergone another torque reversal, and resumed spinning down on around March 2, thereby ending an extended spin-up episode that began on 1994 October 30 (IAUC 6105). On March 17.0 UT, the barycentric pulse frequency was $(8.21119 \pm 0.00002) \times 10^{-3}$ s^{-1}, with a mean frequency derivative of $(-1.25 \pm 0.04) \times 10^{-12}$ s^{-2}. The phase-averaged pulsed intensity on this date was $(9.0 \pm 0.9) \times 10^{-4}$ photon cm^{-2} s^{-1} keV^{-1} at 30 keV, with a power-law photon index of 2.6 ± 0.2 for the 20–100 keV pulsed flux."

Appendix J

GX 1+4 Observational Data

To facilitate further torque-luminosity studies of GX 1+4, and also to provide an accurate pulse frequency ephemeris for this widely observed source, the archival timing data and the BATSE timing and flux data are summarized here.

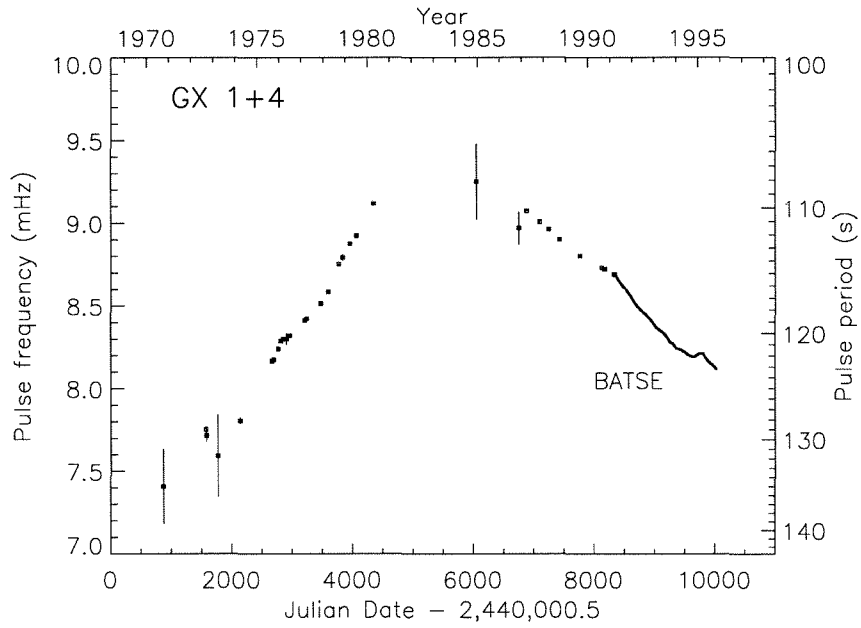

Figure J.1: Pulse frequency history of GX 1+4

Table J.1. Archival Timing Observations of GX 1+4

Epoch		Pulse period		
Date	MJD	(s)	Instrument	Reference
1970 Oct 16.5	40875.5	135(4)	MIT balloon	Lewin et al. 1971
1972 Sep 11.5	41571.5	129.0(3)	*Copernicus*	White et al. 1976
1972 Sep 18.5	41578.5	129.6(6)	*Copernicus*	White et al. 1976
1973 Mar 25.5	41766.5	131.7(42)	*Copernicus*	White et al. 1976
1974 Apr 2.5	42139.5	128.1(3)	Rice balloon	Koo and Haymes 1980
1975 Sep 15.5	42670.5	122.46(3)	*OSO-8*	Becker et al. 1976
1975 Oct 10.2	42695.2	122.34(6)	*SAS-3*	Doty et al. 1981
1975 Dec 26.8	42772.8	121.367(4)	*SAS-3*	Doty et al. 1981
1976 Feb 4.1	42812.1	120.6589(3)	*SAS-3*	Doty et al. 1981
1976 Mar 16.5	42853.5	120.493(3)	*OSO-8*	Cutler et al. 1986
1976 May 11.3	42909.3	120.5(5)	NRL balloon	Strickman et al. 1980
1976 Jul 4.2	42963.2	120.19(5)	*SAS-3*	Doty et al. 1981
1977 Mar 11.5	43213.5	118.873(5)	*OSO-8*	Cutler et al. 1986
1977 Apr 11.5	43244.5	118.715(5)	*Ariel 5*	Coe et al. 1981
1977 Nov 23.6	43470.6	117.45(20)	NRL balloon	Strickman et al. 1980
1978 Mar 26.5	43593.5	116.49(10)	*OSO-8*	Cutler et al. 1986
1978 Sep 21.0	43772.0	114.254(11)	*OSO-8*	Cutler et al. 1986
1978 Nov 22.5	43834.5	113.75(25)	MPI/AIT balloon	Kendziorra et al. 1982
1979 Mar 20.5	43952.5	112.68(3)	*Einstein*/MPC	Elsner et al. 1985
1979 Jul 8.95	44062.95	112.076(3)	*Ariel 6*	Ricketts et al. 1982
1980 Apr 17.95	44346.95	109.668(3)	*Ariel 6*	Ricketts et al. 1982
1984 Dec 18.0	46052.0	108.1(26)	TIFR balloon	Damle et al. 1988, Leahy 1989
1986 Nov 20.25	46754.25	111.5(12)	Tasmania balloon	Greenhill et al. 1993
1987 Mar 31.0	46885.0	110.233(3)	*Ginga*	Makishima et al. 1988
1987 Oct 31.54	47099.54	111.03(2)	*Mir/Kvant*/HEXE	Mony et al. 1991
1988 Mar 27.3	47247.3	111.59(2)	*Ginga*	Dotani et al. 1989
1988 Sep 25.6	47429.61	112.359(5)	*Mir/Kvant*/HEXE	Mony et al. 1991
1989 Aug 27.47	47765.47	113.626(2)	*Ginga*	Sakao et al. 1990
1990 Aug 23.8	48126.8	114.540(62)	*Granat*/ART-P	Lutovinov et al. 1994
1990 Oct 7.7	48171.7	114.657(14)	*Granat*/ART-P	Lutovinov et al. 1994
1991 Mar 22.87	48337.87	115.06(3)	*Granat*/SIGMA	Laurent et al. 1993
1991 Apr 1.52	48347.52	115.086(5)	*Granat*/SIGMA	Laurent et al. 1993
1991 Sep 8.7	48507.7	116.158(57)	*Granat*/ART-P	Lutovinov et al. 1994
1991 Oct 14.90	48543.90	116.38(10)	*Granat*/SIGMA	Laurent et al. 1993
1991 Oct 18.39	48547.39	116.43(5)	*Granat*/SIGMA	Laurent et al. 1993
1993 Dec 11.2	49332.2	121.0(4)	TIFR balloon	Rao et al. 1994

Table J.2. BATSE Observations of GX 1+4

Epoch		Pulse Frequency	20–60 keV Pulsed Flux
Date	MJD	(mHz)	erg cm^{-2} s^{-1}
1991 Apr 22.50	48368.50	8.67845(12)	$3.9(2) \times 10^{-10}$
1991 Apr 27.50	48373.50	8.67591(17)	$3.0(3) \times 10^{-10}$
1991 May 2.50	48378.50	8.67354(19)	$3.8(4) \times 10^{-10}$
1991 May 7.50	48383.50	8.67076(12)	$4.7(5) \times 10^{-10}$
1991 May 12.50	48388.50	8.66804(12)	$5.9(5) \times 10^{-10}$
1991 May 17.50	48393.50	8.66467(11)	$6.6(4) \times 10^{-10}$
1991 May 22.50	48398.50	8.66126(11)	$5.6(4) \times 10^{-10}$
1991 May 27.50	48403.50	8.65800(10)	$5.6(4) \times 10^{-10}$
1991 Jun 1.50	48408.50	8.65537(10)	$4.3(4) \times 10^{-10}$
1991 Jun 6.50	48413.50	8.65301(13)	$2.7(3) \times 10^{-10}$
1991 Jun 11.50	48418.50	8.65068(19)	$2.8(4) \times 10^{-10}$
1991 Jun 16.50	48423.50	8.64810(16)	$3.8(4) \times 10^{-10}$
1991 Jun 21.50	48428.50	8.64590(14)	$3.0(4) \times 10^{-10}$
1991 Jun 26.50	48433.50	8.64282(16)	$3.3(2) \times 10^{-10}$
1991 Jul 1.50	48438.50	8.64022(12)	$3.3(3) \times 10^{-10}$
1991 Jul 6.50	48443.50	8.63790(15)	$3.3(3) \times 10^{-10}$
1991 Jul 11.50	48448.50	8.63490(17)	$3.2(3) \times 10^{-10}$
1991 Jul 16.50	48453.50	8.63199(13)	$4.5(4) \times 10^{-10}$
1991 Jul 21.50	48458.50	8.62935(15)	$3.9(4) \times 10^{-10}$
1991 Jul 26.50	48463.50	8.62702(19)	$2.8(4) \times 10^{-10}$
1991 Jul 31.50	48468.50	8.62446(13)	$2.5(4) \times 10^{-10}$
1991 Aug 5.50	48473.50	8.62233(18)	$2.7(3) \times 10^{-10}$
1991 Aug 10.50	48478.50	8.61969(17)	$3.6(4) \times 10^{-10}$
1991 Aug 15.50	48483.50	8.61785(46)	$1.1(3) \times 10^{-10}$
1991 Aug 20.50	48488.50	8.61587(39)	$1.5(6) \times 10^{-10}$
1991 Aug 25.50	48493.50	8.61460(28)	$1.7(4) \times 10^{-10}$
1991 Aug 30.50	48498.50	8.61230(23)	$1.8(5) \times 10^{-10}$
1991 Sep 4.50	48503.50	8.61036(30)	$1.5(3) \times 10^{-10}$
1991 Sep 9.50	48508.50	8.60887(20)	$1.8(3) \times 10^{-10}$
1991 Sep 14.50	48513.50	8.60734(16)	$1.8(4) \times 10^{-10}$
1991 Sep 19.50	48518.50	8.60496(74)	$0.7(3) \times 10^{-10}$
1991 Sep 24.50	48523.50	8.60258(74)	$0.5(6) \times 10^{-10}$
1991 Sep 29.50	48528.50	8.60021(74)	$0.7(3) \times 10^{-10}$
1991 Oct 4.50	48533.50	8.59783(32)	$1.6(3) \times 10^{-10}$
1991 Oct 9.50	48538.50	8.59688(21)	$2.7(4) \times 10^{-10}$
1991 Oct 14.50	48543.50	8.59318(10)	$6.0(3) \times 10^{-10}$
1991 Oct 19.50	48548.50	8.58953(10)	$6.8(4) \times 10^{-10}$
1991 Oct 24.50	48553.50	8.58636(30)	$1.8(2) \times 10^{-10}$
1991 Oct 29.50	48558.50	8.58554(39)	$1.4(4) \times 10^{-10}$
1991 Nov 3.50	48563.50	8.58301(21)	$1.7(4) \times 10^{-10}$
1991 Nov 8.50	48568.50	8.58059(25)	$1.7(3) \times 10^{-10}$
1991 Nov 13.50	48573.50	8.57800(11)	$4.3(4) \times 10^{-10}$

Table J.2—Continued

Epoch		Pulse Frequency	20–60 keV Pulsed Flux
Date	MJD	(mHz)	erg cm^{-2} s^{-1}
1991 Nov 18.50	48578.50	8.57521(13)	$3.7(4) \times 10^{-10}$
1991 Nov 23.50	48583.50	8.57270(14)	$3.3(3) \times 10^{-10}$
1991 Nov 28.50	48588.50	8.56952(30)	$1.8(3) \times 10^{-10}$
1991 Dec 3.50	48593.50	8.56722(21)	$1.9(10) \times 10^{-10}$
1991 Dec 8.50	48598.50	8.56445(19)	$2.8(3) \times 10^{-10}$
1991 Dec 13.50	48603.50	8.56231(14)	$4.0(3) \times 10^{-10}$
1991 Dec 18.50	48608.50	8.55944(15)	$3.7(4) \times 10^{-10}$
1991 Dec 23.50	48613.50	8.55682(15)	$3.7(4) \times 10^{-10}$
1991 Dec 28.50	48618.50	8.55364(11)	$5.2(5) \times 10^{-10}$
1992 Jan 2.50	48623.50	8.55076(12)	$4.3(5) \times 10^{-10}$
1992 Jan 7.50	48628.50	8.54761(11)	$5.1(4) \times 10^{-10}$
1992 Jan 12.50	48633.50	8.54460(9)	$6.9(4) \times 10^{-10}$
1992 Jan 17.50	48638.50	8.54152(9)	$5.2(2) \times 10^{-10}$
1992 Jan 22.50	48643.50	8.53842(10)	$4.7(2) \times 10^{-10}$
1992 Jan 27.50	48648.50	8.53561(13)	$3.7(2) \times 10^{-10}$
1992 Feb 1.50	48653.50	8.53225(14)	$3.9(3) \times 10^{-10}$
1992 Feb 6.50	48658.50	8.52951(14)	$3.3(3) \times 10^{-10}$
1992 Feb 11.50	48663.50	8.52592(10)	$4.3(3) \times 10^{-10}$
1992 Feb 16.50	48668.50	8.52277(8)	$5.2(2) \times 10^{-10}$
1992 Feb 21.50	48673.50	8.51944(9)	$4.3(2) \times 10^{-10}$
1992 Feb 26.50	48678.50	8.51625(10)	$4.4(3) \times 10^{-10}$
1992 Mar 2.50	48683.50	8.51321(11)	$3.5(2) \times 10^{-10}$
1992 Mar 7.50	48688.50	8.51073(22)	$2.8(2) \times 10^{-10}$
1992 Mar 12.50	48693.50	8.50861(39)	$2.8(1) \times 10^{-10}$
1992 Mar 17.50	48698.50	8.50579(72)	$2.1(1) \times 10^{-10}$
1992 Mar 22.50	48703.50	8.50297(20)	$2.5(1) \times 10^{-10}$
1992 Mar 27.50	48708.50	8.50124(29)	$1.5(1) \times 10^{-10}$
1992 Apr 1.50	48713.50	8.49920(26)	$2.2(1) \times 10^{-10}$
1992 Apr 6.50	48718.50	8.49659(17)	$2.8(2) \times 10^{-10}$
1992 Apr 11.50	48723.50	8.49415(25)	$1.7(2) \times 10^{-10}$
1992 Apr 16.50	48728.50	8.49243(29)	$1.5(2) \times 10^{-10}$
1992 Apr 21.50	48733.50	8.49047(29)	$2.2(2) \times 10^{-10}$
1992 Apr 26.50	48738.50	8.48892(32)	$1.8(3) \times 10^{-10}$
1992 May 1.50	48743.50	8.48720(42)	$1.2(3) \times 10^{-10}$
1992 May 6.50	48748.50	8.48503(19)	$3.8(2) \times 10^{-10}$
1992 May 11.50	48753.50	8.48321(72)	$1.9(2) \times 10^{-10}$
1992 May 16.50	48758.50	8.48140(27)	$1.9(3) \times 10^{-10}$
1992 May 21.50	48763.50	8.47948(21)	$2.6(2) \times 10^{-10}$
1992 May 26.50	48768.50	8.47706(14)	$2.3(2) \times 10^{-10}$
1992 May 31.50	48773.50	8.47538(17)	$1.8(2) \times 10^{-10}$
1992 Jun 5.50	48778.50	8.47371(31)	$1.7(2) \times 10^{-10}$
1992 Jun 10.50	48783.50	8.47166(72)	$1.7(3) \times 10^{-10}$

Table J.2—Continued

Epoch		Pulse Frequency	20–60 keV Pulsed Flux
Date	MJD	(mHz)	erg cm^{-2} s^{-1}
1992 Jun 15.50	48788.50	8.46961(33)	$1.3(3) \times 10^{-10}$
1992 Jun 20.50	48793.50	8.46853(34)	$1.3(2) \times 10^{-10}$
1992 Jun 25.50	48798.50	8.46682(57)	$1.4(3) \times 10^{-10}$
1992 Jun 30.50	48803.50	8.46500(72)	$1.4(6) \times 10^{-10}$
1992 Jul 5.50	48808.50	8.46319(38)	$1.8(3) \times 10^{-10}$
1992 Jul 10.50	48813.50	8.46081(48)	$1.1(2) \times 10^{-10}$
1992 Jul 15.50	48818.50	8.45933(33)	$1.7(3) \times 10^{-10}$
1992 Jul 20.50	48823.50	8.45797(30)	$1.6(2) \times 10^{-10}$
1992 Jul 25.50	48828.50	8.45630(44)	$1.1(2) \times 10^{-10}$
1992 Jul 30.50	48833.50	8.45605(59)	$1.1(2) \times 10^{-10}$
1992 Aug 4.50	48838.50	8.45362(36)	$1.4(4) \times 10^{-10}$
1992 Aug 9.50	48843.50	8.45227(30)	$1.4(5) \times 10^{-10}$
1992 Aug 14.50	48848.50	8.45065(40)	$1.8(3) \times 10^{-10}$
1992 Aug 19.50	48853.50	8.44915(71)	$0.9(4) \times 10^{-10}$
1992 Aug 24.50	48858.50	8.44765(26)	$2.8(5) \times 10^{-10}$
1992 Aug 29.50	48863.50	8.44594(51)	$1.6(3) \times 10^{-10}$
1992 Sep 3.50	48868.50	8.44536(31)	$2.4(15) \times 10^{-10}$
1992 Sep 8.50	48873.50	8.44249(18)	$2.6(3) \times 10^{-10}$
1992 Sep 13.50	48878.50	8.44042(35)	$1.3(3) \times 10^{-10}$
1992 Sep 18.50	48883.50	8.43816(51)	$1.6(4) \times 10^{-10}$
1992 Sep 23.50	48888.50	8.43646(32)	$1.3(3) \times 10^{-10}$
1992 Sep 28.50	48893.50	8.43464(23)	$2.1(3) \times 10^{-10}$
1992 Oct 3.50	48898.50	8.43215(17)	$2.7(2) \times 10^{-10}$
1992 Oct 8.50	48903.50	8.42979(15)	$3.3(2) \times 10^{-10}$
1992 Oct 13.50	48908.50	8.42786(17)	$2.8(2) \times 10^{-10}$
1992 Oct 18.50	48913.50	8.42504(17)	$2.8(2) \times 10^{-10}$
1992 Oct 23.50	48918.50	8.42292(17)	$2.7(2) \times 10^{-10}$
1992 Oct 28.50	48923.50	8.42142(28)	$1.8(2) \times 10^{-10}$
1992 Nov 2.50	48928.50	8.41959(26)	$1.7(3) \times 10^{-10}$
1992 Nov 7.50	48933.50	8.41763(16)	$2.6(3) \times 10^{-10}$
1992 Nov 12.50	48938.50	8.41505(14)	$3.5(2) \times 10^{-10}$
1992 Nov 17.50	48943.50	8.41269(14)	$3.6(2) \times 10^{-10}$
1992 Nov 22.50	48948.50	8.41010(14)	$3.7(3) \times 10^{-10}$
1992 Nov 27.50	48953.50	8.40789(19)	$2.3(3) \times 10^{-10}$
1992 Dec 2.50	48958.50	8.40589(32)	$1.8(2) \times 10^{-10}$
1992 Dec 7.50	48963.50	8.40324(18)	$2.8(3) \times 10^{-10}$
1992 Dec 12.50	48968.50	8.40146(27)	$1.5(3) \times 10^{-10}$
1992 Dec 17.50	48973.50	8.40032(28)	$1.5(3) \times 10^{-10}$
1992 Dec 22.50	48978.50	8.39784(21)	$2.4(3) \times 10^{-10}$
1992 Dec 27.50	48983.50	8.39556(16)	$3.3(3) \times 10^{-10}$
1993 Jan 1.50	48988.50	8.39290(14)	$4.7(2) \times 10^{-10}$
1993 Jan 6.50	48993.50	8.38969(14)	$4.8(3) \times 10^{-10}$

Table J.2—Continued

Epoch		Pulse Frequency	20–60 keV Pulsed Flux
Date	MJD	(mHz)	erg cm^{-2} s^{-1}
1993 Jan 11.50	48998.50	8.38663(14)	$5.7(2) \times 10^{-10}$
1993 Jan 16.50	49003.50	8.38386(20)	$2.8(2) \times 10^{-10}$
1993 Jan 21.50	49008.50	8.38186(29)	$1.3(2) \times 10^{-10}$
1993 Jan 26.50	49013.50	8.37921(27)	$1.5(2) \times 10^{-10}$
1993 Jan 31.50	49018.50	8.37601(18)	$2.7(2) \times 10^{-10}$
1993 Feb 5.50	49023.50	8.37366(12)	$2.9(2) \times 10^{-10}$
1993 Feb 10.50	49028.50	8.37136(14)	$3.1(2) \times 10^{-10}$
1993 Feb 15.50	49033.50	8.36900(16)	$2.3(2) \times 10^{-10}$
1993 Feb 20.50	49038.50	8.36760(19)	$2.1(2) \times 10^{-10}$
1993 Feb 25.50	49043.50	8.36563(31)	$2.3(4) \times 10^{-10}$
1993 Mar 2.50	49048.50	8.36427(19)	$1.6(4) \times 10^{-10}$
1993 Mar 7.50	49053.50	8.36276(31)	$1.4(2) \times 10^{-10}$
1993 Mar 12.50	49058.50	8.36139(29)	$2.0(3) \times 10^{-10}$
1993 Mar 17.50	49063.50	8.36003(20)	$2.6(2) \times 10^{-10}$
1993 Mar 22.50	49068.50	8.35812(19)	$2.3(3) \times 10^{-10}$
1993 Mar 27.50	49073.50	8.35674(21)	$2.1(4) \times 10^{-10}$
1993 Apr 1.50	49078.50	8.35465(22)	$1.5(4) \times 10^{-10}$
1993 Apr 6.50	49083.50	8.35344(33)	$1.3(2) \times 10^{-10}$
1993 Apr 11.50	49088.50	8.35176(30)	$1.9(2) \times 10^{-10}$
1993 Apr 16.50	49093.50	8.35046(32)	$1.5(3) \times 10^{-10}$
1993 Apr 21.50	49098.50	8.34882(29)	$1.7(2) \times 10^{-10}$
1993 Apr 26.50	49103.50	8.34817(54)	$1.1(2) \times 10^{-10}$
1993 May 1.50	49108.50	8.34621(20)	$1.8(2) \times 10^{-10}$
1993 May 6.50	49113.50	8.34481(70)	$2.9(3) \times 10^{-10}$
1993 May 11.50	49118.50	8.34341(33)	$1.2(4) \times 10^{-10}$
1993 May 16.50	49123.50	8.34260(41)	$1.1(3) \times 10^{-10}$
1993 May 21.50	49128.50	8.34100(51)	$1.6(3) \times 10^{-10}$
1993 May 26.50	49133.50	8.33959(48)	$1.2(3) \times 10^{-10}$
1993 May 31.50	49138.50	8.33825(27)	$2.1(3) \times 10^{-10}$
1993 Jun 5.50	49143.50	8.33671(70)	$1.5(5) \times 10^{-10}$
1993 Jun 10.50	49148.50	8.33516(26)	$1.7(4) \times 10^{-10}$
1993 Jun 15.50	49153.50	8.33338(38)	$1.6(4) \times 10^{-10}$
1993 Jun 20.50	49158.50	8.33190(24)	$3.5(4) \times 10^{-10}$
1993 Jun 25.50	49163.50	8.33024(18)	$2.9(3) \times 10^{-10}$
1993 Jun 30.50	49168.50	8.32801(12)	$4.4(3) \times 10^{-10}$
1993 Jul 5.50	49173.50	8.32638(10)	$3.1(5) \times 10^{-10}$
1993 Jul 10.50	49178.50	8.32450(11)	$3.4(2) \times 10^{-10}$
1993 Jul 15.50	49183.50	8.32241(12)	$4.1(3) \times 10^{-10}$
1993 Jul 20.50	49188.50	8.32014(12)	$3.6(2) \times 10^{-10}$
1993 Jul 25.50	49193.50	8.31802(14)	$3.4(2) \times 10^{-10}$
1993 Jul 30.50	49198.50	8.31570(19)	$1.8(3) \times 10^{-10}$
1993 Aug 4.50	49203.50	8.31254(29)	$1.4(2) \times 10^{-10}$

Table J.2—Continued

Epoch		Pulse Frequency	20–60 keV Pulsed Flux
Date	MJD	(mHz)	erg cm^{-2} s^{-1}
1993 Aug 9.50	49208.50	8.31083(39)	$1.6(2) \times 10^{-10}$
1993 Aug 14.50	49213.50	8.30585(54)	$1.3(6) \times 10^{-10}$
1993 Aug 19.50	49218.50	8.30503(19)	$1.5(5) \times 10^{-10}$
1993 Aug 24.50	49223.50	8.30323(18)	$2.1(2) \times 10^{-10}$
1993 Aug 29.50	49228.50	8.29961(11)	$5.0(3) \times 10^{-10}$
1993 Sep 3.50	49233.50	8.29620(9)	$8.7(3) \times 10^{-10}$
1993 Sep 8.50	49238.50	8.29267(11)	$12.4(3) \times 10^{-10}$
1993 Sep 13.50	49243.50	8.28869(10)	$11.6(4) \times 10^{-10}$
1993 Sep 18.50	49248.50	8.28489(20)	$4.2(4) \times 10^{-10}$
1993 Sep 23.50	49253.50	8.28328(29)	$2.1(3) \times 10^{-10}$
1993 Sep 28.50	49258.50	8.28095(32)	$2.0(3) \times 10^{-10}$
1993 Oct 3.50	49263.50	8.27994(24)	$2.6(4) \times 10^{-10}$
1993 Oct 8.50	49268.50	8.27721(36)	$1.5(3) \times 10^{-10}$
1993 Oct 13.50	49273.50	8.27558(52)	$0.9(4) \times 10^{-10}$
1993 Oct 18.50	49278.50	8.27558(59)	$1.3(2) \times 10^{-10}$
1993 Oct 23.50	49283.50	8.27539(68)	$1.4(6) \times 10^{-10}$
1993 Oct 28.50	49288.50	8.27521(29)	$2.5(6) \times 10^{-10}$
1993 Nov 2.50	49293.50	8.27523(23)	$3.6(7) \times 10^{-10}$
1993 Nov 7.50	49298.50	8.27334(29)	$3.1(5) \times 10^{-10}$
1993 Nov 12.50	49303.50	8.27114(31)	$2.4(5) \times 10^{-10}$
1993 Nov 17.50	49308.50	8.26878(22)	$3.6(4) \times 10^{-10}$
1993 Nov 22.50	49313.50	8.26638(17)	$4.1(5) \times 10^{-10}$
1993 Nov 27.50	49318.50	8.26389(13)	$3.4(3) \times 10^{-10}$
1993 Dec 2.50	49323.50	8.26158(13)	$3.3(3) \times 10^{-10}$
1993 Dec 7.50	49328.50	8.25921(14)	$2.7(3) \times 10^{-10}$
1993 Dec 12.50	49333.50	8.25680(16)	$3.4(2) \times 10^{-10}$
1993 Dec 17.50	49338.50	8.25447(14)	$4.3(3) \times 10^{-10}$
1993 Dec 22.50	49343.50	8.25155(33)	$2.5(4) \times 10^{-10}$
1993 Dec 27.50	49348.50	8.24900(68)	$0.8(5) \times 10^{-10}$
1994 Jan 1.50	49353.50	8.24645(68)	$1.7(7) \times 10^{-10}$
1994 Jan 6.50	49358.50	8.24390(68)	$1.3(5) \times 10^{-10}$
1994 Jan 11.50	49363.50	8.24135(29)	$1.6(5) \times 10^{-10}$
1994 Jan 16.50	49368.50	8.24093(49)	$1.0(3) \times 10^{-10}$
1994 Jan 21.50	49373.50	8.24087(68)	$0.9(4) \times 10^{-10}$
1994 Jan 26.50	49378.50	8.24082(68)	$0.7(5) \times 10^{-10}$
1994 Jan 31.50	49383.50	8.24077(68)	$0.9(5) \times 10^{-10}$
1994 Feb 5.50	49388.50	8.24072(33)	$1.2(4) \times 10^{-10}$
1994 Feb 10.50	49393.50	8.24003(68)	$1.8(4) \times 10^{-10}$
1994 Feb 15.50	49398.50	8.23934(42)	$2.3(10) \times 10^{-10}$
1994 Feb 20.50	49403.50	8.23739(57)	$1.1(6) \times 10^{-10}$
1994 Feb 25.50	49408.50	8.23714(47)	$0.8(4) \times 10^{-10}$
1994 Mar 2.50	49413.50	8.23667(37)	$1.3(2) \times 10^{-10}$

Table J.2—Continued

Epoch		Pulse Frequency	20–60 keV Pulsed Flux
Date	MJD	(mHz)	erg cm^{-2} s^{-1}
1994 Mar 7.50	49418.50	8.23605(31)	$1.5(3) \times 10^{-10}$
1994 Mar 12.50	49423.50	8.23442(20)	$1.7(6) \times 10^{-10}$
1994 Mar 17.50	49428.50	8.23430(68)	$1.2(4) \times 10^{-10}$
1994 Mar 22.50	49433.50	8.23417(68)	$0.8(4) \times 10^{-10}$
1994 Mar 27.50	49438.50	8.23404(54)	$0.9(3) \times 10^{-10}$
1994 Apr 1.50	49443.50	8.23240(22)	$2.1(4) \times 10^{-10}$
1994 Apr 6.50	49448.50	8.23150(18)	$3.9(3) \times 10^{-10}$
1994 Apr 11.50	49453.50	8.23098(18)	$3.2(5) \times 10^{-10}$
1994 Apr 16.50	49458.50	8.22860(37)	$1.7(3) \times 10^{-10}$
1994 Apr 21.50	49463.50	8.22736(68)	$1.1(4) \times 10^{-10}$
1994 Apr 26.50	49468.50	8.22619(50)	$1.0(6) \times 10^{-10}$
1994 May 1.50	49473.50	8.22493(25)	$1.2(5) \times 10^{-10}$
1994 May 6.50	49478.50	8.22360(23)	$1.4(3) \times 10^{-10}$
1994 May 11.50	49483.50	8.22228(26)	$2.2(2) \times 10^{-10}$
1994 May 16.50	49488.50	8.22145(30)	$1.7(6) \times 10^{-10}$
1994 May 21.50	49493.50	8.22201(50)	$1.3(4) \times 10^{-10}$
1994 May 26.50	49498.50	8.22118(28)	$1.9(7) \times 10^{-10}$
1994 May 31.50	49503.50	8.21900(42)	$1.6(2) \times 10^{-10}$
1994 Jun 5.50	49508.50	8.21847(28)	$2.2(5) \times 10^{-10}$
1994 Jun 10.50	49513.50	8.21612(50)	$1.1(4) \times 10^{-10}$
1994 Jun 15.50	49518.50	8.21363(38)	$1.9(7) \times 10^{-10}$
1994 Jun 20.50	49523.50	8.21328(29)	$1.6(4) \times 10^{-10}$
1994 Jun 25.50	49528.50	8.21092(25)	$1.7(4) \times 10^{-10}$
1994 Jun 30.50	49533.50	8.20956(26)	$1.5(4) \times 10^{-10}$
1994 Jul 5.50	49538.50	8.20781(20)	$2.3(3) \times 10^{-10}$
1994 Jul 10.50	49543.50	8.20593(53)	$1.1(3) \times 10^{-10}$
1994 Jul 15.50	49548.50	8.20546(20)	$2.2(3) \times 10^{-10}$
1994 Jul 20.50	49553.50	8.20412(67)	$1.9(4) \times 10^{-10}$
1994 Jul 25.50	49558.50	8.20279(15)	$4.3(3) \times 10^{-10}$
1994 Jul 30.50	49563.50	8.20229(11)	$6.1(3) \times 10^{-10}$
1994 Aug 4.50	49568.50	8.20139(27)	$2.9(4) \times 10^{-10}$
1994 Aug 9.50	49573.50	8.19986(18)	$2.6(4) \times 10^{-10}$
1994 Aug 14.50	49578.50	8.19886(24)	$1.1(3) \times 10^{-10}$
1994 Aug 19.50	49583.50	8.19818(20)	$1.4(2) \times 10^{-10}$
1994 Aug 24.50	49588.50	8.19780(21)	$1.4(2) \times 10^{-10}$
1994 Aug 29.50	49593.50	8.19677(31)	$1.5(2) \times 10^{-10}$
1994 Sep 3.50	49598.50	8.19647(22)	$1.6(3) \times 10^{-10}$
1994 Sep 8.50	49603.50	8.19559(23)	$2.3(3) \times 10^{-10}$
1994 Sep 13.50	49608.50	8.19496(15)	$2.3(3) \times 10^{-10}$
1994 Sep 18.50	49613.50	8.19387(16)	$3.1(3) \times 10^{-10}$
1994 Sep 23.50	49618.50	8.19325(12)	$2.8(4) \times 10^{-10}$
1994 Sep 28.50	49623.50	8.19231(12)	$2.9(2) \times 10^{-10}$

Table J.2—Continued

Epoch		Pulse Frequency	20–60 keV Pulsed Flux
Date	MJD	(mHz)	erg cm^{-2} s^{-1}
1994 Oct 3.50	49628.50	8.19184(17)	$2.6(2) \times 10^{-10}$
1994 Oct 8.50	49633.50	8.19089(12)	$3.1(4) \times 10^{-10}$
1994 Oct 13.50	49638.50	8.19010(9)	$4.6(3) \times 10^{-10}$
1994 Oct 18.50	49643.50	8.18958(10)	$6.1(2) \times 10^{-10}$
1994 Oct 23.50	49648.50	8.18915(10)	$6.9(3) \times 10^{-10}$
1994 Oct 28.50	49653.50	8.18883(9)	$6.4(3) \times 10^{-10}$
1994 Nov 2.50	49658.50	8.18894(8)	$8.0(3) \times 10^{-10}$
1994 Nov 7.50	49663.50	8.18975(8)	$8.6(3) \times 10^{-10}$
1994 Nov 12.50	49668.50	8.19101(8)	$9.0(3) \times 10^{-10}$
1994 Nov 17.50	49673.50	8.19209(8)	$9.5(2) \times 10^{-10}$
1994 Nov 22.50	49678.50	8.19352(7)	$9.6(3) \times 10^{-10}$
1994 Nov 27.50	49683.50	8.19477(7)	$12.3(4) \times 10^{-10}$
1994 Dec 2.50	49688.50	8.19613(7)	$8.6(4) \times 10^{-10}$
1994 Dec 7.50	49693.50	8.19752(8)	$12.4(3) \times 10^{-10}$
1994 Dec 12.50	49698.50	8.19891(8)	$9.3(4) \times 10^{-10}$
1994 Dec 17.50	49703.50	8.20004(8)	$8.0(3) \times 10^{-10}$
1994 Dec 22.50	49708.50	8.20112(8)	$7.9(3) \times 10^{-10}$
1994 Dec 27.50	49713.50	8.20239(8)	$8.1(3) \times 10^{-10}$
1995 Jan 1.50	49718.50	8.20368(8)	$9.5(3) \times 10^{-10}$
1995 Jan 6.50	49723.50	8.20481(8)	$9.9(3) \times 10^{-10}$
1995 Jan 11.50	49728.50	8.20578(8)	$9.7(3) \times 10^{-10}$
1995 Jan 16.50	49733.50	8.20665(6)	$8.7(3) \times 10^{-10}$
1995 Jan 21.50	49738.50	8.20760(6)	$9.0(2) \times 10^{-10}$
1995 Jan 26.50	49743.50	8.20840(9)	$8.0(3) \times 10^{-10}$
1995 Jan 31.50	49748.50	8.20940(9)	$9.0(4) \times 10^{-10}$
1995 Feb 5.50	49753.50	8.21009(9)	$7.5(4) \times 10^{-10}$
1995 Feb 10.50	49758.50	8.21066(10)	$8.2(4) \times 10^{-10}$
1995 Feb 15.50	49763.50	8.21117(10)	$7.9(4) \times 10^{-10}$
1995 Feb 20.50	49768.50	8.21165(7)	$10.8(4) \times 10^{-10}$
1995 Feb 25.50	49773.50	8.21178(8)	$9.8(3) \times 10^{-10}$
1995 Mar 2.50	49778.50	8.21186(10)	$10.1(3) \times 10^{-10}$
1995 Mar 7.50	49783.50	8.21187(8)	$10.0(5) \times 10^{-10}$
1995 Mar 12.50	49788.50	8.21158(8)	$7.5(4) \times 10^{-10}$
1995 Mar 17.50	49793.50	8.21095(8)	$7.8(3) \times 10^{-10}$
1995 Mar 22.50	49798.50	8.21020(12)	$6.1(4) \times 10^{-10}$
1995 Mar 27.50	49803.50	8.20946(13)	$4.9(4) \times 10^{-10}$
1995 Apr 1.50	49808.50	8.20837(19)	$3.1(4) \times 10^{-10}$
1995 Apr 6.50	49813.50	8.20750(31)	$1.7(4) \times 10^{-10}$
1995 Apr 11.50	49818.50	8.20592(46)	$1.5(3) \times 10^{-10}$
1995 Apr 16.50	49823.50	8.20070(45)	$1.3(6) \times 10^{-10}$
1995 Apr 21.50	49828.50	8.19745(67)	$0.8(3) \times 10^{-10}$
1995 Apr 26.50	49833.50	8.19421(16)	$3.4(5) \times 10^{-10}$

Table J.2—Continued

Epoch		Pulse Frequency	20–60 keV Pulsed Flux
Date	MJD	(mHz)	erg cm^{-2} s^{-1}
1995 May 1.50	49838.50	8.18930(12)	$3.6(4) \times 10^{-10}$
1995 May 6.50	49843.50	8.18678(30)	$1.2(3) \times 10^{-10}$
1995 May 11.50	49848.50	8.18497(14)	$3.4(4) \times 10^{-10}$
1995 May 16.50	49853.50	8.18295(13)	$4.4(3) \times 10^{-10}$
1995 May 21.50	49858.50	8.18081(12)	$6.7(3) \times 10^{-10}$
1995 May 26.50	49863.50	8.17784(14)	$4.7(4) \times 10^{-10}$
1995 May 31.50	49868.50	8.17528(11)	$7.5(3) \times 10^{-10}$
1995 Jun 5.50	49873.50	8.17277(20)	$6.5(4) \times 10^{-10}$
1995 Jun 10.50	49878.50	8.17050(19)	$3.3(5) \times 10^{-10}$
1995 Jun 15.50	49883.50	8.16841(11)	$8.6(6) \times 10^{-10}$
1995 Jun 20.50	49888.50	8.16626(10)	$6.5(4) \times 10^{-10}$
1995 Jun 25.50	49893.50	8.16421(11)	$5.5(4) \times 10^{-10}$
1995 Jun 30.50	49898.50	8.16195(14)	$4.9(4) \times 10^{-10}$
1995 Jul 5.50	49903.50	8.16068(15)	$4.0(4) \times 10^{-10}$
1995 Jul 10.50	49908.50	8.15896(10)	$7.4(3) \times 10^{-10}$
1995 Jul 15.50	49913.50	8.15747(11)	$8.2(3) \times 10^{-10}$
1995 Jul 20.50	49918.50	8.15660(12)	$4.9(3) \times 10^{-10}$
1995 Jul 25.50	49923.50	8.15475(10)	$7.9(2) \times 10^{-10}$
1995 Jul 30.50	49928.50	8.15195(12)	$4.6(3) \times 10^{-10}$
1995 Aug 4.50	49933.50	8.15028(9)	$6.0(3) \times 10^{-10}$
1995 Aug 9.50	49938.50	8.14882(11)	$5.7(2) \times 10^{-10}$
1995 Aug 14.50	49943.50	8.14712(15)	$4.1(4) \times 10^{-10}$
1995 Aug 19.50	49948.50	8.14533(24)	$2.1(4) \times 10^{-10}$
1995 Aug 24.50	49953.50	8.14542(10)	$6.7(4) \times 10^{-10}$
1995 Aug 29.50	49958.50	8.14388(11)	$5.8(3) \times 10^{-10}$
1995 Sep 3.50	49963.50	8.14249(9)	$12.2(3) \times 10^{-10}$
1995 Sep 8.50	49968.50	8.13965(13)	$10.2(4) \times 10^{-10}$
1995 Sep 13.50	49973.50	8.13773(14)	$5.5(5) \times 10^{-10}$
1995 Sep 18.50	49978.50	8.13649(9)	$15.7(4) \times 10^{-10}$
1995 Sep 23.50	49983.50	8.13355(10)	$6.5(5) \times 10^{-10}$
1995 Sep 28.50	49988.50	8.13177(11)	$6.0(3) \times 10^{-10}$
1995 Oct 3.50	49993.50	8.13015(11)	$5.1(4) \times 10^{-10}$
1995 Oct 8.50	49998.50	8.12903(10)	$4.7(4) \times 10^{-10}$
1995 Oct 13.50	50003.50	8.12765(9)	$12.6(2) \times 10^{-10}$
1995 Oct 18.50	50008.50	8.12537(11)	$7.3(4) \times 10^{-10}$
1995 Oct 23.50	50013.50	8.12235(10)	$9.4(4) \times 10^{-10}$
1995 Oct 28.50	50018.50	8.12007(11)	$4.3(3) \times 10^{-10}$
1995 Nov 2.50	50023.50	8.11853(10)	$11.5(5) \times 10^{-10}$

References

Becker, R., Boldt, E., Holt, S., Pravdo, S., Rothschild, R., Serlemitsos, P., & Swank, J. 1976. Spectral variability in the X-ray pulsar GX 1+4. *Astrophys. J.*, **207**, L167.

Coe, M. J., Engel, A. R., Evans, A. J., & Quenby, J. J. 1981. Ariel 5 hard X-ray studies of the Galactic center region. *Astrophys. J.*, **243**, 155.

Cutler, E. P., Dennis, B. R., & Dolan, J. F. 1986. An elliptical binary orbit model of GX 1+4. *Astrophys. J.*, **300**, 551.

Damle, S. V., Kunte, P. K., Leahy, D. A., Naranan, S., Streekantan, B. V., & Venkatesan, D. 1988. High energy X-ray timing and spectral observations of Sco X-1, Cyg X-1, GX 5–1, Cyg X-3, and GX 1+4. *Adv. Space Res*, **8**, (2)415.

Dotani, T., Kii, T., Nagase, F., Makishima, K., Ohashi, T., Sakao, T., Koyama, K., & Tuohy, I. R. 1989. Peculiar pulse profile of GX 1+4 observed in the spin-down phase. *Pub. Astron. Soc. Japan*, **41**, 427.

Doty, J., Hoffman, J., & Lewin, W. H. G. 1981. SAS-3 observations of GX 1+4. *Astrophys. J.*, **243**, 257.

Elsner, R. F., Weisskopf, M. C., Apparao, K. M. V., Darbro, W., Ramsey, B. D., Williams, A. C., Grindlay, J. E., & Sutherland, P. G. 1985. X-ray observations of GX 1+4 with the Monitor Proportional Counter on board the Einstein Observatory. *Astrophys. J.*, **297**, 288.

Greenhill, J. G., Sharma, D. P., Dieters, S. W. B., Sood, R. K., Waldron, L., & Storey, M. C. 1993. Observations and modelling of the hard X-ray emission from GX 1+4. *Mon. Not. R. Astron. Soc.*, **260**, 21.

Kendziorra, E., Staubert, R., Reppin, C., Pietsch, W., Voges, W., & Trumper, J. 1982. The pulsating X-ray source GX 1+4 (4U 1728–24). In *Galactic X-Ray Sources*, ed. P. Sanford, P. Laskarides, & J. Salton (New York: Wiley), 205.

Koo, J. W. & Haymes, R. C. 1980. The hard X-ray periodicity of GX 1+4. *Astrophys. J.*, **239**, L57.

Laurent, P. et al. 1993. Photon spectrum and period evolution of GX 1+4 as observed at hard X-ray energies by SIGMA. *Astron. & Astrophys.*, **278**, 444.

Leahy, D. 1989. Determination of pulse period of GX 1+4 in hard X-rays. *Bull. Amer. Astron. Soc.*, **21**, 749.

Lewin, W. H. G., Ricker, G. R., & McClintock, J. E. 1971. X-rays from a new variable source GX 1+4. *Astrophys. J.*, **169**, L17.

Lutovinov, A. A., Grebenev, S. A., Sunyaev, R. A., & Pavlinsky, M. N. 1994. Timing of X-ray pulsars from data obtained with the ART-P telescope of the Granat space observatory in 1990–1992. *Astron. Lett.*, **20**, 538.

Makishima, K. et al. 1988. Spin-down of the X-ray pulsar GX 1+4 during an extended low state. *Nature*, **333**, 746.

Mony, B. et al. 1991. Hard X-ray observations of GX 1+4. *Astron. & Astrophys.*, **247**, 405.

Rao, A. R., Paul, B., Chitnis, V. R., Agrawal, P. C., & Manchanda, R. K. 1994. Detection of a very hard X-ray pulse fraction in the bright state of GX 1+4. *Astron. & Astrophys.*, **289**, L43.

Ricketts, M., Hall, R., Page, C., Whitford, C., & Pounds, K. 1982. GX 1+4: pulse period measurement and detection of phase-variable iron line emission. *Mon. Not. R. Astron. Soc.*, **201**, 759.

Sakao, T. et al. 1990. When will the peculiar X-ray pulsar GX 1+4 resume fast spin-up? *Mon. Not. R. Astron. Soc.*, **246**, 11P.

Strickman, M. S., Johnson, W. N., & Kurfess, J. D. 1980. The hard X-ray pulse profile of GX 1+4. *Astrophys. J.*, **240**, L21.

White, N., Mason, K., Huckle, H., Charles, P., & Sanford, P. 1977. Periodic modulations of three Galactic X-ray sources. *Astrophys. J.*, **209**, L119.

Colophon

This thesis was produced using the LaTeX version 2.09 document preparation system by Leslie Lamport and the TeX version 3.141 typesetting system by Donald Knuth. The LaTeX output was converted to printable PostScript page description language using version 5.58b of the `dvips` program. Stuart Anderson adapted the `ucthesis` LaTeX 2.09 style file and AASTeX macros from the American Astronomical Society to produce the `srlthesis` style file, which conforms to the Caltech guidelines due to his efforts. This thesis uses a variant of this style file created by the present author, `srlthesis_chapref`.

Most of the figures were created using the IDL version 3.5.1 scientific data analysis system by Research Systems, Inc. The figures for Chapter 4 were produced using the SM version 2.2.1B plotting program by Robert Lupton and Patricia Monger. The figure for Appendix E was created using Claris CAD version 2.0v3 for the Apple Macintosh.